

*Nanoscale Dispensing
of
Single Ultrasmall Droplets*

INAUGURALDISSERTATION

zur

Erlangung der Würde eines Doktors der Philosophie

vorgelegt der

Philosophisch-Naturwissenschaftlichen Fakultät

der Universität Basel

von

André Meister

aus Matzendorf (So)

Basel, 2005

Genehmigt von der Philosophisch-Naturwissenschaftlichen Fakultät auf Antrag
der Herren

Professor Dr. E. Meyer

Privatdozent Dr. H. Heinzelmann

Basel, den 21. September 2004

Prof. Dr. Hans-Jakob Wirz, Dekan

Abstract

Nanoscale dispensing (NADIS) is a novel technique to deposit material at micrometric and submicrometric dimensions. It has great flexibility in feature shape and choice of deposited material. Due to its expected low cost and short turn-around time, it has the potential to be an interesting tool complementary to standard lithographic processes. Furthermore, NADIS has a great potential in the creation of high-density microarrays used in proteomics or genomics.

The key feature of NADIS is the deposition of a liquid through an aperture created in a scanning force microscopy probe tip. The liquid is loaded into the hollow back of the pyramidal probe tip. Upon contact, liquid is transferred from the tip to the substrate surface. The transfer of liquid occurs without any external pressure. The control of the NADIS probe displacement is achieved using a standard atomic force microscope.

Two different approaches to fabricate tips with apertures were investigated. The first approach relies on opening the tip during the microfabrication of the probe, whereas the second approach implies a modification of commercially available probes by focused ion beam milling. Both kinds of probes have shown their ability to perform successfully the dispensing of droplets.

Nanoscale dispensing has been demonstrated for deposition of ultrasmall single droplets with volumes down to 5 attoliters in a controlled way and with high lateral accuracy. The smallest droplet spacing that has been achieved was less than 500 nm. The size of the droplets and the possible droplet density are largely dependent on the aperture diameter and on the surface wettability.

Nanoparticles and fluorescent molecules were also dispensed. In such cases, the liquid is used as a transport medium for the substances to be deposited.

By moving the NADIS probe during contact on the substrate, it was possible to write features such as lines with sizes that can be as small as 400 nm.

Some theoretical aspects are discussed, in particular the capillary forces associated with axisymmetric liquid menisci. Experimentally measured capillary forces during the dispensing are compared with theoretically determined values.

Acknowledgments

Many people have helped me, directly or indirectly, to bring to end my thesis presented herein.

I would like to express my sincere gratitude to my supervisor, PD. Dr. Harry Heinzlmann from CSEM SA, who gave me the opportunity to do my graduate study in the best conditions. He offered me the possibility to work in an independent way, and was always available to answer my question, despite his busy agenda.

I would like to address my cordial thanks to Prof. Dr. Ernst Meyer from the University of Basel, who spontaneously accepted to be my Faculty Responsible.

I would also like to express my thanks to Dr. Terunobu Akiyama, Prof. Dr. Urs Staufer and Prof. Dr. Nico De Rooij, from IMT at the University of Neuchâtel for supplying me with the probes with microfabricated apertures and for valuable discussions, and to Phillippe Gasser from EMPA for operating the FIB instrument.

I am particularly indebted to the entire nano and bio group, especially to Sivashankar Krishnamoorthy and to Dr. Christian Hinderling for providing me with the substrates made of PS-b-P2VP micelles, to Dr. Raphaël Pugin, my superior, and to Dr. Martha Liley for their many enlightening discussions and continuous encouragements, but also to Dr. Caterina Minelli, Dr. Kaspar Cottier, Dr. Rolf Eckert, Dr. Rino E. Kunz, Dr Guy Voirin, Myriam Losson, Véronique Monnier, Eric Bernard, Nicolas Blondiaux, and Réal Ischer. All have participated to continuously maintain a friendly environment.

I am very grateful to Prof. Dr. Jürgen Brugger, Prof. Dr. Peter Vettiger and Prof. Dr. Rolf P. Steiger for their numerous interesting discussions.

A special thanks to Top Nano 21, to the National Center of Competence in Research (NCCR) in nanoscale science, and to the Swiss Federal Office for Education and Science (OFES) in the framework of the EC-funded project NaPa (Contract no.NMP4-CT-2003-500120) for their partial financial support.

And last but not least, I would like to sincerely thank my wife Carole, who had always trust in my work, even in the periods where I was full of doubt. She gave me continuous support, and was of valuable assistance.

Table of contents

1. Introduction	1
2. Theoretical background.....	5
2.1. Forces that hold together atoms or molecules in a condensate.....	5
2.1.1. The Origins of the forces	5
2.1.1.1. Electrostatic and electrodynamic interaction	6
2.1.1.1a. Purely electrostatic interactions	6
2.1.1.1b. Polarization forces	7
2.1.1.1c. London dispersion forces	7
2.1.1.2. Van der Waals forces	8
2.1.2. Molecular and atomic condensates	9
2.1.2.1. Intramolecular interactions (atoms form molecules)	9
2.1.2.2. Intermolecular interactions (molecules form a condensate)	10
2.1.2.3. Interatomic interactions (atoms form a condensate)	10
2.2. Interactions between macroscopic bodies.....	12
2.2.1. Surface Free Energy and Cohesion	12
2.2.2. Interfacial Energy and Adhesion.....	14
2.2.2.1. Film pressure.....	15
2.2.3. Forces between condensed bodies	16
2.2.3.1. Adhesion forces between macroscopic objects.....	16
2.2.3.2. Van der Waals forces between macroscopic objects	16
2.3. Liquids on surfaces	18
2.3.1. Laplace pressure.....	18
2.3.2. Contact angle	20
2.3.2.1. Spreading coefficient	22
2.3.2.2. Influence of the surface roughness on the contact angle	23
2.3.2.2a. Wenzel's approach	23
2.3.2.2b. Cassie's approach	23
2.3.2.3. Contact line tension	24
2.3.2.4. Contact angle hysteresis.....	25
2.3.3. Hydrostatic equilibrium	26
2.3.4. Numerical construction of an axisymmetric liquid-gas interface	27
2.3.4.1. Shapes of pendent and sessile drops	28
2.3.4.2. Axisymmetric shapes when neglecting gravity	29
2.3.4.2a. Axisymmetric shapes with a zero mean surface curvature	30
2.3.4.2b. Axisymmetric shapes with a positive mean surface curvature	30
2.3.4.2c. Axisymmetric shapes with a negative mean surface curvature	31
2.3.4.3. Meniscus stability	32
2.3.5. Capillary forces.....	33
2.3.5.1. Capillary force due to the surface tension.....	33
2.3.5.2. Capillary force due to the Laplace pressure.....	34
2.3.5.3. Capillary force for axisymmetric meniscus	34
2.3.6. Thermodynamic equilibrium and spontaneous condensation	35
2.3.6.1. Capillary force induced by a spontaneously condensed meniscus.....	37

3. Experimental setup	38
3.1. Atomic force microscope.....	38
3.1.1. Typical AFM set-up.....	38
3.1.1.1. AFM operating modes	39
3.1.1.2. Hysteresis of the piezoelectric scanner	40
3.2. Contact angle measurement.....	41
3.2.1. Surface tension measurement of liquids	42
3.3. Miscellaneous	43
4. Probes realization	44
4.1. Microfabrication	44
4.2. Probes with microfabricated apertures	46
4.2.1. 1 st version of microfabricated probes.....	46
4.2.1.1. Cantilever stiffness and loading area	47
4.2.2. 2 nd version of microfabricated probes	48
4.3. Probes with apertures opened by FIB.....	50
4.3.1. Reflection of the laser beam for V-shaped cantilever with loading area	55
5. Methods	57
5.1. List of chemicals.....	57
5.1.1. Choice of liquid to be deposited	57
5.1.2. List of solvents and chemicals	57
5.2. Preparation of the substrate	59
5.2.1. Substrate materials	59
5.2.2. Substrate cleaning	59
5.2.2.1. Piranha	59
5.2.2.2. SC-1	60
5.2.2.3. Oxygen plasma	60
5.2.3. Surface treatment	60
5.2.4. Behavior of the deposited liquids on the substrates	61
5.3. Probe preparation and characterization	63
5.3.1. Preparation of the loading area for the FIB-modified probes	63
5.3.1.1. Hydrophobic-hydrophilic contrast of gold relative to silicon nitride.....	63
5.3.2. Spring constant determination	64
5.3.2.1. Resonance frequency	65
5.3.2.2. Thermally induced oscillation.....	69
5.4. Dispensing of the droplets	73
5.4.1. Loading of the probe.....	73
5.4.1.1. Shape of the loading area.....	73
5.4.1.2. Filling of the hollow tip	74
5.4.1.3. Determination of the amount of loaded liquid.....	75
5.4.1.3a. Evaporation of the liquid from the loading area	76
5.4.2. Transfer of liquid characterization by deflection-distance curves	77
5.4.3. Measurement of the capillary force	79
5.4.4. Dispensing of the droplets to form a pattern.....	79
5.4.5. Cleaning of the probe.....	80
5.5. Characterization of the droplets.....	81

5.5.1. How to determine the volume of the deposited drop	81
5.5.1.1. By the droplet dimension	81
5.5.1.2. By the shift in resonance frequency	82
5.5.1.3. By the capillary force	82
5.5.2. Visualization of the deposited droplets	82
5.5.2.1. Optical imaging	82
5.5.2.2. AFM imaging	82
5.5.2.2a. Localization of the deposition area	83
5.5.2.2b. What is seen after the deposition	83
6. Results and discussion	84
6.1. Typical results of droplet deposition	84
6.1.1. Deposition using probes with microfabricated aperture	84
6.1.2. Deposition using FIB-modified probes	85
6.2. Parameters that influence the amount of deposited liquid	86
6.2.1. Aperture size and tip geometry	86
6.2.1.1. Position of the aperture in the FIB-modified probes	87
6.2.2. Surface energy of the sample	88
6.2.2.1. Hydrophilic substrate with hydrophilic outer tip wall	89
6.2.3. Contact time and number of contacts	91
6.2.3.1. Influence on the droplet diameter	91
6.2.3.2. Influence on the droplet height	92
6.2.4. Withdrawal speed	94
6.2.5. Laplace pressure	95
6.3. Capillary force measurements and meniscus shapes	96
6.3.1. Example of a meniscus shape with a probe having a microfabricated aperture	98
6.3.2. Example of a meniscus shape with a FIB-modified probe	99
6.4. Evaporation of the droplets and residual dots	100
6.4.1. Evaporation time	100
6.4.2. Residual dots after the evaporation	104
6.4.2.1. Position of the residual dot	107
6.5. Deposition of molecules, and nanoparticles	109
6.5.1. Deposition of droplets with fluorescent molecules	109
6.5.2. Deposition of droplets with nanoparticles	109
6.5.2.1. Deposition of droplets with 365 nm wide silicon dioxide particles	110
6.5.2.2. Deposition of droplets with 20 nm wide polystyrene nanoparticles	111
6.5.2.2a. Dispensing with probes having a microfabricated aperture	111
6.5.2.2b. Dispensing with probe modified by FIB	112
6.6. Deposition on hydrophobic substrates for small droplet spacing	115
6.7. Modification of block-copolymer micelle layers	117
7. Conclusion	121
7.1. Application of nanodispensing	122
7.2. Outlook	123
8. Annexes	124
8.1. Annex 1	124
8.1.1. Young's equation	124

8.2. Annex 2	126
8.2.1. Program.....	127
8.3. Annex 3	130
8.4. Annex 4	134
8.4.1. Evaporation of a sessile droplet	134
8.4.1.1. With a pinned three-phase contact line.....	134
8.4.1.2. With a constant contact angle	134
9. References	136

1. Introduction

Liquid handling has various aspects and is involved in a large range of activities, from water distribution in a building to the precise deposition of a drop of ink onto paper in an inkjet printer. The devices used for the different applications of liquid handling are based on diverse technologies as various as sanitary facilities or high-tech microelectromechanical systems (MEMS). The usual containers for liquid found in daily life permit the control of volumes that are between some liters and a centiliter. A controlled handling of smaller volumes of liquids, e.g. for the preparation of a solution with a precise concentration in a chemical laboratory, usually involves syringes or pipettes. Medical syringes handle volumes in the milliliter range and above, pipettes deal with volumes in the milliliter to microliter range, and the sub-microliter domain is accessible with Hamilton syringes [1].

The pharmaceutical industry commonly uses microtiter plates (or microplates) in combinatorial chemistry or in high throughput screening. Standard microplates have 96, 384 or 1536 wells, with volume of liquid in each well of about 100, 20 and 5 microliters respectively. Because manual pipetting is limited in turn-around time, the microplate platform uses dispensing robots with many pipettes in parallel for a higher throughput and automated use [2]. Normal pipetting systems are limited to volumes above 200 nanoliters, because of problems of drop release from the pipette nozzle.

Another dispensing method used with microplates is the dosing system. In this method, the liquid is pressurized using a pump unit, and a high-speed valve releases the liquid through a narrow orifice. The liquid is expelled as a free flying jet. The volume of the dispensed liquid is controlled through the opening time of the valve. Such dispenser robots are able to control volumes down to 25 nanoliters [3].

The emergence of the microarray platform in the nineties has further increased the throughput of chemical and biological analyses, and, in parallel, considerably reduced the consumption of chemicals in the assays. Microarrays are highly parallel biological assays, which rely on the affinity between two molecules (receptor and analyte molecules). The two molecules can be complementary ssDNA (single strand deoxyribonucleic acid), or antigen antibody pair. The two complementary molecules react together with a lock-and-key effect. During the creation of microarrays, different receptor molecules are fixed on a substrate (usually a glass slide) to form a matrix of spots with different functionalities. The sample (liquid containing the analyte molecules) is brought into contact with the fixed receptor molecules. If two complementary molecules come close together, they bind and remain bound during rinsing and washing of the substrate. Detection is performed using e.g. fluorescent or chemiluminescent labels. The readout is done by the determination of the fluorescence or chemiluminescence pattern relative to the positions of the spots of receptor molecules.

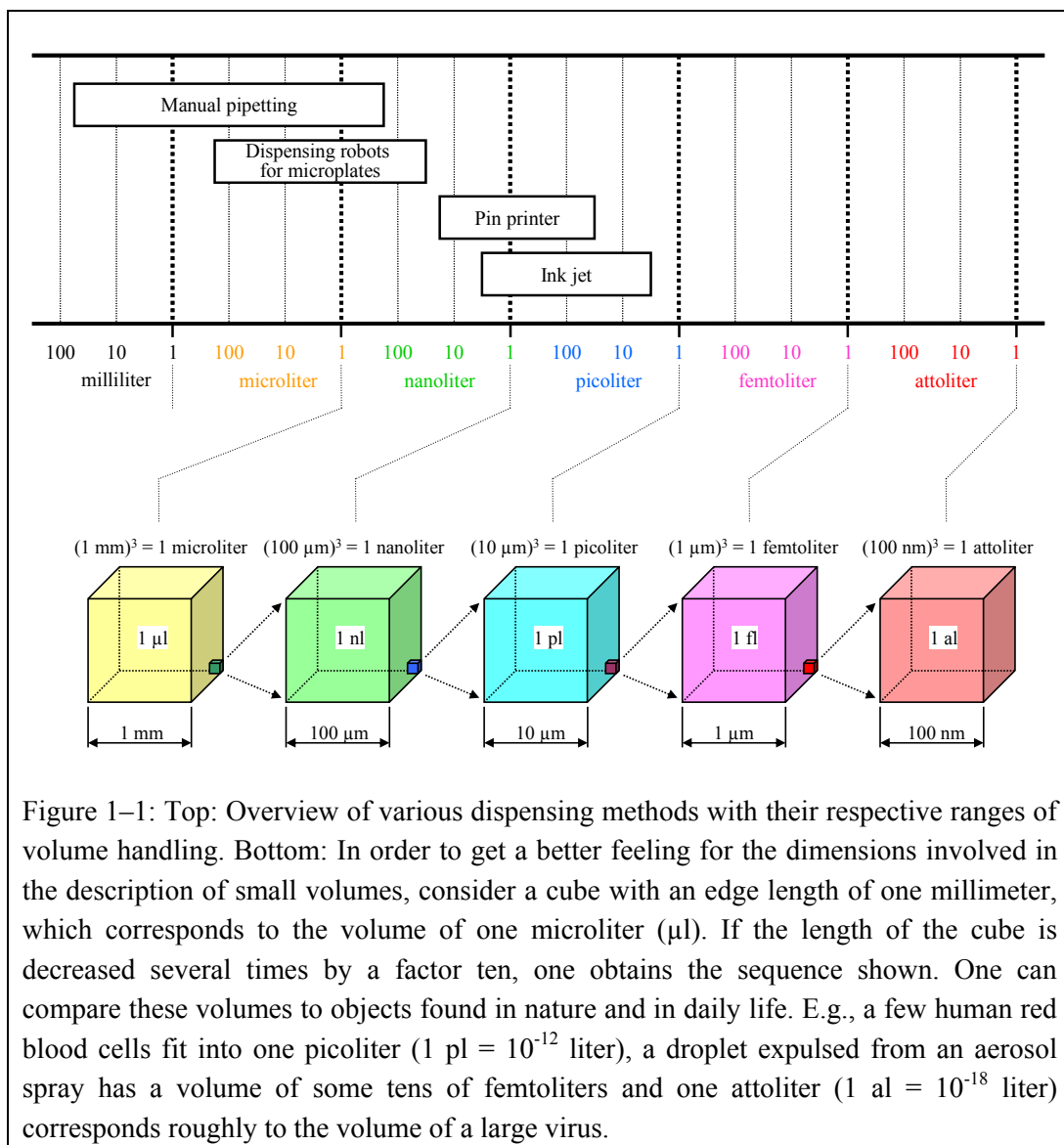
Two main approaches are available for the production of microarrays. The first approach is to synthesize a DNA sequence in situ directly on the substrate [4]. The second approach is to deliver the receptor molecule to the substrate. The delivery of the receptor molecules can again be separated into two classes, namely non-contact and contact printing methods.

The most common non-contact printing tool is probably the head of an inkjet printer, which ejects droplets from a nozzle onto the substrate. Such droplets typically have volumes down to a few picoliters. Although the inkjet technique is mainly used for color printing, it is also involved in other domains, such as the fabrication of microarrays for biomedical and pharmaceutical applications. The

droplet is ejected from the head by applying a short pulse of pressure to the liquid located in a chamber that is connected to the nozzle by a small channel. The pressure in the chamber is built up either by a compression of the liquid volume by the action of a piezoelectric element, or by the expansion of a steam bubble produced by local heating. For the specific application of microarray printing, MEMS based drop-on-demand dispensers have also been developed, and allow the delivery of larger droplets, up to some nanoliters [5].

Contact based deposition of liquids can be realized by pin spotting or pin-and-ring spotting. These techniques use an array of pins. Each pin is dipped in a different solution containing the different receptor molecules. A mechanical contact between the wetted pins and the substrate takes place, and the liquid is transferred during the contact [6]. Spotting pins produce dots with typical sizes of about hundred microns.

These different methods are summarized in Figure 1–1.



Using microfabrication techniques, news dispensers have been created that allow the dispensing of droplets in the picoliter and femtoliter range, with spot diameters of 2 to 3 μm [7,8].

Dispensing methods based on nanopipettes have also been developed. In one approach, the nanopipette is filled with the material to be deposited. The material is then pushed out by applying a pressure at the larger opening of the nanopipette while the tapered end of the nanopipette is in vicinity of the substrate surface [9,10]. The liquid inside the nanopipette can also be delivered by a combination of electroosmotic flow, electrophoresis, and dielectrophoresis [11]. In such cases, the nanopipette must be immersed in a bath of ionic solution.

Driven by the motivation to push back the limit of liquids dispensing, the aim of this thesis was the deposition of volumes of liquid in the attoliter range. By deposition of attoliter volumes, one means not only small volumes, but also a precise manipulation of the liquid. The goal was to dispense individual droplets on-demand, and to deposit them with a high lateral accuracy onto specific locations of a substrate, e.g. to form an array with a high density of droplets.

The interest was to investigate the feasibility of liquid handling with small volumes, to reach high spot densities and for an economical use of the liquid, and in parallel to understand the different parameters and limitations that are involved in it.

The method presented here and developed during this thesis, called **nanoscale dispensing (NADIS)**, is a contact-based dispensing of ultrasmall droplets. The probe used in nanoscale dispensing, the nanodispenser, is based on a similar concept to a probe for scanning near field optical microscopy, which has an optical aperture. The nanodispenser consists of a flexible cantilever which ends in a tip, similarly to an atomic force microscopy probe, but with an aperture at the tip. For the deposition process, the back of the tip is loaded with the liquid to be dispensed. When the tip comes into contact with the substrate, the liquid wets the substrate surface. As the probe is withdrawn, the meniscus of liquid which forms a bridge between the tip and the surface, is stretched and finally breaks, and a small droplet remains on the substrate. This transfer of liquid is based only on capillarity and on surface wettability. No external pressure is applied to the liquid. A schematic of the process is shown in Figure 1–2.

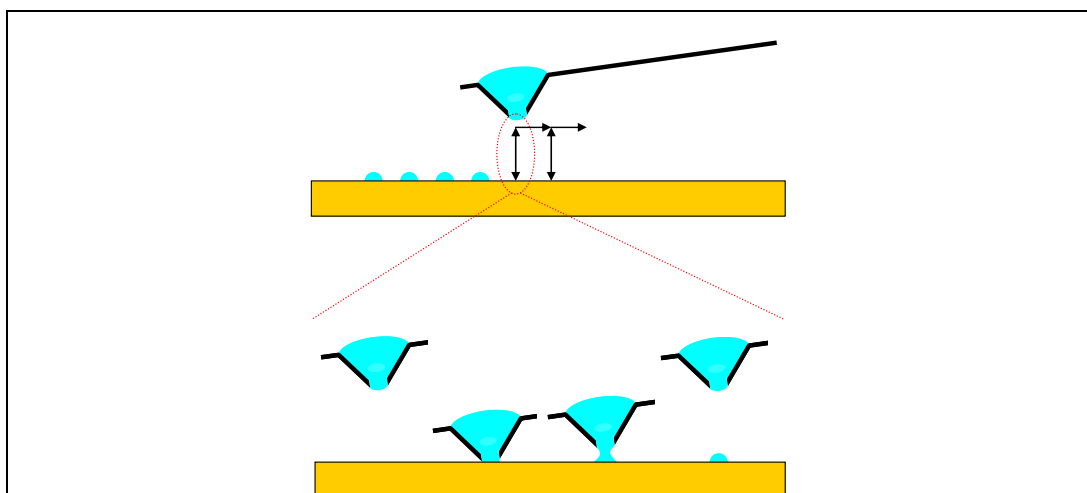


Figure 1–2: A conceptual sketch of nanoscale dispensing. The nanodispenser, a hollow AFM tip with an aperture, is loaded with a liquid. By bringing the tip briefly into contact with the substrate, some liquid is transferred to the surface.

The NADIS probe is mounted on a conventional atomic force microscope (AFM), and force feedback allows control of the tip-to-sample distance during the deposition process. The control software permits the addressing of individual points on the scanned surface where specific actions can be performed, such as lowering the probe to make contact with the substrate.

The NADIS method presented here permits the on-demand deposition of small individual droplets in an ambient environment at a predetermined location on a sample. A high lateral positioning accuracy is provided by the piezoelectric scanner of the AFM itself. Furthermore, a small droplet size combined with small droplet spacing allows the creation of arrays with high droplet densities.

Nanoscale dispensing is a maskless dispensing method, and offers a high degree of flexibility in the pattern design, and in the liquid to be used. The method can be extended to dispense other materials, such as biological molecules or nanoparticles. In such cases, the liquid acts as a transport medium for the components suspended in it.

A paper describing the method and the first results can be found in reference [12].

Although the concept is simple, a deeper understanding of the phenomena involved requires some theoretical consideration. It is known that, in contradiction to the macroscopic world that is dominated by volume forces, in a microscopic world surface forces prevail. This is because, as dimensions decrease, the surface-to-volume ratio increases. Thus, the surface tension of liquids or the driving forces of capillarity are predominant when ultras-small volumes of liquids are considered. The next chapter will address some theoretical aspects related to these phenomena.

2. Theoretical background

In this chapter, some physical aspects will be considered to get a better understanding of liquids, such as the shape of small droplets and their interaction with solid substrates, and capillary forces. Our understanding of liquids relies mostly on an analysis of surface and interfacial energies, and their implications. Interfacial energies originate in interatomic and intermolecular forces. Therefore, the chapter will start with a description of those forces.

It will be shown that the description of capillary phenomena is based on three fundamental equations. The first takes into account the hydrostatic equilibrium across the liquid-gas interface (Laplace pressure), the second deals with the thermodynamic equilibrium of the interfacial energies and leads to an understanding of the contact angle at the three-phase contact line (Young's equation), and the last treats the thermodynamic equilibrium over the liquid-gas interface with respect to evaporation or condensation (Kelvin's equation).

2.1. Forces that hold together atoms or molecules in a condensate

2.1.1. The Origins of the forces

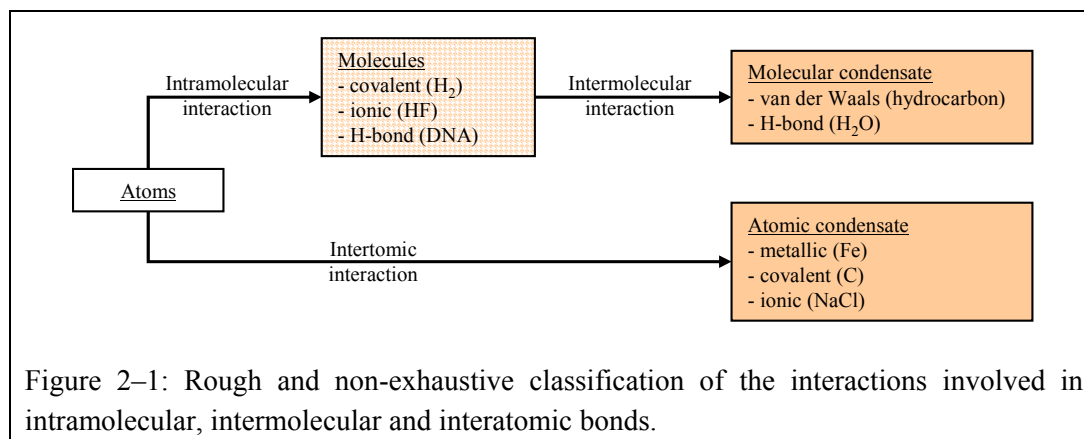
The various attractive forces that hold together molecules or atoms to form a liquid or solid condensate, are different in nature. One can mention those arising from electrostatic and electrodynamic interactions, involving charges, permanent dipoles and induced dipoles. Ionic and van der Waals forces belong to this category, as well as those interactions responsible for hydrogen bonds. Another category of attractive forces is formed by the short-range forces that are quantum mechanical in nature, such as covalent and metallic bonds.

The repulsive forces that balance the attractive forces between atoms at very small interatomic distances are mainly due to the overlap of electron clouds, according to the Pauli exclusion principle. These interactions are also known as exchange, hard-core or steric repulsion. These forces have a very short range, and increase very sharply as two molecules or atoms are brought together.

At this point, to get a better overview, one should roughly classify the different interactions with the different actors involved, i.e. atoms and molecules:

- Intramolecular interactions are involved in the bonding between the atoms to form a molecule.
- Intermolecular interactions are involved in the bonding between molecules to form a molecular condensate.
- Interatomic interactions are involved in the bonding between atoms to form an atomic condensate.

These different interactions are shown in Figure 2–1. One kind of interaction can be present in more than one of the three mentioned groups.



Firstly, some of the different interactions will be described, without taking account on their organization in the three different groups.

2.1.1.1. Electrostatic and electrodynamic interaction

Electrostatic and electrodynamic interactions can be subdivided into the following subclasses:

2.1.1.1.a. Purely electrostatic interactions

Purely electrostatic interactions are those involving the charge of ions and the permanent dipole of polar molecules. Charge-charge, charge-dipole and dipole-dipole interactions belong to this category. For dipoles, one must differentiate between angularly fixed and freely rotating dipoles. In general, a dipole with a moment, u , in an electric field, E , is angularly fixed when the thermal energy $k_B T$ is much weaker than the interaction energy uE , or freely rotating if $uE \ll k_B T$.

A special kind of electrostatic interaction is the Keesom interaction, also called the orientation interaction. This occurs when two freely rotating polar molecules mutually interact. The Keesom interaction energy is a Boltzmann-weighted and angle-averaged energy, and depends on the thermal energy $k_B T$.

Another electrostatic interaction is the hydrogen-bond, which is a dipole-dipole interaction. This interaction exists between strongly electronegative^{a)} atoms, such as O, N, F or Cl, and hydrogen atoms covalently bound to similar atoms. These bonds always involve hydrogen atoms, which can be easily positively polarized and are exceptionally small. The intramolecular covalent bond between H and an electronegative atom (e.g. $O^{\delta-}-H^{\delta+}$) is highly polar. Additionally, due to the size of the electron depleted hydrogen atom, the dipole feels a very strong electrostatic field because it can get very close to a nearby negatively charged electronegative atom of another molecule, leading to a hydrogen-bond ($O^{\delta-}-H^{\delta+}\cdots O^{\delta-}$). Such hydrogen-bonds are highly directional. They are the origin of the particular properties of water,^{b)} and play a predominant role in biology, e.g. binding two polynucleotide chains to form the inter-twisted DNA double helix (see Figure 2–2), or governing the folding of macromolecular structures like proteins.

^{a)} The electronegativity of an atom is its affinity to capture additional electrons.

^{b)} Water has an unexpectedly high melting and boiling point, compared with its low molecular weight. H-bonds can also explain the density maximum at 4°C, and the phenomena that the solid (ice) is lighter than the liquid.

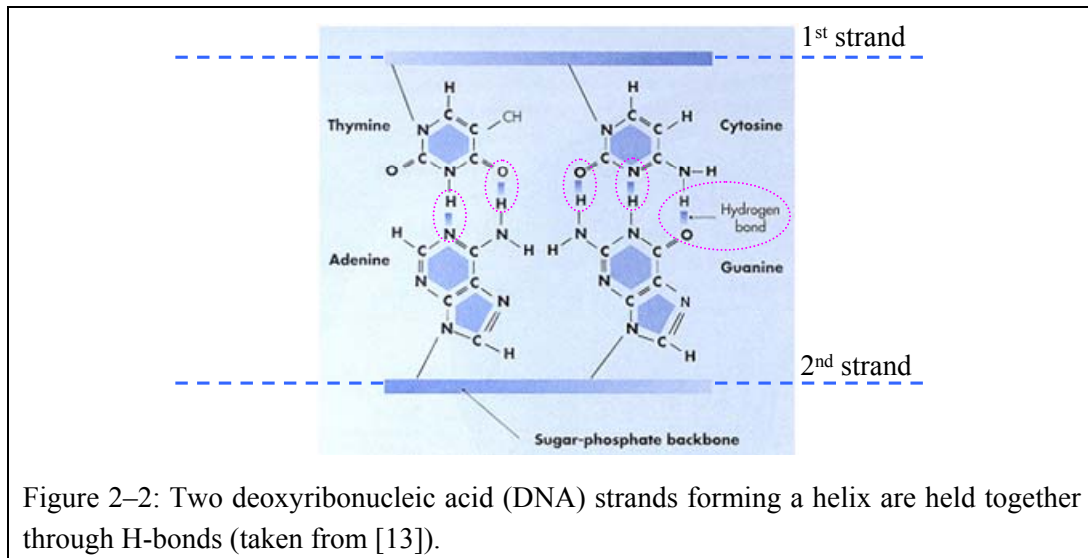


Figure 2–2: Two deoxyribonucleic acid (DNA) strands forming a helix are held together through H-bonds (taken from [13]).

2.1.1.1b. Polarization forces

These forces arise when a dipole moment, u_{ind} , is induced in a molecule by the electric field E of a nearby charge or a permanent dipole. The electronic polarizability, α_0 , of a molecule results from the displacement of the negatively charged electron clouds relative to the positively charged nucleus in the presence of an electric field, leading to an induced dipole moment $u_{ind} = \alpha_0 \cdot E$. Both polar and non-polar molecules can be polarized in this way.

Such an interaction between the freely rotating dipole of a polar molecule and the induced dipole of a neighboring molecule is known as a Debye interaction.

Freely rotating polar molecules with a dipole moment, u , exposed to an electric field can have an additional orientation polarizability, α_{ori} . The time-averaged dipole moment $\langle u \rangle$ of a freely rotating polar molecule in an electric-field-free environment is zero. However, in the presence of a weak electric field E ($uE \ll k_B T$), the dipole will be weighted along the field and the time-averaged dipole moment will no longer vanish. Instead $\langle u \rangle$ will be equal to $\alpha_{ori} \cdot E$. The mutual interaction between two polar molecules due to orientation polarizability is identical to the time-averaged dipole-dipole Keesom interaction.

2.1.1.1c. London dispersion forces

These long-range forces, also called electrodynamic forces, induced-dipole–induced-dipole forces, or charge-fluctuation forces, are quantum mechanical in origin. They act between all atoms or molecules, even totally neutral and non-polar atoms such as helium. To understand this interaction, consider an atom in the Bohr's model, where the electrons are orbiting around the nucleus. For a non-polar atom, the time-averaged dipole is zero. However, the instantaneous position of the electrons leads to a finite dipole moment. This dipole will fluctuate according to the charge distribution in the atom. The electric field arising from such a fluctuating dipole can polarize a nearby molecule or atom, inducing a dipole in it. The interaction between the charge-fluctuating dipole and the induced dipole leads to dispersion forces. The dispersion interaction can be seen as a quantum mechanical polarization interaction.

A summary of some of the above-mentioned interactions is given in Table 2–1, together with their respective intermolecular distance r and temperature T dependencies. [14]

Type of interaction	Common name	Interaction energy
Charge – Charge	Coulomb or ionic interaction	$\propto 1/r$
Charge – Fixed Dipole		$\propto 1/r^2$
Charge – Freely rotating dipole		$\propto 1/(k_B T r^4)$
Charge – Induced dipole		$\propto 1/r^4$
Freely rotating dipole – Freely rotating dipole	Keesom interaction	$\propto 1/(k_B T r^6)$
Freely rotating dipole – Induced dipole	Debye interaction	$\propto 1/r^6$
Induced dipole – Induced dipole	London dispersion interaction	$\propto 1/r^6$

Table 2–1: Common interactions between atoms, ions and molecules. The interaction force is obtained by differentiating the energy with respect to the distance r . The Keesom, Debye and London dispersion interactions have the same intermolecular distance dependencies, and together constitute the van der Waals interaction. The attractive covalent, metallic and hydrogen-bonding interactions, as well as the repulsive interactions, are not included in this table.

2.1.1.2. Van der Waals forces

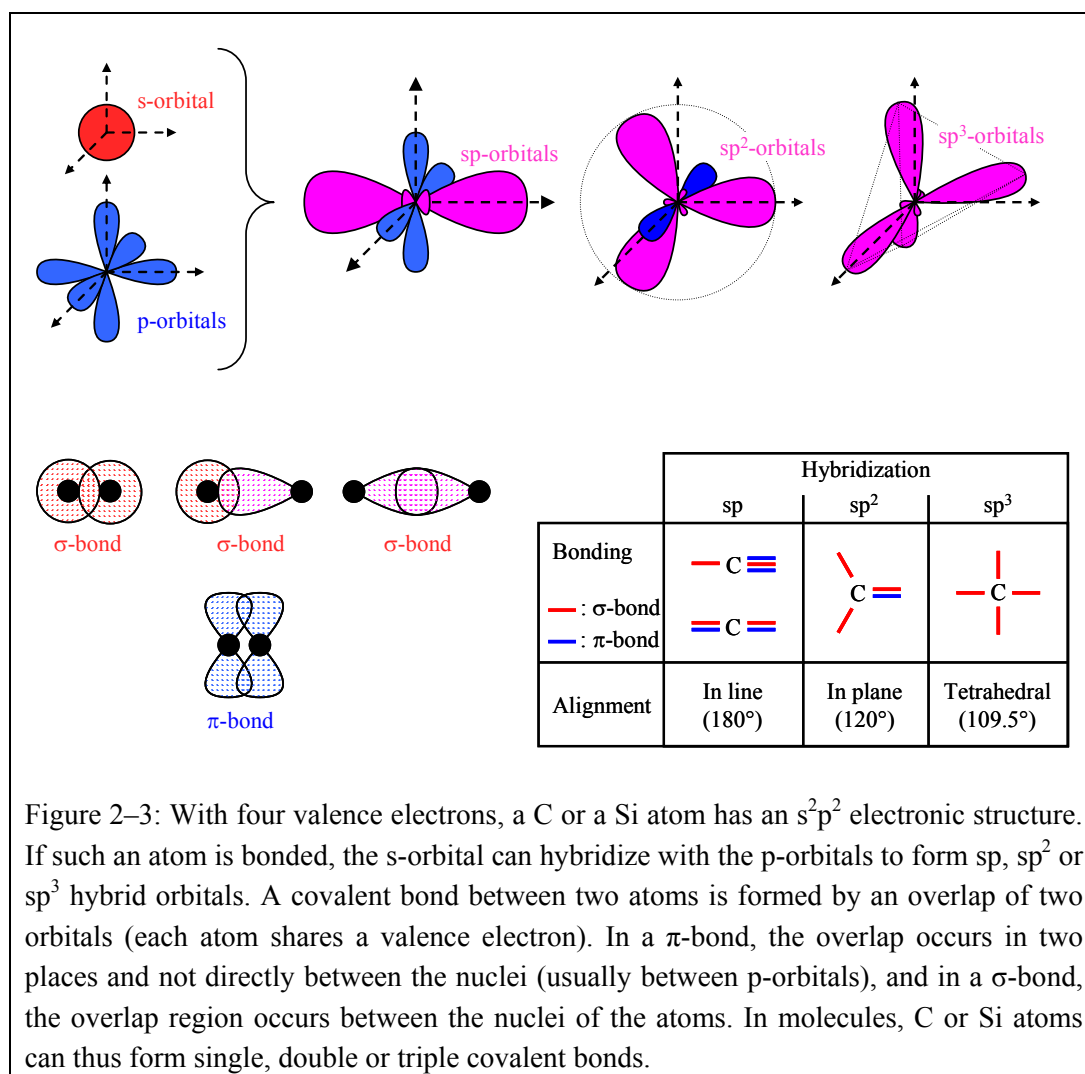
Van der Waals forces were first described by the physicist and Nobel Prize winner Johannes Diderik van der Waals [15] who derived the famous equation of state for liquids and gases: $(P + a/V^2)(V - b) = RT$. Thus, he took into account the effects of the attractive intermolecular forces (the van der Waals forces) by adding the term a/V^2 to the pressure P , and the finite size of the molecules by subtracting the term b from the molar volume V . The van der Waals forces are the combination of three distinct forces between freely rotating molecules, such as those found in liquids or gases. These three forces are the orientation force, the induction force and the dispersion force: $F_{vdW} = F_{orient} + F_{ind} + F_{disp}$. The three forces correspond to the Keesom interaction, the Debye interaction and the London dispersion interaction, respectively (see Table 2–1). All three have a $1/r^6$ dependency in their free energies, where r is the intermolecular distance. Van der Waals interactions between non-polar molecules consist of London dispersion interactions only. Van der Waals interactions with a hard-core repulsion can be described by the Lennard-Jones potential: $E(r) = -C_{vdW}/r^6 + C_{rep}/r^{12}$.

Dispersion forces generally exceed the dipole-dependent induction or orientation forces except for small and highly polar molecules, such as water. Furthermore, in an interaction involving to dissimilar molecules of which one is non-polar, the van der Waals interaction is almost completely dominated by the dispersion contribution. The London dispersion interaction feels also from the retardation effect. The retardation effect takes place when the two atoms (or molecules) are separated by a large distance, i.e. the fluctuation period of the instantaneous dipole is comparable with the time needed for the electric field to propagate from one atom to the other. When the electric field from the induced dipole reaches the initial dipole, the direction of the initial dipole has already changed, with the consequence that the attractive dispersion interaction becomes weaker. Thus, for large distances, the dispersion interaction between two atoms decays faster than $1/r^6$, approaching a $1/r^7$ dependency. Note that the Keesom and Debye interactions remain non-retarded at all separations.

2.1.2. Molecular and atomic condensates

2.1.2.1. Intramolecular interactions (atoms form molecules)

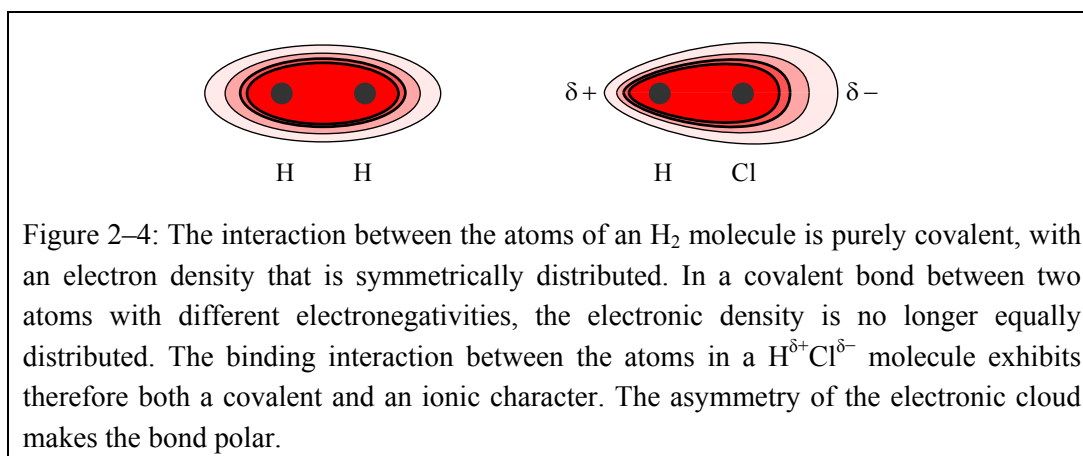
The simplest molecule is composed of two covalently bound hydrogen atoms. The bond between those two atoms emerges from the covalent interaction, which is quantum mechanical in nature. This interaction can be understood as a common sharing of the valence electrons of both H atoms. Quantum mechanically, it is an overlapping of two electronic s-orbitals to form a σ -bond. More generally, a covalent bond can be described by a linear combination of atomic orbitals (LCAO). The wave function that describes quantum mechanically the interaction of such bonds has not a broad expansion, compared to the interatomic separation. The covalent forces are therefore of short range, and the bonds have a directionality, that is, they are spatially oriented relative to each other. For example, a C or Si atom, with its s^2p^2 electronic structure, has four valence electrons. Figure 2–3 shows the s and the p_x , p_y , p_z orbitals (each p-orbital exhibits two lobes).



If such an atom is bonded, the s-orbital can hybridize with one, two or all three p-orbitals to form two sp, three sp² or four sp³ hybrid orbitals respectively. There is an angle of 180° between the two sp orbitals. The three sp² orbitals lie in a plane perpendicular to the remaining p-orbital. They are separated by 120°. The four sp³ orbitals, which form a tetrahedral structure, are separated from each

other by 109.5° . These orbital orientations influence the directionality of the bonds involving the respective orbitals. Depending on the hybridization, C can build single, double or triple covalent bonds with two, three or four neighboring atoms, with the above defined orientation between each bonds (see Figure 2–3).

In a covalent bond between two identical atoms, the electron density is symmetrically distributed between the two nuclei. However, two different atoms involved in a covalent bond can possess different electronegativities. The electron density is higher around the most electronegative atom at the expense of the other, which deforms the electronic cloud (Figure 2–4). As a result, the two atoms are partially and oppositely charged. The bond has therefore an ionic component and is no longer purely covalent. Another important consequence of this difference in electronegativity is that the bond acquires a polar character, and the molecule can have a dipole moment.



2.1.2.2. Intermolecular interactions (molecules form a condensate)

To form a molecular condensate, the molecules must interact attractively. Depending on the nature of the condensate (e.g. involving one or several kinds of molecules) different interactions can occur. One can cite the above-mentioned van der Waals forces and H-bonds. For non-polar molecules, such as benzene or hydrocarbons, the condensate exists solely because of the London dispersion interactions. These condensates are known as van der Waals liquids or solids, and the molecules interact in a weak and undirected manner. In a condensate composed of polar molecules, there are additional attractive intermolecular forces resulting from the dipole-dipole interactions. The dipole can be permanent (Keesom) or induced (Debye). Moreover, the character of a molecule can be influenced by the environment, such as when the molecule is dissolved in a solvent such as water. An amine group of a non-charged molecule exposed to water can be protonated ($-\text{NH}_2$ becomes $-\text{NH}_3^+$), or an alcohol group can be deprotonated ($-\text{OH}$ becomes $-\text{O}^-$), so that the molecules have a net charge and their dipole moment is modified. In this way, the interactions involving polar molecules or ions in solvents can become very complex.

2.1.2.3. Interatomic interactions (atoms form a condensate)

An atomic condensate, made of atoms instead of molecules, usually has a crystalline structure in the solid state. The three main types of bonds that form a crystal are the ionic, the covalent and the metallic interaction.

The ionic bond is an electrostatic interaction between positively and negatively charged ions, involving usually a halogen^{a)}, such as in Na^+Cl^- . This interaction can be reasonably well explained by classical theory. In ionically bonded crystals, no free electrons are present, since they are quasi-bonded to the halogen. Therefore, ionic crystals have poor electrical and thermal conductivities.

An example of a covalently bound crystal is the diamond lattice of C or Si atoms in the sp^3 -hybridized form. The covalent bond in the crystal is identical to the intramolecular covalent bond described above. Due to the high strength of the bonds, such crystals are stiff and brittle. Identically to ionically bound crystals, covalently bound crystals conduct heat and electricity poorly.

The atoms that form metallic crystals have only a few, weakly bound, valence electrons. In contrast to the covalent bond where the shared electrons are confined near the bond, the valence electrons of a metallic crystal have an expanded wave function, compared to the interatomic distance. As a result, the valence electrons are delocalized over the entire crystal. Furthermore, the metallic interaction can only occur when the crystal is composed of a large number of atoms. Metallic crystals are more ductile than covalently bound crystals, and are typically good electrical and thermal conductors.

The forces in a real atomic crystal are best described as a mixture of these three specific interactions.

The intermolecular or interatomic forces leading to the formation of a condensate (whether liquid or solid) are known as cohesion forces.

^{a)} Elements found in the group VII of the periodic table, such as fluorine, chlorine, bromine, or iodine.

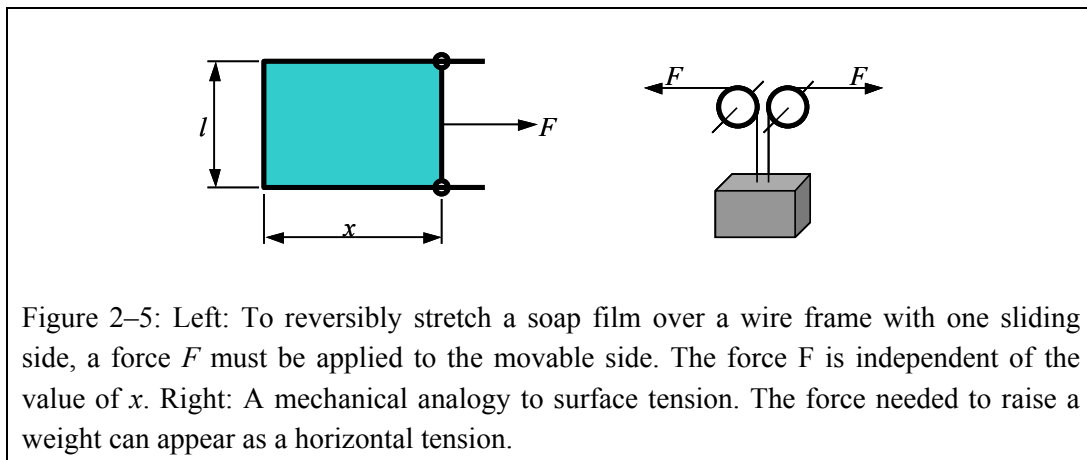
2.2. Interactions between macroscopic bodies

2.2.1. Surface Free Energy and Cohesion

The surface tension of liquids is a phenomenon that we observe daily. Water striders running on the surface of a pond without sinking, or rain droplets captured on a spider's web, are examples of surface tension leading to unusual effects.

Surface tension is related to the attractive cohesive forces acting between the molecules (or atoms) of a liquid. In the bulk liquid, one molecule is isotropically surrounded by other molecules, so that the resultant intermolecular force exerted by all the neighboring molecules is zero. However, the resultant intermolecular force acting on a molecule located at the surface of the liquid is non-zero because of the missing neighbors in the upper half-space. This non-vanishing force points inwards into the liquid. Therefore, work is required to bring a molecule from the bulk to the surface, and thus to increase the surface area. This work can be regarded as a surface tension, also described as surface free energy. To reach thermodynamic equilibrium, a one-component system must minimize its surface. For this reason, a drop in a gravity-free environment takes on a spherical shape, since the sphere is the geometrical object with the smallest surface-to-volume ratio.

The surface tension may equally well be thought of as a force per unit length. Consider a soap film stretched over a rectangular wire frame with one sliding side of length l , as shown in Figure 2–5.



The sliding side can be reversibly moved along the x -axis. To keep the film stretched a force F must be applied to the sliding side. Thus the surface tension γ is defined by:

$$F = \gamma \cdot 2 \cdot l \quad (2-1)$$

The factor 2 arises because the soap film has an upper and a lower surface. The surface tension can also be considered as a surface free energy, which is defined as the reversible work per unit area to create a surface. Moving the sliding side over a distance Δx requires an energy E equal to $F \cdot \Delta x$, while the surface area of the soap film is increased by a value $\Delta A = 2 \cdot l \cdot \Delta x$. Therefore, the surface free energy γ can also be defined as:

$$E = \gamma \cdot \Delta A \quad (2-2)$$

Equation (2-2) differs from equation (2-1) only by a factor Δx , and both describe the same physical concept.

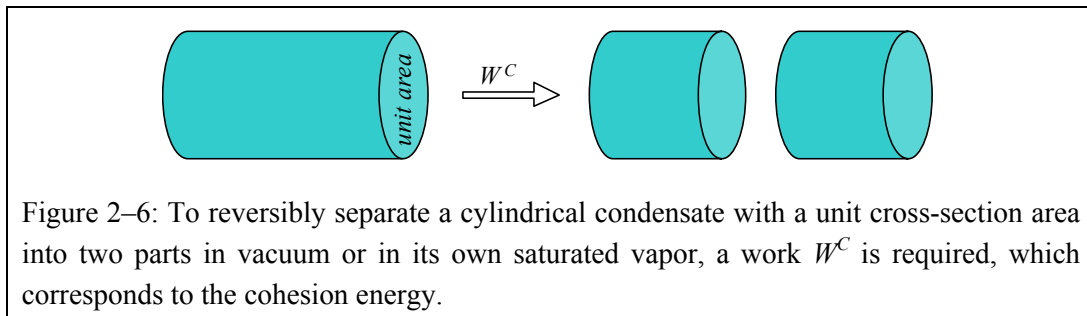
The strength of the surface tension depends on the strength of the intermolecular interaction. A liquid condensed by dispersion forces only will therefore have a weaker surface tension than a liquid formed by dipole-dipole interaction or H-bonds. Surface tension values for some liquids are given in Table 2–2. The intermolecular forces are temperature dependent, and thus, the surface tension is also influenced by the temperature. An increase in temperature will lower the surface tension. For water, the surface tension at 0 °C is 75.6 mN/m, and drops to 58.9 mN/m at 100 °C [16].

	Interactions	γ [mN/m]
n-Pentane (C ₅ H ₁₂)	vdW	16.1
n-Octane (C ₈ H ₁₈)	vdW	21.6
n-Hexadecane (C ₁₆ H ₃₄)	vdW	27.5
Glycerol (C ₃ H ₈ O ₃)	vdW + H-bond	63.4
Water (H ₂ O)	vdW + H-bond	72.8
Mercury (Hg)	Metallic	486.5

Table 2–2: Surface tension for different liquids at 20 °C [14,17].

As already seen, the intermolecular forces generate the surface tension of a liquid, and are also related to the cohesion energy. The relationship between surface free energy, γ , and cohesion energy, W^C , is shown in the gedanken experiment, in which a cylinder of liquid is split into two parts. The work needed to separate a liquid cylinder of unit area is equal to the cohesion energy (see Figure 2–6). However, at the same time, the surface area of the liquid is increased by two unit areas. Thus:

$$\gamma = \frac{1}{2} W^C \quad (2-3)$$



The same physical concepts of surface free energy and cohesion also exist for a solid-phase condensate. For a solid, the process of forming a new fresh surface is divided in two distinct steps. First, the solid is cleaved to expose a new surface, keeping the atoms in the same position as in the bulk. Second, the atoms of the surface region rearrange to their equilibrium position. For liquids the two steps occurs as one, and the thermodynamic equilibrium is almost instantaneously reached because of the high mobility of the molecules. However, for solids that are far below their melting point, the rearrangement of the surface atoms in a freshly cleaved surface occurs slowly.

Moreover, in contrast to liquids where a surface increase always occurs by moving molecules from the bulk to the surface, a solid surface area can also be increased by elastic stretching. Such elastic deformation leads to a surface stress, defined as the reversible work per area to stretch a surface elastically. A change in the surface stress can e.g. be measured by the bending of a cantilever [18,19].

For a crystal, the cohesion energy is dependent on the crystallographic plane, and the surface energy shows an identical dependence [20]. Some approximate values for the surface energies of solids are given in Table 2–3.

	Involved interactions	γ [mJ/m ²]
Aluminum	Metallic	1100
Silver	Metallic	1500
Copper	Metallic	2000
Iron	Metallic	2400
Tungsten	Metallic	4400
Silicon	Covalent	1400
PTFE (Teflon)	vdW	18

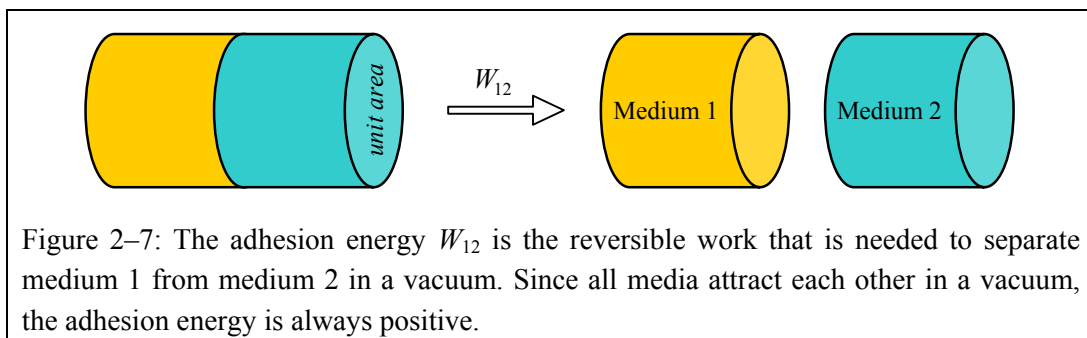
Table 2–3: Surface free energies of some solids at room temperature [17,21]. The values given for the crystalline materials are only approximate, since they depend on the crystallographic plane.

The surface energies for different solids span two orders of magnitude (compare tungsten with PTFE). Strongly bonded solids will keep their high surface energy only if the surface is protected from surface contamination, for example in vacuum or in inert gas environment. When a solid is exposed to an ambient environment, its high surface energy will be reduced by the adsorption of molecules that have a lower surface tension. E.g., a metallic surface exposed to air will be quickly covered by a thin film of water or hydrocarbon molecules that reduce the surface energy. PTFE has an extreme low surface energy. Thus, adsorption on a PTFE surface is usually energetically less favorable. This gives to the PTFE surface its anti-adhesive property.

2.2.2. Interfacial Energy and Adhesion

The previous chapter described the surface free energy, γ , for a one-phase system, the solid or liquid phase being exposed to a vacuum or to its own saturated vapor. One should now consider the interactions between two different condensed phases.

The adhesion energy, W_{12} , is the reversible work per unit area needed to separate the two phases in a vacuum, as shown in Figure 2–7. Indices 1 and 2 denote the two different media, which are usually represented by S for solids and L for liquids. If the two media are identical, the adhesion energy becomes the cohesion energy: $W_{11} = W^C$.



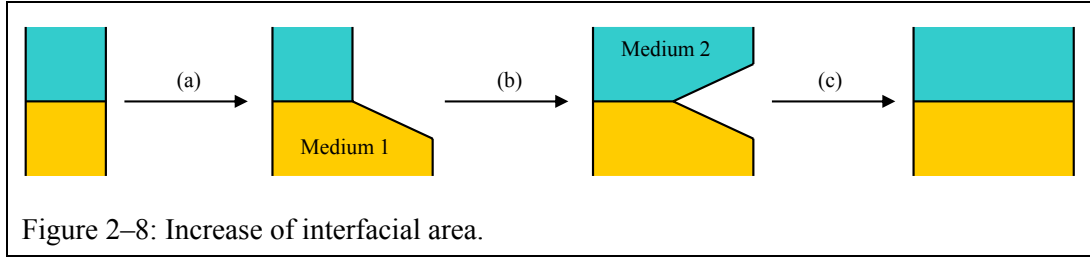


Figure 2–8: Increase of interfacial area.

The increase of an interfacial area proceeds in three steps, as shown in Figure 2–8. Firstly, the surface of the first medium is increased in vacuum (a), secondly the same is done for the other medium (b), and thirdly the two newly created areas are brought in contact (c). Thus, the interfacial energy γ_{12} (or interfacial tension), which is defined as the work needed to increase the interfacial area by one unit area, is given by:

$$\gamma_{12} = \gamma_1 + \gamma_2 - W_{12} \quad (2-4)$$

2.2.2.1. Film pressure

If a condensed phase is exposed to a gaseous phase (denoted as G), gas molecules can adsorb on the surface of the condensed phase, thus changing its surface properties including surface energy. The adsorption of gaseous molecules on a surface is associated with a reduction of the surface energy of the condensate. This decrease in energy is the film pressure, π , also known as surface pressure or spreading pressure. Let γ_i be the surface energy of a condensate exposed to its own saturated vapor, and γ_{iG} the interfacial tension of the condensate exposed to another gaseous phase. Then:

$$\pi_{LG} = \gamma_L - \gamma_{LG} \quad \Leftrightarrow \quad \gamma_{LG} = \gamma_L - \pi_{LG} \quad (2-5)$$

$$\pi_{SG} = \gamma_S - \gamma_{SG} \quad \Leftrightarrow \quad \gamma_{SG} = \gamma_S - \pi_{SG} \quad (2-6)$$

In an ambient environment, adsorbed water or hydrocarbons can significantly change surface properties. For example, mica cleaved under high vacuum has a surface energy of $\gamma_S \approx 4500 \text{ mJ/m}^2$, whereas cleaved in a humid environment, the interfacial energy decreases to $\gamma_{SG} \approx 300 \text{ mJ/m}^2$, due to water adsorption [14]. The film pressure of an adsorbed layer on a liquid phase can be measured by a Wilhelmy plate balance. The Wilhelmy plate will be discussed in section 2.3.5.1.

Figure 2–9 summarizes the difference between the concepts of surface energy, interfacial energy and film pressure.

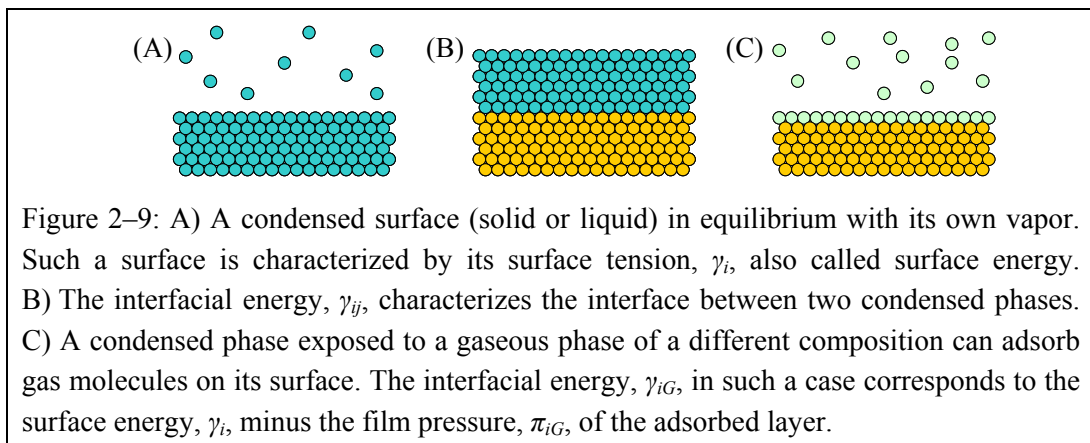


Figure 2–9: A) A condensed surface (solid or liquid) in equilibrium with its own vapor. Such a surface is characterized by its surface tension, γ_i , also called surface energy. B) The interfacial energy, γ_{ij} , characterizes the interface between two condensed phases. C) A condensed phase exposed to a gaseous phase of a different composition can adsorb gas molecules on its surface. The interfacial energy, γ_{iG} , in such a case corresponds to the surface energy, γ_i , minus the film pressure, π_{iG} , of the adsorbed layer.

Usually, all solids exposed to a gas phase exhibit a positive interfacial energy. For this reason a highly porous material can sinter into a solid bulk at high temperature. Nevertheless, negative surface energies can be found, e.g. on some crystalline structures of alumina [22].

2.2.3. Forces between condensed bodies

2.2.3.1. Adhesion forces between macroscopic objects

The force arising from the adhesion between contacting bodies will now be considered. For two spherical rigid objects in a vacuum, one may use the Derjaguin approximation^{a)} to determine the attractive adhesion force [14]:

$$F_{sphere1-sphere2} = -2\pi \cdot \frac{R_{S1} \cdot R_{S2}}{R_{S1} + R_{S2}} \cdot W_{12} \quad (2-7)$$

$$F_{sphere-surface} = -2\pi \cdot R \cdot W_{12} \quad (2-8)$$

The values R , R_{S1} , and R_{S2} correspond to the spheres' radii, and W_{12} to the adhesion work per unit area. If the two objects are composed of the same material, the adhesion work, W_{12} , is replaced by the cohesion work, $W_{11} = W^C = 2 \cdot \gamma_S$. If the objects are placed in a liquid or gaseous environment, γ_S is replaced by γ_{SL} or γ_{SG} respectively. Since γ_{SL} (or γ_{SG}) is smaller than γ_S , the adhesion force will also be smaller than in a vacuum.

2.2.3.2. Van der Waals forces between macroscopic objects

In section 2.1.1.2, we saw that the van der Waals (vdW) interaction between two molecules or atoms is of the form $E(r) = -C_{vdW}/r^6$. To investigate the force generated by the vdW interaction acting between macroscopic objects, one may sum (or integrate) the interaction energies of all atoms in the first object with all atoms in the second object. This can be expressed as:

$$E_{body1-body2} = -C_{vdW} \cdot \int_{V_1} \int_{V_2} \frac{\rho_1 \cdot dV_1 \cdot \rho_2 \cdot dV_2}{r^6} \quad (2-9)$$

where ρ_1 and ρ_2 are the number of atoms per unit volume of the bodies, and r the distance between the two infinitesimal volume elements dV_1 and dV_2 . For simple objects such as flat surfaces, cylinders or spheres, the integral can be approximated, under the condition that the spacing s between the objects must be much smaller than the characteristic size of the objects. Some examples are:

$$E_{sphere1-sphere2} = -\frac{A}{6s} \cdot \frac{R_{S1} \cdot R_{S2}}{R_{S1} + R_{S2}} \quad (2-10)$$

$$E_{sphere-surface} = -\frac{A \cdot R}{6s} \quad (2-11)$$

^{a)} The Derjaguin approximation gives the force between two spheres in terms of the free energy per unit area of two flat surfaces at the same separation. For this approach to be valid, the radii of the spheres have to be much larger than the separation distance. For two spheres in contact, the free energy becomes the adhesion energy W_{12} .

$$E_{\text{surface-surface}} = -\frac{A}{12\pi s^2} \quad (2-12)$$

The values R , R_{S1} , and R_{S2} correspond to the radii of the spheres. One may notice that the interaction energy decays with $1/s$ or $1/s^2$ respectively, a much slower decay than the $1/r^6$ dependence of the intermolecular pair interaction. In equations (2-11) the surface is assumed to be infinitely large. Equation (2-12) corresponds to the energy between a unit area of one surface and an infinite large area of another surface. The constant A appearing in all three equations is called the Hamaker constant, and is defined as:

$$A = \pi^2 \cdot C_{vdW} \cdot \rho_1 \cdot \rho_2 \quad (2-13)$$

The Hamaker constant, A , contains all the information about the material properties related to vdW interactions, so that the interaction energy between the two bodies becomes a function of A times an expression related to the geometry. Typical values for the Hamaker constant of condensed phases (liquid or solid) in vacuum or air are around 10^{-19} J [23]. From equations (2-10) to (2-12), one can easily determine the force between the bodies using $F = -\partial E/\partial s$. E.g. for the sphere-surface pair, one obtains the attractive force:

$$F_{\text{sphere-surface}} = -\frac{A \cdot R}{6s^2} \quad (2-14)$$

For a sphere of radius $R = 100$ nm separated from the surface by $s = 10$ nm, one obtains an attractive force of about 0.1 nN, and for $s = 1$ nm the force increases to 10 nN.

The difference between equations (2-8) and (2-14) lies in the fact that the first equation describes the adhesion force between contacting objects, whereas the second describes the attractive force due to the vdW interaction between non-contacting objects separated by a distance s .

2.3. Liquids on surfaces

2.3.1. Laplace pressure

The interfacial tension described in the previous sections can be seen as a two-dimensional pressure acting in the plane of the interface. The effect of that interfacial tension on a curved liquid-gas interface will be described here. The curved interface between two immiscible liquids can be described in the same manner. Two approaches are possible, a more mechanical one, and a thermodynamical one.

To explain the mechanical effect of the surface tension on the interface, consider an interface that is slightly bent, like a cylindrical surface, as sketched in Figure 2–10 A. Let the bending radius be R . To keep the interface bent, one has to apply an excess pressure ΔP inside the bent surface. The forces per unit length are in equilibrium when:

$$\Delta P \cdot R \cdot d\alpha = 2 \cdot \gamma_{LG} \cdot \sin(d\alpha/2) \quad \Rightarrow \quad \Delta P = \frac{\gamma_{LG}}{R} \quad (2-15)$$

If the interface is now curved in two directions, like an ellipsoidal surface, an additional excess pressure must be applied in order to compensate for the bending in the second direction. The equation therefore becomes:

$$\Delta P = \gamma_{LG} \left(\frac{1}{R_1} + \frac{1}{R_2} \right) \quad (2-16)$$

Equation (2-16) is known as the **Young-Laplace equation**, and ΔP corresponds to the Laplace pressure.

It is worth considering in detail the two radii R_1 and R_2 , and the associated excess pressure ΔP . The expression $(1/R_1 + 1/R_2)$ corresponds mathematically to the mean curvature κ of a surface, which is the inverse of the mean radius of curvature R_κ .

$$\kappa = \frac{1}{R_\kappa} = \frac{1}{R_1} + \frac{1}{R_2} \quad (2-17)$$

For an arbitrary surface, the mean curvature can be different at each point of the surface. To determine R_1 and R_2 at a point P on the surface, define a normal to the surface through the point P. The intersection of the surface with a plane containing the normal will define a line. Let the curvature of that intersection line at point P be R_1 . The second radius of curvature is obtained by defining a second plane, containing also the normal, and perpendicular to the first plane. The intersection of this second plane with the surface gives a second curve, with curvature R_2 at point P. Even if the choice of the angular orientation of the first plane influences the value R_1 , the sum of the inverse of the two radii of curvature remains invariant (although the second plane is always perpendicular to the first).

Until now, no attention was paid to signs of radii R_1 and R_2 . Clearly a surface like a sphere will not have the same mean surface curvature as a saddle point. Since the surface represents the liquid-gas interface, one can choose the Laplace pressure to be:

$$\Delta P = P_L - P_G \quad (2-18)$$

with P_L the pressure in the liquid phase and P_G in the gaseous phase. The sign of R_1 or R_2 will be defined, accordingly to equation (2-18), by the direction of the center of each radius: positive if the center points into the liquid, and negative if the center points towards the gas phase. Thus, the interface of a liquid droplet will have a positive mean surface curvature, whereas an air bubble imprisoned in a liquid will have a negative mean surface curvature. A saddle point as shown in Figure 2–10 C has two radii of curvature with opposite signs.

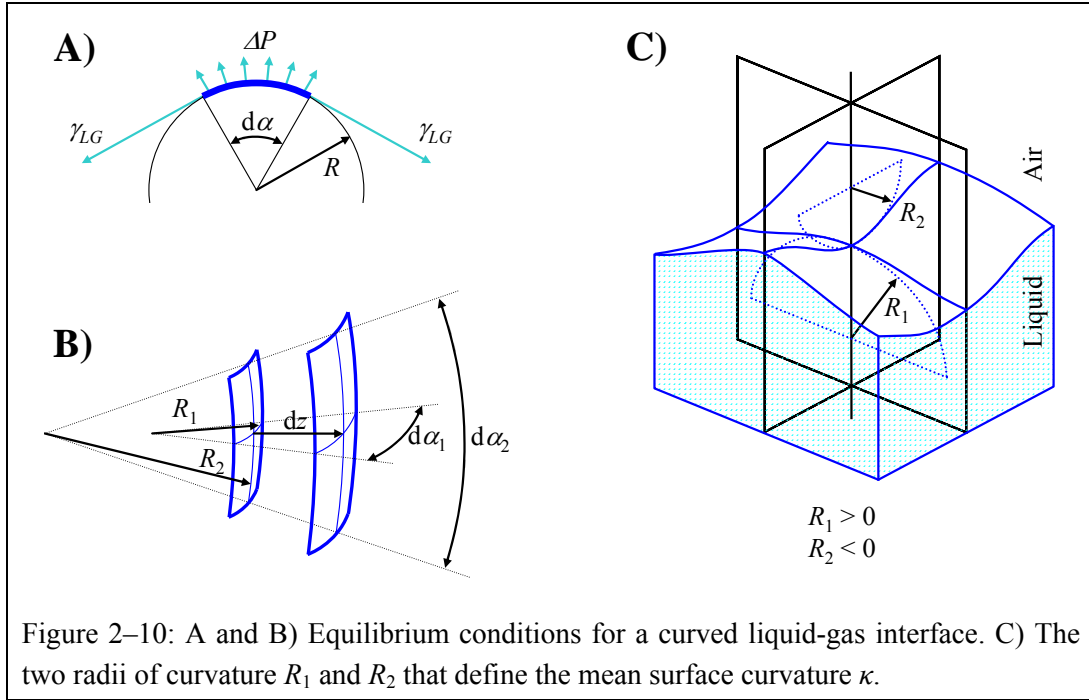


Figure 2–10: A and B) Equilibrium conditions for a curved liquid-gas interface. C) The two radii of curvature R_1 and R_2 that define the mean surface curvature κ .

Equation (2-16) was derived from a mechanical point of view. The same can be done by considering the surface energy. The interfacial energy γ_{LG} was defined to be the energy necessary to increase by one unit area the interfacial surface. Thus, to minimize the total surface energy, the liquid-gas interface should have the minimum surface area. Because of the conservation of mass, a reduction in interfacial area is accompanied by a change of pressure in the media enclosed by the interface. Consider an interfacial surface, spanned over two angles $d\alpha_1$ and $d\alpha_2$ lying in perpendicular planes as shown in Figure 2–10 B. The area of the initial surface element is defined by the two radii of curvature R_1 (in the plane of $d\alpha_1$) and R_2 (in the plane of $d\alpha_2$): $A(z) = R_1 \cdot d\alpha_1 \cdot R_2 \cdot d\alpha_2$. If the surface is displaced to the right by a distance dz , the new area will be $A(z+dz) = (R_1+dz) \cdot d\alpha_1 \cdot (R_2+dz) \cdot d\alpha_2$, so that in a first order approximation the increase of the surface will be: $dA = (R_1+R_2) \cdot d\alpha_1 \cdot d\alpha_2 \cdot dz$. There will be a pressure difference ΔP across the surface, acting over the area $A(z)$. In equilibrium, one has $\gamma_{LG} \cdot dA = \Delta P \cdot A(z) \cdot dz$:

$$\gamma_{LG} \cdot (R_1 + R_2) \cdot d\alpha_1 \cdot d\alpha_2 \cdot dz = \Delta P \cdot R_1 \cdot d\alpha_1 \cdot R_2 \cdot d\alpha_2 \cdot dz \quad (2-19)$$

or:

$$\Delta P = \gamma_{LG} \cdot \left(\frac{R_1 + R_2}{R_1 \cdot R_2} \right) = \gamma_{LG} \cdot \left(\frac{1}{R_1} + \frac{1}{R_2} \right) \quad (2-20)$$

which is again as expected the Young-Laplace equation. It is important to note, that the radius with the smaller modulus contributes most to the Laplace pressure.

The Young-Laplace equation is one of the fundamental relationships in the description of capillarity or other phenomena associated with liquid surfaces. The equation tells us that the crossing of a curved liquid-gas (or liquid-liquid) interface is always accompanied by a change in pressure. The change in pressure is proportional to the mean surface curvature κ of the interface. A higher interfacial curvature results in a higher Laplace pressure.

It is noteworthy that a two-dimensional pressure (the surface tension) can generate a true three-dimensional pressure.

2.3.2. Contact angle

When a drop of liquid is placed on a solid surface, the drop can either spread over the surface, or remain in a ball-like shape. The driving force to reach the final state is the tendency to reduce the total interfacial energies, viz. the solid-gas (SG), solid liquid (SL), and liquid-gas (LG) interfaces. Thermodynamic equilibrium is achieved when the total surface free energy is minimized, with the additional constraint of mass conservation for the droplet (or volume conservation, since a liquid is almost incompressible). The total surface energy is determined as following

$$W_{tot} = A_{SL} \cdot \gamma_{SL} + A_{SG} \cdot \gamma_{SG} + A_{LG} \cdot \gamma_{LG} = A_{SL} \cdot (\gamma_{SL} - \gamma_{SG}) + A_{LG} \cdot \gamma_{LG} + \text{const.} \quad (2-21)$$

where A_{ij} is the surface area of the respective ij -interface. At thermodynamic equilibrium, dW_{tot} must be zero. That means

$$dW_{tot} = dA_{SL} \cdot (\gamma_{SL} - \gamma_{SG}) + dA_{LG} \cdot \gamma_{LG} = 0 \quad (2-22)$$

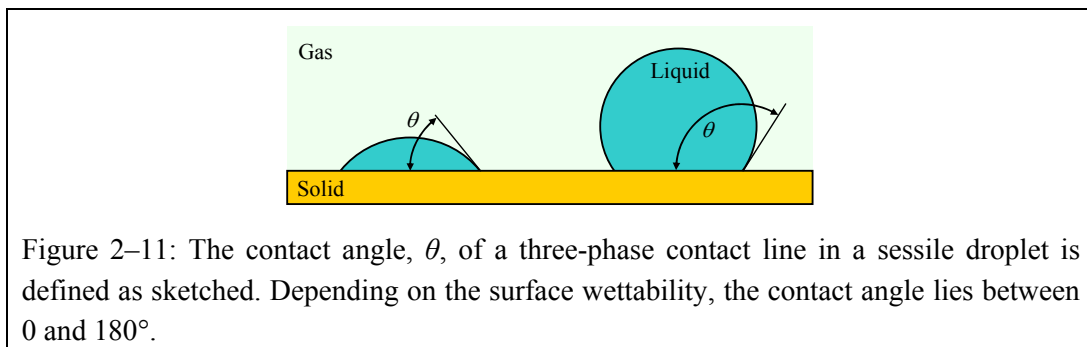
or

$$\gamma_{SG} = \gamma_{SL} + \gamma_{LG} \cdot \left(\frac{dA_{LG}}{dA_{SL}} \Big|_{V=\text{const.}} \right) \quad (2-23)$$

In a free-standing droplet, the minimization of surface energy leads to a spherical drop shape. It is therefore reasonable to assume that a drop sitting on a homogenous surface has a shape like a spherical cap, as shown in Figure 2–11. Thus, it is possible to work out the differential of Equation (2-23). The detailed derivation is given in Annex 1, section 8.1.

$$\frac{dA_{LG}}{dA_{SL}} \Big|_{V=\text{const.}} = \cos(\theta) \quad (2-24)$$

The variable, θ , is the contact angle, which is the angle between the plane of the surface and a tangential plane to the liquid surface at the three-phase contact line. The angle that lies inside the liquid is given.



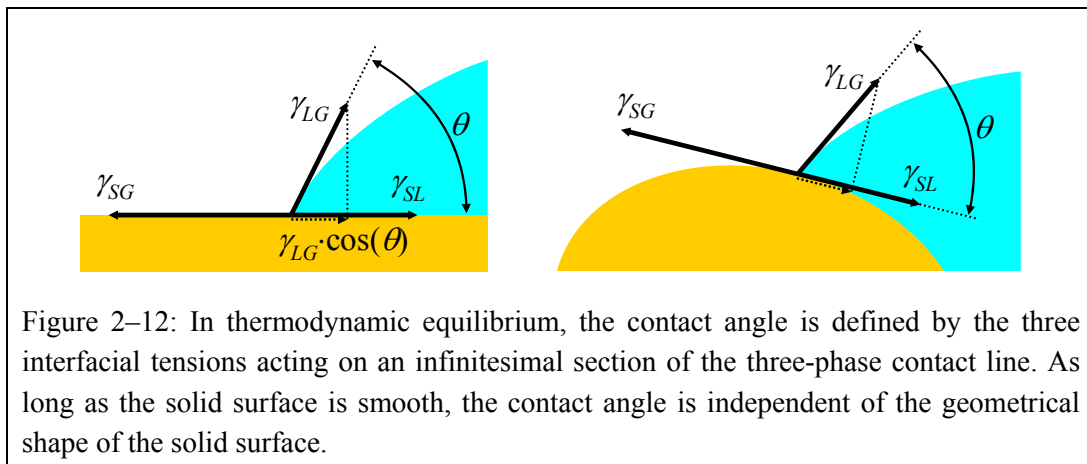
Inserting Equation (2-24) in Equation (2-23) leads to the famous **Young's equation**:

$$\boxed{\gamma_{SG} = \gamma_{SL} + \gamma_{LG} \cdot \cos(\theta)} \quad (2-25)$$

When no adsorption is present, neither on the solid surface nor on the liquid (film pressure $\pi \approx 0$), Equation (2-25) becomes $\gamma_s = \gamma_{SL} + \gamma_L \cdot \cos(\theta)$.

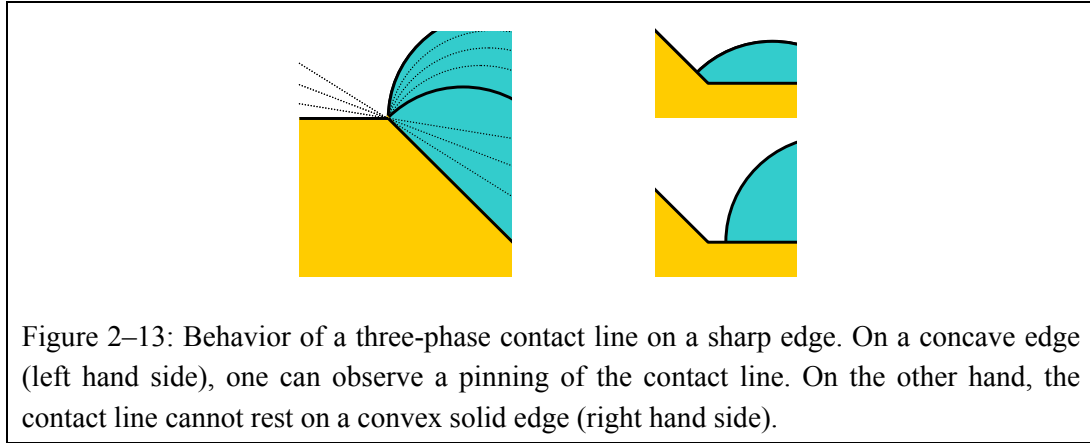
A complete derivation, taking gravity into account and without restriction to a spherical-cap shaped drop, leads to an identical result [24].

Young's equation describes the equilibrium in the solid plane of the three forces resulting from the three interfacial tensions, acting on an infinitesimal section of the three-phase contact line. This is shown on the left-hand side of Figure 2–12. If the solid surface is curved but still smooth, Equation (2-25) remains valid at each point of the three-phase contact line: the force equilibrium in a plane tangential to the solid surface at the point of interest is considered (illustrated on the right-hand side of Figure 2–12). Thus, Young's equation is independent of the surface geometry as long as the solid surface is smooth. In thermodynamic equilibrium, the contact angle is the same on a flat surface, inside a capillary, or at any point of a three-phase contact line lying on any irregularly shaped surface.



A surface with a large contact angle is described as hydrophobic, whereas a surface with a low contact angle is described as hydrophilic. The denotation "hydrophobic" or "hydrophilic" refers usually to water. Since the contact angle depends on the liquid surface tension, and on the SL interfacial tension, measurements with different liquids on the same surface will result in different contact angle values.

A solid surface having sharp concave or convex edges is no longer smooth (not continuously differentiable). The edges influence the concept of contact angle described above. Let us first consider a section of the three-phase contact line lying on a concave edge. Several "tangential" planes to the edge top can now be constructed, so that the direction of the liquid-gas interface, which arises from the contact line, is no longer unique. Such a situation is sketched on the left in Figure 2–13. However, on a convex solid edge, there is no plane that both contains the edge and does not cross the solid body. Thus, a three-phase contact line cannot rest on a convex solid edge, but will lie slightly displaced from it, as shown in the left part of Figure 2–13.



Let us consider the in-plane force equilibrium sketched in Figure 2–12; what happens when $\gamma_{SG} > \gamma_{SL} + \gamma_{LG}$? The contact angle cannot be smaller than zero degree. Young's equation seems also to fail when $\gamma_{SL} > \gamma_{SG} + \gamma_{LG}$. Let us first consider the latter case, where the SL interfacial energy is higher than the sum of the SG and LG interfacial energies. For a weightless drop lying on a surface, the three-phase system would always gain energy during the separation of the liquid phase from the solid phase. Thus, a complete dewetting will occur, so that there is no contact between the liquid and the solid surface.

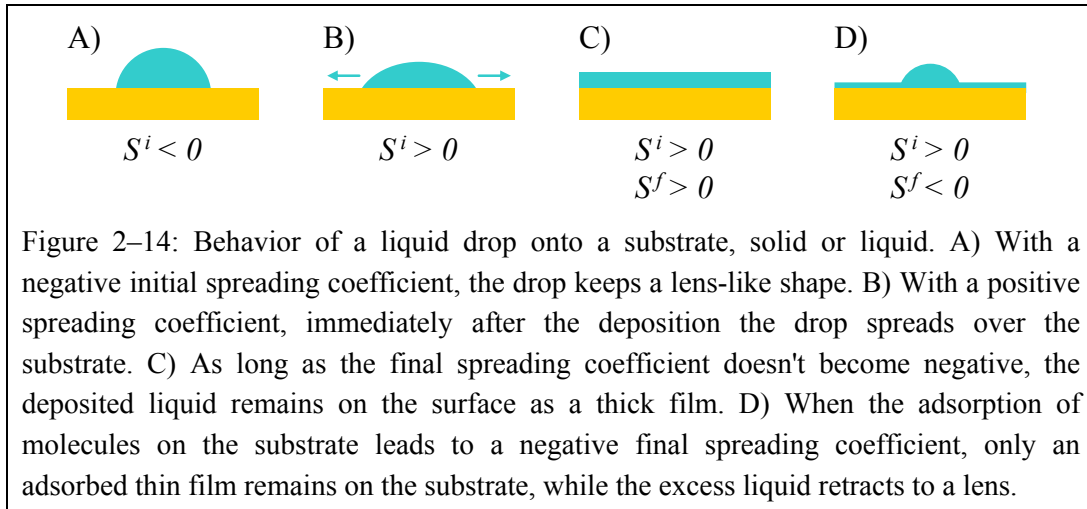
2.3.2.1. Spreading coefficient

When the SG interfacial energy exceeds the sum of the SL and LG interfacial energies, an increase in the SL interface area, together with an increase of the LG surface, and at the cost of SG surface, will reduce the total interfacial energy. Thus, the liquid will spontaneously spread over the solid surface to form a thin film. The contact angle can clearly not be used to characterize this effect. Instead, the spreading coefficient S is used, defined in the following way:

$$S_{LG/SG}^i = \gamma_{SG} - (\gamma_{SL} + \gamma_{LG}) \quad (2-26)$$

The index "i" refers to the fact, that initially no molecules of the liquid are adsorbed at the solid-gas interface. A spreading coefficient is positive if the spreading is accompanied by a decrease in free energy, that is, when it occurs spontaneously.

The spreading that occurs when a liquid with a low surface tension is placed on a liquid with a high surface tension, such as toluene on water, can be described in a similar manner. However, when two liquids are in contact, diffusion occurs until they become mutually saturated, which also influences their interfacial tensions. For a benzene drop placed on a water surface, the benzene lens first rapidly spreads out, and then, as mutual saturation occurs, the benzene retracts back to a lens. The water that is left behind is not pure, but is saturated and recovered by a thin layer of benzene. For pure water at 20 °C, the surface tension is 72.8 mN/m. Nevertheless, the film pressure π (see equation (2-5)) due to the thin benzene layer, lowers the surface tension to 62.2 mN/m, leading to a final spreading coefficient $S^f = S^i - \pi$ that is negative, inducing the retraction of the liquid back to a lens [17,25,26]. Figure 2–14 shows the different possible behaviors when a drop is deposited on a substrate.



2.3.2.2. Influence of the surface roughness on the contact angle

Young's equation is valid for a smooth and homogenous surface, where the local contact angle, θ , is defined with respect to a plane that is tangential to the surface at one local point of the three-phase contact line. Other approaches are needed to describe the global (or apparent) contact angle of a droplet on a rough or inhomogeneous surface.

2.3.2.2a. Wenzel's approach

If a liquid drop lies on a rough surface, the apparent contact angle θ' (measured with respect to the averaged surface) can be different from the local contact angle (with respect to the tangential plane at one local point of the three-phase contact line). One explanation of this behavior was given by Wenzel [27,28]. He stated that the interfacial energy per unit area is higher on a rough surface than on a flat surface. Thus, Young's equation must be corrected by a factor, r , which is the ratio of the actual area to the projected area of the solid surface ($r \geq 1$), leading to the Wenzel's equation:

$$r \cdot \gamma_{SG} = r \cdot \gamma_{SL} + \gamma_{LG} \cdot \cos(\theta') \quad (2-27)$$

or:

$$\left. \begin{array}{l} \cos(\theta') = 1 \\ \cos(\theta') = r \cdot \cos(\theta) \\ \cos(\theta') = -1 \end{array} \right\} \text{if } \left\{ \begin{array}{l} r \cdot \cos(\theta) > 1 \\ -1 \leq r \cdot \cos(\theta) \leq 1 \\ r \cdot \cos(\theta) < -1 \end{array} \right. \quad (2-28)$$

Surface roughness will therefore make a hydrophilic surface even more hydrophilic, and on a hydrophobic surface even more hydrophobic. The effect of the roughness will be even more pronounced if the initial surface is highly hydrophilic or highly hydrophobic.

2.3.2.2b. Cassie's approach

In the presence of a flat, but inhomogeneous surface, Cassie and Baxter [29,30] developed another method. This is to assume that the surface is made of two distinct surface properties, with local contact angles, θ , and θ_1 respectively. Let f be the fractional part of the first kind of surface, and $(1-f)$ that of the second. The apparent contact angle, θ' , on the composite surface will therefore be:

$$\cos(\theta') = f \cdot \cos(\theta) + (1 - f) \cdot \cos(\theta_1) \quad (2-29)$$

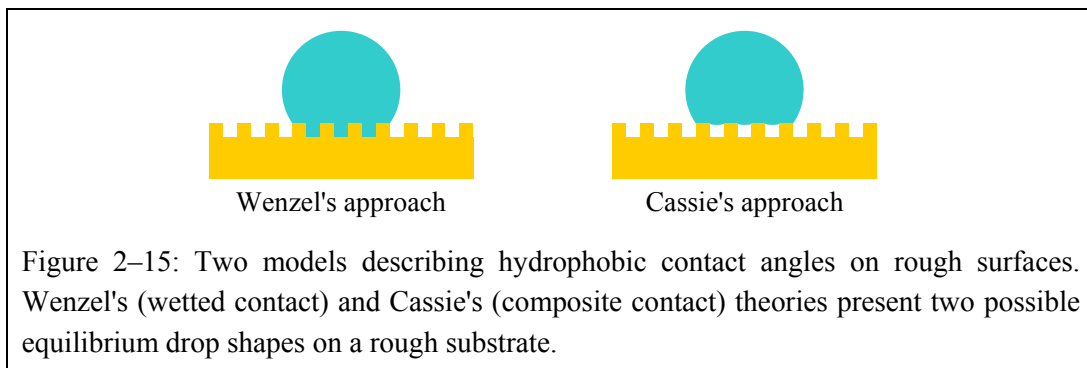
For a homogeneous hydrophobic and highly rough surface, air can be trapped among the hydrophobic structures under the liquid, as shown at the right hand side of Figure 2–15. In a gedanken experiment

one can substitute the areas where the liquid doesn't touch the surface with a flat surface with a contact angle of $\theta_l = 180^\circ$. Therefore, for a hydrophobic and highly rough surface when the SL interface is not fully wetted, one has:

$$\cos(\theta') = f \cdot \cos(\theta) + f - 1 \quad (2-30)$$

Here, f is the fraction of the area that is wetted by the liquid, and θ the local contact angle.

In summary, a liquid drop on a hydrophobic and rough surface can be described by the Wenzel's equation (2-28) when the liquid completely wets the solid surface. If air is trapped at the solid-liquid interface, Cassie's equation (2-30) can be used. Both approaches are sketched in Figure 2–15. It is to date not clear, when one or the other model should be used, since both can exhibit local minima in energy [31].



The combination of a high roughness with hydrophobic contact angles can be used to produce so-called superhydrophobic surfaces with apparent contact angles higher than 170° . Substrates structured to have an array of small pillars, created by microfabrication techniques [32,33], or substrates with a fractal-like topography [34,35] could be used as surfaces having a high roughness.

2.3.2.3. Contact line tension

Young's equation (2-25) was derived by minimizing the free energy of the three interfaces. In the same way than molecules inside the liquid have a lower energy than molecules located at the surface, a molecule located at the three-phase contact line can have a different energy than one lying at the interface. This leads to line tension, a one-dimensional analog of surface tension. The contact line tension, τ , can be given in N or in J/m. Taking account of the contact line tension in equation (2-21) gives a total free energy of:

$$W_{tot} = A_{SL} \cdot (\gamma_{SL} - \gamma_{SG}) + A_{LG} \cdot \gamma_{LG} + P_{SLG} \cdot \tau + \text{const.} \quad (2-31)$$

where P_{SLG} is the length of the three-phase contact line. To obtain the thermodynamic equilibrium, W_{tot} must be minimized. Thus

$$dW_{tot} = dA_{SL} \cdot (\gamma_{SL} - \gamma_{SG}) + dA_{LG} \cdot \gamma_{LG} + dP_{SLG} \cdot \tau = 0 \quad (2-32)$$

or, together with the boundary condition of volume conservation for the liquid:

$$\gamma_{SG} = \gamma_{SL} + \gamma_{LG} \cdot \left(\frac{dA_{LG}}{dA_{SL}} \Big|_{V=\text{const.}} \right) + \tau \cdot \left(\frac{dP_{SLG}}{dA_{SL}} \Big|_{V=\text{const.}} \right) \quad (2-33)$$

For a spherical-cap shaped droplet, the first differential was already calculated in Annex 1, and is equal to $\cos(\theta)$. The second differential can be easily evaluated, using r as the radius of curvature of the three-phase contact line:

$$\left. \frac{dP_{SLG}}{dA_{SL}} \right|_{V=\text{const.}} = \frac{\left. \frac{dP_{SLG}}{dr} \right|_{V=\text{const.}}}{\left. \frac{dA_{SL}}{dr} \right|_{V=\text{const.}}} = \frac{\frac{d}{dr} 2\pi r}{\frac{d}{dr} \pi r^2} = \frac{1}{r} \quad (2-34)$$

Thus, the modified Young's equation is obtained:

$$\gamma_{SG} = \gamma_{SL} + \gamma_{LG} \cdot \cos(\theta) + \frac{\tau}{r} \quad (2-35)$$

which can also be written as

$$\cos(\theta) = \cos(\theta_\infty) - \frac{\tau}{r \cdot \gamma_{LG}} \quad (2-36)$$

where θ_∞ is the contact angle in the limit of a very large drop ($r \rightarrow \infty$). Equation (2-36) shows that the contact line tension will only affect the contact angle for a high curvature of the three-phase contact line.

Both the sign and magnitude of the line tension are still under debate [36]. Theoretical calculations predict τ to be on the order of some 10^{-11} J/m [36,37], whereas experimental values are much more controversial [36,38,39]. However, assuming the theoretical values are correct, the influence of contact line tension should be experimentally significant only if $r < \tau/\gamma_{LG} \approx 10^{-11} \text{ Jm}^{-1} / 10^{-2} \text{ Jm}^{-2} = 1$ nm. In other words, a measurable influence of the contact line tension is to be expected in the nanometer range, while in large systems, interfacial energies will dominate.

2.3.2.4. Contact angle hysteresis

The derivation of the Young's equation was based on thermodynamics, so that one could imagine a unique and well defined contact angle for a given solid-liquid-gas set. Nevertheless, in experimental observations (see Section 3.2), one usually observes a difference between the contact angle of an advancing three-phase contact line (the line is moved towards the solid-gas interface) and a receding line (moved towards the solid-liquid interface). The advancing contact angle θ_{adv} is always higher than the receding contact angle θ_{rec} , leading to the contact angle hysteresis.

It is due to contact angle hysteresis that a drop doesn't roll or flow under gravity on a tilted surface. A low hysteresis will immobilize the drop only on a slightly tilted surface. The immobilization of a drop on a vertical surface can be guaranteed only with a higher hysteresis.

A complete understanding of the hysteresis observed in the contact angle measurements has not yet been achieved. One explanation for the hysteresis can be found in surface heterogeneities and surface roughness.

A heterogeneous surface is shown in Figure 2–16, where the surface has locally different contact angles. As the drop moves, the advancing three-phase contact line will remain pinned at the hydrophilic-hydrophobic transition, and will start to move only when it is energetically more favorable, i.e. when the local contact angle of drop is slightly larger than the contact angle of the hydrophobic area. When the advancing front leaves the hydrophobic area and enters a hydrophilic one, the three interfacial forces will be suddenly unbalanced, and the advancing contact line will "jump" over the hydrophilic area until a new local minimum in energy is found, e.g. at the next hydrophilic-

hydrophobic transition. The contact angle of the advancing contact line will therefore be close to the contact angle of the hydrophobic area. Similarly, the receding contact line will jump from one hydrophilic area to the other. This so-called pinning effect results in contact angle hysteresis.

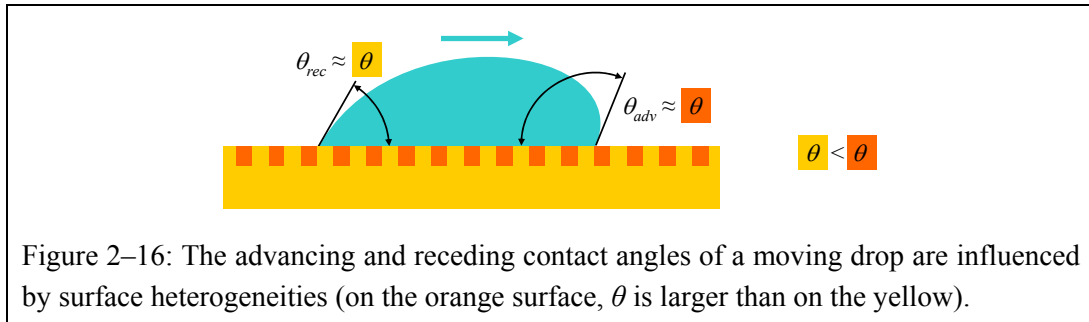


Figure 2-16: The advancing and receding contact angles of a moving drop are influenced by surface heterogeneities (on the orange surface, θ is larger than on the yellow).

Similarly, on a rough surface, the advancing and receding lines will be pinned on a downhill-slope, arising from a difference between the apparent advancing contact angle θ_{adv} and apparent receding contact angle θ_{rec} , even if the local contact angle θ is identical at both sections of the moving three-phase contact line (see Figure 2-17).

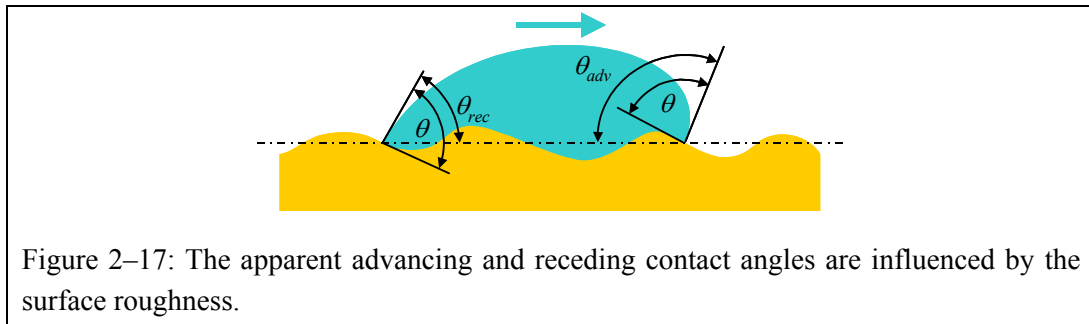


Figure 2-17: The apparent advancing and receding contact angles are influenced by the surface roughness.

Other reasons that explain the presence of the hysteresis can be the adsorption on the solid surface of molecules dissolved in the liquid, or rearrangement or alteration of the solid surface by the liquid.

The static contact angle θ_{sta} refers to the contact angle measured on a fixed three-phase contact line. It lies between the two limits given by the advancing and receding contact angles. Otherwise, the three-phase contact line would start to move until a new equilibrium position is reached. The advancing and receding contact angle values therefore better describe a surface with respect to a liquid, compared to the static contact angle alone. Nevertheless, if a liquid drop is gently deposited onto the surface, the static contact angle will be quite close to the advancing contact angle.

2.3.3. Hydrostatic equilibrium

The conditions necessary to reach a hydrostatic equilibrium for a system involving a solid, a liquid and a gaseous phase will be considered. The shapes of the SL and SG interfaces are defined by the shape of the solid body, except for the position of the three-phase contact line boundary. Less obvious is the shape that the LG interface will take.

The Bernoulli equation states that the sum of the dynamic pressure, the static pressure, and the pressure given by the height of the liquid is constant inside the bulk liquid. In a hydrostatic consideration, the dynamic pressure vanishes, and the Bernoulli equation reduces to:

$$P_L + \rho gz = \text{const.} \quad (2-37)$$

where P_L is the static pressure inside the liquid, ρ the density of the liquid, g is the gravitational field, and z the height measured upwards on a axis along the gravitational field.

From the Laplace pressure derived in equation (2-20) it follows that a curvature of the LG interface induces a pressure change ΔP when crossing the LG interface. Hence, over a non-horizontal LG interface, the "potential pressure" $\rho g z$ must be compensated by the Laplace pressure.

$$P_L = P_G + \Delta P = P_G + \gamma_{LG} \left(\frac{1}{R_1} + \frac{1}{R_2} \right) \quad (2-38)$$

This equation defines the equilibrium condition over the LG interface. Thus, knowing the local mean surface curvature at one point on the LG interface, the equation allows the determination of the mean surface curvature at any other point on the interface. For hydrostatic equilibrium, the equation must be fulfilled at all points of the LG interface. For a hydrostatic equilibrium, this condition is mandatory, but is not sufficient alone to determine the shape of a LG interface.

A second condition is related to the minimization of the total interfacial energy. This is given by Young's equation (2-25), which defines the contact angle with respect to the three interfacial energies. The second condition must be fulfilled at each point of the three-phase contact line.

Thus, the conditions that define the shape of a liquid-gaseous interface are given by the following set of equations:

$$\begin{cases} P_G + \gamma_{LG} \left(\frac{1}{R_1} + \frac{1}{R_2} \right) + \rho g z = \text{const.} \\ \cos(\theta) = \frac{\gamma_{SG} - \gamma_{SL}}{\gamma_{LG}} \end{cases} \quad (2-39)$$

In addition, other boundary conditions can be present, such as a constant volume of the liquid. One should mention that, if one shape of the LG interface is fulfilling both equations, this corresponds to a local minimum in energy. Another shape, also fulfilling both equations, can exist with a lower total interfacial energy. Additionally, we have seen that the contact angle suffers from a hysteresis, leading to even more local minima.

In this work, when small amounts of liquid are considered, the Laplace pressure is of much higher importance than the "potential pressure" $\rho g z$, and gravity can be neglected. If additionally the pressure P_G is constant over the entire LG interface, the first condition of equation (2-39) reduces to an identical curvature at each point of the LG interface.

2.3.4. Numerical construction of an axisymmetric liquid-gas interface

It is not possible to solve equation (2-39) analytically. In order to simplify the derivation of a solution, only the upper condition in equation (2-39) is considered. Furthermore, some other simplifications can be made, by assuming:

- first, a constant gas pressure P_G over the entire LG interface,
- second, the shape of the LG interface to be a surface of revolution around the z -axis,
- and third, that the liquid lies in the inner volume defined by the rotational symmetric surface (i.e. we consider droplets and not voids surrounded by liquid).

Instead of taking the entire 3-dimensional LG interface, it is then possible to consider only one meridian of the surface of revolution. This leads to the equation:

$$\frac{1}{R_1} + \frac{1}{R_2} + \frac{\rho g}{\gamma_{LG}} z = \text{const.} \quad (2-40)$$

Even with this simplification, it is still not possible to solve equation (2-40) analytically. Nevertheless, it is possible to solve the equation numerically, and to reconstruct the meridian by iteration. A well-known start condition comprises the coordinates x and z of the start point, the slope α of the meridian and the interfacial local mean surface curvature κ at the start point. Additionally, one has to know the interfacial tension γ_{LG} , the density of the liquid ρ , and the strength of the gravitational field g .

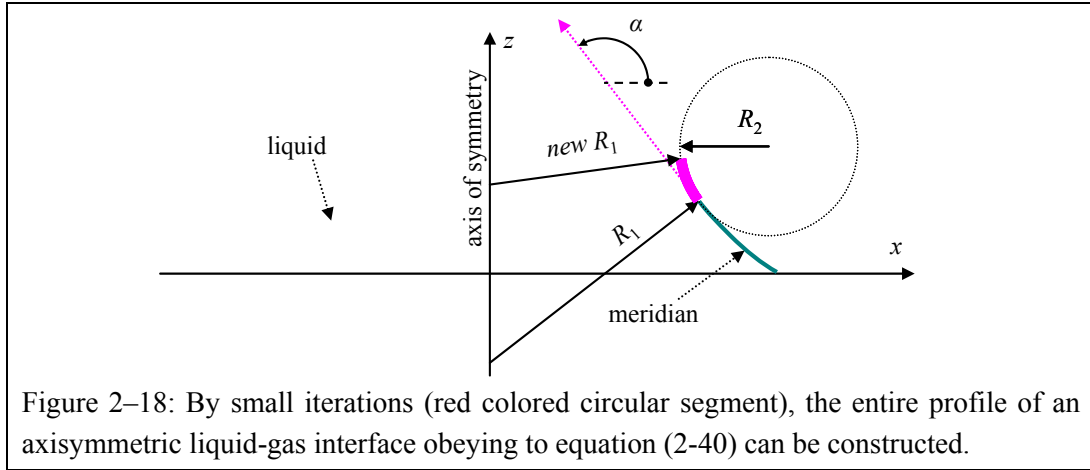


Figure 2–18: By small iterations (red colored circular segment), the entire profile of an axisymmetric liquid-gas interface obeying to equation (2-40) can be constructed.

From the start parameters (x, z^a, α, κ) , one first determines geometrically the radius R_1 (see Figure 2–18), which is the distance from the point (x, z) to the intersection point of the z -axis with the normal to the meridian at the point (x, z) . R_1 is taken to be positive, since its center points into the liquid. The radius R_2 can then be determined by:

$$R_2 = \left(\kappa - \frac{1}{R_1} \right)^{-1} \quad (2-41)$$

A circular segment of arc $\Delta\alpha$ and radius R_2 can then be drawn, starting from the point (x, z) and tangentially to the direction α . The sign of R_2 must be respected. The end-point of the circular segment will be the starting point of the next iteration. The slope α_i at the new point i will be $\alpha_{i-1} + \Delta\alpha$, and the new κ_i :

$$\kappa_i = \kappa_{i-1} + \frac{\rho g}{\gamma_{LG}} (z_{i-1} - z_i) \quad (2-42)$$

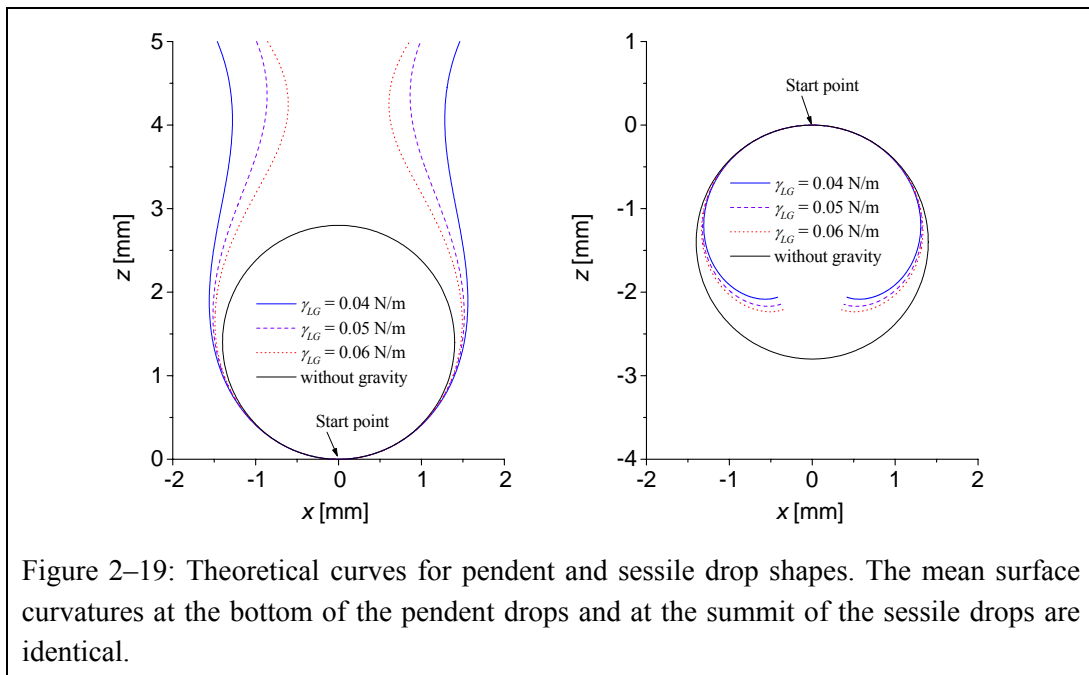
A full description of the iterations and a short program performing the iterations are given with more details in Annex 2, section 8.2.

2.3.4.1. Shapes of pendent and sessile drops

This method permits the construction of the profile shape of a sessile or pendant drop, starting the iterations from the summit of the sessile drop, or from the base of the pendent drop (see Figure 2–19).

^{a)} The coordinate z is not really a true start parameter, since it does not influence the shape of the meridian constructed, but only shifts the meridian along the z -axis.

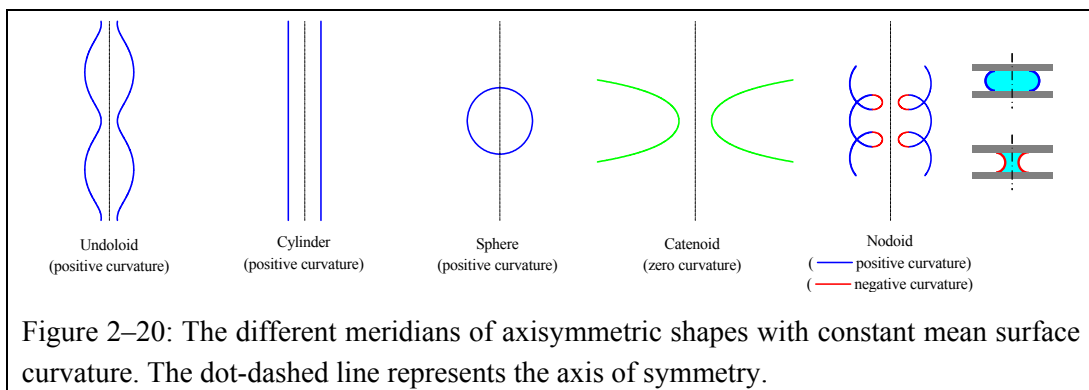
At these two points, the radii of curvature R_1 and R_2 are equal, because of the symmetry of revolution. Furthermore, the tangential plane to the interface is horizontal, leading to the starting value $\alpha = 0$. Let the points have the coordinates $x = 0$ and $y = 0$. Thus, only two free parameters remain: R_1 and the ratio $\rho g/\gamma_{LG}$. By varying the two free parameters, a line can be constructed by iteration to fit to a profile shape that is known from experiments (see section 3.2). In this way the LG interfacial tension liquid can be measured experimentally, since the density ρ is easily measurable, and g is usually known. Figure 2–19 shows the influence of the LG interfacial tension γ_{LG} for a pendent drop and for a sessile drop (R_1 at the start point is constant).



2.3.4.2. Axisymmetric shapes when neglecting gravity

When gravity can be neglected, the main curvature κ is no longer dependent on the z -coordinate, and is constant over the entire LG interface. The direction of the z -axis can be arbitrarily chosen, and is independent of the direction of the gravitational field.

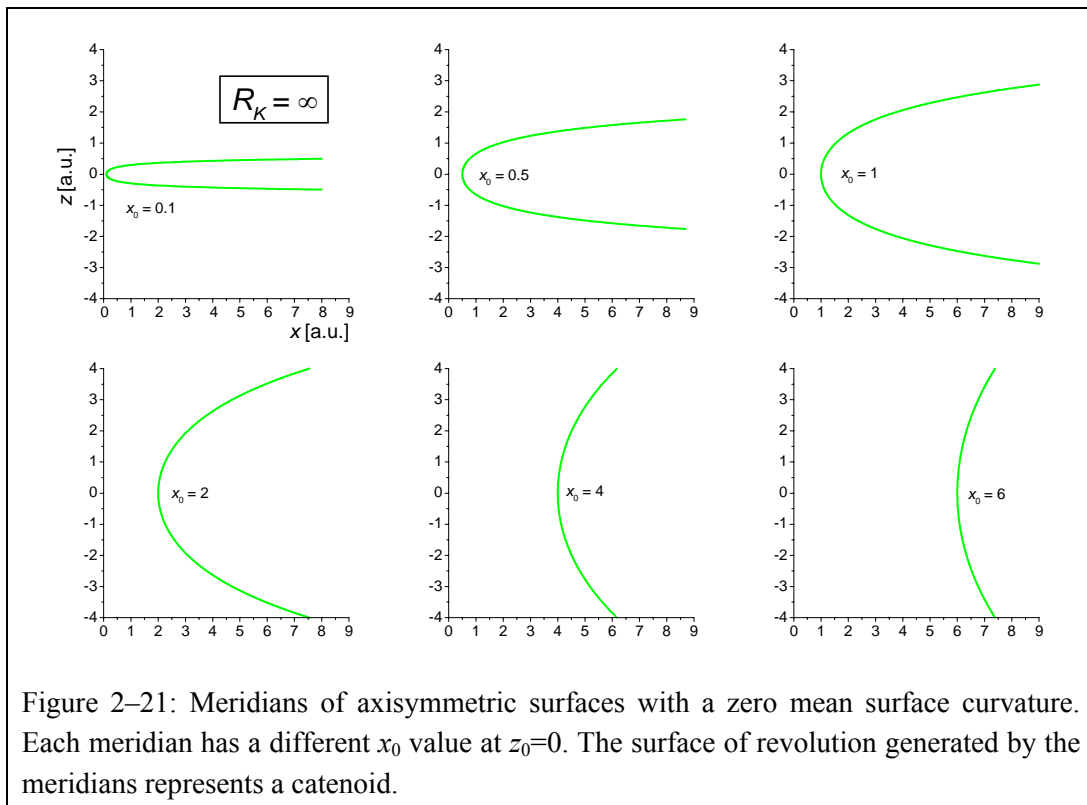
There are five known surfaces with a constant mean surface curvature and cylindrical symmetry [40,41]. The five are: the unduloid, the cylinder, the sphere, the catenoid, and the nodoid. The catenoid, together with the sphere and the cylinder, can be analytically described. The unduloid and the nodoid can only be solved by numerical iteration, using the method described in Annex 2, with a gravitational strength $g = 0$. The five meridians are represented in Figure 2–20.



The sign of the curvature depends only on the choice of which side of the axisymmetric surface the liquid is placed. It is assumed that the liquid is in the inner volume defined by the rotational symmetric surface. Thus, the unduloid, the cylinder and the sphere have a positive surface curvature. The catenoid has by definition a zero mean surface curvature. The meridian of a nodoid can be split into several parts. The liquid between two blue segments has a positive mean curvature, whereas the liquid between two red segments has a negative mean surface curvature. However, the absolute values of both curvatures are equal.

2.3.4.2a. Axisymmetric shapes with a zero mean surface curvature

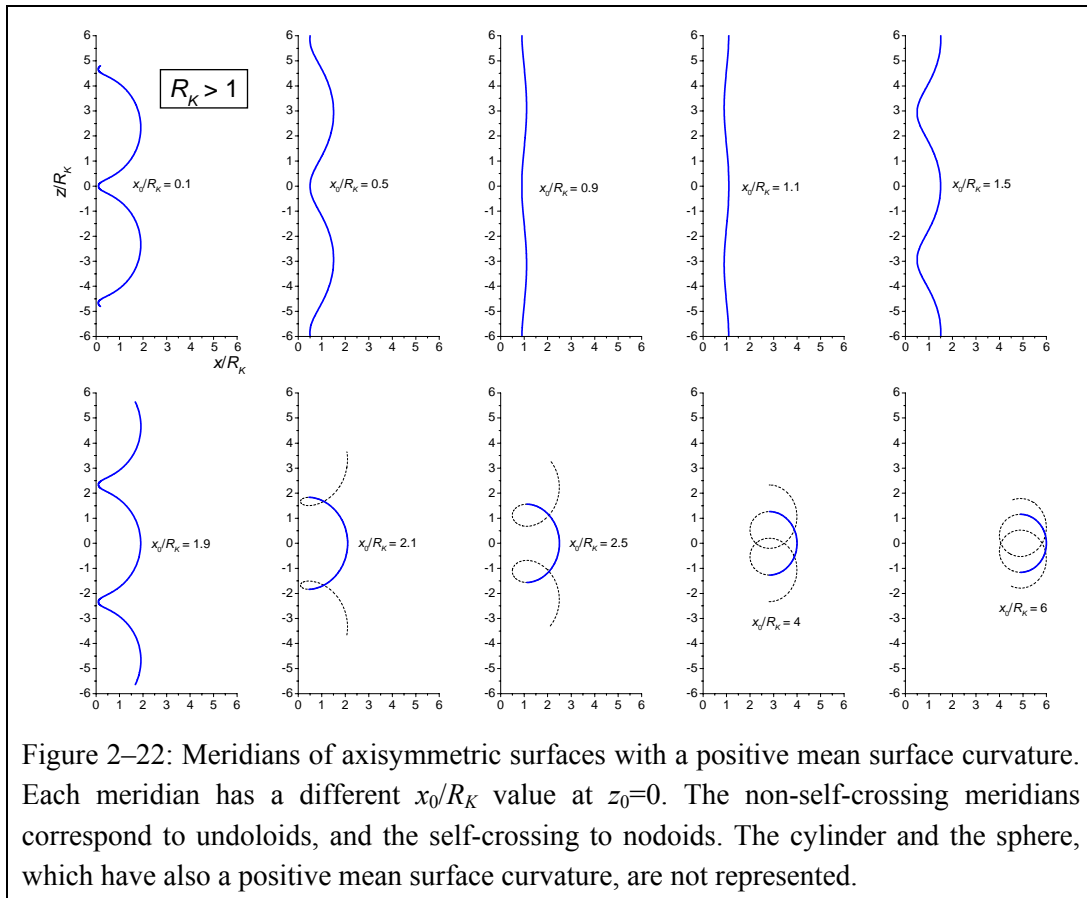
The catenoid is a surface of revolution with a zero mean surface curvature, i.e. $\kappa = 0$, which is equivalent to $R_2 = -R_1$ (see Figure 2–18). The catenoid is the surface with the minimum surface area spanned between two circular frames, which have their centers on the axis of symmetry, and their planes perpendicular to the axis of symmetry. If a film of liquid can be spanned between two such circular frames, it will spontaneously form a catenoid. The analytical solution of its meridian, called a catenary, is given by the equation $x = c \cdot \cosh(z/c)$ where c is a constant [42]. The constant c corresponds to the x coordinate at the neck of the meridian. Some examples of catenaries are shown in Figure 2–21. The z -axis is the axis of symmetry.



2.3.4.2b. Axisymmetric shapes with a positive mean surface curvature

The meridians of surfaces of revolution with a positive mean surface curvature surrounding a liquid body will now be considered. Figure 2–22 shows some of them. The meridians are constructed by iteration (see Annex 2, section 8.2) and are therefore numerical solutions, and not necessary physical ones. They are normalized with respect to the mean radius of curvature R_K . The iterations were done varying the start value x_0/R_K , while the other start values were kept constant ($z = 0, \alpha = 90^\circ$). Since $\alpha = 90^\circ$ at the start point of the iteration, the start point will be located at a neck or at a bulge of the

axisymmetric liquid body. The self-crossing meridians are nodoids, while the others are unduloids. The types of surfaces as function of the start value of the meridian are given in Table 2–4.



The meridians of unduloids with a starting value x_0/R_K in the interval $]0,1[$ are identical to those with x_0/R_K in the interval $]1,2[$, except for a shift in the z -direction. For the meridians of nodoids, which are self-crossing, the blue parts represent the fraction that has a physical meaning, e.g. for a volume of liquid compressed between two parallel and highly hydrophobic plates.

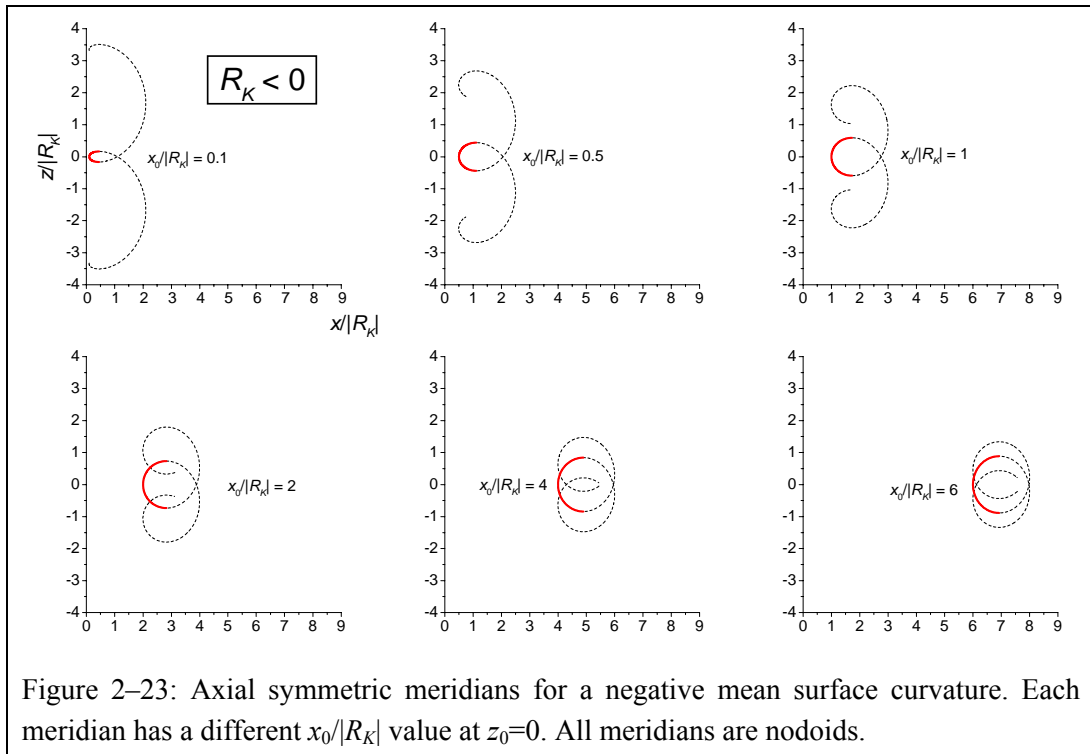
$0 < x_0/R_K < 1$	Unduloid	
$x_0/R_K = 1$	Cylinder	(borderline case)
$1 < x_0/R_K < 2$	Unduloid	
$x_0/R_K = 2$	Sphere	(borderline case)
$x_0/R_K > 2$	Nodoid	(self-crossing)

Table 2–4: Classification of the positively-curved axisymmetric shapes. Depending on the initial values for an iterative solution, different kinds of meridian are generated.

2.3.4.2c. Axisymmetric shapes with a negative mean surface curvature

The last group is formed by axisymmetric bodies with a negative mean surface curvature. Figure 2–23 shows some of them, calculated by iteration. An axisymmetric body with a negative mean surface curvature always has a nodoid meridian. The red colored fraction of each meridian represents the LG interface of a volume of liquid compressed between two parallel and highly hydrophilic plates. One can recognize that the nodoids in Figure 2–22 and Figure 2–23 are similar. The only difference is in

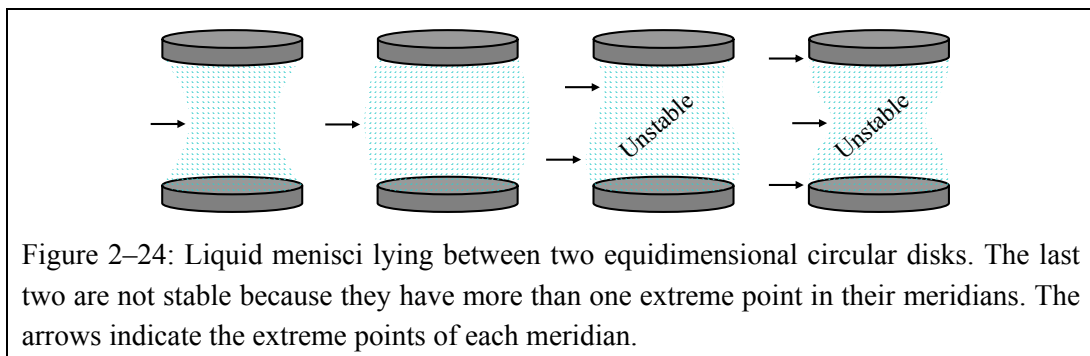
the part of the section that is taken into account (outer lobe for a positive mean surface curvature and inner lobe for a negative mean surface curvature), and in a shift in the z -direction.



For the catenoid, nodoid and cylinder, the mathematical solution implies that an infinitely high liquid column could exist. Nevertheless, a very high column of liquid will not be physically stable. The stability conditions are discussed in section 2.3.4.3.

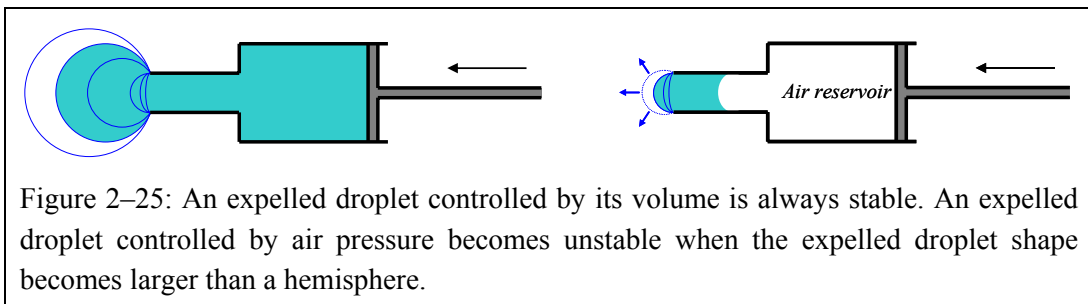
2.3.4.3. Meniscus stability

Liquid bridges between solid bodies have been the focus of numerous theoretical and experimental investigations since the early work by Plateau more than a century ago [43]. Most theoretical investigations were done on weightless liquid menisci lying between two coaxial equidimensional circular disks. According to Slobozhanin et al. [44], an axisymmetric weightless liquid bridge between two circular disks cannot be stable if the meridian has more than one extreme point (located at the neck or bulge). Some examples are shown in Figure 2-24.



However, a liquid bridge with only one extreme point is not necessarily stable. Having only one extreme point is a necessary but not sufficient condition for equilibrium. E.g. a catenoid will become unstable if the ratio of height to neck diameter is larger than 2.238 [45]. A cylindrical column of liquid higher than its circumference is unstable too.

There are two regimes of stability. The first is defined by a controlled volume of the meniscus while the second one involves a controlled pressure inside the liquid meniscus [46]. To illustrate this difference, consider the stability criteria for a drop of liquid slowly expelled out of a filled syringe, first by a controlled movement of the piston (volume controlled), and second by applying a controlled pressure inside the syringe (see Figure 2–25). In the case of the pressure-controlled extruded drop, as long as the drop is smaller than a hemisphere, it will be stable. However, once the shape of the expelled liquid becomes larger than a hemisphere, it becomes unstable and will grow continuously, because the Laplace pressure inside the droplet decreases as the drop volume increases. When the extruded drop is controlled through its volume, the instability does not appear.

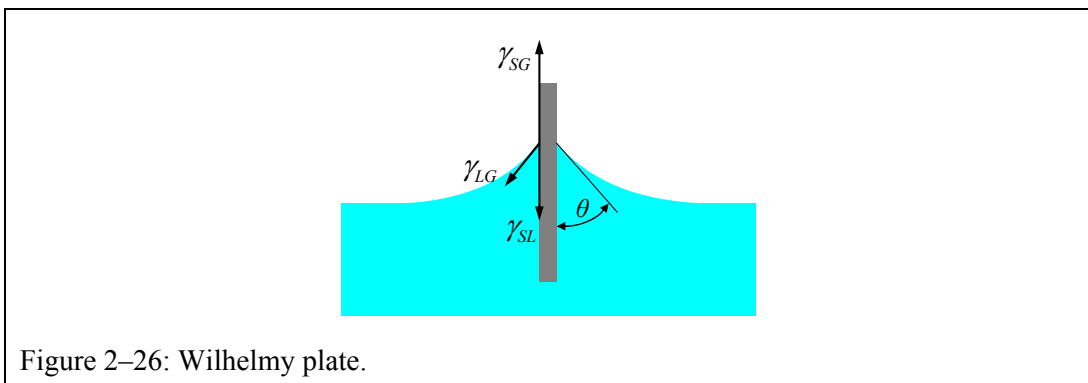


2.3.5. Capillary forces

The capillary force exerted by a liquid meniscus on a solid body has two components. The first is related to the surface tension of the liquid, and the second to the Laplace pressure inside the liquid.

2.3.5.1. Capillary force due to the surface tension

Consider an infinitesimal thin Wilhelmy plate, partially immersed and oriented perpendicularly to the liquid surface (see Figure 2–26).



In agreement with equation (2-39), a meniscus will be present around the perimeter of the plate. The equation describing the profile of such a meniscus can be found in reference [42]. Let θ be the contact angle of the liquid with the plate, and L the perimeter of the plate. By raising the plate a distance dz , the total free interfacial energy will be changed by an amount $dE = L \cdot dz \cdot (\gamma_{SG} - \gamma_{SL})$. Thus, a force F is exerted on the plate at the three-phase contact line:

$$F = -\frac{dE}{dz} = -L \cdot (\gamma_{SG} - \gamma_{SL}) = -L \cdot \gamma_{LG} \cdot \cos(\theta) \quad (2-43)$$

The capillary force due to the liquid surface tension at the three-phase line will thus pull the plate into the liquid if the contact angle is smaller than 90° . For contact angles higher than 90° , the plate will be pushed out.

2.3.5.2. Capillary force due to the Laplace pressure

The second component of a capillary force is due to the Laplace pressure inside the liquid, itself induced by the curvature of the LG interface, acting on the wetted solid surfaces. Figure 2–27 shows two examples, where a constant volume, V , of liquid is compressed between two parallel plates. In the top example, the liquid forms a contact angle of 0° (fully hydrophilic) whereas in the lower one the contact angle is 180° (fully hydrophobic).

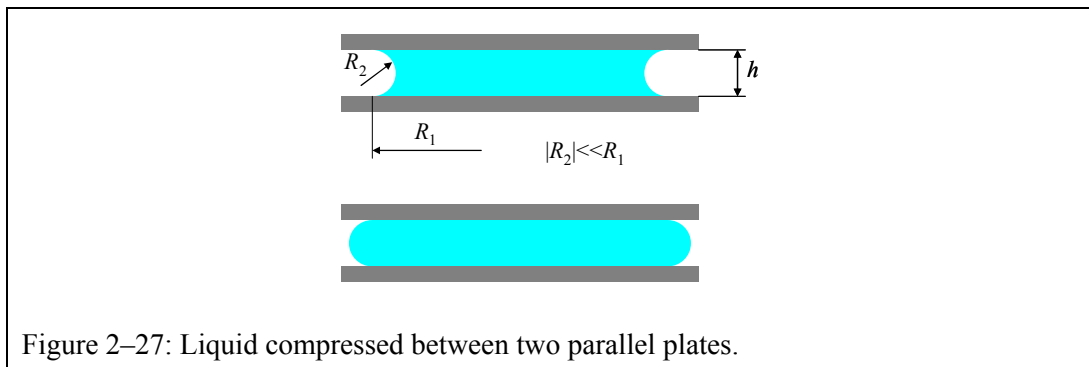


Figure 2–27: Liquid compressed between two parallel plates.

If $R_1 \rightarrow \infty$, the meridian of the axisymmetric volume can be described as a constant radius R_2 (see also the last nodoid in Figure 2–22 and Figure 2–23). The pressure P_L inside the liquid, which corresponds to the Laplace pressure, exerts a force between the two plates:

$$F = P_L \cdot A = \gamma_{LG} \left(\frac{1}{R_1} + \frac{1}{R_2} \right) \cdot \pi R_2^2 \approx \pm 2 \cdot \gamma_{LG} \cdot \frac{V}{h^2} \quad (2-44)$$

The capillary force is attractive between the fully hydrophilic plates, where the meridian radius R_2 is negative, whereas the force is repulsive between the fully hydrophobic plates where the meridian radius R_2 is positive.

2.3.5.3. Capillary force for axisymmetric meniscus

The capillary force exerted by the meniscus can be calculated at each cross section that is perpendicular to the axis of symmetry of the meniscus.

Equation (2-43) is valid as long as the surface of the Wilhelmy plate is perpendicular to the liquid surface. More generally, one can consider the effect of the liquid surface tension on the solid surface, or on the cross section, as a two-dimensional pressure acting along the entire three-phase contact line and along the direction of the LG interface.

Equation (2-44) is also a special case of the capillary force component due to the Laplace pressure. It is easy to generalize it by defining the force component due to the Laplace pressure as the force exerted by the liquid pressure over the wetted surface of the solid, or over the cross section.

Assuming an axisymmetric liquid meniscus, one can calculate the capillary force along the axis of revolution by:

$$F_{cap} = \underbrace{-2\pi \cdot x \cdot \gamma_{LG} \cdot |\sin(\alpha)|}_{\text{surface tension}} + \underbrace{\pi \cdot x^2 \cdot \gamma_{LG} \cdot \kappa}_{\text{Laplace pressure}} \quad (2-45)$$

$$\left(F_{cap} > 0 \Leftrightarrow F_{cap} \text{ is repulsive} \right)$$

$$\left(F_{cap} < 0 \Leftrightarrow F_{cap} \text{ is attractive} \right)$$

The angle α corresponds to the slope of the meridian, as shown in Figure 2–18. The component due to the surface tension of the liquid is always attractive, whereas the component due to the Laplace pressure can be attractive or repulsive, depending on the sign of the mean surface curvature κ .

It is now possible to determine the kind of capillary force (attractive or repulsive) as a function of the type of weightless axisymmetric meniscus (see Figure 2–21, Figure 2–22, and Figure 2–23). The following table summarizes the results:

Mean surface curvature κ	Kind of meniscus surface	Capillary force
negative	Nodoid	attractive
zero	Catenoid	attractive
positive	Undoloid	attractive
	Cylinder	attractive
	Sphere	zero
	Nodoid	repulsive

Table 2–5: Sign of the capillary force exerted by an axisymmetric liquid bridge.

When the meniscus is a zone of a sphere, the “surface tension” and the “Laplace pressure” components of the capillary force cancel out. This is not surprising, since a sessile drop does not exert any force on a solid surface apart from gravitational forces.

Knowing the shape of an axisymmetric liquid body (pendent or sessile drop, meniscus), equation (2-45) defines the capillary force at any perpendicular plane to the z -axis. By knowing the strength of the capillary force, one can also construct the meridian even if one value of the starting points (x , α , κ) is missing.

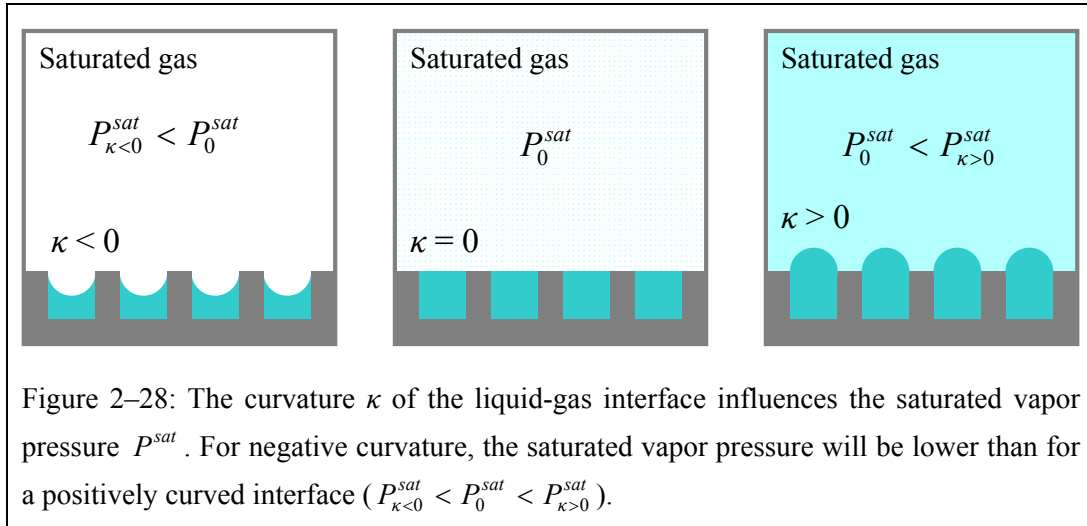
2.3.6. Thermodynamic equilibrium and spontaneous condensation

In section 2.3.3, hydrostatic equilibrium considerations were used to develop the possible shapes of axisymmetric menisci. The thermodynamic equilibrium was taken into account to develop the concept of contact angle, assuming that no exchange occurs through the LG interface. However, if a liquid phase is exposed to an environment unsaturated in its own vapor, evaporation will occur. With a saturated vapor pressure, condensation can take place.

The saturated vapor pressure P_0^{sat} is usually measured with respect to a flat liquid-gas interface. However, if the LG interface is not flat, the value of the saturated vapor pressure will be influenced by the surface curvature. This effect is described by the **Kelvin equation** [17,47]:

$$\ln\left(\frac{P_\kappa^{sat}}{P_0^{sat}}\right) = \frac{V_m \cdot \gamma_L}{R \cdot T} \cdot \kappa \quad \Leftrightarrow \quad R_K = \frac{V \cdot \gamma_L}{R \cdot T} \cdot \frac{1}{\ln\left(\frac{P_\kappa^{sat}}{P_0^{sat}}\right)} \quad (2-46)$$

In the Kelvin equation, P_{κ}^{sat} is the saturated vapor pressure for the curved LG interface, P_0^{sat} for a flat interface. V_m is the molar volume of the liquid and R the universal gas constant ($8.31 \text{ JK}^{-1}\text{mol}^{-1}$). R_K is the mean radius of curvature, and is the inverse of κ . For a negatively curved LG interface, the saturated vapor pressure will be lower than P_0^{sat} and it will be higher for a positive curvature of the interface (see Figure 2–28).



In a normal ambient environment (relative vapor pressure: $0 < P/P_0^{sat} < 1$), a drop of liquid with its positive curvature will therefore always evaporate ($P/P_0^{sat} < 1 \Rightarrow P/P_{\kappa>0}^{sat} < 1$). But a negatively curved liquid surface can remain in thermodynamic equilibrium (neither evaporation nor condensation) when $P/P_{\kappa<0}^{sat} = 1$. (This is not in contradiction with $P/P_0^{sat} < 1$ since $P_{\kappa<0}^{sat} < P_0^{sat}$). Furthermore, since water is always present as vapor in ambient environment, capillary condensation can spontaneously occur in hydrophilic pores or around contact points between two solid bodies (e.g. between an AFM tip and the sample surface) when at least one of them is hydrophilic^{a)}. The mean radius of curvature, R_K , of such a capillary condensate is also defined by the Kelvin equation (2-46). Some values are given in Table 2–6.

Relative humidity	Mean radius of curvature
P/P_0^{sat}	R_K [nm]
0%	0
10%	-0.23
50%	-0.78
90%	-5.1
100%	∞

Table 2–6: Mean radius of curvature for water capillary condensates at a temperature of 20 °C for different relative humidities.

^{a)} If both surfaces are hydrophobic (contact angle higher than 90°), no condensed-water meniscus will be present, since, due to the geometry, only a liquid meniscus with a positive mean surface curvature can exist and thus will fully evaporate.

2.3.6.1. Capillary force induced by a spontaneously condensed meniscus

The presence of a liquid meniscus of condensed water between two bodies will induce a capillary force. The capillary force exerted between a flat surface and a sphere, for the case where the sphere radius R_S is much larger than R_K , is mainly due to the force component issue from the Laplace pressure. The capillary force can be estimated by [48]:

$$F_{cap} = -2 \cdot \pi \cdot R_S \cdot \gamma_L \cdot (\cos(\theta_1) + \cos(\theta_2)) \quad (2-47)$$

where θ_1 and θ_2 are the contact angles of water on the flat surface and on the spherical surface respectively. In this approximation, the curvature radius of equation (2-46) does not appear in equation (2-47), indicating that the relative humidity does not play a role. This is because, even if R_K and ΔP depends on the humidity, the product of the Laplace pressure with the area on which it acts remains constant. Using the construction of theoretical axisymmetric menisci (see sections 2.3.4) in order to determine the capillary force (equation (2-45)), comparable results are obtained, as shown in Table 2–7.

		Sphere radius R_S		
		$R_S = 5 \text{ nm}$	$R_S = 20 \text{ nm}$	$R_S = 100 \text{ nm}$
Relative humidity P/P^0	10%	-4.2 nN (-4.6)	-17 nN (-18)	-90 nN (-91)
	50%	-3.9 nN (-4.6)	-17 nN (-18)	-88 nN (-91)
	90%	-3.1 nN (-4.6)	-15 nN (-18)	-83 nN (-91)

Table 2–7: Capillary force resulting from a condensed-water meniscus, acting between a sphere of radius R_S and a flat surface, both fully hydrophilic ($\theta_1 = \theta_2 = 0^\circ$). The values are calculated from equation (2-45), once the shape was estimated by tangentially fitting an axisymmetric meridian. The values in brackets are those given by equation (2-47).

Nevertheless, equation (2-47) is only valid for a sphere on a flat surface and for a liquid meniscus that is in hydrostatic and thermodynamic equilibrium (i.e. the mean surface curvature fulfills the Kelvin equation). For a random geometry, the determination of the capillary force can be quite complicated. As long as the meniscus conserves an axisymmetric shape, even if an external source supplies liquid inside the meniscus (Kelvin equation no longer fulfilled), one can estimate the strength of the capillary force using equation (2-45) once the shape of the meridian has been determined.

This chapter has shown that our understanding of capillary phenomena, such as capillary forces or the equilibrium shapes of small amounts of liquids, is based on several physical concepts. Intermolecular and interatomic forces build up a surface tension, which induces a Laplace pressure at a curved interface. Surfaces can have different wettabilities (hydrophobic or hydrophilic), which change the behavior of the liquid that contacts the surface because of the different contact angles. All of these points are necessary to be able to describe what is happening when the tip of the nanodispenser touches the substrate, and how and why liquid is transferred to the substrate.

3. Experimental setup

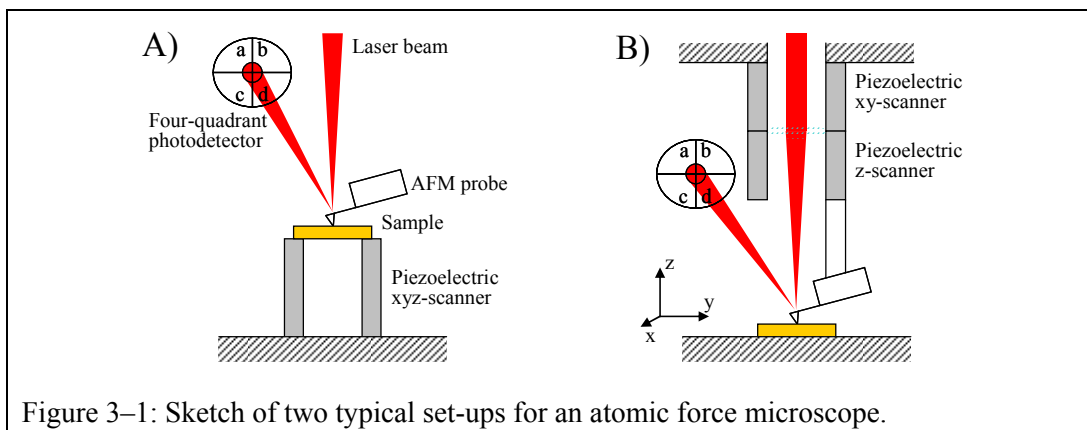
In this section a list is given of the instruments used, along with some basic explanations for the two most important.

3.1. Atomic force microscope

The invention of the scanning tunneling microscope (STM) in 1982 [49,50], followed by the atomic force microscope (AFM) in 1986 [51], has been major factor in the emergence of the nanotechnology field. The large family of scanning probe microscopes (SPM), to which belongs e.g. the scanning near-field optical microscope (SNOM), has the common feature that they analyze a surface with a local probe. Instead of acquiring the entire micrograph at once like in a conventional optical microscope, in an SPM the micrograph is constructed by scanning the probe over the area to be analyzed, and composing the picture electronically. The characteristic range of the interaction between the local probe and the surface is much smaller than the characteristic wavelength of the interaction. Thus, SPM's do not suffer from the limitation associated with phenomena such as diffraction, like in optical microscopy.

3.1.1. Typical AFM set-up

Most of today's AFM's consist of a flexible probe that is a microfabricated thin cantilever with a sharp tip at its end, a scanner based on piezoelectric elements, a system that measure the deflection of the cantilever due to the interaction between the tip and the surface, and control electronics. The deflection of the cantilever is usually measured by reflecting a focused laser beam off the extremity of the cantilever. The bending of the cantilever will change the direction of the reflected beam, which can be measured using a four-quadrant photodetector (see Figure 3–1). The four-quadrant photodetector allows the simultaneous detection of the vertical cantilever deflection by measuring the signal between upper and lower quadrants (signal $(a+b)-(c+d)$) as well as the detection of the cantilever torsion by measuring the signal between left and right quadrants (signal $(a+c)-(b+d)$).

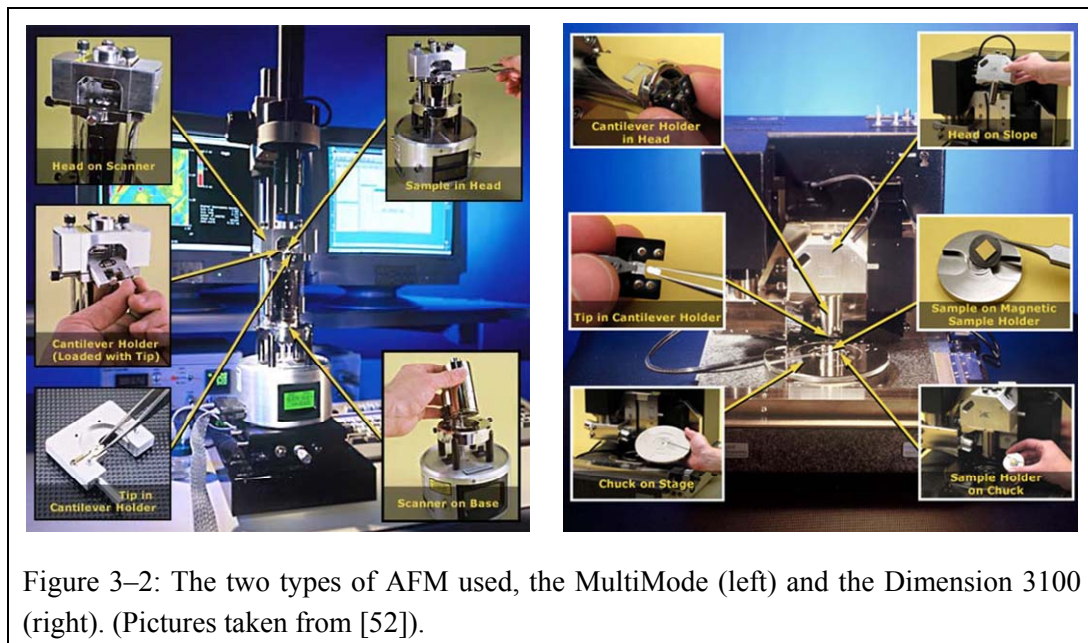


Two commercially available AFM's were used for the experiments, a MultiMode and a Dimension 3100, both manufactured by Digital Instruments - Veeco (Santa Barbara, USA, [52]). They are shown in Figure 3–2.

The Multimode AFM, equipped with a Nanoscope IV controller and a JV scanner, has an immobile probe whereas the sample is placed on the scanner (Figure 3–1 A).

The Dimension 3100, equipped with a Nanoscope III-A controller, has the probe mounted on the piezoelectric scanner and the sample remains immobile during the scanning (Figure 3–1 B). This allows the investigation of large samples. The samples can furthermore be mounted on a plate driven by electrical stepping motors. Since it is the probe that is scanned, the laser beam has to follow the cantilever during the scanning. This is done by placing the focusing lens of the beam at the free end of the xy-scanner.

Both AFM's were equipped with a CCD camera permitting the visualization of the probe and of the substrate (top view). Furthermore, on the Dimension 3100 AFM, a frame grabber allows the capture of the optical images.



3.1.1.1. AFM operating modes

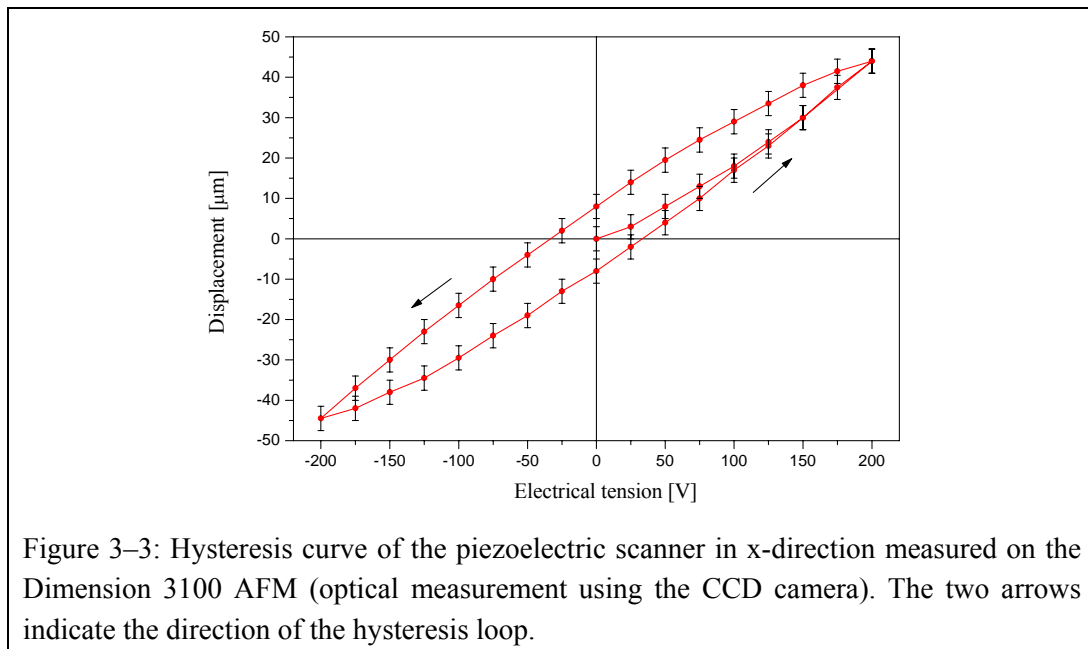
There are two main modes to operate an AFM, the contact and the tapping modes. In the contact mode, the probe is brought in repulsive contact with the sample surface. The flexible cantilever will therefore slightly bend due to the forces acting between the tip and the sample surface. While the tip scans over the surface, the deflection of the cantilever is continuously measured. A feedback loop controls via the z-scanner the vertical position of the probe relative to the sample in order to keep a constant cantilever deflection. The value of the vertical position versus the x-y position provides topographic information of the sample surface (height micrograph). Simultaneously, the cantilever deflection versus the x-y position can be acquired. The deflection micrograph corresponds to the vertical error of the height micrograph. By choosing the fast scanning axis to be perpendicular to the cantilever axis, additional information on the friction between tip and sample can be gained by monitoring the torsion of the cantilever (friction micrograph).

In the tapping mode, the cantilever is mechanically excited by a piezoelectric actuator in order to vibrate it vertically, close to its resonance frequency. The amplitude of the vibration is measured by

the photodetector. As the oscillating probe is brought into vicinity of the sample surface, the surface will exert a force on the tip, changing the amplitude of the cantilever oscillation. Similarly to the contact mode, a feedback loop controls the vertical position of the scanner in order to keep a constant amplitude of the cantilever oscillation during scanning. Generated are the height and amplitude micrographs. Furthermore, the tapping mode allows one to measure the phase shift between the oscillation of the actuator and the oscillation of the cantilever (phase micrograph). Such phase signal provides additional information on the sample surface, such as the surface elasticity.

3.1.1.2. Hysteresis of the piezoelectric scanner

The software that is used to operate the AFM allows the possibility to freely program the scanner movement, using the in-built NanoScript™ language. The program controls the electrical voltages applied on the electrodes of the piezoelectric ceramics, and thus controls the tip displacement relative to the sample surface. However, the effective displacement of the scanner is not linear to the applied electrical tension, and suffers from a strong hysteresis, as shown in Figure 3–3.

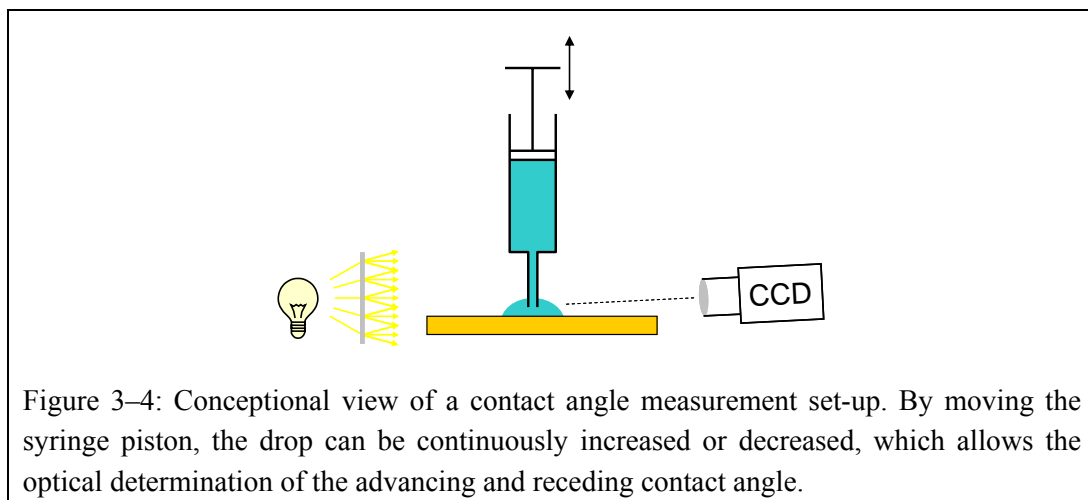


Suppose we start at zero applied voltage, gradually increase the voltage to some finite value, and then decrease the voltage to a negative value, and again increase the voltage to some positive value. If we plot the displacement of the piezoelectric scanner as a function of the applied voltage, the reverse curve does not perfectly retrace the ascending curve, it follows a different path. Such hysteresis will lead to some inaccuracy in the positioning of the probe relative to the applied electrical tensions. The piezoelectric scanner suffers additionally from creep.

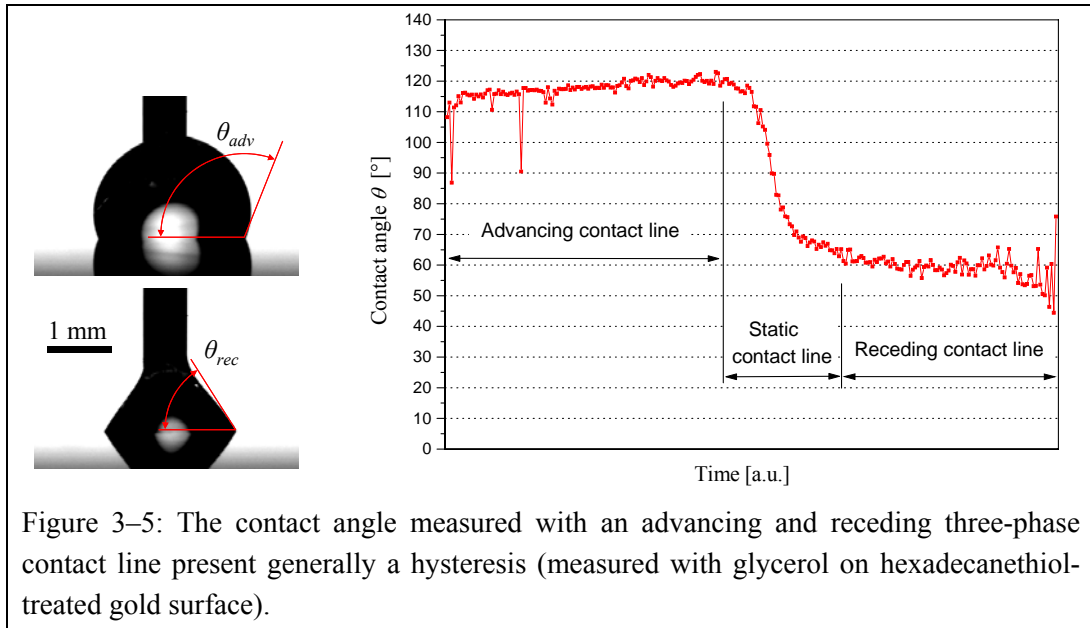
3.2. Contact angle measurement

The contact angle measurements were done on a commercial apparatus, a Drop Shape Analysis System DSA10 provided by Krüss (Hamburg, Germany, [53]). The set-up is shown in Figure 3–4. A syringe filled with the liquid to be measured is kept fixed over the sample surface, with the extremity of the needle close to the sample surface. The piston of the syringe is connected to a small longitudinal motor that will pull or push the piston. A drop of liquid is expelled and contacts the sample surface. By slowly moving the piston downwards, the expelled drop becomes larger, and the three-phase contact line moves over the sample surface. A CCD camera, connected to a PC, images the drop shape. The orientation of the optical axis of the CCD camera lies almost parallel to the sample surface, thus the shape of the drop as well as the mirror image of the drop is recorded. A software, provided from the manufacturer, allows the online analysis of the shape of the drop via the CCD camera, and the determination of the contact angle formed by the liquid on the sample surface (see section 2.3.2).

The advancing contact angle θ_{adv} is measured while the syringe piston is push downwards and the three-phase contact line is moving towards the solid-gas interface. By inverting the displacement direction of the piston, the drop volume will now slowly decrease. At first, the three-phase contact line can stay immobile, even if the drop volume decreases, leading to a contact angle hysteresis. The contact angle will therefore continuously diminish, until the three-phase contact line starts again to move, this time towards the drop center. The contact angle measurement performed at that moment will correspond to the receding contact angle θ_{rec} . Inverting again the displacement direction of the piston will once more provoke an immobilization of the three-phase contact line with an increasing contact angle, until the maximum value corresponding to θ_{adv} is again reached. The reasons that lead to a hysteresis were discussed in section 2.3.2.4.



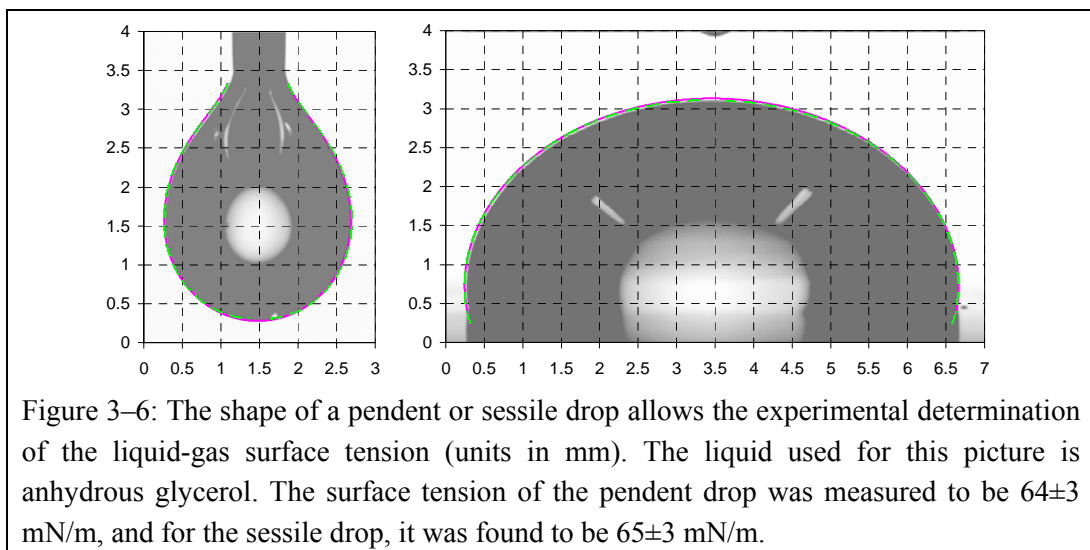
The hysteresis between the advancing and receding contact angle can be quite important. Figure 3–5 gives an example with glycerol on gold surface coated with a self-assembled monolayer of hexadecanethiol.



One might think that the value of the contact angle is also influenced by the global shape of the drop, e.g. by the wettability of the syringe needle. Indeed a static contact angle, i.e. when the three-phase contact line is immobile, is not univocally defined. However, for a moving three-phase contact line, the displacing of the line is only provoked by a non-equilibrated forces situation between the three surface tensions (see also Figure 2-12), which is independent of the curvature of the liquid-gas interface, i.e. on the global drop shape. Thus, both θ_{adv} and θ_{rec} are well defined as long as they are measured while the three-phase contact line is moving.

3.2.1. Surface tension measurement of liquids

The apparatus presented above allows also the imaging of a pendent drop or of a sessile drop. Using the numerical construction of axisymmetric liquid shape, one can fit a theoretical shape to a true shape, and thus determine the strength of the liquid-gas surface tension (see section 2.3.4). In such applications, it is not the contact angle that is of interest, but the influence of the gravity on the drop shape. An example is given in Figure 3-6.



The violet curve is the trace going from the summit of the drop to the base, and the green curve corresponds to the retrace. See Annex 2 (section 8.2) for more details. In contrast to the contact angle measurement, a picture used for the determination of the surface tension has to be well calibrated in size.

3.3. Miscellaneous

In addition to atomic forces microscopes, various other microscopes were used. The most important instruments were:

- Scanning electron microscope (SEM): Philips, model XL 30 ESEM-FEG.
- Optical microscope: Reicher Jung, model Polyvar MET, mounted with a Nikon color CCD camera, model Coolpix 995.
- Optical microscope: Zeiss, model Axiovert S 100, mounted with a Kappa B&W CCD camera (Gleichen, Germany, [54]), model CF 8/4 DXC.
- Optical microscope: Nikon, mounted with a JAI color CCD camera, model 2040.
- Stereomicroscope: Olympus, models SZX7 and SZ-11, and Wild, model M5-40430.

The equipment used for surface cleaning included:

- Reactive ion etching: Oxford Instruments (Bristol, UK, [55]), model Plasmalab 80Plus.
- Ultra-sound bath: Bandelin Electronic (Berlin, Germany, [56]), model Sonorex Digital 10 P, DK 102 P.
- Ultra pure water preparation: Millipore (Billerica, USA, [57]), model Milli-Q Plus 185.

The metal evaporation was made with:

- Thermal evaporator: Edwards (Crawley, UK, [58]), model AUTO 306.

The fine manipulation such as probe loading was done using:

- Micromanipulator: Research Instruments (Falmouth, UK, [59]), model D25P.

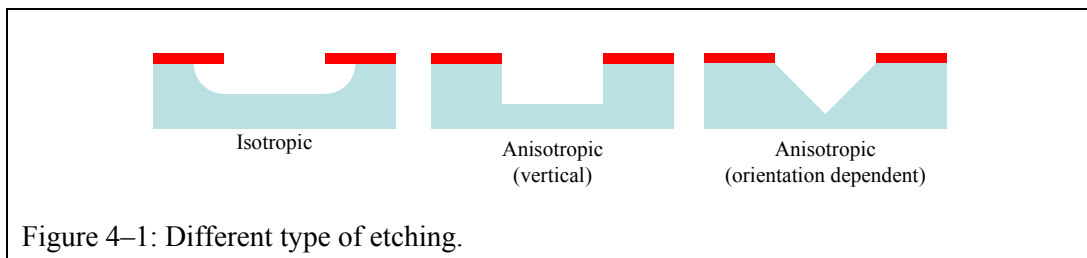
4. Probes realization

The emergence and continuous improvement of atomic force microscopy is also due to the progress made in the field of the microfabrication, which allowed the production of probes with sharp tips in a reproducible way. The realization of the AFM probes used today is based on processes identical to those used in the production of microelectromechanical systems (MEMS). Some aspects of microfabrication will be shortly given in the first section.

One of the key points that permit nanoscale dispensing, is to have a probe that allows a liquid transfer from the upper cantilever side to the sample surface. For that purpose, an aperture at the tip is primordial. Two different approaches to produce such probes were investigated. The first is to include the creation of the aperture amidst the different steps needed for fabricating the probe. The second approach consists of modifying commercially available AFM probes. A focused ion beam (FIB) was used to mill the tip aperture. Both methods will be described in the following sections.

4.1. Microfabrication

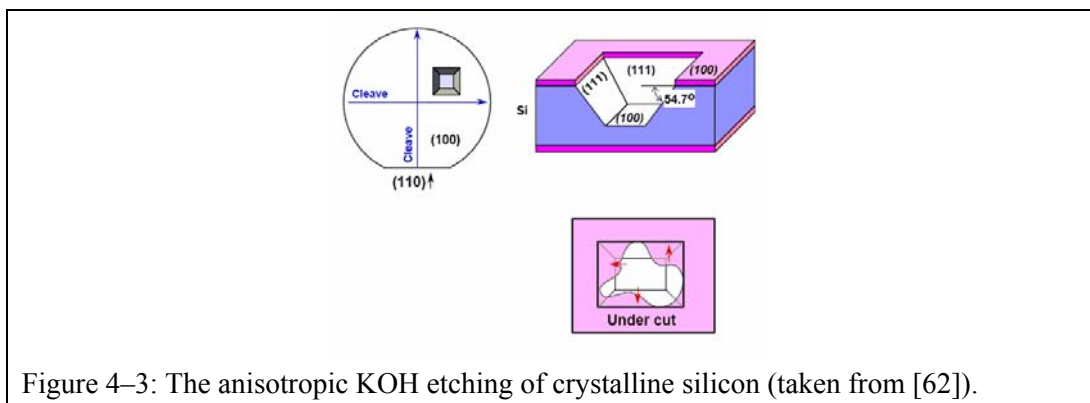
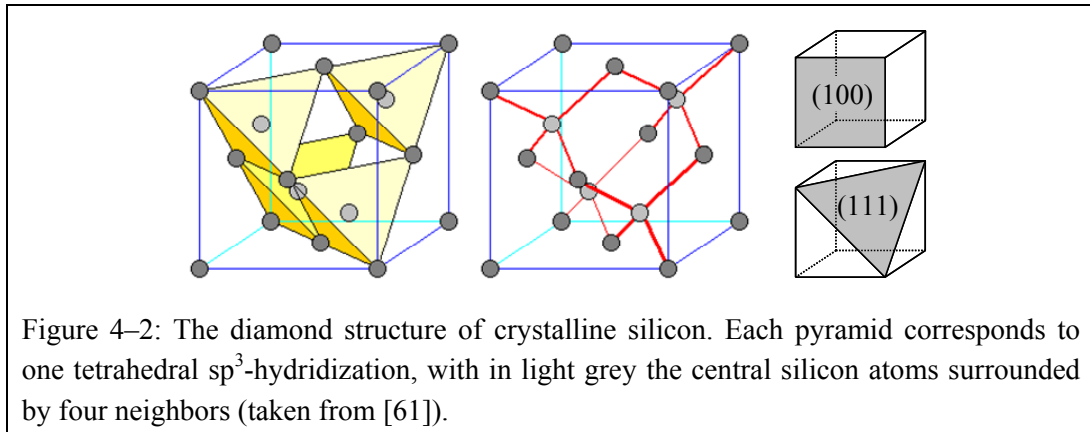
Microfabrication has been developed to advance the semiconductor and IC industry [60]. Because it is not possible to machine a wafer made of silicon with conventional milling machine, one instead uses etch processes that involve exposing the wafer surface to a reactive environment. A film of photoresist, deposited by spin-coating, is patterned using photolithography or e-beam lithography. After development, the photoresist shields the zones that have to be protected against the etching. Thus, the pattern that is formed by the photoresist can be transferred into silicon. The characteristics of the etch process will result in different shapes of etch pits (see Figure 4–1).



Different kinds of etching exist, such as wet (chemical) or dry etching. In wet etching, the photoresist structure is transferred into the substrate by exposing the surface of the wafer to a reactive base such as potassium hydroxide (KOH) or buffered hydrofluoric acid (BHF). Whereas many wet chemical etching procedures are isotropic in nature, the KOH etching of crystalline silicon is of special interest. Remember that the Si atoms are covalently bound via sp^3 hybridization (see section 2.1.2.1), and such hybridization exhibits a tetrahedral structure with one atom in the centre of the tetrahedron bonded to the four neighboring atoms at the corner. The crystalline structure of silicon is therefore like diamond, which is represented in Figure 4–2. The (111) plane of silicon is much more etch resistant to a KOH exposure than the (100) or (110) planes, and can so be used as an etch stopper. Thus, any silicon surface that is not a (111) face will be attacked by the KOH. Such strong anisotropic etching

allows e.g. the formation of pyramidal shaped structures on a silicon (100) wafer, such as those used as tip in an AFM probe (see Figure 4–3). Besides the (111) crystallographic plane of silicon, a silicon dioxide surface will also be etch-resistant to KOH. In order to take advantage of such orientation-dependent anisotropic etching, monocrystalline silicon wafers with an appropriate crystalline orientation are required.

BHF will mainly attack silicon dioxide isotropically, and is less aggressive against silicon and silicon nitride.



Reactive ion etching (RIE) is a dry etching process, where the wafer is exposed to reactive plasma. Such etching attacks the wafer mainly perpendicular to the surface (vertical anisotropic etching).

An example of a microfabrication process is given in the next section, describing the steps used to create probes with an aperture on the tip.

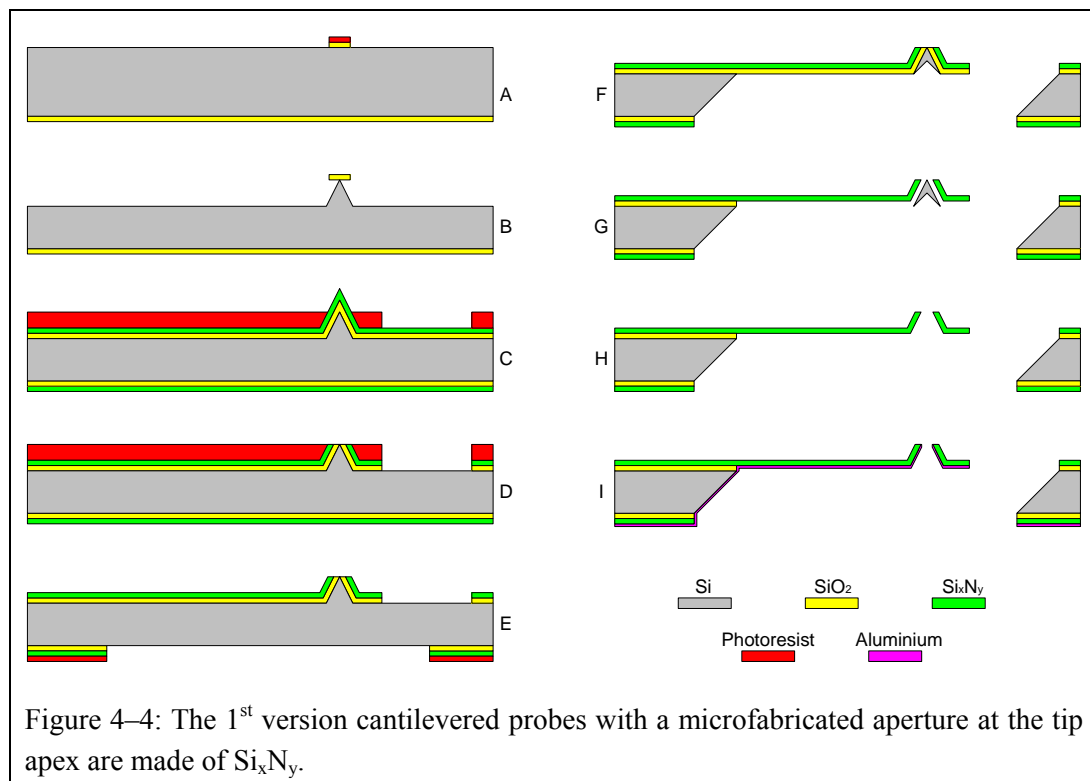
4.2. Probes with microfabricated apertures

The probes with microfabricated apertures at the tip apex were produced at the Institute of Microtechnology (IMT, [63]) from the University of Neuchâtel (Switzerland), in a co-development with the Swiss Center for Electronics and Microtechnology (CSEM S.A., [64]) from Neuchâtel (Switzerland).

The photolithographic masks were designed to have six cantilevers of different lengths on each silicon chip (about 2 mm by 3 mm). At one side there are the 145, 320, and 520 μm long cantilevers, whereas at the opposite side are the cantilevers with a length of 220, 420, and 620 μm . The width of the cantilevers is constant at 110 μm .

4.2.1. 1st version of microfabricated probes

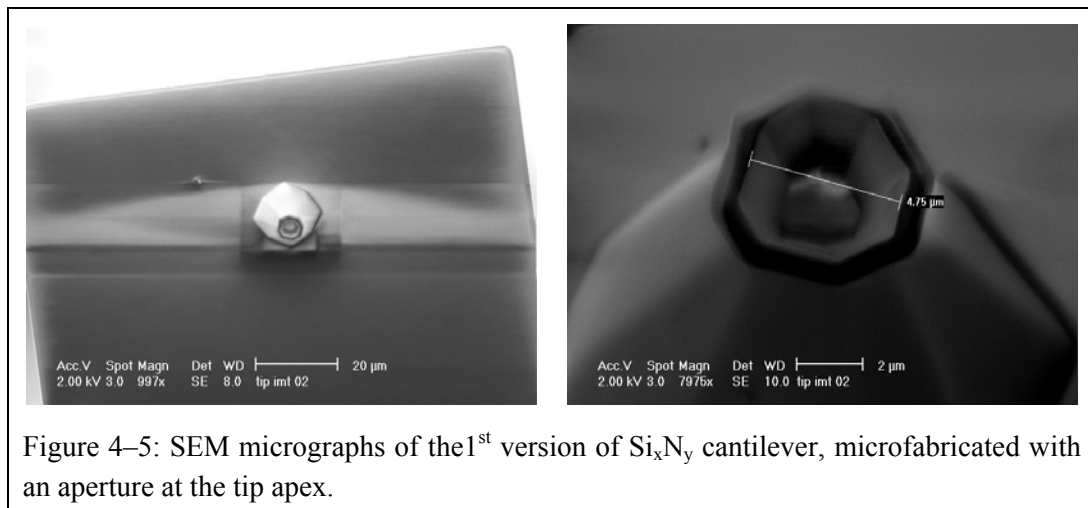
The first version of cantilevers were microfabricated on a (100) silicon wafer. Its microfabrication is based on a molding process, combined with anisotropic KOH silicon etching. The fabrication flow-chart is shown in Figure 4-4.



The different steps are:

- A) First, a photoresist mask for the tip is created by lithography on a silicon wafer previously oxidized. The wafer is etched by RIE to remove the unprotected SiO_2 layer, and the remaining photoresist is eliminated.
- B) The wafer is etched by KOH, and a pyramid is formed below the silicon dioxide (SiO_2). Afterwards the silicon dioxide is removed.

- C) The wafer is then thermally oxidized (oxide thickness 30 nm) and low-stress LPCVD^{a)} silicon nitride (Si_xN_y) of 1 μm thickness is deposited, which forms a mold of the oxidized pyramid. Spin-coating thick resist leaves the apex of the tip uncovered. The photoresist is structured by lithography to define the cantilever shape.
- D) RIE opens the nitride and dioxide layers. The tip apex is etched without any lithography step.
- E) Photolithography on the backside of the wafer is employed to open a window in the Si_xN_y and SiO_2 layers by means of RIE.
- F) KOH etching releases the cantilever.
- G) The silicon dioxide layer on the cantilever and inside the tip is then removed by means of BHF etching.
- H) The remaining silicon in the tip is punctured through by KOH etching.
- I) A thin layer (10 nm) is evaporated on the cantilever backside to enhance the reflectivity.
- Some SEM pictures of the resulting probes are shown in Figure 4–5. The tip apex like a suction cup can also be achieved by partially etching the plain silicon during the first RIE etching.



4.2.1.1. Cantilever stiffness and loading area

Unfortunately, the thin silicon cantilever proved to be too weak when used as nanodispenser. During the withdrawal of the probe from the surface, the repulsive force exerted by the cantilever bending did often not exceed the attractive capillary forces. Often, it was not possible to release the tip from the sample surface, at least not within the range of movement in z-direction of the piezoelectric scanner (about 4 microns on both AFM's). In these cases, the motorized displacement of the optical head of the AFM had to be used to separate tip and sample, with the disadvantage of losing the possibility to directly reengage the tip again on the surface. It was thus decided to produce cantilevers with higher stiffness.

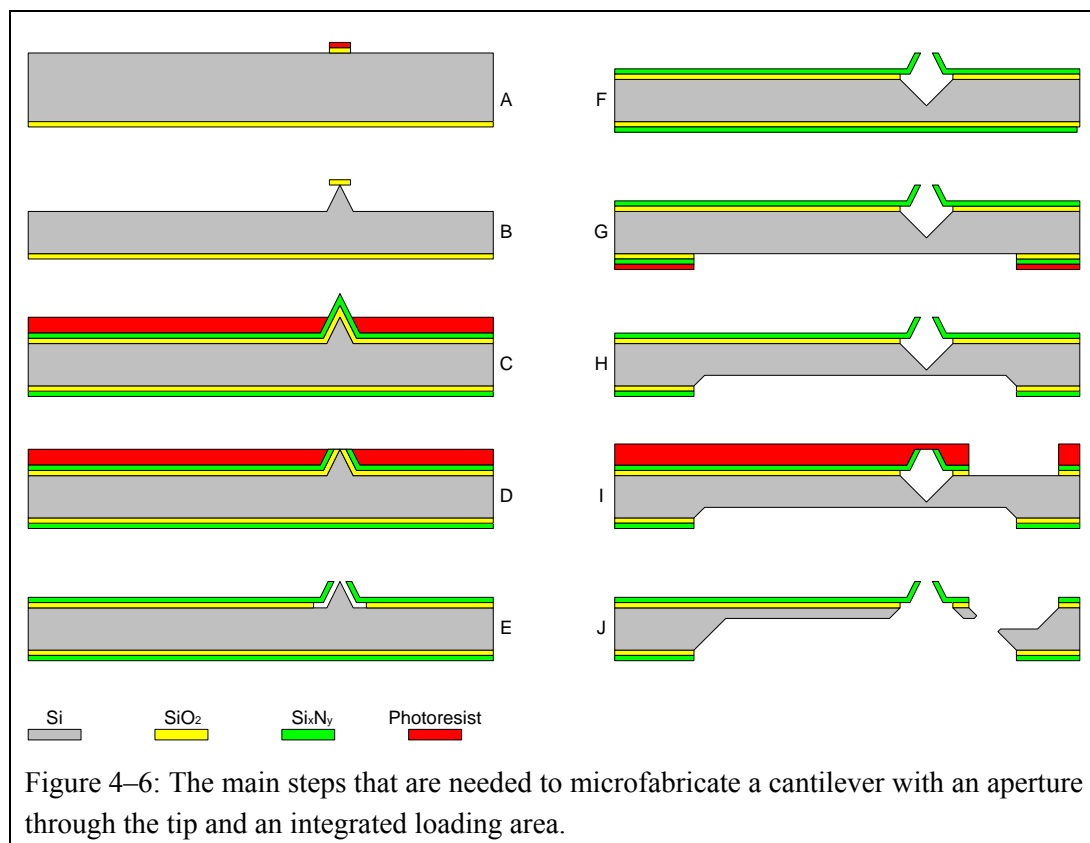
The liquid loaded on the cantilever backside (the side opposite to the tip) showed a tendency to spread over the entire cantilever. To avoid an overflow of the liquid over the cantilever border, and to avoid a wetting of the cantilever area where the laser beam is reflected, it was necessary to confine the loaded liquid laterally. The second series of microfabricated probes thus included a loading area for the liquid, which provides such a confinement.

^{a)} Low pressure chemical vapor deposition.

4.2.2. 2nd version of microfabricated probes

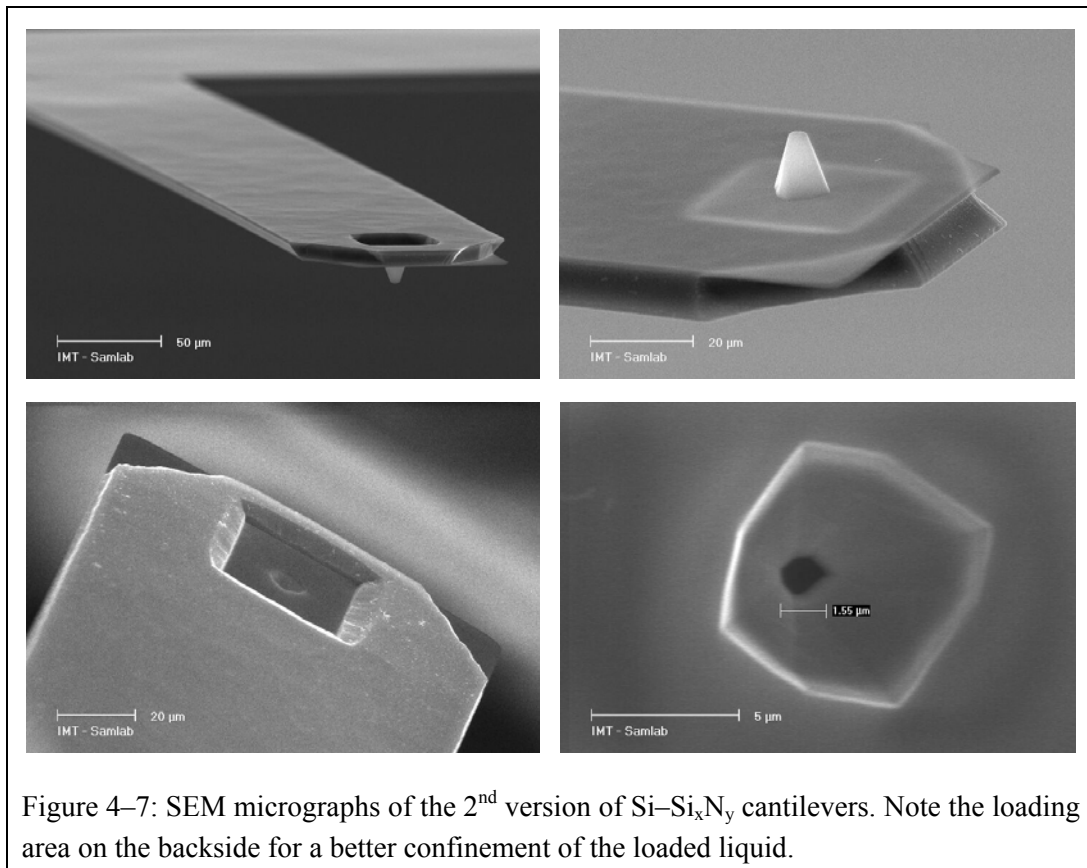
In order to increase the cantilever thickness and to have the possibility to include a loading area for the liquid, the 2nd version of probes comprised a hollow tip on a Si-Si_xN_y compound cantilever. The other dimensions (length and width) remained identical to those of the 1st version of cantilevers. The same lithographic masks could therefore be used. The fabrication flow-chart is shown in Figure 4–6.

- A) to D) Analog to 1st version.
- E) After the stripping of the resist, the opening in the Si_xN_y layer is transferred into the underlying SiO₂ in BHF.
- F) The Si-core of the tip is then etched in KOH
- G) Photolithography on the backside of the wafer is employed to open a window in the Si_xN_y and SiO₂ layer over the future cantilever area by means of RIE.
- H) This allows the creation of a membrane in KOH underneath the cantilever.
- I) In the next step, the frontside Si_xN_y is structured to define the cantilever by means of photolithography and subsequent RIE.
- J) Finally, the cantilever is released and the hole underneath the tip is punctured through by KOH etching. The final cantilever thickness amounts to 7–8 μm.



The loading area is created without specific lithography steps. Its size depends on the SiO₂-free area created in the step E. The square shape is due to the orientation of the (111) crystalline plane of the silicon (see also Figure 4–3).

Figure 4–7 shows some micrographs of the microfabricated cantilevers.



Notice that the difference between the 1st and 2nd version of cantilever resides only in a different sequence of microfabrication steps. The same lithographic masks were used for both cantilever types.

Nevertheless, the control of the numerous parameters involved in the microfabrication to reach reproducible aperture dimensions is really challenging, especially with the aim of producing smaller holes.

4.3. Probes with apertures opened by FIB

Another possibility to create an aperture in an AFM tip is to make use of the extraordinary capabilities offered by focused ion beam (FIB) milling. A FIB is based on a similar principle than an SEM, with the major difference that instead of lightweight electrons, heavy gallium ions are accelerated towards the surface. A FIB can therefore be seen as a scanning ion microscope. The FIB not only allows the generation of high resolution images of a sample, but allows also the machining on a microscopic scale. In the milling mode, one uses the focused gallium beam as a sputtering tool on a sharp localized area. The spatially precise machined areas can be inspected and analyzed in situ.

The imaging using the ion beam can damage the surface because of the heavy mass of the gallium ions. Thus, the last generation of FIB's is equipped, in addition to the ion beam, with a additional electron beam that is less harmful. Such machine is called "dual beam FIB". Long acquisition time with the ion beam could damage the sample, whereas the electron beam is much less aggressive. An image of the used dual beam FIB (FEI Company, Hillsboro, USA, [65]) is shown in Figure 4–8.



Figure 4–8: The FIB used for this study is located at the Swiss Federal Laboratories for Materials Testing and Research (EMPA, [66]) in D dendorf (Switzerland).

Different commercially available probes were used to perform the FIB modification. All probes were made entirely of silicon nitride for both the cantilever and the hollow pyramidal shaped tip. V-shaped as well as rectangular-shaped cantilevers were used. The cantilever backside (opposite to the tip) was covered by a thin gold layer to enhance the reflectivity of the laser beam during AFM operation. Some cantilevers had a double-side gold coating^{a)}. The Table 4–1 resumes the different probes:

^{a)} The gold coating at the front side (where the tip is) allows one to functionalize the tip, e.g. for biophysical experiments.

Model	Provider	Shape	Gold coating
DNP-S	Veeco (Santa Barbara, USA, [67])	V	Single side
Olympus OMCL-RC800PSA	AtomicForce F&E (Mannheim, Germany [68])	Rectangular	Single side
Olympus OMCL-RC800PB	AtomicForce F&E	Rectangular	Double side

Table 4-1: List of the different AFM probes to be modified by FIB.

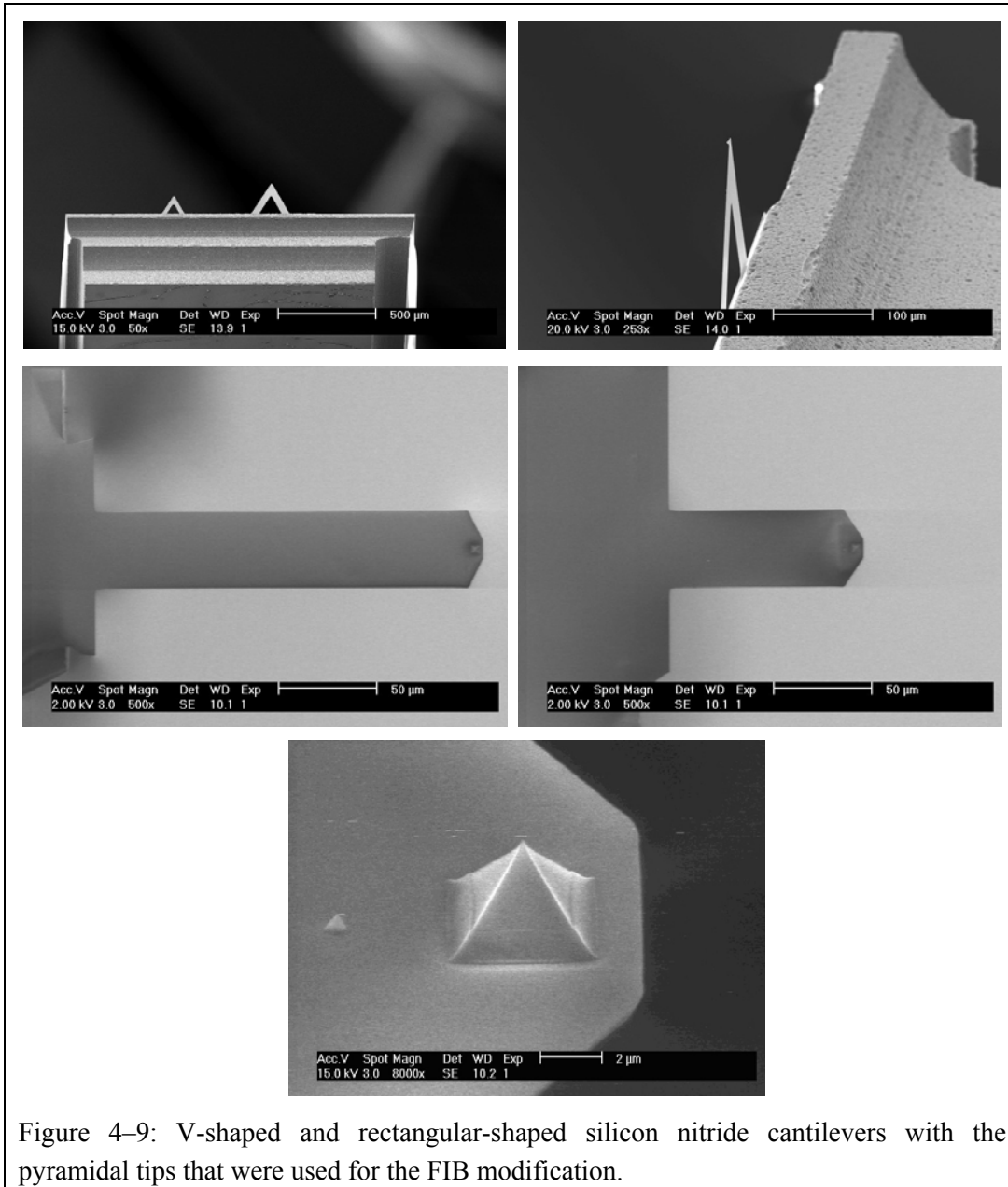


Figure 4-9: V-shaped and rectangular-shaped silicon nitride cantilevers with the pyramidal tips that were used for the FIB modification.

For all three kinds of AFM probes, four different cantilevers were attached to the holding chip with different geometries and stiffness. On one side there are larger cantilevers attached (one long and one short), whereas on the other side there are the two narrower cantilever located.

Besides for creating the aperture to permit the liquid transfer through the tip, the FIB was also used to create a loading area for the liquid. To this purpose, the reflective gold layer covering the backside of the cantilever was removed around and inside the hollow tip, leaving an unexposed silicon nitride surface. While the remaining gold was made hydrophobic by chemical treatment (see section 5.3), the bare silicon nitride remained hydrophilic. The hydrophilic-hydrophobic contrast serves as virtual wall for confinement of the liquid inside the loading area.

The cantilevers with the larger widths were chosen to be FIB modified, because they were stiffer (i.e. easier tip-sample release during probe withdrawal) and they offer a larger surface to integrate the loading area. The cantilevers used for FIB modification are shown in Figure 4–9.

The first FIB milling revealed that it was almost impossible to avoid charging effects on the cantilevers with a single-side gold coating by operating the ion beam alone, even by providing an electrical path from the evaporated gold layer on the chip to the ground. Probably it was due to a shadowing effect during metal evaporation, leaving an area with incomplete metal coverage that broke the electrical path between cantilever and chip. To avoid such charging effects, it is possible to operate the ion beam simultaneously with the electron beam in such a way that the resulting total charging vanishes.

The opening of the tip aperture by FIB can be made at the tip apex, or slightly off-center in order not to destroy the tip apex. The aperture diameter can also be freely chosen. The smallest achieved apertures are around 200 nm. We failed to get smaller apertures, probably due to deposition of the milled material onto the wall of the aperture, provoking a continuous refill of the hole during the FIB milling.

The selective removal of the gold layer to create the loading area was done in different steps. The entire area is made of a superposition of basic geometrical forms allowed by the FIB software (see Figure 4–10). This also permits to mill each respective area with an appropriated ion current. Low current allows a better control of the charging effects, but is more time consuming. One has to take care to leave a gold band remaining at the border of the cantilever around the outer shape of the cantilever in vicinity of the tip.

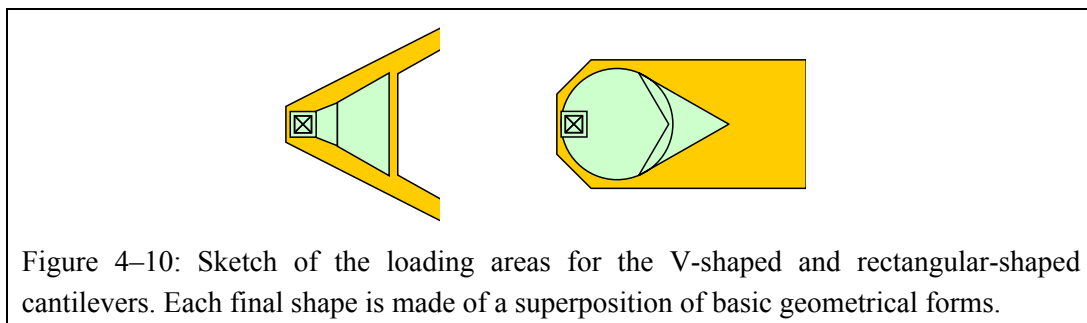


Figure 4–10: Sketch of the loading areas for the V-shaped and rectangular-shaped cantilevers. Each final shape is made of a superposition of basic geometrical forms.

Table 4–2 gives typical value for the FIB operation. For the cantilever with a double side coating, no charging effect was observed, and the milling could be performed without simultaneous electron shower.

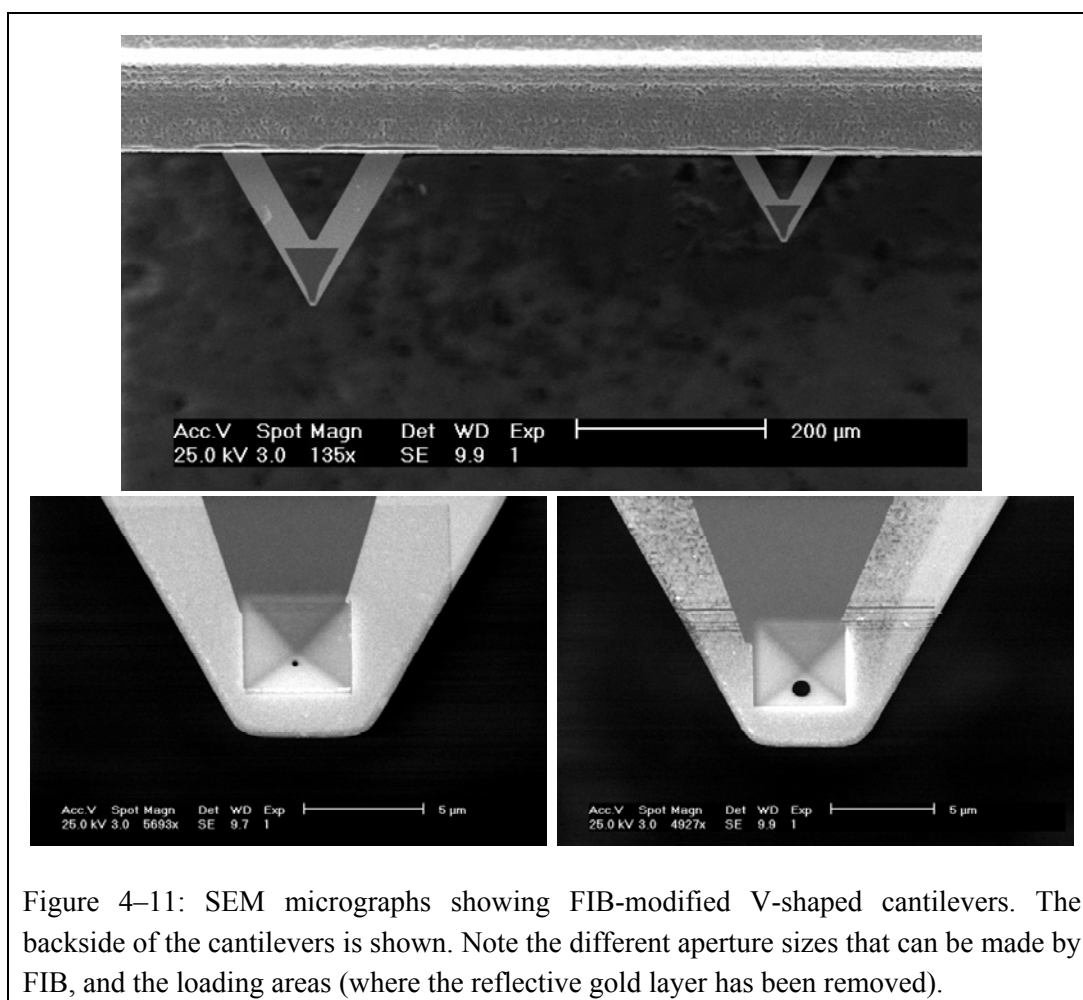
	Tip aperture	Loading area
Single-side coated cantilever	Ga ⁺ beam: 50-100 pA, 30 kV e ⁻ beam: 80 nA, 5kV	Ga ⁺ beam: 50-300 pA, 30 kV e ⁻ beam: 200 nA, 5kV
Double-side coated cantilever	Ga ⁺ beam: 50 pA, 30 kV	Ga ⁺ beam: 500 pA, 30 kV

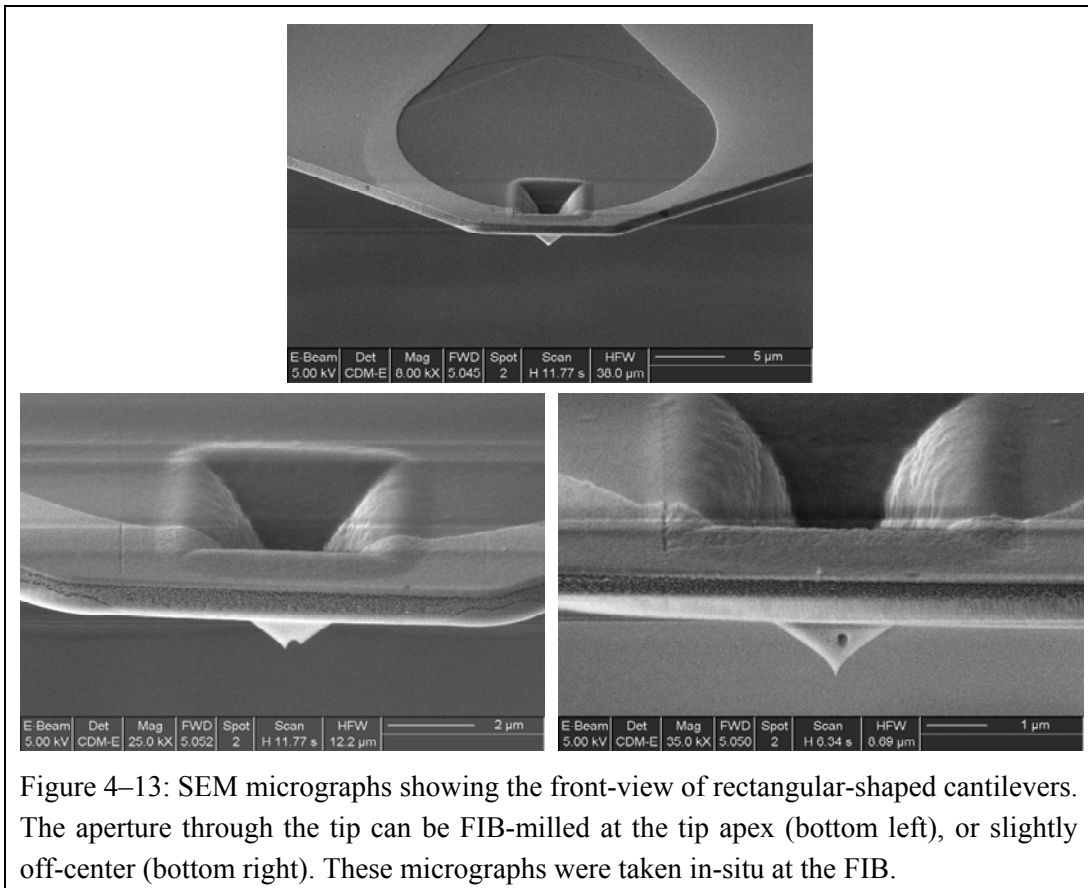
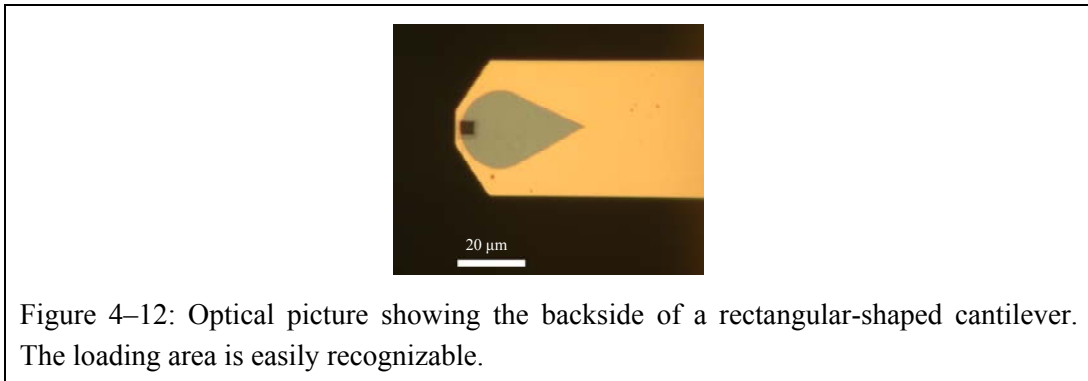
Table 4–2: FIB milling parameters. For the double-side gold-coated cantilevers, no simultaneous electron beam during FIB operation was necessary.

SEM micrographs provide an easy way to control of the features realized by FIB milling. Charging effects occurred also while acquiring a high resolution SEM images on the single-side gold-coated cantilevers, leading to some artifacts in the corresponding micrographs.

Figure 4–11 shows the V-shaped cantilevers after FIB milling. The smaller tip aperture (bottom left image) is about 200 nm wide.

The rectangular-shaped cantilevers are shown in Figure 4–12 to Figure 4–14.





The FIB offers a high flexibility in the design of the milled structures (aperture size, aperture location, shape of loading area). Furthermore, since such technique does not involve any lithographic steps (and thus any masks that are usually time consuming to be created), FIB milling is especially appropriate if several modifications are necessary during the development, since they can be rapidly implemented.

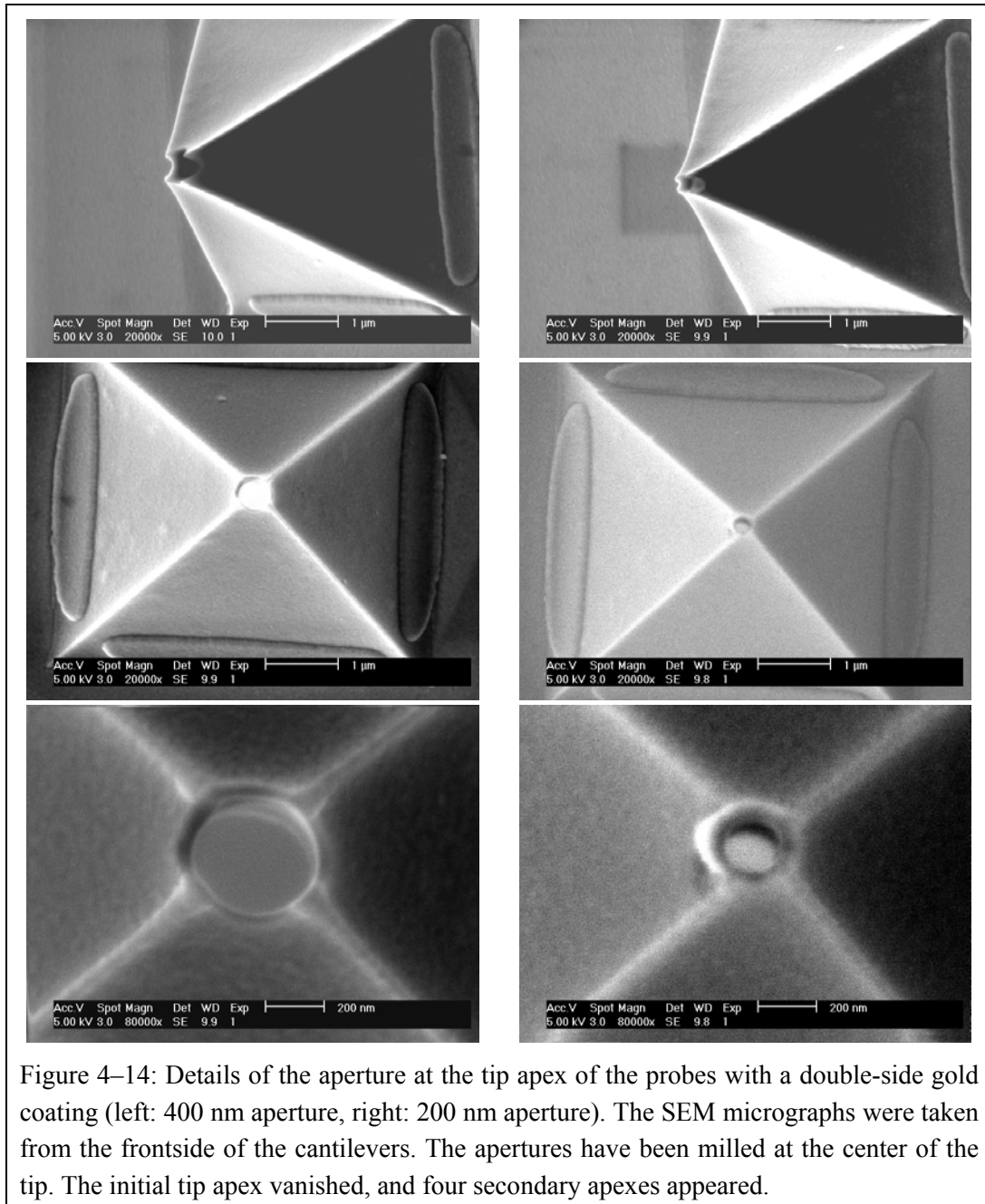


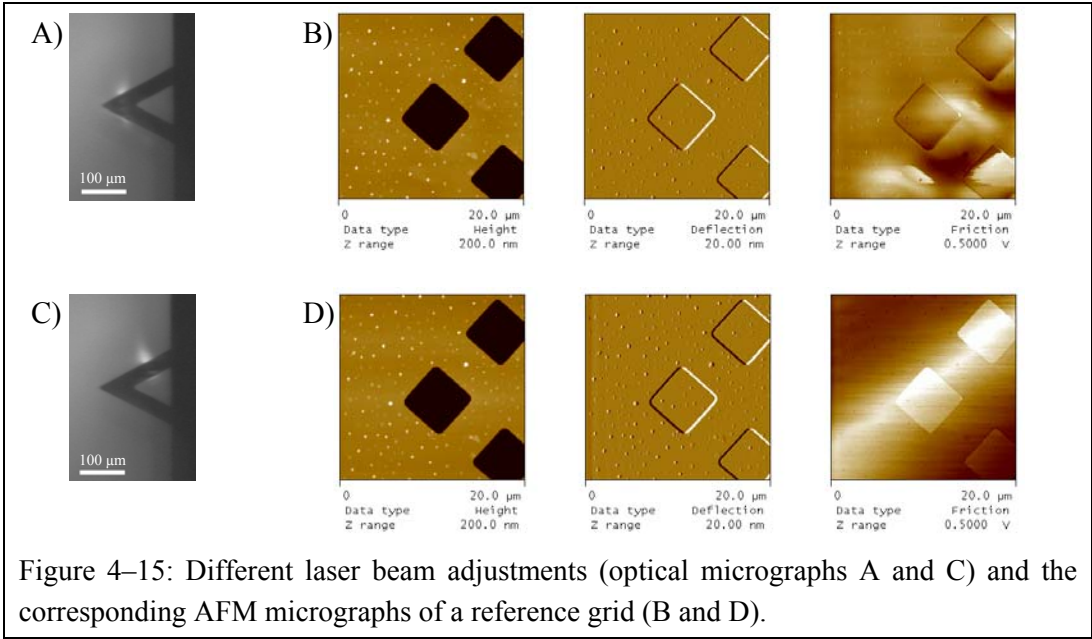
Figure 4–14: Details of the aperture at the tip apex of the probes with a double-side gold coating (left: 400 nm aperture, right: 200 nm aperture). The SEM micrographs were taken from the frontside of the cantilevers. The apertures have been milled at the center of the tip. The initial tip apex vanished, and four secondary apices appeared.

4.3.1. Reflection of the laser beam for V-shaped cantilever with loading area

In normal AFM operation, the laser beam used for the deflection detection is reflected off the free end of the cantilever. On the FIB-modified cantilever, because of the presence of the loading area at the cantilever end, the laser beam has to be reflected off from another area. On the rectangular shaped cantilever, the laser was focused directly behind the loading area.

On the V-shaped cantilever, the laser spot was reflected off one arm of the cantilever. To ensure that the choice of positioning the laser on one arm does not affect the AFM operation, a reference grid dedicated to piezoelectric scanner calibration was imaged with an unmodified V-shaped cantilever. Firstly, the laser beam was adjusted to be reflected off the extremity of the cantilever (Figure 4–15 A) and an AFM micrograph was acquired (Figure 4–15 B). The laser beam was then set to reflected off

one arm (Figure 4–15 C), the deflection sensitivity^{a)} was again adjusted, and another AFM micrograph was acquired (Figure 4–15 D).



As can be seen, the location of the reflected laser beam did not influence significantly the operation of the AFM. The height and deflection micrographs for both laser adjustments are similar.

Note that in both friction micrographs, artifacts are induced by interference in the optical path of the laser beam. The interference arises, firstly between the beam that is partially reflected off the cantilever towards the photodetector and the beam that is scattered from the sample surface, and secondly between the beam that reaches the cantilever and the beam that is scattered back into the laser cavity.

^{a)} The response of the photodetector respective to the location of the incoming laser beam is measured in Volt. The sensitivity is the ratio of the change of cantilever bending (in nm) to the respective change in the photodetector signal (in Volt).

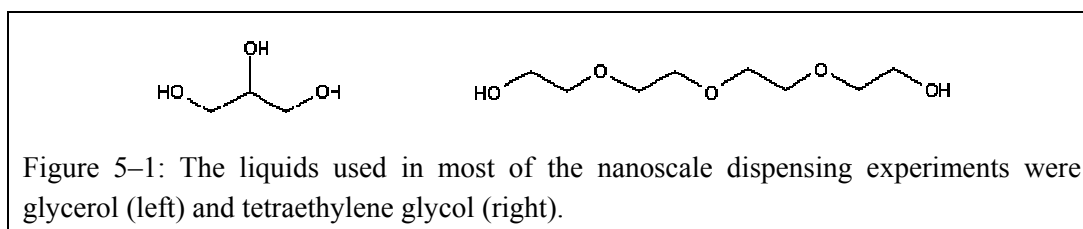
5. Methods

This chapter describes all steps and processes needed for the realization and characterization of nanoscale dispensing. This includes the substrate preparation, the loading of the probe, and the dispensing process itself. The determination of the spring constant of the cantilever will be discussed, as well as a method to determine the amount of loaded liquid.

5.1. List of chemicals

5.1.1. Choice of liquid to be deposited

A point that turned out to be significant was the choice of the liquid to be deposited. The first tests rapidly revealed that nanoscale dispensing using water-based liquids was impossible. Since all experiments were performed in ambient environment, the evaporation of the liquid loaded at the backside of the cantilever is a critical issue, because of the small volume present. In the case where Millipore water was loaded, the liquid evaporated within a few seconds, a lot too fast for a dispensing experiment to be executed. For that reason, the choice of the liquid was restricted to fluids having a small evaporation rate, i.e. having a high boiling point while being still liquid at room temperature. A good candidate for that purpose was glycerol, a non-hazardous liquid that is often used in cosmetics. Pure glycerol is hygroscopic, and is saturated when about 13% water is present in the liquid. Both saturated and anhydrous glycerol were used during the experiments^{a)}. Polyethylene glycol (PEG), a class of polymers that are also water-soluble and non-hazardous, was also considered. Out of these, the polymer with the highest molecular weight that is still liquid at room temperature is tetraethylene glycol (TetraEG), and was therefore chosen. Both molecules are represented in Figure 5–1.



Some dispensing experiments were also realized with heptadecane and hexadecanethiol, whereas hexadecane also evaporated too fast to perform an experiment.

5.1.2. List of solvents and chemicals

The following Table 5–1 resumes the solvents and chemicals mentioned in this thesis, with their respective provider.

^{a)} Saturated glycerol will be called "glycerol" in this thesis.

		Purity	Provider
Acetone		Uvasol	
Ethanol		Uvasol	Merck KGaA
Hexadecane		for synthesis	(Darmstadt, Germany, [69])
n-Hexane		Uvasol	
Anhydrous glycerol	(Fluka)	Puriss. p.a.	
Fluorinert™ Fluid FC-77	(Fluka)	Purum	
Glycerol solution 86-88%	(Fluka)	Puriss. p.a.	
Heptadecane	(Fluka)	Puriss. p.a.	Sigma-Aldrich
Octadecyltrichlorosilane	(Aldrich)	95%	(St. Louis, USA, [70])
Tetraethylene glycol	(Fluka)	Puriss.	
Toluene	(Riedel-de Haën)	Spectranal	
n-Hexadecanethiol		98%	Lancaster Synthesis (Morcambe, UK, [71])
Perfluorodecyltrichlorosilane SIH5841		97%	ABCR (Karlsruhe, Germany, [72])
Ammonium hydroxide 28%		MOS	
Hydrogen peroxide 30%		VLSI	Rockwood Electronic Materials
Sulfuric acid 96%		VLSI	(Riddings, UK, [73])

Table 5–1: List of solvent and chemicals.

5.2. Preparation of the substrate

5.2.1. Substrate materials

Most of the experiments involving the deposition of liquids by nanoscale dispensing were done on a silicon surface with a native layer of silicon dioxide. The samples were taken out of a wafer by cleaving. A typical sample had a shape of a square with 1 cm side length. The wafers (Hyperpur Silicon (100), p-doped (B), resistivity 15-24 Ωcm , diameter 100 mm, thickness 500 μm) were provided by Wacker Siltronic (Munich, Germany, [74]). The side of the wafer used for the dispensing was polished by the provider. The surface roughness was better than 0.2 nm RMS over a 10 by 10 μm^2 area, as measured by topographic tapping mode AFM, on images previously treated with a third-order plane fit followed by a zero-order flattening.

Besides the oxidized silicon surface, mica sheets Grade V-1 provided by Structure Probe – SPI Supplies (West Chester, USA, [75]), and 76 mm by 26 mm microscope glass slides from Menzel-Gläser (Braunschweig, Germany, [76]) were also used.

The samples made of glass and those made of silicon covered with a silicon dioxide layer have about the same chemical composition at their surfaces. Thus, they behave almost identically during cleaning or surface chemical treatments. The most important difference between both samples lies in the fact that the silicon wafer has a lower surface roughness than a glass slide.

The mica sheets used as sample surface needs no cleaning, since they could be easily cleaved directly before their utilization.

5.2.2. Substrate cleaning

Prior to the utilization of a new glass or oxidized silicon sample, it had to be carefully cleaned. The cleaning of a new sample started systematically with:

- Washing in ultrasonic bath during 3 minutes in acetone at room temperature.
- Washing in ultrasonic bath during 3 minutes in ethanol at room temperature.
- Rinse with Millipore water.
- Dry under a filtered nitrogen stream.

Glass or oxidized silicon samples that were stored in ambient environment had a rather low surface energy (i.e. they had a relative hydrophobic character) after the cleaning procedure. This is due to the fact that molecules, mostly organic ones, were adsorbed on the sample surface and were not completely removed during cleaning.

In order to remove all contamination of the sample surface and therefore to increase the surface energy, a cleaning of the sample in piranha solution followed by an SC-1 cleaning was performed. Another possibility of cleaning was to expose the sample surface to oxygen plasma.

5.2.2.1. Piranha

This powerful chemical wet cleaning method removes all organic material from the surface. The employed procedure is as follows:

- Ensure that the Pyrex glass container is dry.

- Pour sulfuric acid H_2SO_4 (concentration $\sim 96\%$) in hydrogen peroxide H_2O_2 (concentration $\sim 30\%$) in the volume ratio 2:1. During the mixing, the temperature of the blend increases to about $70\text{ }^\circ\text{C}$.
- Heat the blend to $120\text{ }^\circ\text{C}$ while stirring.
- Dip the samples to be cleaned during 10 minutes in the hot solution.
- Rinse the samples copiously with Millipore water and dry them.

Special care had to be taken for handling the piranha solution, because of its high reactivity. Furthermore, piranha solution is highly hygroscopic, and storage will increase the amount of liquid in the recipient.

5.2.2.2. SC-1

While the piranha cleaning removes the organic material, the SC-1 chemical wet cleaning removes inorganic particles (such as small fragments that issue from the cleaving). The solution is a blend made of Millipore water H_2O , hydrogen peroxide H_2O_2 (concentration $\sim 30\%$), and ammonium hydroxide NH_4OH (concentration $\sim 28\%$). The blend of $H_2O : H_2O_2 : NH_4OH$ is prepared with a volumetric ratio of 5:1:1. The different steps are:

- Pour the NH_4OH in H_2O .
- Heat the mixture to $70\text{ }^\circ\text{C}$ while stirring.
- Remove the recipient from the hot plat.
- Add H_2O_2 .
- Place the solution on the hot plate and heat to $70\text{ }^\circ\text{C}$ while stirring.
- Dip the samples to be cleaned during 10 minutes in the hot solution.
- Rinse the samples copiously with Millipore water and dry them.

This cleaning method can also slightly attack the silicon dioxide surface itself. The corresponding increase in surface roughness was however not significantly a problem during the experiments.

5.2.2.3. Oxygen plasma

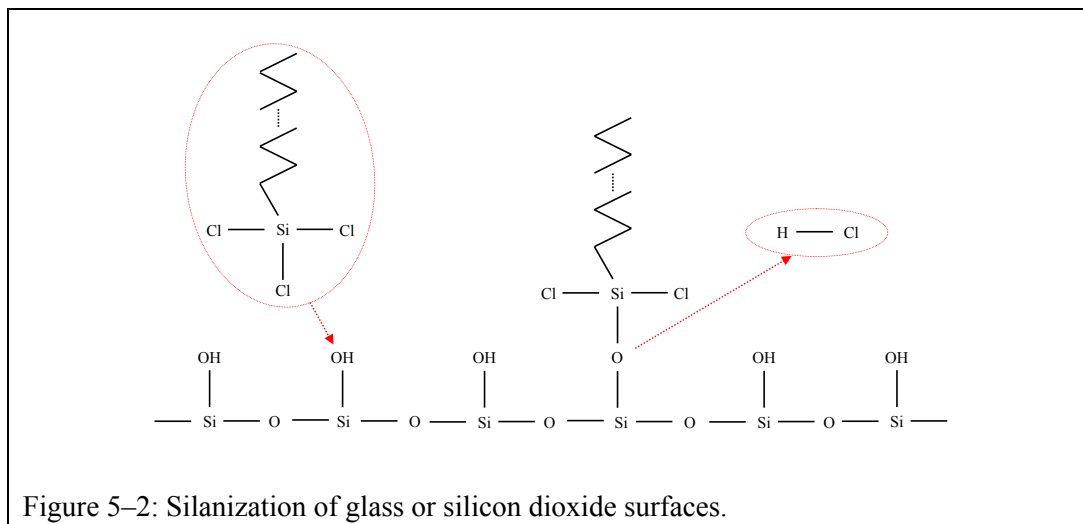
In this cleaning method the substrate was exposed to oxygen plasma. The sample was placed in a vacuum chamber of the Plasmalab 80 Plus, and the chamber was pumped down to $5e-5$ mbar. Oxygen was then let into the chamber (oxygen inlet line open at 100%), and an automatically controlled valve kept the pressure inside the chamber at 200 mTorr. The plasma was generated by radio frequency at a power of 50 W. The sample surface was exposed to the oxygen plasma for 3 minutes. The chamber was then pumped down again, and vented with nitrogen until atmospheric pressure was reached and the chamber could be opened.

The silicon dioxide or glass surfaces cleaned with piranha and SC-1, or by exposure to oxygen plasma were highly hydrophilic. The advancing contact angle measured with glycerol was less than 5° , and the receding one was not measurable since an optically visible film of liquid remains on the wetted surface while the liquid was pulled back into the syringe. Nevertheless, the hydrophilic character continuously degraded during the storage at ambient environment. To keep the hydrophilicity of the surface for a period of a few days, the sample could be stored in Millipore water to avoid exposure to ambient air.

5.2.3. Surface treatment

In order to get a hydrophobic surface with a controlled surface energy, the glass or silicon dioxide surface could be chemically treated with molecules containing a Si-X functional group, such as

octadecyltrichlorosilane. These molecules possess an alkane chain terminated by a silicon atom which is bonded to three chlorine atoms. Such molecules can covalently bind to a silicon oxide or glass surface, and expose their hydrophobic tail to the environment (see Figure 5–2). Prior to the chemical treatment, the surface was cleaned by piranha or by oxygen plasma in order to activate the OH groups at the sample surface.



The silanization was done by dipping the clean sample for 30 minutes in a solution of 10 mM octadecyltrichlorosilane in hexadecane. Afterwards, the sample was rinsed in hexadecane, in hexane, in acetone, in ethanol and finally in Millipore water. The success of the chemical surface treatment was confirmed if the sample was dry when it came out of the water.

A similar treatment but with perfluorodecyltrichlorosilane could also be performed. These molecules are composed of a perfluoroalkane chain (...-CF₂-CF₂-CF₃) instead of the alkane chain, i.e. the hydrogen atoms are replaced by fluorine atoms. The sample is dipped in a 50 mM solution of perfluorodecyltrichlorosilane in Fluorinert for 10 minutes, rinsed in Fluorinert and dried. The treated substrate has surface properties similar to Teflon.

5.2.4. Behavior of the deposited liquids on the substrates

One possibility to characterize the behavior of a liquid on a substrate is to perform contact angle measurements (see section 3.2). One has to note that the measurement of the contact angles gave no clearly reproducible values. The reason is that the contact angle is highly sensitive to surface contamination, especially on substrates with high surface energies. Furthermore, most measurements showed a significant hysteresis in the contact angle values. Nevertheless, a rough classification of the different substrates can be given (Table 5–2).

Glass, silicon dioxide	Oxygen plasma, or SC-1, or piranha	Hydrophilic
Glass, silicon dioxide	Washed in ultrasonic bath (acetone, ethanol, H ₂ O)	Hydrophobic
Gold	Covered by hexadecanethiol	Highly hydrophobic
Glass, silicon dioxide	Covered by octadecyltrichlorosilane	
Glass, silicon dioxide	Covered by perfluorodecyltrichlorosilane	

Table 5–2: Wettability character of the substrates after different cleaning or treatment.

The three liquids used (glycerol, anhydrous glycerol and TetraEG) did show a similar behavior on hydrophilic substrates. The advancing contact angle was smaller than 20° , and the receding angle was smaller than 10° . Often, a receding contact angle of zero was observed, i.e. a film of liquid remained on the substrate as the drop was pulled back into the syringe (no movement of the three-phase contact line towards the center of the drop).

The surfaces classified as hydrophobic caused advancing angles below 70° , and receding angles higher than 10° .

On highly hydrophobic substrates, the advancing angles could reach between 90° and 130° , and receding angles more than 45° . The surface covered with the perfluoro-chains had the strongest hydrophobic character.

5.3. Probe preparation and characterization

5.3.1. Preparation of the loading area for the FIB-modified probes

For the probes with the microfabricated apertures, no special treatment was performed prior to an experiment

On the probes with a FIB-milled aperture, a loading area was milled by removing locally the reflective gold layer at the backside of the cantilever. The loading area presents therefore a bare silicon nitride surface. In order to have a good confinement of the liquid inside the loading area, the surface that forms the loading area has to be hydrophilic, whereas the area surrounding the loading area should be hydrophobic. A difference in the surface composition between both areas allows a different surface bonding chemistry. It is well established that alkanethiols can form a self-assembled monolayer (SAM) on gold [77]. Such SAM's are furthermore hydrophobic, due to the alkane tail. Therefore the remaining gold surrounding the loading area on the cantilever can so be made hydrophobic, while the bare silicon nitride remains hydrophilic.

In section 5.3.1.1 the values of the contact angles for treated gold surface and for a silicon nitride surface that had undergone the same treatment are given.

For a FIB-modified probe, the following recipe was used to make gold hydrophobic:

- Cleaning in oxygen plasma for 3 minutes (100% O₂, 200 mTorr, 50 W RF).
- Dipping for 30 minutes in a solution of 10 mM hexadecanethiol in ethanol.
- Rinsing in ethanol and in Millipore water.

Toluene or hexadecane could also be used as solvent, with the same concentration of hexadecanethiol. In the first case, the probe was rinsed in toluene, in acetone, in ethanol, and in Millipore water, and in the second, the rinsing was done in hexadecane, hexane, acetone, ethanol, and Millipore water.

5.3.1.1. Hydrophobic-hydrophilic contrast of gold relative to silicon nitride

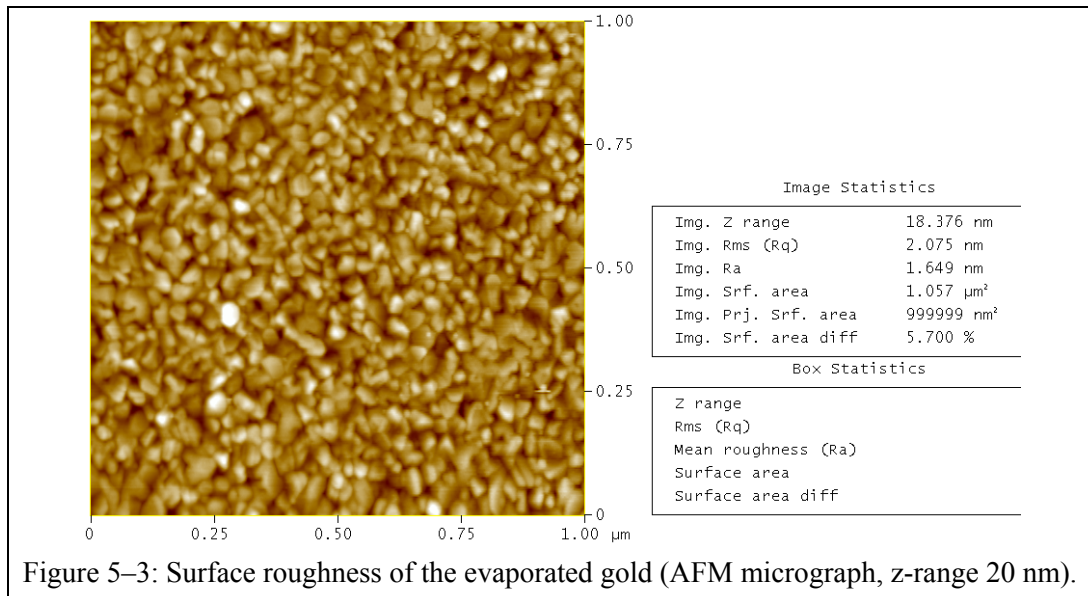
In order to ensure that the hexadecanethiol treatment does not affect the bare silicon nitride inside the loading area, a control experiment was performed. Measuring the advancing and receding contact angles on the cantilever surface was not possible with the available instrumentation. Instead, a 90 nm thick gold metallization (with an underlying 2 nm thick chromium layer to enhance the gold adhesion) was evaporated onto two macroscopic silicon nitride surfaces. An area on the samples was protected with a glass slide against the metallization by a shadowing effect. On the same samples there were therefore two distinct surface areas, one composed of silicon nitride, and the other of gold. Since both kinds of surfaces are present on the same sample, the subsequent chemical treatment will be entirely identical on both. The samples were cleaned by oxygen plasma (3 min., 100% O₂, 200 mTorr, 50 W RF). The samples were then dipped in a solution of 10 mM hexadecanethiol in ethanol. The first sample was dipped for 3 minutes and the second for 90 minutes. They were then rinsed in ethanol and in Millipore water, and dried under a N₂ stream. The contact angles with glycerol were then measured. The results are given in Table 5-3.

	Dipping time	on Au	on SiN
Advancing contact angle θ_{adv}	3 min.	110±5°	12±5°
	90 min.	120±5°	15±5°
Receding contact angle θ_{rec}	3 min.	55±5°	3±3°
	90 min.	57±5°	5±3°

Table 5–3: Contact angles with glycerol on SiN and Au surface after a hexadecanethiol treatment.

The duration of dipping did not influence significantly the contact angle values. This indicates that the hexadecanethiol layer self-assembled almost fully within a few minutes. Since the receding contact angle on the hexadecanethiol-treated gold is higher than the advancing angle on silicon nitride, the liquid should be confined inside the hydrophilic loading area (at least as long as the volume of liquid is not too large).

The surface roughness of the evaporated gold was much larger than the silicon nitride surface. Figure 5–3 shows an AFM micrograph of the gold surface.



The measured contact angle on the rough gold can be corrected to get the value corresponding to a flat gold surface, accordingly to Wenzel’s theory (see section 2.3.2.2a). The ratio of projected surface area to the solid surface area is 1.057. Using equation (2-28), the influence of the surface roughness on both advancing and receding angles is about 2° (120° becomes 118.2°, and 55° becomes 57.1°), less than the accuracy of the contact angle measurements. Despite that the surface roughnesses of the silicon nitride and gold on the cantilever are not known, their influence is small, so it can be assumed that the virtual wall formed by the hydrophobic-hydrophilic contrast is sufficient to confine the liquid on the loading area.

5.3.2. Spring constant determination

The determination of the spring constant of the cantilever is primordial in order to be able to express the cantilever deflection in corresponding force. For small deflections compared to the cantilever length, one can assume that the deformation occurs elastically. Thus, according to the

Hooke's law, the spring constant c of a cantilever is defined as the ratio of the force F (applied perpendicularly to the cantilever axis) to the corresponding deflection d , both measured at the free end of the cantilever (see Figure 5-4).

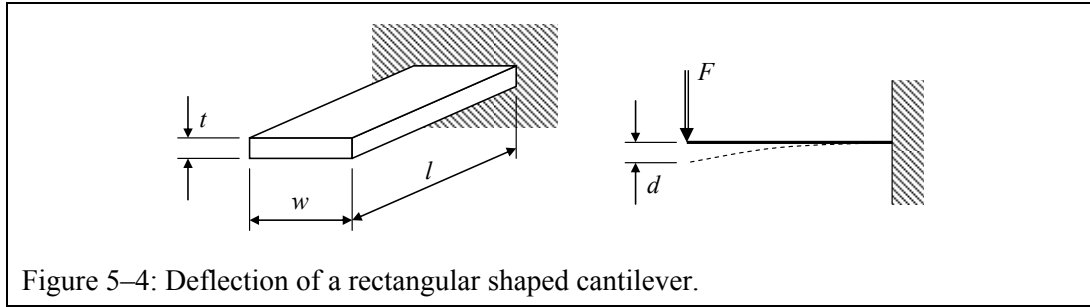


Figure 5-4: Deflection of a rectangular shaped cantilever.

For a cantilever with a constant rectangular cross section, c is:

$$c = \frac{F}{d} = \frac{Ewt^3}{4l^3} \quad (5-1)$$

where E is the Young's modulus, l , w and t , the length, the width and the thickness, respectively. For the cantilever of an AFM probe, it is nevertheless quite difficult to measure the thickness because of its small size. Moreover, the thickness has to be determined with a good accuracy, since the force constant depends on the third power of the thickness.

To circumvent the uncertainties in estimating c , researchers have developed different strategies.

5.3.2.1. Resonance frequency

One method to determine the spring constant is to measure the resonance frequency ν_1 , which is the first eigenfrequency when solving the equation of motion of a rectangular-shaped cantilever. The eigenfrequencies are given by [78]:

$$\nu_n = \frac{\alpha_n^2}{4\pi\sqrt{3}} \frac{t}{l^2} \sqrt{\frac{E}{\rho}}, \quad n = 1, 2, \dots \quad (5-2)$$

where ρ is the density of the cantilever material. The α_n are numerically calculated:

$$\alpha_1 = 1.8751, \quad \alpha_2 = 4.6941, \quad \alpha_3 = 7.8548, \quad \lim_{n \rightarrow \infty} \alpha_n = \pi \left(n - \frac{1}{2} \right) \quad (5-3)$$

The different frequencies ν_n correspond to different vibrating states of the cantilever. The frequency ν_1 corresponds to the fundamental oscillation, ν_2 to the oscillation with one knot in the $z(x, t)$ function describing the motion of the cantilever, ν_3 to the oscillation with two knots, and so forth. It should be mentioned that the eigenfrequencies determined by equation (5-2) are valid for a cantilever in vacuum. In ambient environment, the damping due to the presence of air surrounding the cantilever will shift the resonance frequency to a lower value. Typical shifts are 4% for V-shaped cantilevers and 2% for rectangular ones [79].

By including equation (5-2) in equation (5-1), the thickness t can be eliminated.

$$c = \underbrace{\frac{48 \cdot \pi^3 \cdot \sqrt{3}}{\alpha_1^6}}_{\approx 59.3} \cdot \nu_1^3 \cdot l^3 \cdot w \cdot \sqrt{\frac{\rho^3}{E}} \quad (5-4)$$

Thus, by measuring the frequency of the ground oscillation, which can be done with high precision, the spring constant of the cantilever can be calculated. Nevertheless, the Young's modulus and the density of the cantilever material have to be estimated.

For the 2nd type of microfabricated cantilevers (see section 4.2.2), the cantilever is mostly made of crystalline silicon. The density for silicon is 2330 kg/m³ [16]. The crystalline plane that is subject to stress due to the bending is the (110) plane, i.e. the one that lays perpendicular to the cantilever length. The Young's modulus for the plane (110) is 169 GPa [80,81]. The calculated cantilever properties for a theoretical cantilever (thickness 8 μm and width 110 μm) are given in Table 5–4. Nevertheless, the tip is not located at the very end of the cantilever, and the force acting on the cantilever is applied where the tip is. Therefore, the theoretical spring constant of the cantilever has to be corrected by a factor $(l/l_{tip})^3$ where l_{tip} is the distance from the origin of the cantilever to the tip. The corrected values are those given in bracket.

Cantilever length [μm]	Spring constant [N/m]	Resonance frequency [kHz]
145	781 (1410)	524
220	223 (326)	227
320	73 (94)	108
420	32 (39)	62
520	17 (20)	41
620	10 (11)	29

Table 5–4: Theoretical spring constants and resonance frequencies for silicon cantilevers with a width of 110 μm and a thickness of 8 μm. These values correspond roughly to the 2nd generation probes with microfabricated apertures. The values given in bracket are the corrected spring constants accordingly to the tip position.

For the commercially available AFM probes, the theoretical spring constants c_{nom} and resonance frequencies ν_{nom} of the different cantilevers corresponding to the nominal thickness are given by the probe provider. It can be assumed that a change in the resonance frequency is mainly due to a difference in the cantilever thickness^{a)}. Thus, the real spring constant c_{real} can be easily estimated by measuring the real resonance frequency ν_{real} :

$$c_{real} = \left(\frac{\nu_{real}}{\nu_{nom}} \right)^3 \cdot c_{nom} \quad (5-5)$$

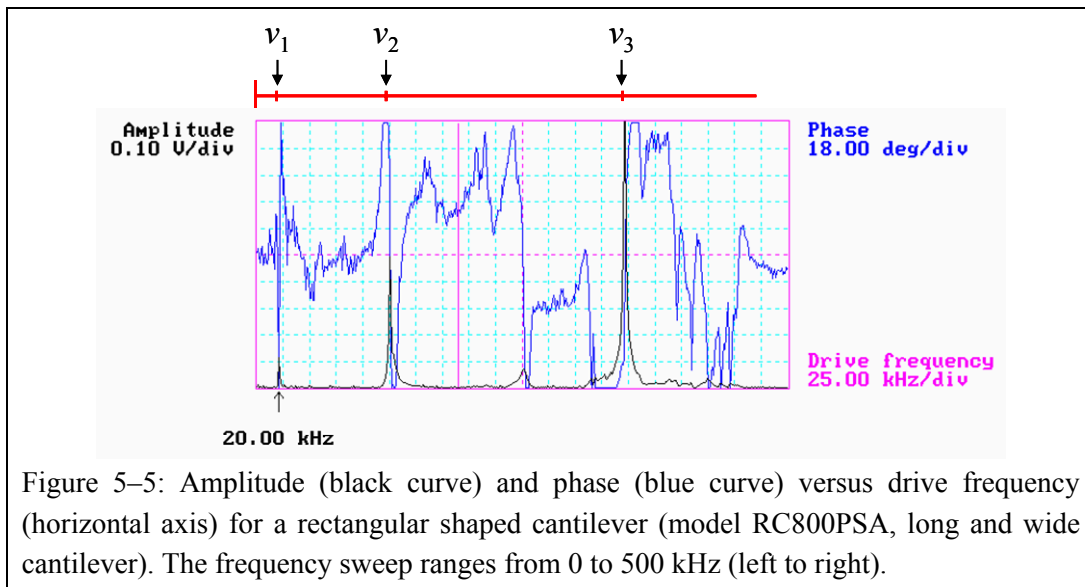
The nominal spring constant and resonance values given by the providers are listed in Table 5–5:

^{a)} The length and width of a microfabricated cantilever, which are mainly defined by the lithographic masks, are more accurate than the thickness, which is defined by parameters of the microfabrication processes itself such as growing rates of layers or etching rates.

AFM probe	Cantilever type	Spring constant [N/m]	Resonance frequency [kHz]
DNP-S	Long and wide	0.12	20
	Short and wide	0.58	57
OMCL-RC800PSA	Long and wide	0.10	19
	Short and wide	0.76	71
OMCL-RC800PB	Long and wide	0.11	17
	Short and wide	0.82	66

Table 5–5: Nominal spring constant and resonance frequency for the different cantilevers used.

The resonance frequency was measured by means of the frequency-sweep mode built-in the AFM. The probe-holder has a small piezoelectric actuator placed under the surface where the chip of the probe is laid down. Driving the actuator with an alternating voltage (the drive amplitude) will induce an oscillation of the same frequency in the cantilever. The frequency-sweep mode measures the amplitude of the cantilever oscillation as a function of the drive frequency of the actuator (while the drive amplitude stays constant). The cantilever amplitude will enter into resonance when the drive frequency is close to one of the resonance frequencies ν_n . The amplitude versus drive frequency curve will therefore present a peak located at the resonance frequencies ν_n . An example of such curve is shown in Figure 5–5 (black curve). The horizontal axis represents the drive frequency of the sweep. The blue curve in the figure describes the shift in the phase between the piezoelectric actuator and the cantilever.

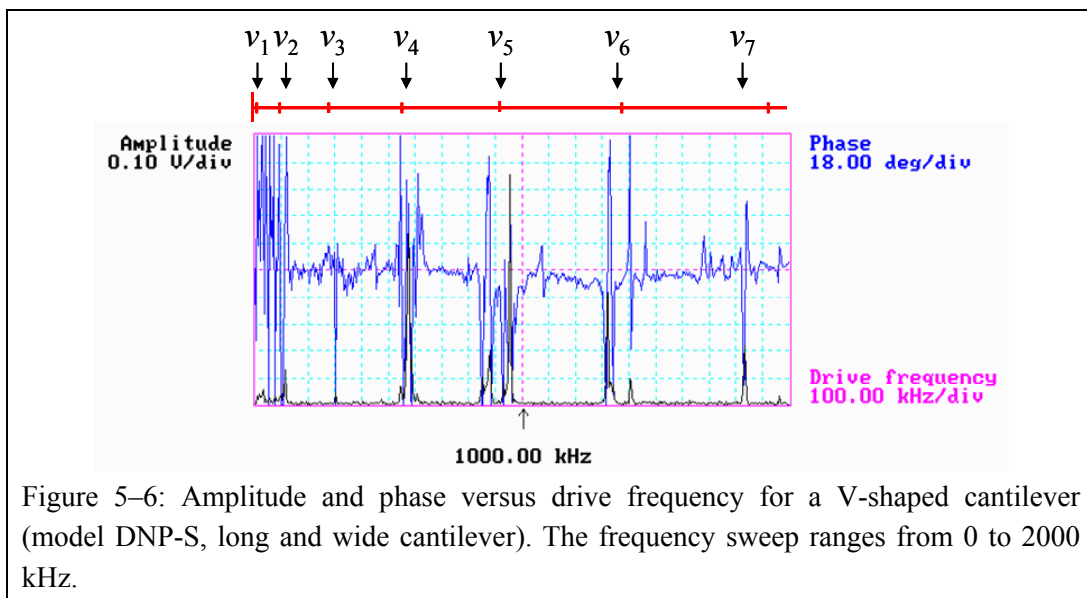


Several amplitude peaks are recognizable in the Figure 5–5. To determine those which belong to the resonance peaks of the cantilever, the theoretical ratio between two resonances frequencies can be used (equations (5-2) and (5-3)):

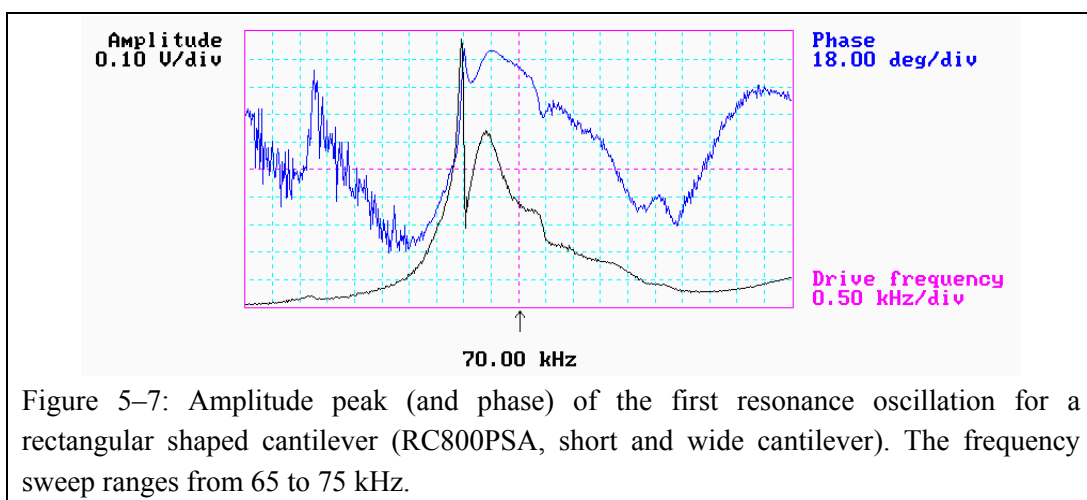
$$v_i = v_j \cdot \left(\frac{\alpha_i}{\alpha_j} \right)^2 \quad (5-6)$$

Equation (5-6) thus defines the relative position of each theoretical resonance peak, which can be fitted to the measured peak by choosing an appropriated value for one of the theoretical resonance frequency. The red axis with the three peaks noticed in the top of the Figure 5-5 corresponds to the theoretical resonance peaks calculated by equation (5-6) fitted to the measured resonance peaks.

The above mentioned derivation is theoretically valid for rectangular shaped cantilever. Since the equation (5-2) is independent of the cantilever width, the two beams of a V-shaped cantilever can be approximated to two beams in parallel. Figure 5-6 represents a frequency sweep for a V-shaped cantilever. The frequencies up to the seventh oscillatory mode are recognizable. The red axis in the top of the figure represents the theoretically calculated resonance frequencies, accordingly to equation (5-6), with an appropriate initial value.



When investigating a cantilever for which no information is available in advance, the ability to recognize several high order peaks in the amplitude versus drive frequency curve can help to choose the one that corresponds to the fundamental resonance frequency.



In particular for those cantilevers having a low resonance frequency (e.g. contact mode probes), the amplitude peak does not always show an ideal shape (square of a Lorentzian's curve), which makes a precise determination of the resonance frequency almost impossible. An example is given in Figure 5-

7. However, the measurement of the thermally induced oscillation of the cantilever allows one to overcome this problem.

5.3.2.2. Thermally induced oscillation

Another method to determine the spring constant is based on the measurement of the thermally induced oscillations of the cantilever. The equipartition theorem applied to a harmonic oscillator that oscillates in response to thermal excitation gives [82]:

$$\left\langle \frac{1}{2} m \omega^2 z^2 \right\rangle = \frac{1}{2} k_B T \quad (5-7)$$

where m is the oscillating mass, ω the resonance angular frequency, z the displacement with respect to the rest position, k_B the Boltzmann's constant, and T the temperature (in Kelvin). Since $\omega^2 = c/m$, the spring constant c can be expressed as:

$$c = \frac{k_B T}{\langle z^2 \rangle} \quad (5-8)$$

To separate the contribution of the thermally induced oscillations from other contributions (e.g. from acoustically induced oscillations), the power spectral density^{a)} (PSD) of the cantilever displacement $z(t)$ can be used. Because the area A under the peak at ω in the power spectral density plot is equal to the mean square of the thermally induced deflection, one obtains:

$$c = \frac{k_B T}{A} \quad (5-9)$$

To get the power spectral density curve of $z(t)$, the PSD facility built-in the AFM was used. The cantilever deflection versus time $z(t)$ was acquired on the AFM, by measuring the deflection at the maximum scan rate while the tip was immobile above the substrate. In such case, the fast scan axis represents the time. In practice, the following method was used.

- Once the AFM probe is mounted in the AFM, the deflection sensitivity is properly determined while the probe is engaged on a hard surface (usually a silicon sample).
- The probe is withdrawn by several millimeters from the surface, the feedback gains (integral and proportional) as well as the scan size are set to zero, and the probe is engaged again, but this time without contacting the sample.
- The deflection limit is reduced to the minimum (maximum sensitivity), and the scan-rate is set to the maximum value (61.035 Hz with the used AFM's).
- An AFM micrograph of the deflection is taken with the maximal number of pixels (512 by 512 pixels with the used AFM's).
- After an image treatment with a third order flatten, the PSD treatment is performed in x direction (the axis representing the time), and the PSD data are exported as an ascii file.
- With the used AFM software, the exported data corresponds to a 256 by 2 matrix. In the first column are the values 512, 512/2, 512/3 and so forth. These values have to be corrected in order to correspond to the respective frequencies (in the i'th line, the correct value is: $2 \cdot i \cdot \text{scan-rate}$)
- A Lorentzian's curve was fitted to the PSD peak by means of appropriate software, and the area of the Lorentzian was determined.

^{a)} The power spectral density corresponds approximately to the square of the Fourier transform times a normalization factor.

The sampling frequency of the acquisition is given by the number of points measured per second, i.e. the number of pixels per line times the scan-rate, multiplied by 2 to take account for trace and retrace. In the present example, this gives: $2 \cdot 512 \cdot 61.035 = 65200$ Hz. The maximum frequency in the PSD curve will be the half of the sampling frequency (Nyquist frequency [83]). The determination of the spring constant with this method was therefore only possible for cantilevers with a resonance frequency smaller than half the sampling frequency.

The equation of the Lorentzian's curve that is fitted to the PSD data is:

$$f(\nu) = H \cdot \frac{W^2}{4 \cdot (\nu - \nu_0)^2 + W^2} \quad (5-10)$$

where H is the height of the peak, W the full width at half maximum (FWHM), and ν_0 the position of the peak. The area A under the peak is:

$$A = \frac{\pi}{2} \cdot H \cdot W \quad (5-11)$$

Because the data obtained in the PSD are discrete (like the input data $z(t)$), one has to take account that the PSD-value for each point corresponds already to the density over to the frequency-interval $\Delta\nu$ between two adjacent points. The frequency-interval $\Delta\nu$ is given by:

$$\Delta\nu = 2 \cdot \frac{\text{sampling frequency}}{\text{number of pixel per line}} = 2 \cdot \text{scan rate} \quad (5-12)$$

In the present case, $\Delta\nu$ is 122.07 Hz.

Despite the advantage that this method needs knowledge about neither geometry nor material properties of the cantilever, the method suffers from other disadvantages. The first is that one has to consider not only the fundamental oscillation of the cantilever, but also the higher order oscillations, as described in equations (5-2) and (5-3). The consideration of the fundamental oscillation alone leads to an error of about 30% [84]. Additionally, the method depends on the ability to properly determine the deflection sensitivity. This is made difficult by the hysteresis of the piezoelectric z -scanner, and because of the dependence on the location where the laser beam is reflected off the cantilever. The directional variation of the reflected laser beam is indeed a function of the slope (dz/dx) of the cantilever area where the beam is reflected, and not a function of the deflection in z -direction. This problem is even more crucial since in our case the laser beam cannot be placed at the extremity of the cantilever because of the presence of the loading area. A test showed that changing the laser spot along the cantilever changed the measured spring constant value by a factor up to 1.6, even after taking into account the change in the deflection sensitivity, which was 95 nm/V (laser spot at the free extremity of the cantilever) and 170 nm/V (spot about in the middle of the cantilever length). The last negative point to mention is a more practical one. The results obtained with this method of thermally induced oscillations were not reproducible enough to be exploited in practice.

Nonetheless, the thermally induced oscillations provided an useful method to precisely determine the resonance frequency, at least as long as the resonance frequency is smaller than half the sampling frequency. In practice, it was useful for the long (and wide) cantilevers of the commercially available probes. An example is given for a RC800PSA cantilever in Figure 5–8, Figure 5–9, and Figure 5–10.

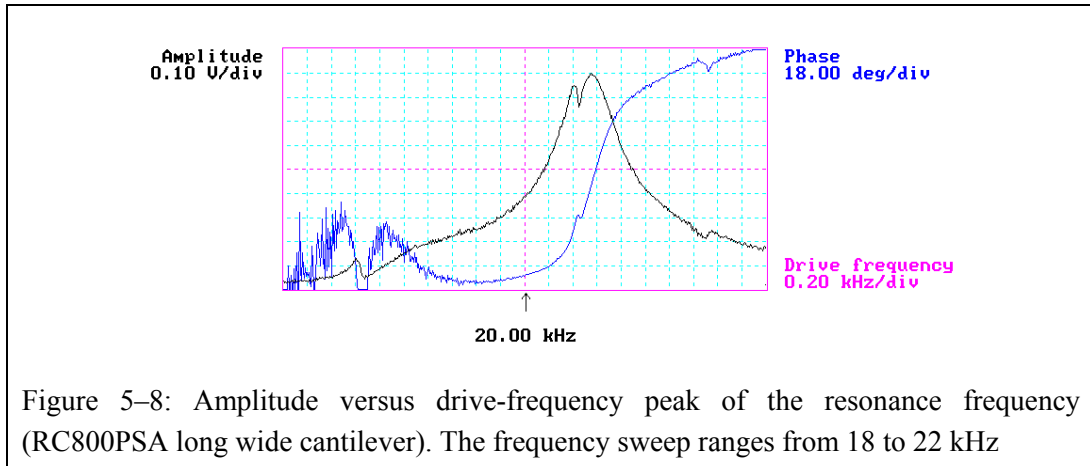


Figure 5–8: Amplitude versus drive-frequency peak of the resonance frequency (RC800PSA long wide cantilever). The frequency sweep ranges from 18 to 22 kHz

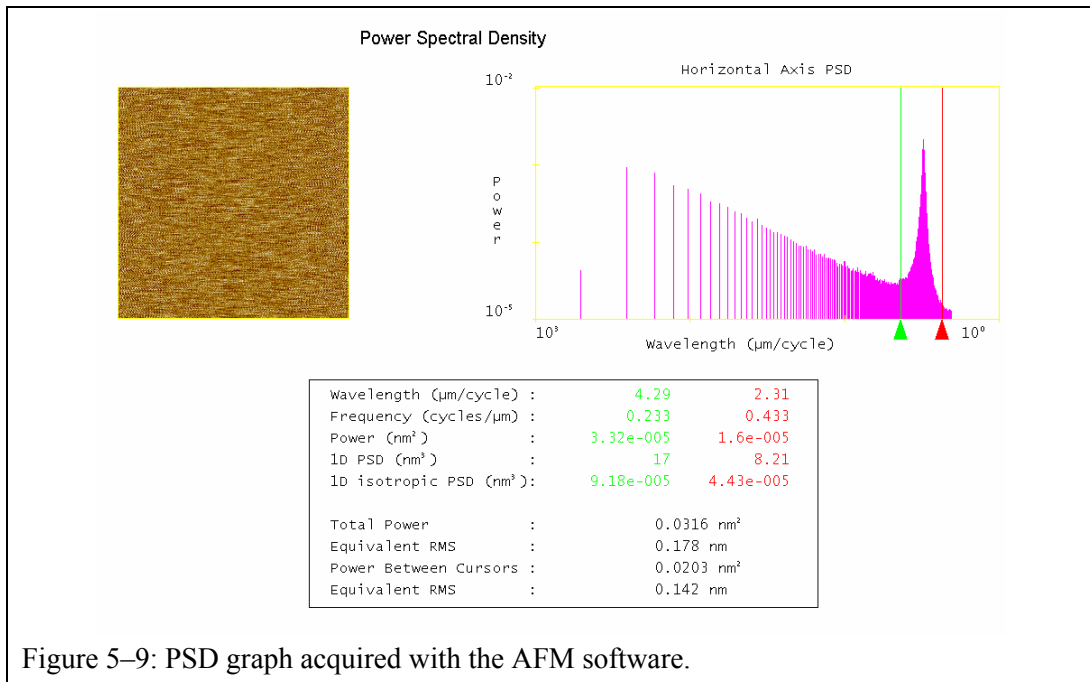


Figure 5–9: PSD graph acquired with the AFM software.

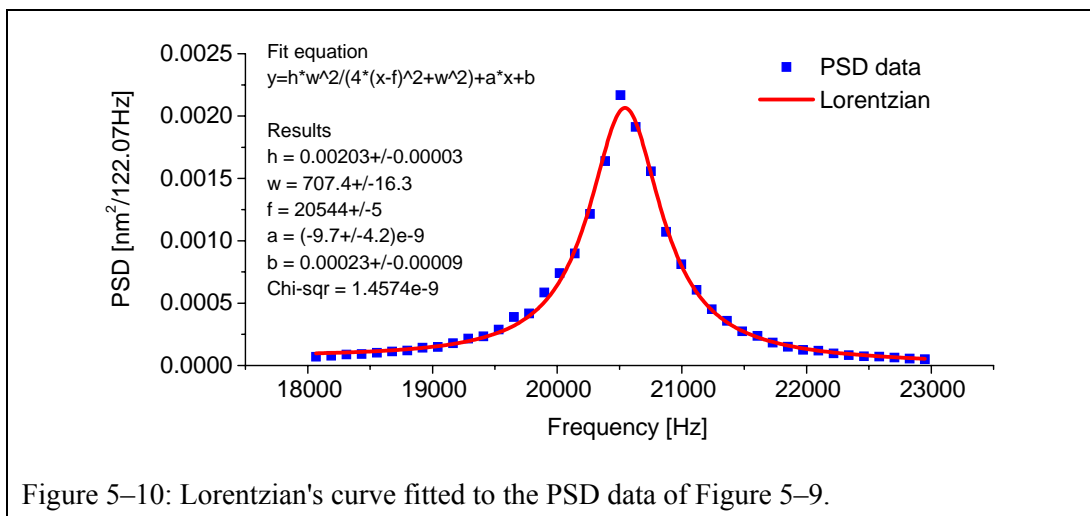


Figure 5–10: Lorentzian's curve fitted to the PSD data of Figure 5–9.

The area under the Lorentzian's curve is $0.0185 \pm 0.0007 \text{ nm}^2$, and using equation (5-9) one obtains $c \approx 0.22 \text{ N/m}$ (at $T = 21 \text{ }^\circ\text{C}$).

The real spring constant can also be estimated by taking into account the ratio of the real resonance frequency to the nominal resonance frequency (value given by the probe provider), accordingly to the equation (5-5), which gives $c_{real} \approx 0.13$ N/m. However, this second value for the spring constant is more reliable, as the used method leads to more reproducible results.

5.4. Dispensing of the droplets

5.4.1. Loading of the probe

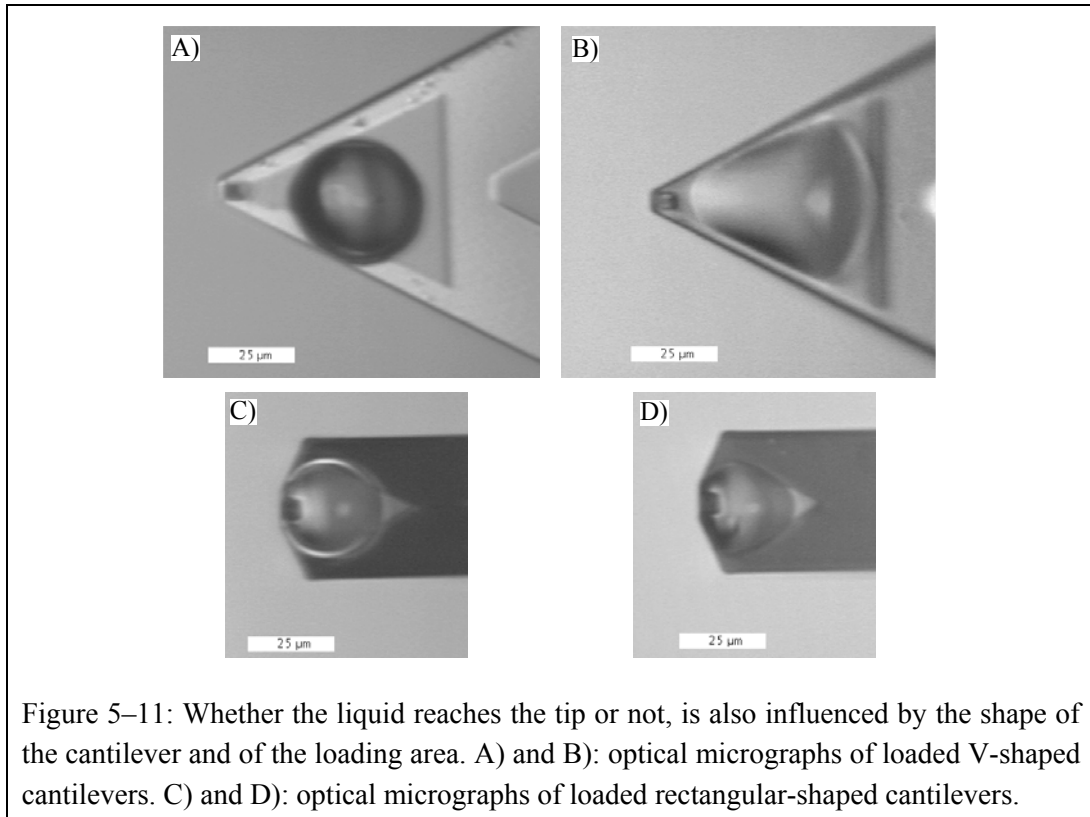
The loading of the liquid to be deposited into the loading area was done by means of a micropipette. The micropipette was produced by heating and pulling a glass pasteur pipette (provider: VWR International, [85]) over a burning gas flame (butane or propane). In a first step, the pulled micropipette had to be closed at the tapered end, which allowed making the outer wall hydrophobic whereas the inner part remained protected. To that purpose, the tapered end was dipped into a solution of 100 mM octadecyltrichlorosilane in toluene during 3 minutes followed by a rinsing in toluene. The micropipette was then opened by breaking the extremity of the tapered end. The outer diameter of the opened micropipette was around 30 to 50 μm . A new micropipette was used for each different liquid to avoid cross-contamination.

Prior to loading the liquid onto the cantilever, the resonance frequency of the empty probe was measured. The probe was then put under a stereomicroscope. The liquid was pulled into the micropipette connected to a syringe by a flexible tube, and transferred onto the loading area. A precise movement of the pipette with respect to the probe was achieved by using micromanipulators.

The hydrophobic outer part of the micropipette prevented the liquid from flowing to the outer surface of the micropipette and ensured the flow to the loading area during the transfer of liquid.

5.4.1.1. Shape of the loading area

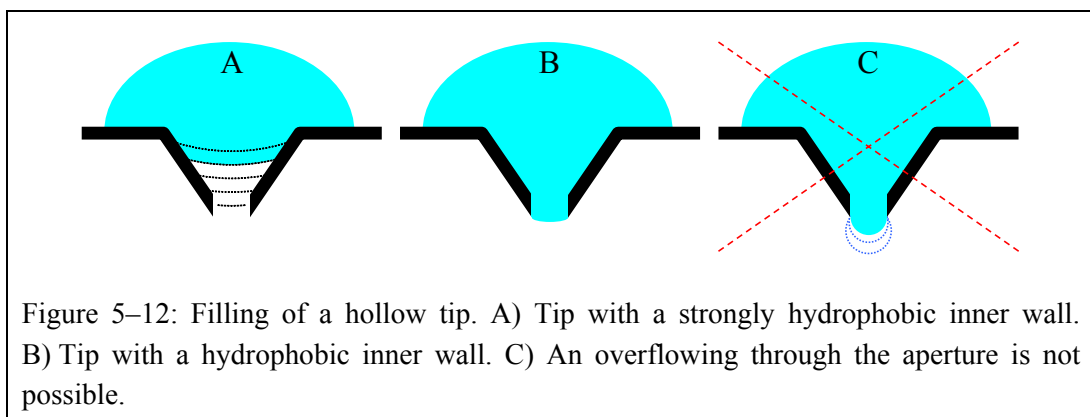
The shape for the loading area on the FIB-modified probes could be freely chosen within the limits defined by the geometry of the cantilever, with the aim of having a larger surface area to facilitate the loading. On the V-shaped cantilevers, the loading area had a triangular shape, mostly due to the cantilever shape. Although the loading area had a comfortable size for loading, the liquid did not always reach the tip, as shown in Figure 5–11 A and B. The explanation can be found in the surface tension of the liquid, which tries to keep the liquid in a circular shape in order to minimize the total surface energy. The micrograph A shows such a circular drop, loaded on a cantilever on which no chemical treatment was done, i.e. without the hydrophilic-hydrophobic virtual wall around the loading area (see section 5.3.1). Because of the geometry of the cantilever, the circular drop could not reach the tip located at the end of the cantilever. The micrograph B show a loaded V-shaped probe with a good confinement of the liquid inside the loading area. Even in that case, despite the confinement, the triangular-shaped loading area compromised the flowing of the liquid to the tip.



To avoid such a limitation, the rectangular-shaped cantilevers were chosen, because they offer more space around the tip and thus allow the creation of a loading area with a smooth contour in the vicinity of the tip (Figure 5-11 C and D).

5.4.1.2. Filling of the hollow tip

The inside of the hollow tip will be fully filled by capillarity if the surface inside is not too hydrophobic. If the surface inside is strongly hydrophobic, the front of liquid flowing towards the aperture will not reach the aperture. This is sketched in Figure 5-12 A.



Let us assume that the tip is axisymmetric. Due to the hydrostatic equilibrium condition, the radius that forms the upper liquid-air interface (over the loading area) has to be identical to the radius of the lower liquid-air interface (inside the tip). Since the total volume of loaded liquid is much larger than the volume inside the tip, one can assume the mean radius of curvature of the liquid to remain constant as the liquid front progresses inside the tip. The closer the liquid front gets to the aperture, the smaller

the contact angle is. Nevertheless, the condition to have an advancing liquid front is lost once the contact angle inside the tip is equal or smaller to the advancing contact angle. The most crucial point is the flow through the aperture. Thus, it will be impossible to fill a tip which is hydrophobic inside.

But is it possible with a hydrophilic tip inner surface that the liquid overflows through the aperture and forms a larger drop (Figure 5–12 C)? To be able to overflow, the liquid will at one time be forced to have a high surface curvature, which implies also a high Laplace pressure, higher than the one induced by the curvature of the liquid on the loading area. However, the height of the column of liquid is not enough to arise to a sufficient high Laplace pressure. The liquid will thus not overflow through the aperture.

5.4.1.3. Determination of the amount of loaded liquid.

The determination of the amount of liquid deposited onto the loading area is based on a method initially developed to calibrate the cantilever spring constant. The method is based on the shift of the cantilever resonance frequency in response to an additional mass at the extremity of the cantilever [86]. The cantilever is considered as a harmonic oscillator, with a fundamental resonance frequency ν_1 defined by equations (5-2) and (5-3). The resonance frequency of a harmonic oscillator having a spring constant c and a mass m_{eff} is given by:

$$\nu = \frac{1}{2\pi} \sqrt{\frac{c}{m_{eff}}} \quad (5-13)$$

Using equation (5-1) and (5-2) one obtains for the fundamental oscillation of the cantilever:

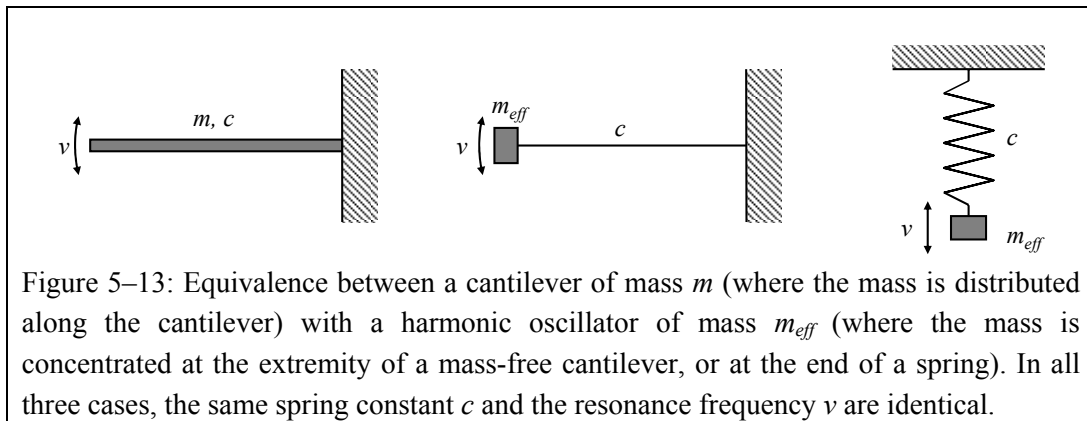
$$\nu_1 = \frac{\alpha_1^2}{2\pi\sqrt{3}} \sqrt{\frac{c}{m}} \quad (5-14)$$

where m corresponds to the real mass of the cantilever ($m = \rho \cdot l \cdot w \cdot t$).

In order to arrive at equivalent systems for both the harmonic oscillator and the cantilever, the respective resonance frequencies and spring constants have to be equal. Thus, a relation between the effective mass m_{eff} and the real mass m of the cantilever can be extracted.

$$m_{eff} = \frac{3}{\alpha_1^4} m \approx 0.243m \quad (5-15)$$

The effective mass can be seen as the equivalent mass of a harmonic oscillator having the same spring constant and the same resonance frequency as the cantilever (see Figure 5–13).



For a cantilever, the spring constant is defined as the ratio of force to deflection measured at the free end of the cantilever (see equation (5-1)). Because of the equivalence between the harmonic oscillator system and the cantilever system, on the mass-free cantilever, the effective mass m_{eff} has to be located at the same point where the force used for the spring constant definition is applied, i.e. at the extremity of the mass-free cantilever.

If now a mass M is added to the effective masse m_{eff} at the end of the cantilever, the resonance frequency ν_M will be, according to equation (5-13):

$$\nu_M = \frac{1}{2\pi} \sqrt{\frac{c}{m_{eff} + M}} \quad (5-16)$$

The presence of an additional mass M will thus induce a decrease in resonance frequency. From equations (5-13) and (5-16), the spring constant c and the effective masse m_{eff} can be easily determined knowing ν , ν_M and M [86]. The same equations can also be used to determine in a simple way the value of the additional mass M , if the spring constant c is known:

$$M = \frac{c}{4\pi^2} \left(\frac{1}{\nu_M^2} - \frac{1}{\nu^2} \right) \quad (5-17)$$

The possibility to correctly determine the additional mass M depends on the knowledge of the spring constant c .

However, this method suffers from the fact that the additional mass M is in reality not exactly a point mass placed at the cantilever extremity. In the case of a liquid, the mass is distributed over the entire loading area. The mass M given by equation (5-17) can thus be seen as a lower limit of the real mass M_{real} . And an upper limit can be calculated for the case where M is uniformly distributed over the entire cantilever giving a same frequency ν_M . Accordingly to equation (5-15), the upper limit will be about 4.12 times higher than M . Thus:

$$M \leq M_{real} \leq \frac{\alpha_1^4}{3} M \approx 4.12 \cdot M \quad (5-18)$$

Despite the fact that only an lower and upper limit value for the additional mass of liquid is known, the real mass M_{real} lies closer to the value of the minimum mass M , since the liquid is confined to the loading area which is located at the free end of the cantilever.

Typical volumes of loaded liquid were found to be about 20 pl for the probes with microfabricated apertures, and about 2 pl for the FIB-modified probes. Volumes estimated by optical observation gave comparable results.

5.4.1.3a. Evaporation of the liquid from the loading area

The resonance frequency of a loaded probe increased continuously, because of the loss of liquid due to evaporation, until the resonance frequency of the empty cantilever was reached. Tracking this increase over time allows one to determine the loss of mass of liquid by:

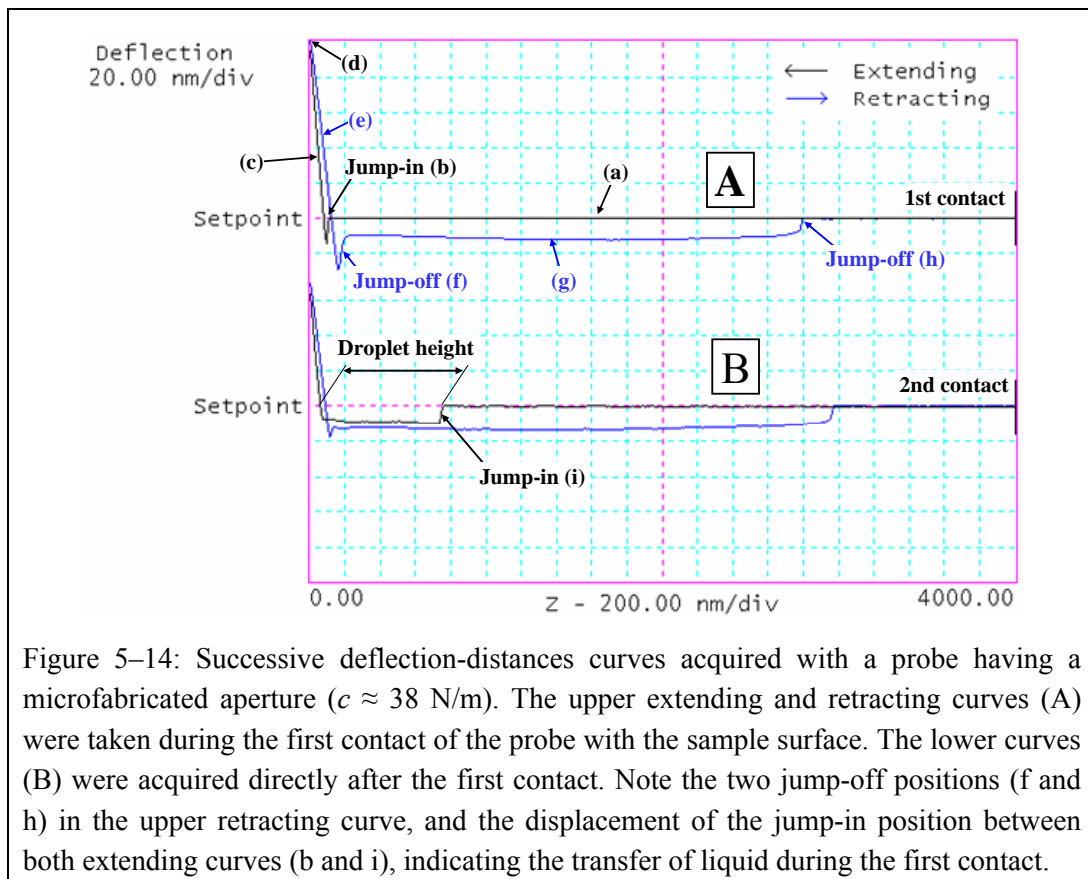
$$\frac{dM}{dt} = - \frac{c}{4\pi^2} \frac{1}{\nu_M^3} \frac{d\nu_M}{dt} \quad (5-19)$$

The evaporation rate of the liquid could thus be determined. At about 21 °C, the evaporation rates for glycerol, anhydrous glycerol and for TetraEG were measured to be approximately 40 al/min/ μm^2 (attoliters per minute per square micron). The area of the liquid surface was determined by optical

observation. The relative vapor pressure for both liquids was unknown, but they can be assumed to be small, since the evaporated amount of liquid is negligible compared to the volume of the room where the experiments took place. The determination of the evaporation rate permits to get an idea of the evaporation time of droplets deposited on the surface.

5.4.2. Transfer of liquid characterization by deflection-distance curves

Before starting the dispensing of a full array of droplets, the transfer of liquid leading to a droplet deposition was characterized. To control that a liquid transfer from the probe to the substrate really occurs, successive deflection-displacement curves acquired at the same location on the substrate can be used. A deflection-displacement curve represents the deflection of the cantilever as a function of the probe-sample distance^{a)}. The curves are acquired by, firstly driving the probe against the substrate until the cantilever is bent due to the tip-substrate contact, and secondly withdrawing the probe from the substrate, i.e. an extending and a retracting of the piezoelectric z-scanner is performed. Simultaneously, the deflection of the cantilever is acquired.

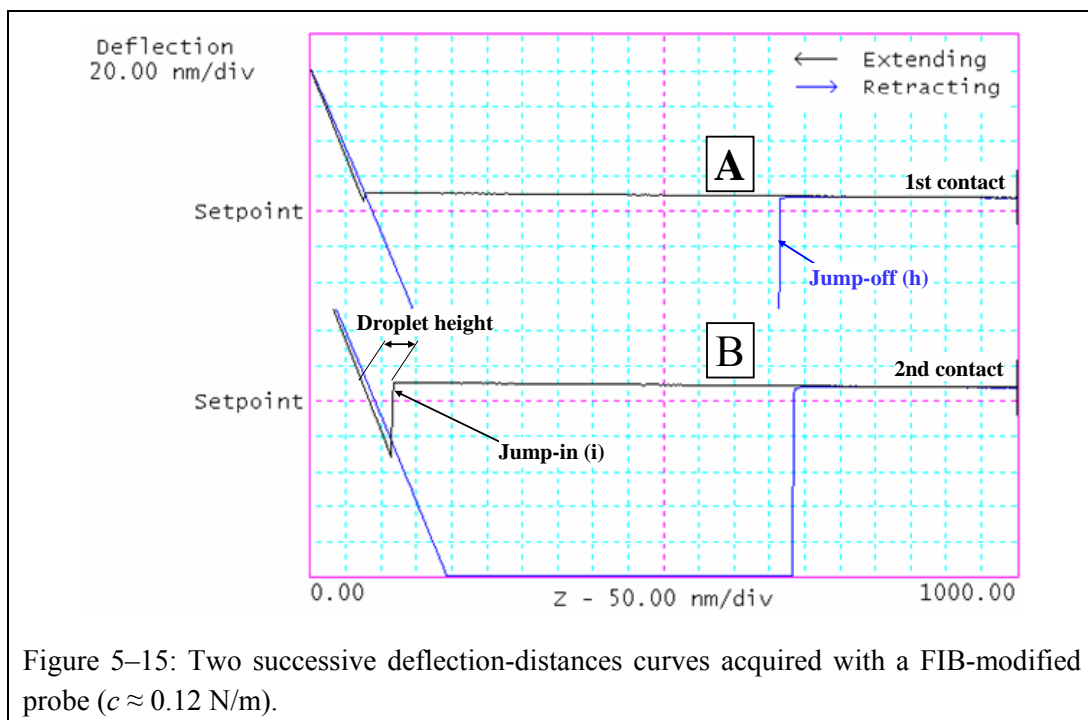


During the first of the successive deflection-displacement curves acquisition (see Figure 5–14 A), as the probe is lowered, the deflection remains null until the probe reaches the vicinity of the substrate (see index (a) in Figure 5–14 A). A jump-in is usually observed just before the tip contacts the

^{a)} The probe-sample distance should not be confused with the tip-sample separation. The probe-sample distance does not take into account the deflection of the cantilever.

substrate (b), which is when the tip is subject to an attractive force and bends down (negative deflection) until the tip contacts the surface^{a)}. This attractive force is related to e.g. van der Waals forces or capillary forces. While the probe is still lowered, the deflection of the cantilever will now continuously increase (c), because of the repulsive forces between tip and substrate, until the movement of the piezoelectric z-scanner is reversed (d). While the probe is now withdrawn, the deflection decreases (e), becomes negative, until a jump-off occurs (f). This is when the tip is released from the substrate. For an empty probe, the cantilever returns to its rest position (no deflection). But in the case where a liquid transfer from the tip to the substrate occurred, even if the tip is released from the surface, the cantilever is still bent down due to a capillary force resulting from the liquid bridge between tip and substrate (g). As the probe is still withdrawn, a second jump-off occurs (h) when the stretched meniscus between tip and substrate breaks, and the cantilever returns to its rest position.

Thus, the presence of two different jump-off positions indicates that a transfer of liquid occurred during the contact. Nevertheless, for probes with low spring constant, it can happen that the first jump-off does not appear in the curve (see Figure 5–15), because when the deflection is too large the signal on the photodetector gets out-of-range. For this reason, a second deflection-displacement curve is acquired at the same position on the substrate. While the probe is lowered down for the second curve, the jump-in occurs as soon as the tip contacts the surface of the previously deposited droplet (index (i)). The jump-in position on the second acquired curve allows the determination of the droplet height, as shown in Figure 5–14 B and Figure 5–15 B.



The measurement of the height of the deposited droplet is used in the determination of the droplet volume (see section 5.5.1.1). The measured droplet heights allow furthermore the investigation of the influence of various parameters on the deposition. The two most important parameters are:

- Duration of the contact.
- Number of contacts at same location.

^{a)} The tip will jump onto the surface when the gradient of the attractive force exceeds the spring constant of the cantilever.

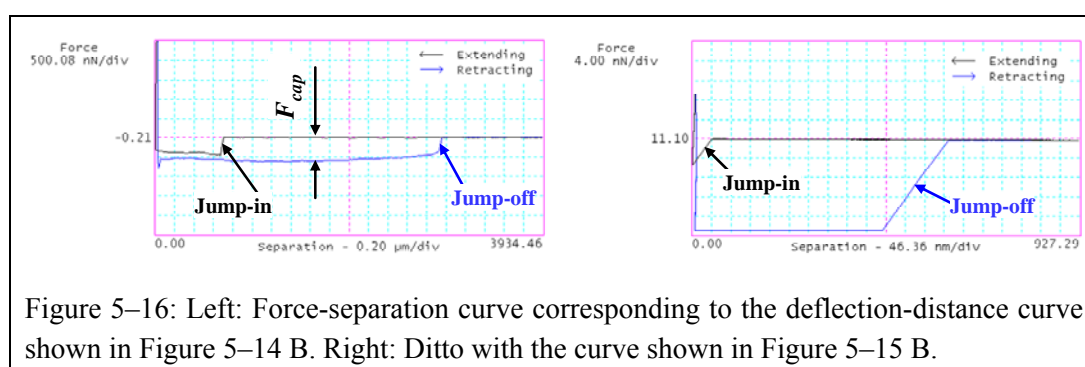
By setting a delay time between the two contacts, one can also investigate the decrease of the droplet height due to evaporation (see section 6.4.1).

The accuracy of measured droplet height value is limited by the resolution of the measurement method. With the AFM's used, a deflection-distance curve (extending or retracting) is usually limited to 512 points. Thus, e.g. for a z-ramp of 4 μm , the resolution (distance between two points) on the probe-sample separation axis is 7.8 nm. The newer version of the AFM software allows nevertheless the acquisition of deflection-displacement curves with more than 512 points per curve.

Another inaccuracy in the droplet height measurement comes from the hysteresis and creep of the piezoelectric scanner in z-direction. The difference in the slopes of the curve-segments C and E in Figure 6–11 results from the hysteresis.

5.4.3. Measurement of the capillary force

If the spring constant of the cantilever is known, a deflection-displacement curve can be transformed into a force-separation curve. A force separation curve represents the force acting on the cantilever (deflection times spring constant) as a function of the tip-sample separation^{a)}. Two examples of force-separation curves are shown in the Figure 5–16, which correspond to the curves shown in Figure 6–11 B and Figure 5–15 B.



The force-separation curve allows the determination of the capillary force F_{cap} acting between tip and substrate during the withdrawal of the probe, as shown on the left hand side in Figure 5–16. It is obvious that a reliable capillary force cannot be determined on the section of curve where the jump-off occurs. Thus, no capillary force can be determined from the curve shown at the right hand side in Figure 5–16.

5.4.4. Dispensing of the droplets to form a pattern

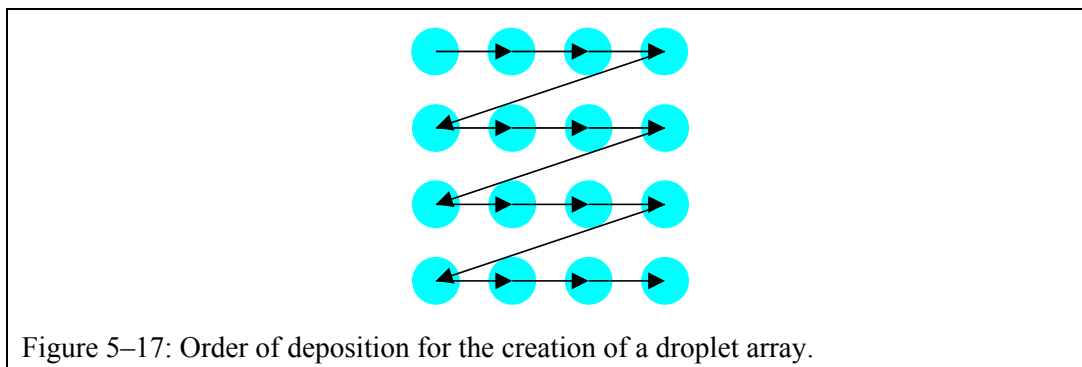
The droplets can be deposited to form a predefined pattern on the surface, e.g. an array, by controlling the xyz-displacement of the piezoelectric scanner. This allows a positioning of the droplets with a high lateral accuracy.

On the AFM's used there exist possibilities either to control all three axes, or to control only the xy displacements while the z position is controlled over the feedback loop of the contact mode. The control of the axes is realized by means of the NanoScriptTM lithography language (based on C++

^{a)} The tip-sample separation is equal to the sum of the probe-sample distance and the cantilever deflection.

language), which is included in the AFM software. An example of such program is given in Annex 3, as well as the procedure to run the program.

The deposition of an array of droplets started always at the top left corner. The deposition sequence went from left to right and from top to bottom until the deposition of the last droplet at the bottom right corner (see Figure 5–17).



5.4.5. Cleaning of the probe

At the end of a deposition experiment, the probe is immersed over night in a solvent to dissolve the remaining liquid on the loading area. For glycerol, anhydrous glycerol or tetraethylene glycol, Millipore water can be used as solvent. When the next experiment involved a different liquid for deposition, for the probes with microfabricated apertures a new one was taken, and for the FIB-modified probes, the probe was cleaned in oxygen plasma and treated again with hexadecanethiol (see section 5.3.1).

5.5. Characterization of the droplets

5.5.1. How to determine the volume of the deposited drop

One important key point was the ability to determine the amount of deposited liquid, i.e. the volume of one droplet. Several approaches were used.

5.5.1.1. By the droplet dimension

One technique to determine the volume of a deposited droplet is to determine its geometrical dimensions. Because of the small droplet size, the forces influencing its shape are dominated by surface tension. The mean surface curvature is therefore constant over the entire droplet, and the shape can thus be approximated by a spherical cap. The volume V of a spherical cap is:

$$V = \frac{\pi}{6} h \left(\frac{3}{4} d^2 + h^2 \right) \quad (5-20)$$

where d is the diameter of the base and h the height. The height of the droplet can be determined by the snap-in position on a deflection-distance curve as explained in the section 5.4.2. To determine the diameter of the droplets, two methods were used.

A rather simple method, limited to larger droplets (several microns in diameter), is to measure the diameter on an optical micrograph taken directly after the deposition.

But the smaller droplets could not be resolved by the optical microscope mounted on the AFM. Instead, an upper limit for the diameter was estimated as the smallest distance between two non-coalescing droplets in an array with diminishing pitches. If during the deposition, the liquid meniscus around the tip touches the previously deposited droplet, the latter will coalesce into the meniscus because of the surface tension (see Figure 5–18). A high resolution micrograph (typically a topographic AFM micrograph) that reveals the positions of the droplets rather than their size can therefore be used.

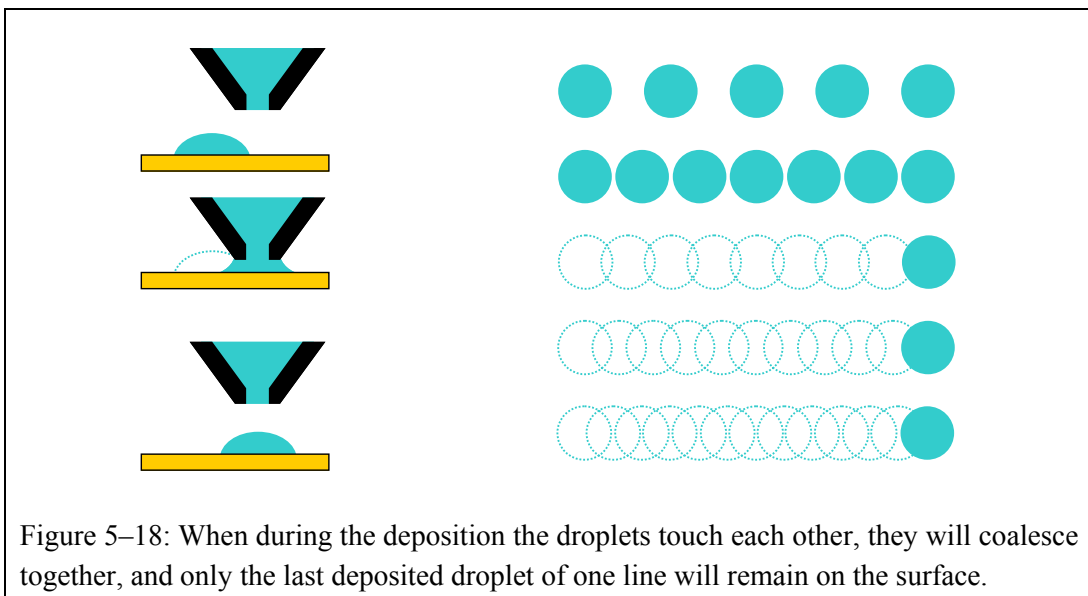


Figure 5–18: When during the deposition the droplets touch each other, they will coalesce together, and only the last deposited droplet of one line will remain on the surface.

An alternative is to measure the contact angle for the liquid that is deposited. Together with the height measurement, it allows also the determination of the size of the sessile droplet. Nevertheless, the contact angle measurements suffer from hysteresis (see section 2.3.2.4). The advancing and the receding contact angle will thus provide a minimum and maximum value for the volume.

5.5.1.2. By the shift in resonance frequency

The second method used to determine the volume of the deposited droplets is to measure the shift in the resonance frequency of the cantilever (see section 5.4.1.3). The shift is induced by the loss of liquid loaded onto the cantilever. By measuring the resonance frequency before and after the deposition process of the droplets, the change in the amount of liquid on the loading area can be determined. Both the dispensed liquid and the loss due to evaporation will reduce the amount of liquid on the cantilever. But the component due to evaporation can be measured independently (section 5.4.1.3a), and subtracted from the total value. Nonetheless, the method of resonance frequency shift provides only approximate values, both for the total loss of liquid and for the loss due to evaporation. Thus, to be able to calculate the loss due to the dispensing with enough accuracy, the loss due to evaporation has to be much smaller than the total loss of liquid. Otherwise, for the loss of liquid due to the deposition, the inaccuracy will be larger than the calculated value.

5.5.1.3. By the capillary force

A last possibility was investigated using the value of the capillary force during the withdrawal of the probe. In section 2.3.5.3 it was shown that the capillary force can be calculated from the four variables: surface tension, diameter, curvature, and slope of the meridian. The surface tension can be determined independently (see section 3.2.1). The curvature of the liquid cannot be larger than the curvature of the liquid in the loading area. And the slope of the meridian can be taken as the supplementary angle of the contact angle, if the diameter corresponds to the wetted area on the sample surface. The diameter and the curvature can be taken as free parameters while trying to reconstruct the meridian of an axisymmetric meniscus that respect the contact angle, the surface tension and the capillary force. The range of solutions should provide some information about the wetted diameter on the sample.

5.5.2. Visualization of the deposited droplets

5.5.2.1. Optical imaging

For the larger-sized droplets that were deposited by the dispenser, the direct observation by means of the in-situ CCD camera was the easiest way to visualize the result. The Dim 3100 AFM with its frame grabber allowed to capture the optical micrographs. The capture was taken directly after the droplet deposition to avoid evaporation from the droplet. If necessary, the option “print screen” was chosen directly after the end of the lithography program running, and before retracting the probe.

Observation using conventional microscopy (bright-field, dark field, fluorescence) was also used.

5.5.2.2. AFM imaging

When the deposited droplets could not be resolved because of their small size, the area of deposition was investigated with conventional AFM techniques to visualize possible surface modifications due to the presence of the deposited liquid. Both tapping and contact mode was used.

The probes used to operate in contact mode were the same as those taken for the V-shaped FIB-modified probes, i.e. model DNP-S from Veeco (see Table 4–1 and Table 5–5).

The tapping mode probes were of the type NSG-01, fabricated by NT-MDT (Moscow, Russia [87]). They are made of silicon, had a cantilever dimensions of 130/35/2 μm , a nominal resonance frequency of 150 kHz and a nominal spring constant of 5.5 N/m.

5.5.2.2a. Localization of the deposition area

After the changing from the nanodispenser probe to a conventional AFM probe, the area of deposition had to be localized again.

On the Dimension 3100 AFM, the combination of the motorized xy-stage with the CCD camera allowed a fast localization. For that purpose, the deposition area coordinates was previously referenced relatively to e.g. the edges or any optical recognizable features on the sample surface that allows the definition of a coordinate system. The localization of a deposition area was therefore also possible if the sample has been removed from the stage.

On the MultiMode AFM, the deposition area had to lie in the vicinity of an optically recognizable surface feature (e.g. a dust particle or a surface scratch), so that the new probe could be brought at the same location relative the surface feature. Nevertheless, removing the sample from the AFM compromised any further localization of a previous deposition.

5.5.2.2b. What is seen after the deposition

As soon the droplet is deposited on the sample surface, the volatile element making the droplets evaporates. Nevertheless, the different liquids used to be deposited were not 100% pure, and the non-volatile elements remained on the surface, leading to a residual dots. Additional material such as nanoparticles could furthermore be added to the liquid before the dispensing, increasing thus the amount of material remaining on the surface.

The presence of the liquid can also induce a change of the sample surface properties. An example of such surface modification will be shown in section 6.7.

6. Results and discussion

This chapter will discuss the main results of nanoscale dispensing obtained with both the probes having microfabricated apertures and the FIB-modified probes. First, some typical depositions realized with both kinds of probes are shown. The transfer of liquid is then discussed, by analyzing the different parameters that influence the volume of the deposited droplets, and the capillary force exerted by the meniscus of liquid during the withdrawal of the probe. The deposition of fluorescent molecules and nanoparticles suspended in the liquid are also shown. And finally, an example of local surface modification is shown, where anhydrous glycerol droplets induce a modification of micelles.

6.1. Typical results of droplet deposition

Before discussing in more detail the different aspects of the results obtained by nanoscale dispensing, it is worthwhile to present some common results, with both kinds of probes (microfabricated and FIB-milled apertures).

6.1.1. Deposition using probes with microfabricated aperture

The deposition performed with probes having microfabricated aperture leads to larger droplets than with the FIB-modified probes. The main reason is that the microfabricated apertures are much larger than the FIB-milled apertures (by about two orders of magnitude). The droplets deposited by the probes having microfabricated aperture were usually visible with the in-situ CCD camera. An example is given in Figure 6–1. This allows an easy and fast way to characterize the deposition.

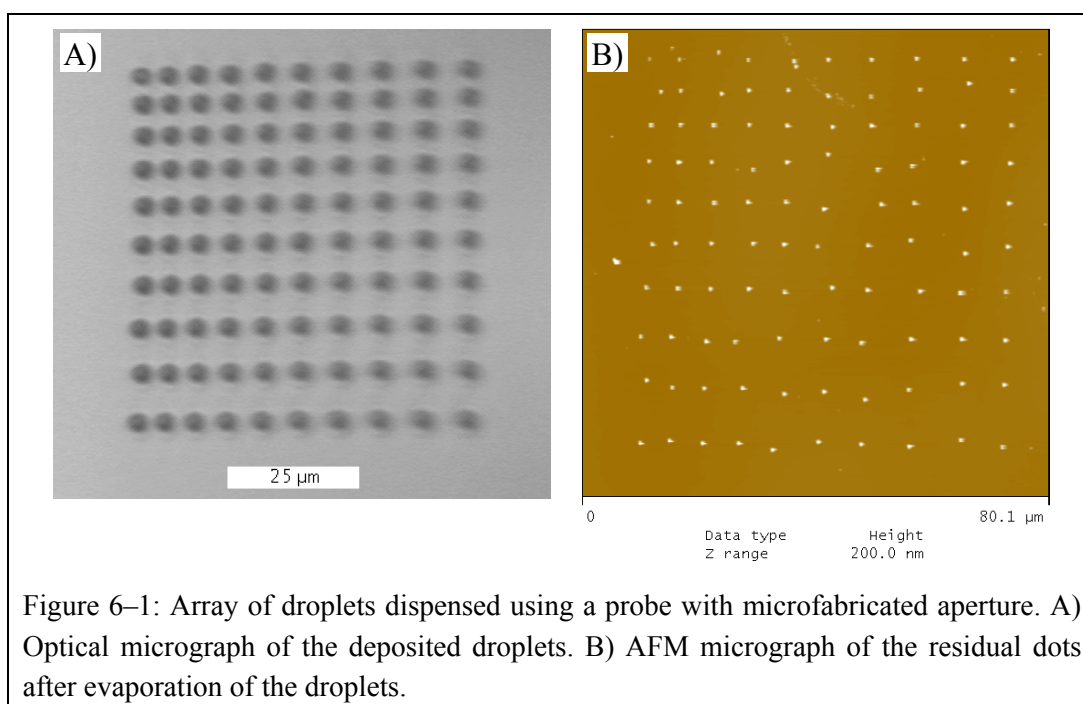


Figure 6–1: Array of droplets dispensed using a probe with microfabricated aperture. A) Optical micrograph of the deposited droplets. B) AFM micrograph of the residual dots after evaporation of the droplets.

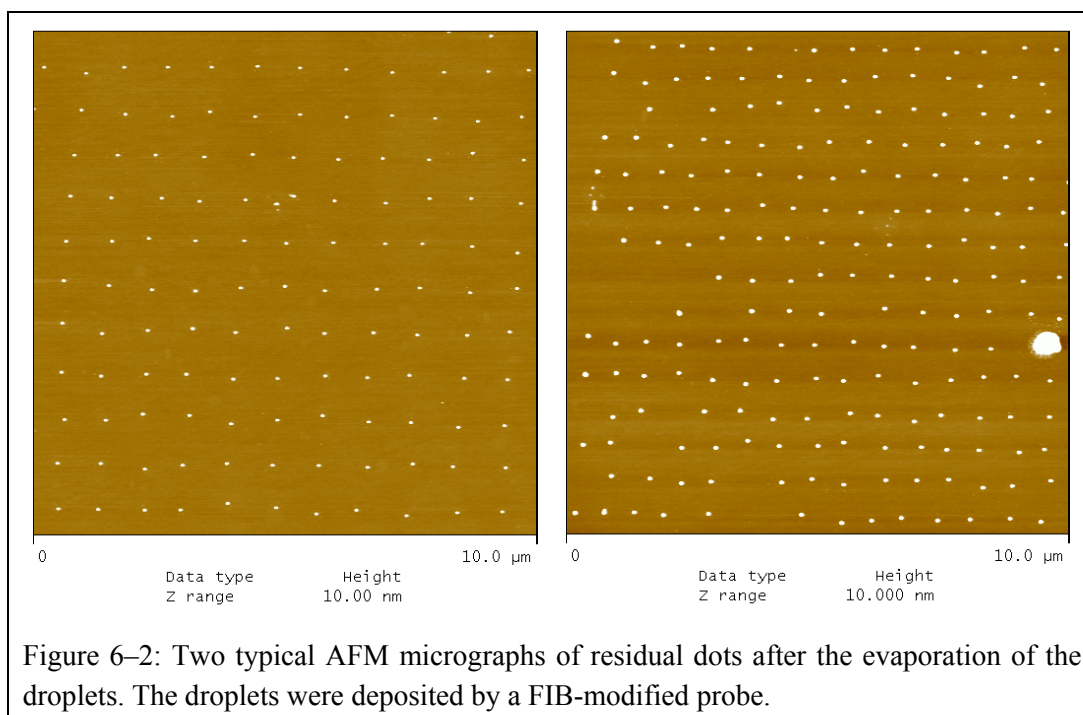
The arrays of droplets shown in Figure 6–1 A are slightly irregular in the droplet position, because of the hysteresis of the piezoelectric scanner. Such inaccuracy can be easily suppressed by using a closed-loop piezoelectric scanner.

Typical droplet diameters encountered during all experiments were between 2 and 8 μm , and the droplet volumes were usually between 1 and 25 femtoliters. The amount of loaded liquid onto the cantilever was approximately 20 picoliters, theoretically enough to achieve the deposition of about thousand droplets without replenishment of the probe.

As described in section 5.5.1.2, it is possible to determine the amount of deposited liquid using the shift in resonance frequency of the cantilever and by taking account of the evaporation from the loading area. The loss of liquid due to evaporation from the loading area had typical values around 40 fl/min. By considering a typical time for dispensing one droplet to be about 2 seconds, and a typical droplet volume to be 5 fl, the decrease of liquid due to the dispensing is approximately 150 fl/min. This is larger than the loss due to evaporation. Thus, the method using the shift in the resonance frequency could be used.

6.1.2. Deposition using FIB-modified probes

The droplets deposited with FIB-modified probes were usually too small to be visible with the in-situ CCD camera. Only the residual dots remaining on the substrate surface after the evaporation of the droplet were visible using AFM imaging. Two examples are shown in Figure 6–2.



Typical droplet diameters were between 800 nm and 1.5 μm . The volumes of the droplets were estimated to be between 10 and 200 attoliters. The amount of liquid loaded on the cantilevers was approximately 2 picoliters.

With the FIB-modified probes, it was not possible to estimate the droplet volume by the method of the resonance shift of the cantilever, because the loss of liquid due to evaporation (about 20 fl/min) was much more important than the decrease due to the droplet deposition. Thus, the latter could not be properly isolated from the global loss of liquid.

6.2. Parameters that influence the amount of deposited liquid

There are a number of various factors that influence the amount of liquid transferred from the probe to the sample surface. Some of them are related to geometrical aspects, others to chemical and physical properties, or to the deposition procedure itself. Most of these parameters are however not independent from each other. Some of them can be well controlled, others not. For those reasons, a complete control of the amount of deposited liquid is rather complex. Some of the parameters are:

- Shape of the tip
- Aperture size
- Surface tension of the liquid
- Viscosity of the liquid
- Contact time
- Number of contacts on the same spot
- Contact angle on the sample surface
- Withdrawal-speed for the tip
- Contact angle on the outer tip wall
- Laplace pressure inside the liquid

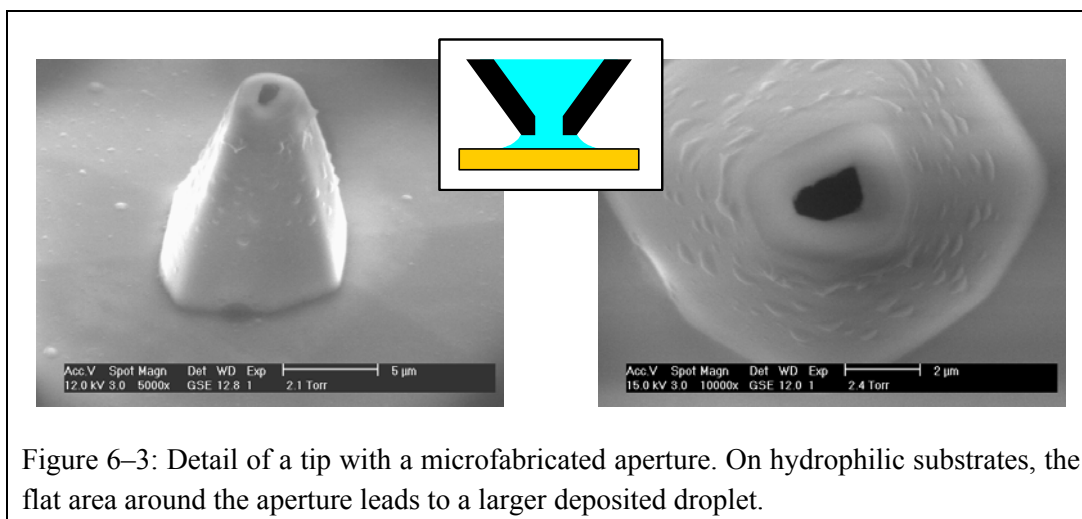
In order to better understand how all those parameters can influence the volume of the deposited droplet, let us imagine what happens during a deposition process. Before the contact, the liquid is in hydrostatic equilibrium, which means that the liquid-air interface has a constant mean curvature at each point, at the aperture as well as over the loading area. Gravity can be neglected because of the small column of liquid involved. When engaging the tip, as the liquid touches the sample surface and slightly spreads out, the hydrostatic equilibrium is broken. The mean curvature of the liquid meniscus between tip and sample has no longer the same mean curvature as the liquid on the loading area, but is smaller. A different mean curvature signifies a different Laplace pressure. A gradient of pressure is therefore present inside the liquid, and will induce a flow through the aperture, increasing the amount of liquid present in the meniscus. The associated decrease of volume on the loading area will also influence the mean curvature of the upper liquid-air interface. As long as a new equilibrium condition is not reached, liquid will flow through the aperture. The conditions to get a new hydrostatic equilibrium are:

- fulfillment of the requirement, relative to the contact angle (which has to lie between the advancing and receding contact angles) on the sample and tip surfaces, and
- identical mean curvature over the entire liquid-air interface.

As the tip is retracted, whether the hydrostatic equilibrium was reached or not, the meniscus will stretch out between tip and sample surface, and finally break, leaving the droplet on the substrate.

6.2.1. Aperture size and tip geometry

The first parameter influencing the amount of deposited liquid is the geometrical shape of the tip extremity and of the aperture. A 200 nm aperture of a FIB-modified probe leads to a smaller droplet than a 1-2 μm wide aperture of microfabricated probes on a same sample surface. Furthermore, the microfabricated apertures are surrounded by a flat zone, leading to a larger gap area that can be filled with liquid as the probe is in contact with the surface (see Figure 6–3).



One could think that if the probe is in contact with the sample surface, the material of the tip surrounding the aperture could act as a sealing and retain the liquid in the aperture, preventing thus a spreading of the liquid. However, the cantilever is not parallel to the sample surface, but is tilted by roughly 11° , which corresponds to the tilt of the probe holder. The tip axis will therefore also be inclined by 11° with respect to the normal of the sample surface. Furthermore, on the probes where the FIB-milling was performed at the tip apex, the aperture is surrounded by four secondary peaks (see Figure 4-14). Thus, a contact of the tip on the surface does not prevent the liquid flow through the opening between the secondary peaks.

6.2.1.1. Position of the aperture in the FIB-modified probes

The FIB milling offers the possibility to open the aperture slightly off-center from the tip apex (example of such probes are shown in Figure 4-11 and Figure 4-13). This has the advantage of keeping a sharp tip for high resolution imaging. However, the functionality of the probe, i.e. transferring liquid to the surface, can be compromised.

In Figure 6-4 is shown an example of a probe with the aperture at the apex (A) and one with the aperture off-center (D). The substrate was freshly cleaved mica, and the liquid TetraEG. First, a deflection-distance curve was taken with the empty probes (B and E). The adhesion force was higher with the first probe (~ 60 nN) than with the second probe (~ 6 nN). This difference arises from the fact that the tip from the first probe was much sharper (see also sections 2.2.3 and 2.3.6). As the first probe was loaded and brought in contact with the mica surface, the loading area got empty within one to two minutes and all TetraEG was transferred to the surface (C,).

With the probe having the aperture off-center, the presence of the liquid in the loading area did not influence significantly the deflection-distance curve (F), indicating thus that no liquid transfer had happened.

This denotes that with an off-center aperture that is not in close vicinity of the tip apex, the liquid does not reach the substrate while the tip is in contact with it, and no transfer of liquid can occur.

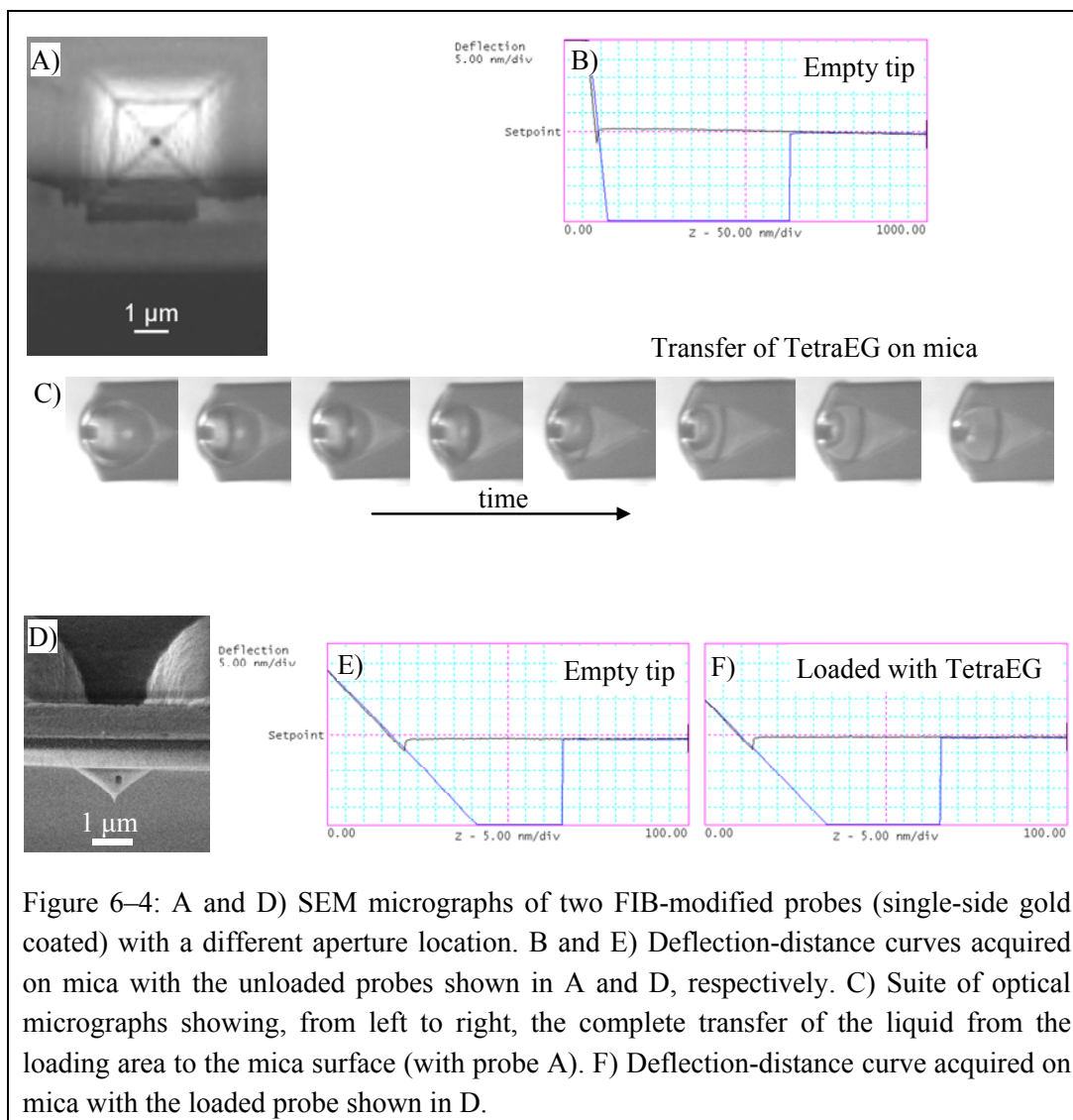


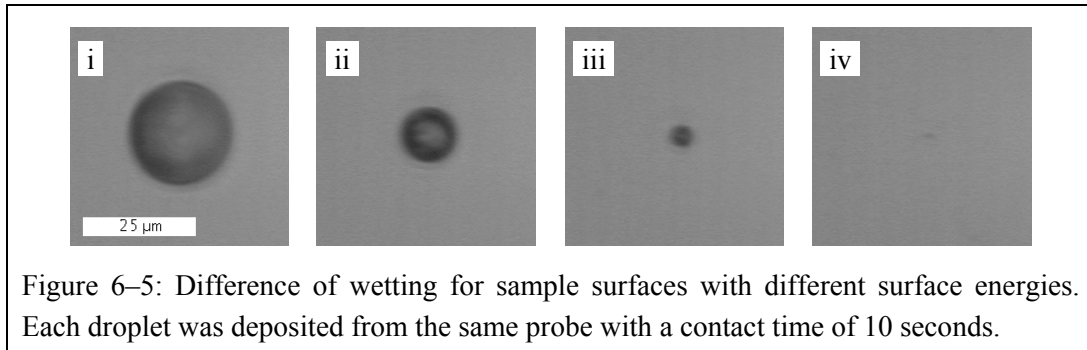
Figure 6-4: A and D) SEM micrographs of two FIB-modified probes (single-side gold coated) with a different aperture location. B and E) Deflection-distance curves acquired on mica with the unloaded probes shown in A and D, respectively. C) Suite of optical micrographs showing, from left to right, the complete transfer of the liquid from the loading area to the mica surface (with probe A). F) Deflection-distance curve acquired on mica with the loaded probe shown in D.

6.2.2. Surface energy of the sample

The surface energy of the substrate plays an important role for the amount of deposited liquid. While the tip contacts the substrate, the more the surface is hydrophilic, the more the liquid spreads out. To show the influence of the substrate wettability, four samples (silicon oxide surface) with different surface energies were prepared (see section 5.2):

- (i) Cleaned with the SC-1 procedure.
- (ii) Cleaned with acetone and ethanol in ultrasonic bath.
- (iii) Octadecyltrichlorosilane coverage.
- (iv) Perfluorodecyltrichlorosilane treatment

A probe with microfabricated aperture was loaded with TetraEG (~15 pl) and was brought in contact during 10 seconds with each sample. An optical micrograph was taken directly after the probe withdrawal. They are shown in Figure 6-5. The spreading is much more pronounced on the hydrophilic sample surface.



Additionally, the advancing and receding contact angles were measured on each sample with TetraEG (see Table 6-1). From the diameter and advancing contact angle values, an upper limit for the droplet volumes can be determined. They are given in Table 6-1 for the four different samples.

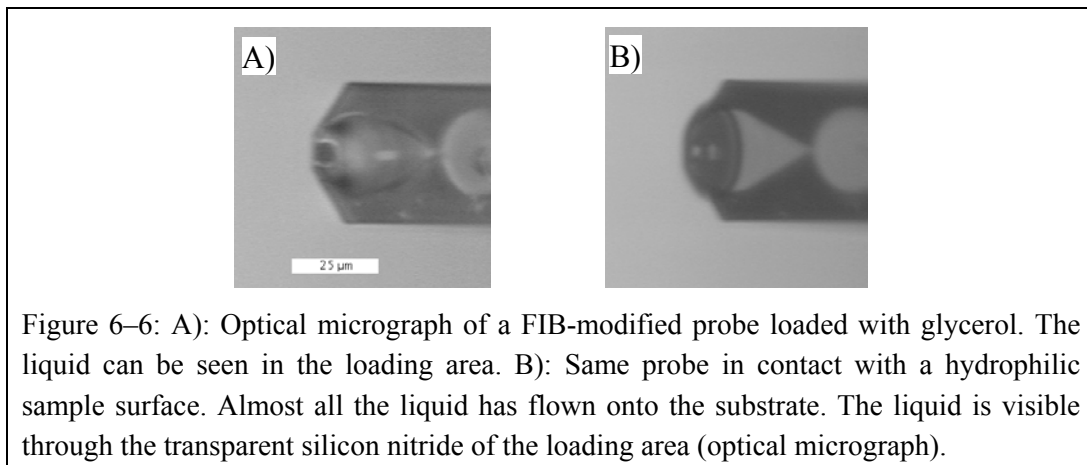
Substrate	(i)	(ii)	(iii)	(iv)
Drop diameter [μm]	23	12	5	<2
Advancing contact angle [$^\circ$]	16	35	54	90
Receding contact angle [$^\circ$]	0	26	44	67
Maximum volume [fl]	340	110	14	<2

Table 6-1: Advancing and receding contact angles measured with TetraEG on the four substrates. The diameter together with the advancing contact angle allows the determination of an upper limit of the volume of the deposited droplet.

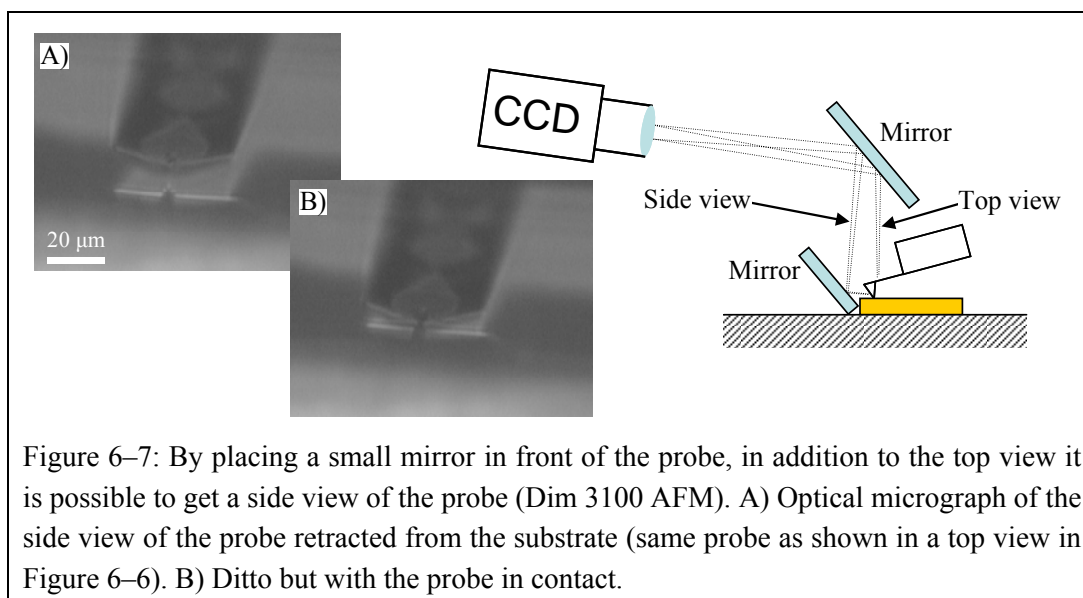
This shows that the probe could deposit on different substrates of different wettability droplets with volumes that differ by two orders of magnitude.

6.2.2.1. Hydrophilic substrate with hydrophilic outer tip wall

When a loaded tip is brought into contact with a hydrophilic sample surface, due to the small contact angle on the sample, the liquid starts to spread out. The spreading is stopped either by a withdrawal of the probe, or when the hydrostatic equilibrium inside the liquid is reached. Often, the hydrostatic equilibrium is reached only when the loading area is almost entirely empty, i.e. when most of the liquid has flown onto the substrate. An example is shown in Figure 6-6.

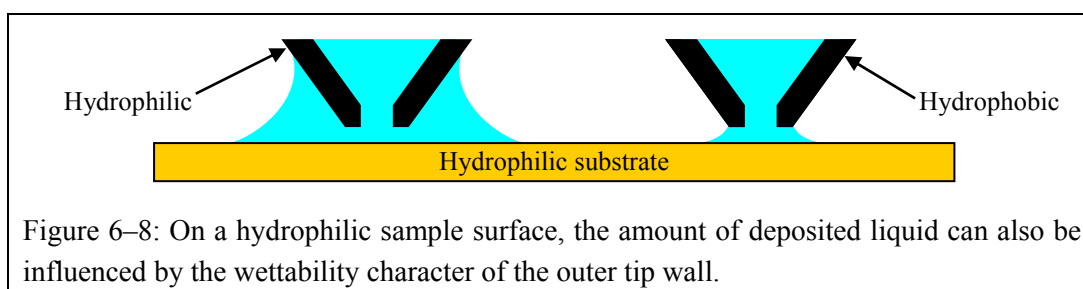


Once the hydrostatic equilibrium is reached (and almost all liquid has flown onto the substrate), it is not clear whether the outer part of the tip was wetted by the liquid, or not. One way to answer that question is to try to visualize with the in-situ CCD camera the meniscus of liquid around the tip while the tip contacts the substrate. To do that, a small mirror was placed at the edge of the substrate, as sketched in Figure 6–7. By changing the focal depth and the direction of the optical axis of the CCD camera mounted on the Dim 3100 AFM, the tip can be observed from the side. Albeit it was indeed possible to get a view on the tip, the resolution of the optical micrograph did not permit a precise determination of the meniscus shape of the liquid.



Nevertheless, optical observation through the transparent silicon nitride cantilever allows one to answer the question. As shown in Figure 6–6 B, the wetted area on the sample surface is not circular. But once the probe was retracted, the deposited droplet became circular in shape (diameter $\sim 25 \mu\text{m}$). This indicates that the presence of the probe influenced strongly the shape of the droplet as the tip was in contact with the surface. That the meniscus is oval-shaped (and not circular shaped) as shown in Figure 6–6 B can be explained only by the contact of the meniscus with a non-symmetric body, such as the cantilever extremity. Therefore, it can be assumed that the meniscus of liquid fills the whole gap between substrate and cantilever. Furthermore, as the probe was withdrawn, it was not possible to release the tip from the substrate within the range of the z-scanner, indicating a capillary force higher than $2.6 \mu\text{N}$. The theoretically constructed meridian of an axisymmetric meniscus corresponding to those conditions showed also that the tip is fully immersed in the meniscus.

Thus, when a hydrophilic tip of a loaded probe is in contact with a hydrophilic substrate, the tip becomes partially (or fully) immersed inside the meniscus of liquid. Such a situation is pictured in Figure 6–8.



To prevent the wetting of the outer tip wall on hydrophilic sample surfaces, the cantilevers with a gold metallization on both sides were used. The chemical treatment with hexadecanethiol (see section 5.3.1) made hydrophobic both, the remaining gold around the loading area and the front side of the cantilever, including the outer wall of the tip. This prevents the wetting of the outer tip wall, and permits the deposition on a hydrophilic substrate of smaller droplets than those obtained with a hydrophilic tip.

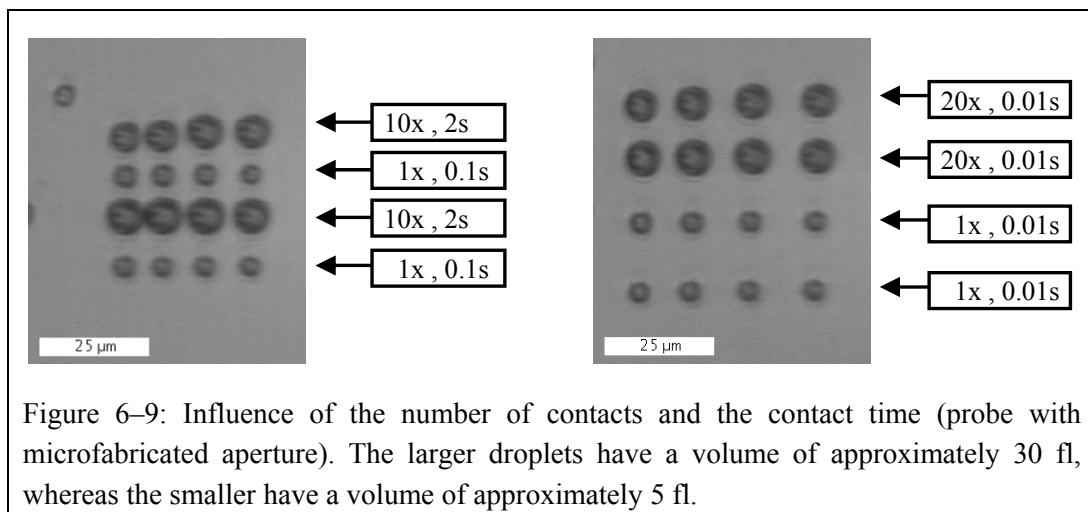
6.2.3. Contact time and number of contacts

The time needed to reach the hydrostatic equilibrium can get longer than the contact time of the probe (typical contact times are between a tenth of a second and a few seconds). Thus, by retracting the tip before the hydrostatic equilibrium is reached, smaller droplets can be deposited. Shorter or longer contact times could thus lead to smaller or larger deposited droplets. Furthermore, as long as the hydrostatic equilibrium is not reached, contacting several times the sample on the same spot can also increase the amount of transferred liquid. Both effects (contact time and the number of contacts) can be investigated by analyzing the diameters or the heights of the droplets.

It is worthwhile to notice that in the following examples, the contact time refers to the time during which the probe remains immobile as the z-scanner is extended. The true contact time of the probe with the substrate, or with the liquid located on the substrate, can therefore be larger.

6.2.3.1. Influence on the droplet diameter

Figure 6–9 shows two examples of droplet deposition on the same silicon dioxide sample using a probe with a microfabricated aperture. The deposited liquid was anhydrous glycerol. The withdrawal speed was programmed to be 100 $\mu\text{m/s}$. For each line of droplets, the number of contacts and the contact time are given.



Longer contact time together with higher number of contacts leads to a larger deposited droplet.

The influence of the contact time on the deposited volume by a FIB-modified probe (single-side gold coating, aperture 200 nm) is shown in Figure 6–10. The liquid loaded on the probe was TetraEG, and the sample surface was silicon dioxide (cleaned with acetone and ethanol in an ultrasonic bath).

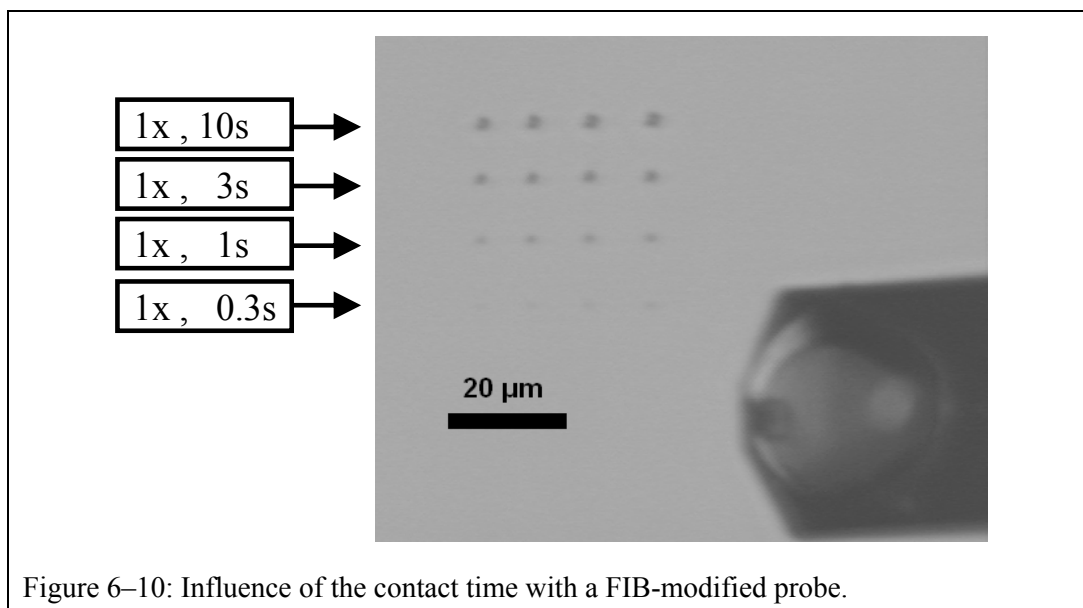


Figure 6–10: Influence of the contact time with a FIB-modified probe.

The four droplets of the last line are almost not visible, because of their small size. One should keep in mind that, because of evaporation, the droplet sizes shown in the optical micrograph can be smaller than directly after the deposition.

6.2.3.2. Influence on the droplet height

The acquisition of successive deflection-distance curves on the same spot allows another possibility to investigate the influence of the contact time and number of contacts on the amount of deposited liquid, by measuring the droplet heights. This was particularly useful when the droplet diameters were too small to be analyzed on optical micrographs, i.e. for droplets deposited with the FIB-modified probes.

An example of successive deflection-distance curves is shown in Figure 6–11. Here, the probe had a double-side gold coating with a FIB-milled aperture, and was loaded with anhydrous glycerol. The sample surface was freshly cleaved mica.

The increase in droplet height, while multiplying the number of contacts, points out to a continuous increase of the deposited amount of liquid, until a leveling off is observed in the droplet height (last curve in Figure 6–11). The leveling-off arises because the hydrostatic equilibrium is reached. The maximum droplet height in the discussed example was 360 nm. After the withdrawal of the probe, a droplet of diameter 6 μm remained on the surface, which corresponds approximately for the sessile droplet to a calculated droplet volume of 5 fl and a contact angle of 15°. The volume of this droplet is much larger than those usually measured for a droplet deposited with a FIB-modified, because of the numerous contacts. However, the volume after the 3rd contact was approximately 100 nl, which corresponds to a volume of about 100 al. It is worth notice that, despite the hydrophilic substrate, the hydrostatic equilibrium was reached without a fully emptying of the loading area (compare with the micrographs shown in Figure 6–4 and Figure 6–6). The reason is that the FIB-modified probe used for the results shown in Figure 6–11 had a tip with a hydrophobic outer wall.

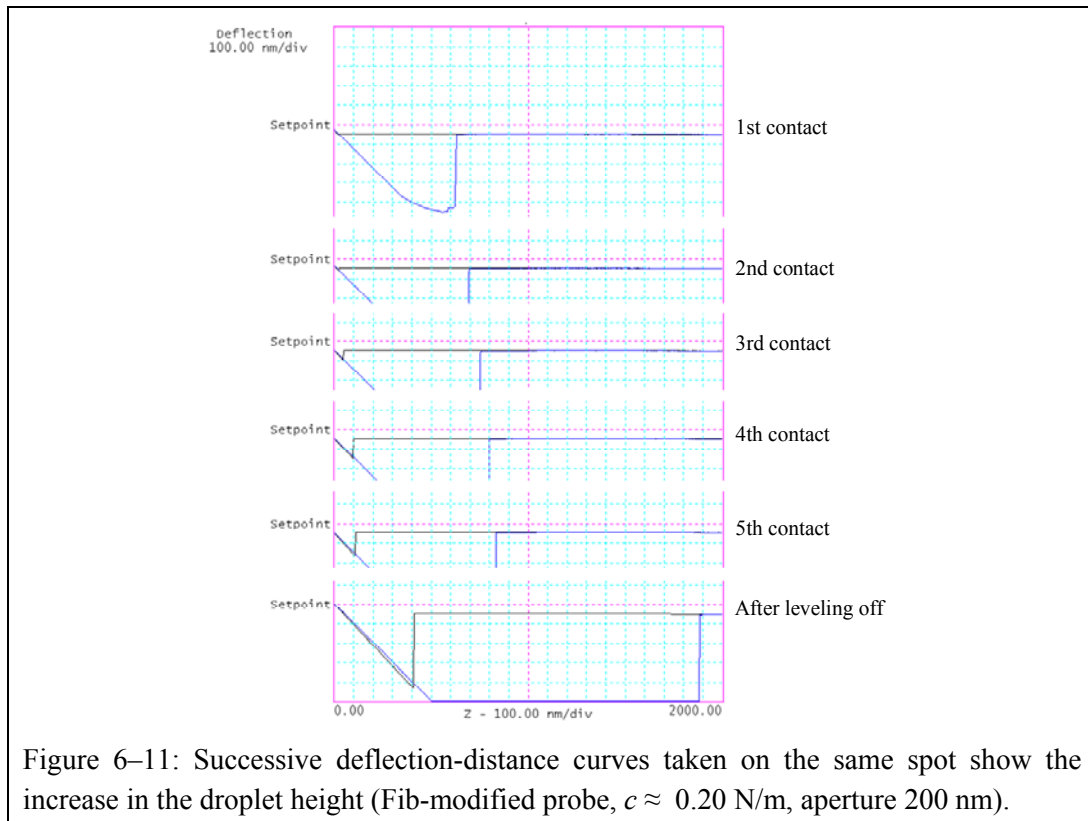


Figure 6–11: Successive deflection-distance curves taken on the same spot show the increase in the droplet height (Fib-modified probe, $c \approx 0.20$ N/m, aperture 200 nm).

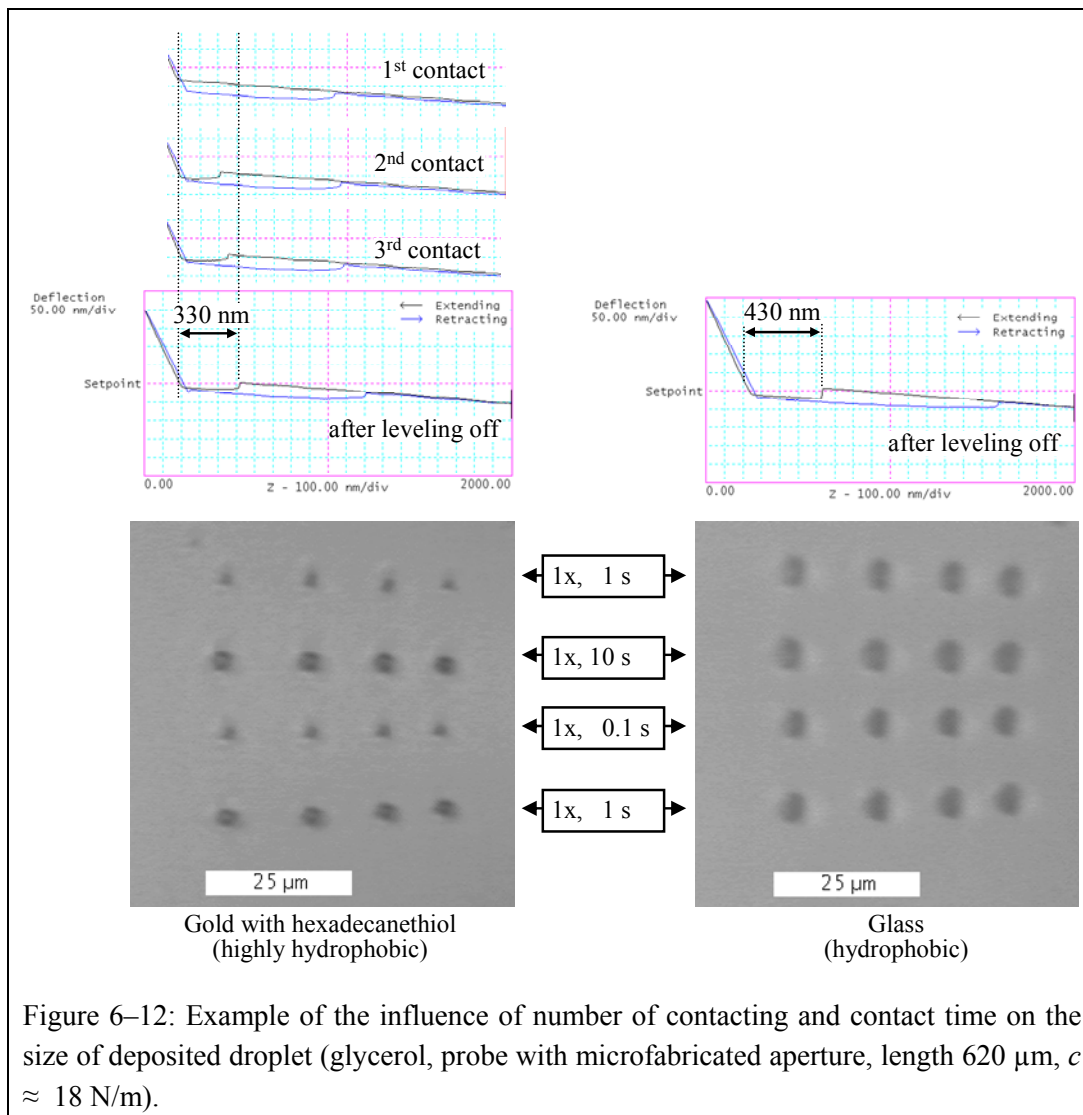
While on a hydrophilic substrate, the number of contacts or the contact time showed always an important influence, on a hydrophobic substrate, the influence was less reproducible.

Another experiment was performed using a FIB-modified probe (double-side gold coated, $c \approx 0.20$ N/m, aperture 200 nm) on a hydrophobic surface (silicon dioxide, washed with acetone and ethanol in ultrasonic bath) with anhydrous glycerol. The following droplet height was measured:

- Second contact: droplet height: 110 ± 5 nm.
- Third contact: droplet height: 117 ± 5 nm.
- After leveling off: droplet height: 111 ± 5 nm

In this experiment, the height of the droplets did not change significantly between the first deposition and with multiple contacts.

Nevertheless, on a hydrophobic substrate, it was not always the case that the final drop height was reached already after the first contact. Two examples are given in Figure 6–12, where a probe with microfabricated aperture was used on two different substrates, a gold surface covered by hexadecanethiol (highly hydrophobic) and glass (hydrophobic). On the hydrophobic gold surface, the droplet height after the first contact was 240 ± 5 nm, and after the leveling off of the droplet height, it was measured to be 330 ± 5 nm. For comparison, the droplet height after leveling off on the glass was measured to be 430 ± 5 nm. Furthermore, both substrates showed an influence on the droplet diameters with different contact times, as can be shown in the optical micrographs in Figure 6–12. The different contact times for each droplet lines are given in the figure. The first and the last lines had the same contact time (1 second) in order to get an idea about the evaporation that occurs between the deposition of the first dot and the last one. A difference (due to evaporation) in the first and last line on the highly hydrophobic substrate is well visible.



These examples show that, from one experiment to the other, the different parameters have not always the same importance on the volume of the deposited droplet.

6.2.4. Withdrawal speed

The speed of the withdrawal of the probe can also influence the amount of transferred liquid. When a difference is observed, a decrease of the withdrawal-speed implies an increase of the volume of the remaining droplet. However, the influence of the withdrawal speed was usually smaller than the influence of the contact time or the number of contacts.

Depending on the speed of the withdrawal one can consider two borderline cases. First, if the withdrawal is infinitely slow, the liquid meniscus between the tip and the substrate is continuously in hydrostatic equilibrium during the withdrawal, because the liquid has time to flow through the aperture to compensate any variation in the Laplace pressure (pressure controlled meniscus, see section 2.3.4.3). Secondly, if the withdrawal is infinitely fast, no liquid will flow through the aperture because of the viscosity of the liquid, and the liquid volume of the meniscus remains constant from the start of the withdrawal until the rupture of the meniscus (volume controlled meniscus).

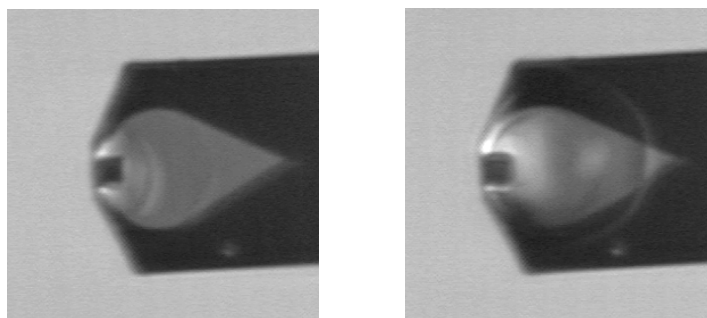
The withdrawal speed corresponds to the speed of the probe. However, the speed of the tip during the withdrawal can be significantly different, due to the bending of the cantilever. E.g., for the softer

cantilever (FIB-modified), while the probe is withdrawn, the jump-off of the tip from the substrate and the jump-off due to the rupture of the meniscus occur often quite simultaneously. The withdrawal speed of the tip is much higher than that of the probe. Thus, for the softer probes, a lower withdrawal speed induces only a longer contacting time followed by an almost simultaneous release of the tip from the substrate and from the droplet.

6.2.5. Laplace pressure

The flow of liquid through the tip aperture is driven by a gradient of pressure (Laplace pressure) inside the liquid. The gradient of pressure arises because of a different mean curvature of the liquid-air interface at the meniscus and over the loading area. Thus, the amount of loaded liquid and its curvature will also influence both the flow through the aperture and the final shape of the meniscus once the hydrostatic equilibrium reached.

In Table 6–2 an example is given where the same probe on a silicon dioxide sample (washed with acetone and ethanol in ultrasonic bath), but with different amount of loaded liquid (and thus different Laplace pressure) gives different height for the respective deposited droplets.



	Droplet height	Droplet height
Second contact	45±5 nm	120±5 nm
Third contact	55±5 nm	150±5 nm
After leveling off	80±5 nm	220±5 nm

Table 6–2: The Laplace pressure resulting from the liquid on the loading area will influence the amount of transferred liquid (TetraEG, probe was single-side gold coated, aperture 200 nm).

To conclude the discussion about some of the parameters influencing the amount of transferred liquid, it is evident that each discussed parameter has a distinct effect on the droplet volume. However, even if it is possible to control some of the parameters and to influence qualitatively on the volume of the droplet, a quantitative control of the volume of the first deposited droplet is more challenging.

6.3. Capillary force measurements and meniscus shapes

The stiffer cantilevers with the microfabricated apertures (2nd generation) were more suitable to extract correct capillary forces from the force-separation curves.

With the FIB-modified probes, which are softer, the optimal conditions (tip released from the surface, cantilever still bent by the capillary force) were not always present. The release of the tip from the substrate often occurred simultaneously to the breaking of the meniscus. In such conditions, the maximal force before the tip release corresponds to the sum of the capillary force and adhesion force (between tip and sample surface). Isolating the pure capillary force from the total force necessitates knowing the strength of the adhesion force. However, the measurements of adhesion forces performed with an unloaded probe gave irreproducible results, and furthermore the adhesion force measured with an unloaded probe cannot be compared with the adhesion force of a loaded probe because of the presence of the deposited liquid around the tip-sample contact point (see section 2.2.3.1).

The numerical construction of a meniscus meridian involves the following parameters (see also equation (2-45), $F_{cap} = f(\gamma_L, x, \alpha, \kappa)$):

- the capillary force,
- the surface tension of the liquid,
- the wetted diameter on the sample,
- the contact angle, and
- the mean curvature of the liquid surface.

Because the gravity is negligible at the scale of the constructed meniscus, the density of the liquid does not influence the shapes of the meniscus. Four of those parameters can be freely chosen, whereas the fifth is dependent on the four others.

Figure 6–13 shows the numerically constructed meridians of different possible axisymmetric menisci in order to show the influence on the meniscus shape of different capillary forces F , surface tensions γ_L , contact angles θ , and diameter d of the size of the deposit on the sample surface. The dependent parameter to construct all those menisci was the mean curvature of the liquid-air interface κ . The black line, which schematically represents the tip, serves as a guide for the eyes. The sample surface is represented by the horizontal line crossing the abscissa at zero.

Figure 6–14 shows the values for the independent parameters F , γ_L , d , and θ used for the numerical construction of each meniscus. The values of the corresponding mean curvatures κ and of the mean radius of curvature $R_\kappa = 1/\kappa$ are also given in the figure. A negative mean curvature implies a negative Laplace pressure (relative to the atmospheric pressure) inside the meniscus.

The shown menisci, even if they are theoretically in hydrostatic equilibrium, are not necessarily stable. It is not easy to know which of the menisci are stable and which not. As mentioned in section 2.3.4.3, a meniscus with two extreme points (neck or bulge) is unstable. But such menisci were practically never encountered when fitting a meniscus profile to real initial parameters.

The goal is now to vary the four initial parameters F , γ_L , d , and θ in order to fit a meniscus meridian to an experimentally determined capillary force F and the corresponding tip-sample separation. The condition is that the numerically constructed meridian has to touch the tip. Some other conditions can be used to decrease the range of possible solutions.

Firstly, the surface tension of the liquid and the substrate surface wettability are usually known.

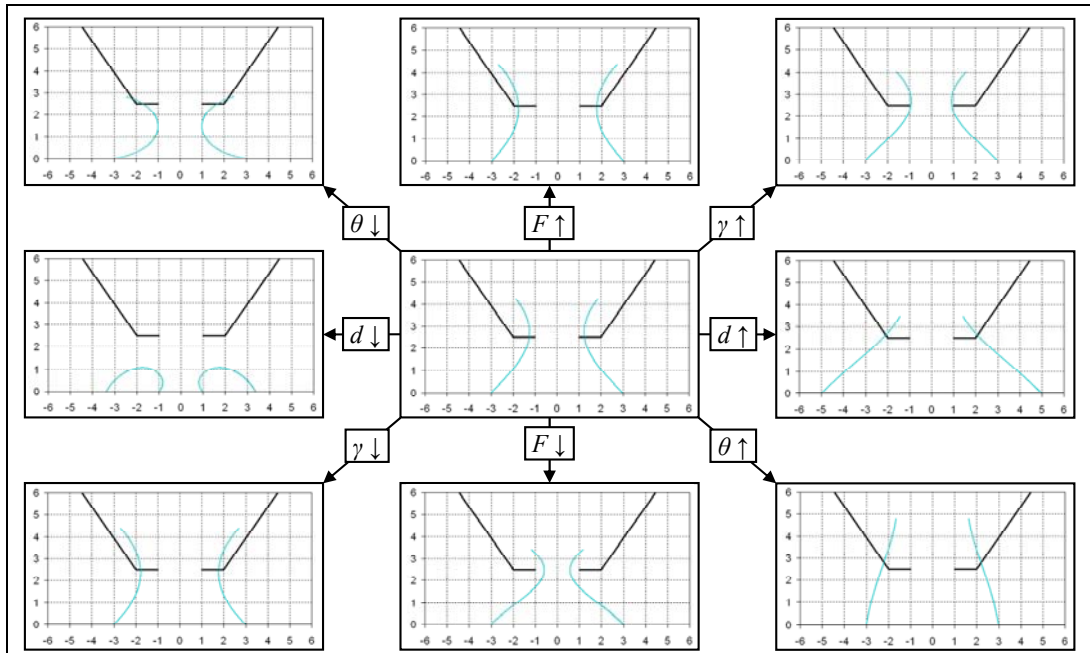


Figure 6–13: Different numerically constructed meniscus meridians which show the influence of the different parameters on the meniscus shape. The values used for each meniscus construction (F , γ_L , d , θ) are given in Figure 6–14. The graph unit is micron.

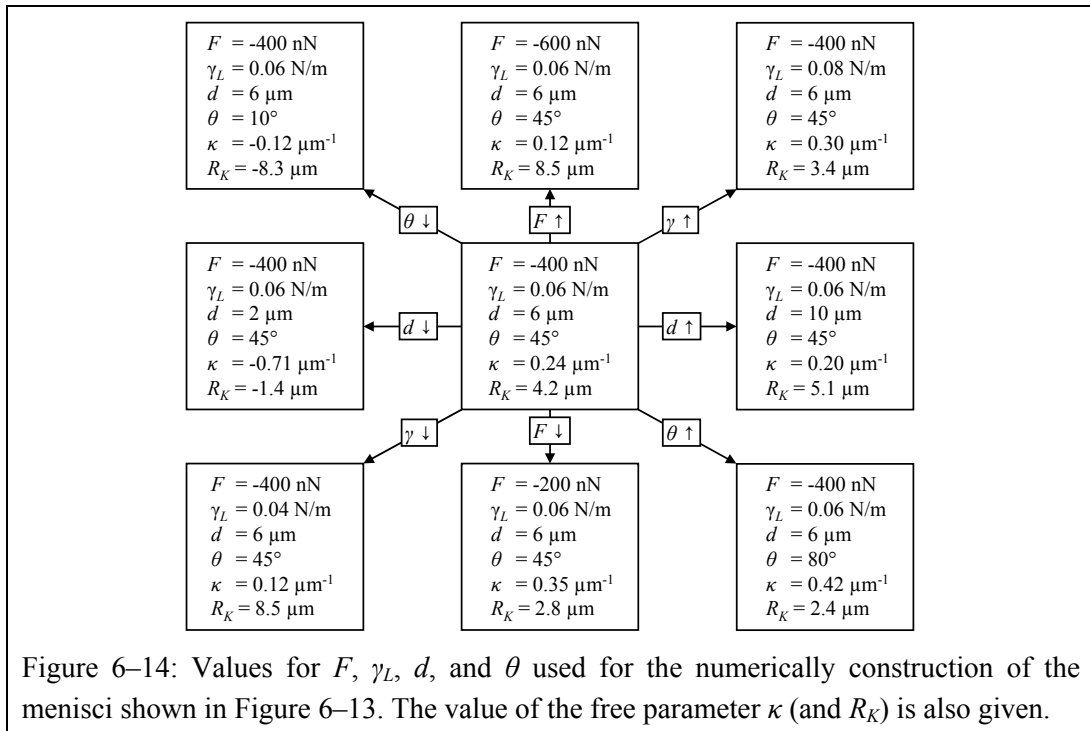


Figure 6–14: Values for F , γ_L , d , and θ used for the numerically construction of the menisci shown in Figure 6–13. The value of the free parameter κ (and R_K) is also given.

Secondly, by choosing the capillary force and the corresponding tip-sample separation near the jump-off induced by the break of the meniscus, one can assume that the stretched meniscus should present a shape that seems to approach instability (e.g. when possessing a neck), and that the meridian crosses the tip at its extremity (at the diameter represented by the tip aperture or at the flat area surrounding the aperture, but not at the flanks of the tip).

Thirdly, if additionally, the diameter of the droplet deposited during the deflection-distance curve acquisition is known, one can assume that the diameter d of the size of the deposit on the sample surface is equal to the droplet diameter.

Fourthly, the height of the deposited droplet provides further information, which together with the diameter allows the determination of the droplet volume. One can now compare the volume of the droplet with the volume of the numerically constructed meniscus, taken from the sample surface until the constriction at the neck. If one assumes that the meniscus breaks at the neck, the two volumes have to be identical.

Fifthly, the mean curvature κ of the meniscus cannot be larger than the mean curvature of the loaded liquid.

6.3.1. Example of a meniscus shape with a probe having a microfabricated aperture

An example of numerically constructed meridian of a meniscus between a substrate and a probe with a microfabricated aperture is shown in Figure 6–15. The meniscus was constructed to have a capillary force of 400 nN, which corresponds to the red mark in the curve A. The deposited droplet (TetraEG, diameter 10 μm , height 900 nm), which is represented by the dotted blue line in the graph B, has the same volume (~ 36 fl) as the part of meniscus lying between its neck and the sample surface (cross-hatched area in graph B).

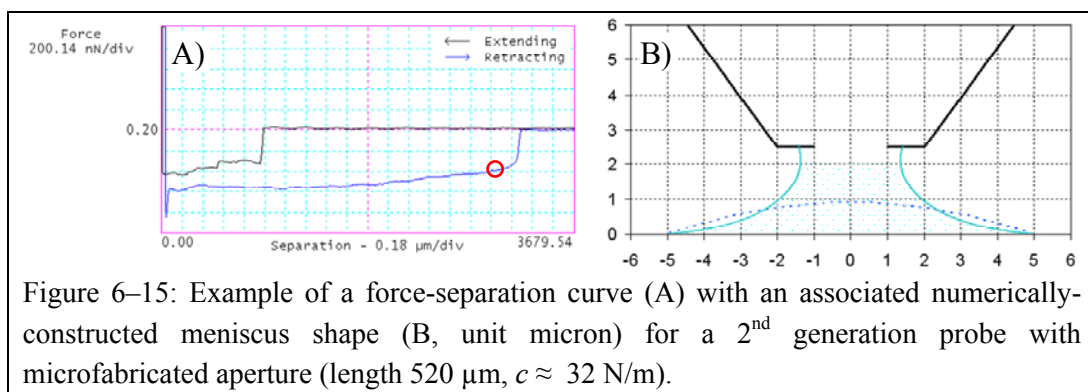


Figure 6–15: Example of a force-separation curve (A) with an associated numerically-constructed meniscus shape (B, unit micron) for a 2nd generation probe with microfabricated aperture (length 520 μm , $c \approx 32$ N/m).

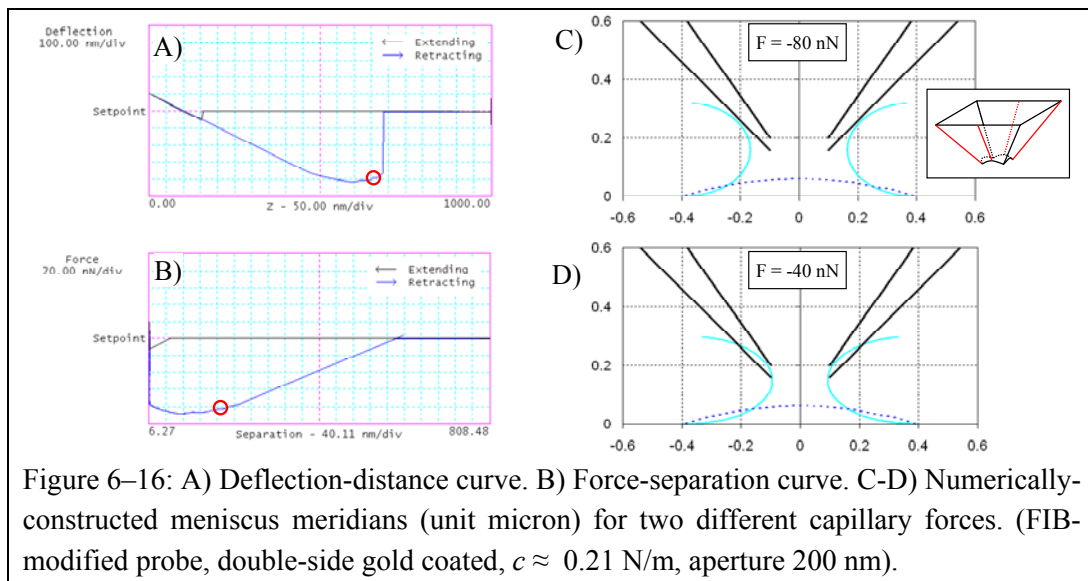
The mean curvature associated with the fitted meniscus is negative ($-0.088 \mu\text{m}^{-1}$), which indicates a negative Laplace pressure (with respect to the atmospheric pressure) inside the stretched meniscus. A negative Laplace pressure implies that during the withdrawal of the probe (withdrawal speed: 8 $\mu\text{m/s}$), the liquid forming the stretched meniscus was not in hydrodynamic equilibrium with the liquid on the loading area (in the loading area a positive Laplace pressure prevails due to the shape of the loaded liquid). The gradient of pressure inside the liquid is probably at its highest in the vicinity of the aperture, where the resistance against the flow of liquid is the highest due to the small cross-section.

The difference in the contact angles between the sessile droplet and the stretched meniscus can be explained by the hysteresis of the contact angle. If during the tip withdrawal, the contact angle gets smaller than the receding contact angle, the triple-phase line will start to move to decrease the wetted area on the surface. After the break of the meniscus, the droplet will take its final shape, which can be larger than the wetted area directly before the break of the meniscus.

6.3.2. Example of a meniscus shape with a FIB-modified probe

For the FIB-modified probes, not every force-separation curve allowed the determination of a capillary force. However, when a capillary force could be determined, was the typical strength of the forces (about 50 to 250 nN) was smaller than those observed for probes with microfabricated apertures (about 300 to 700 nN). This can be explained by the smaller size of the meniscus (see equation (2-45) for the calculation of the capillary force). For the FIB-modified probe, the fitting of a meridian of meniscus that corresponds to the measured capillary force was almost never successful, because the numerically constructed meridian did not cross the extremity of the tip.

An example is shown in Figure 6–16. The deposited liquid was anhydrous glycerol and the substrate, freshly cleaved mica. The red marks in the figures (A) and (B) correspond to a capillary force of 80 nN, at a tip-surface separation of 160 nm. The black lines in the pictures (C) and (D) represent the FIB-modified tip. The two steeper oblique lines correspond to two opposite faces of the pyramidal tip, and the oblique lines at 45° to two opposite edges (see the four red lines in the inset of C). The deposited droplet height was measured at 60 nm (which corresponds to the dotted blue line in (C) and (D)). It was not possible to find a numerical solution of a meniscus meridian that respects the measured capillary force and a crossing of the meridian at the perimeter of the tip aperture (C). But if we could reduce the capillary force from 80 nN to 40 nN, a solution could be found (D). The reason of the discrepancy could partly lie in the inaccuracy of the spring constant of the cantilever.



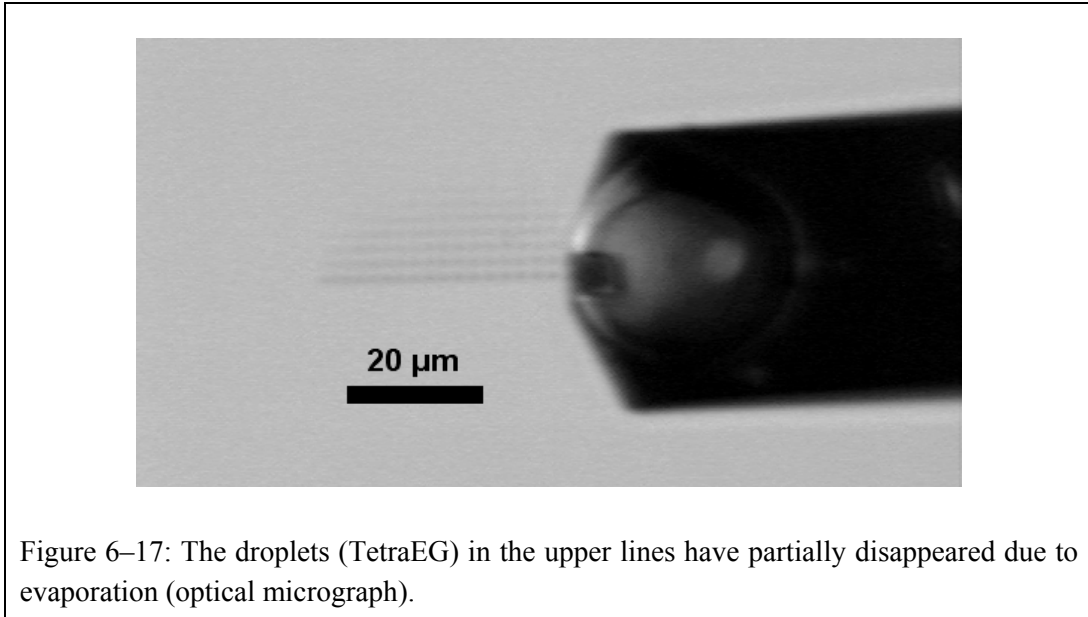
The reasons that explain the better fit of a numerical meridian to a larger meniscus are not clear. Apart from the spring constant, another possible reason can be that the shape of the FIB modified tip is not axisymmetric, but has a pyramidal shape with a quadratic-base. Another reason could be that the aperture is not milled perfectly at the center of the tip apex, which would also break the symmetry of the meniscus. But the numerical construction of a meniscus meridian relies on such an axisymmetry.

One can mention that, although if theoretically it is possible to have a repulsive capillary force (see section 2.3.5.3), such a situation has never been encountered during all experiments. Each time deflection-distance measurements were performed, the deflection showed always a lower value at the left from the snap-in or pull-off positions, indicating thus an attractive capillary force.

6.4. Evaporation of the droplets and residual dots

6.4.1. Evaporation time

Once the droplet is deposited on the sample surface by the dispenser, it will not remain unchanged but will start to evaporate. Large droplets remain on the surface for several minutes, whereas the smaller ones start to disappear even during the deposition. An example is given in Figure 6–17, where an optical micrograph was taken during the dispensing process.



It can be useful to evaluate the time that is needed to reach a full evaporation of the deposited droplet. The evaporation rate r for glycerol, anhydrous glycerol and TetraEG was measured to be in the order of magnitude of $0.04 \text{ fl/min}/\mu\text{m}^2$ (see section 5.4.1.3a).

One can consider two borderline cases for the evaporation of a sessile droplet. Firstly, the triple-phase contact line remains pinned until the full evaporation of the droplet, i.e. the droplet diameter remains constant. Secondly, the contact angle remains constant during the evaporation, whereas the diameter decreases. It is obvious that in the second case, the surface where evaporation occurs is smaller than in the first case. Thus, by assuming that the evaporation rate r is identically in both cases, the first case (constant diameter) leads to a lower limit for the evaporation time ($t_{evap,min}$) whereas the second case (constant contact angle) leads to an upper limit for the evaporation time ($t_{evap,max}$). The second case is an upper limit because in reality, the volume will first decrease without reduction of the droplet diameter until the receding contact angle is attained, leading to a higher surface-to-volume ratio. The two evaporation times $t_{evap,min}$ and $t_{evap,max}$ are derived in Annex 4.

The first column of Table 6–3 shows the dependency of $t_{evap,min}$. The lower limit of the evaporation time $t_{evap,min}$ depends only on the droplet height. Assuming an evaporation rate of $0.04 \text{ fl/min}/\mu\text{m}^2$, the droplet height decreases by 1.3 nm per second.

The second and third column in Table 6–3 are two borderline cases for $t_{evap,max}$, i.e. when $\theta = 90^\circ$ and $\theta \rightarrow 0^\circ$. In such cases, $t_{evap,max}$ is independent of the droplet diameter (also derived in Annex 4).

Assuming an evaporation rate of $0.04 \text{ fl/min}/\mu\text{m}^2$, the droplet height decreases theoretically between 0.44 and 0.67 nm per second.

The decrease in height of the droplets is thus approximately 1 nm/s.




Constant diameter	Constant contact angle	
	$\theta = 90^\circ$	$\theta \rightarrow 0^\circ$
		
$t_{evap,min} = \frac{1}{2} \frac{h}{r}$	$t_{evap,max} = \frac{h}{r}$	$t_{evap,max} = \frac{3}{2} \frac{h}{r}$
$\frac{dh}{dt} = -1.3 \text{ nm/s}$	$\frac{dh}{dt} = -0.67 \text{ nm/s}$	$\frac{dh}{dt} = -0.44 \text{ nm/s}$

Table 6–3: The different kinds of evaporation with their evaporation times (see Annex 4), and calculated time-dependency for the droplet height with $r = 0.04 \text{ fl/min}/\mu\text{m}^2$.

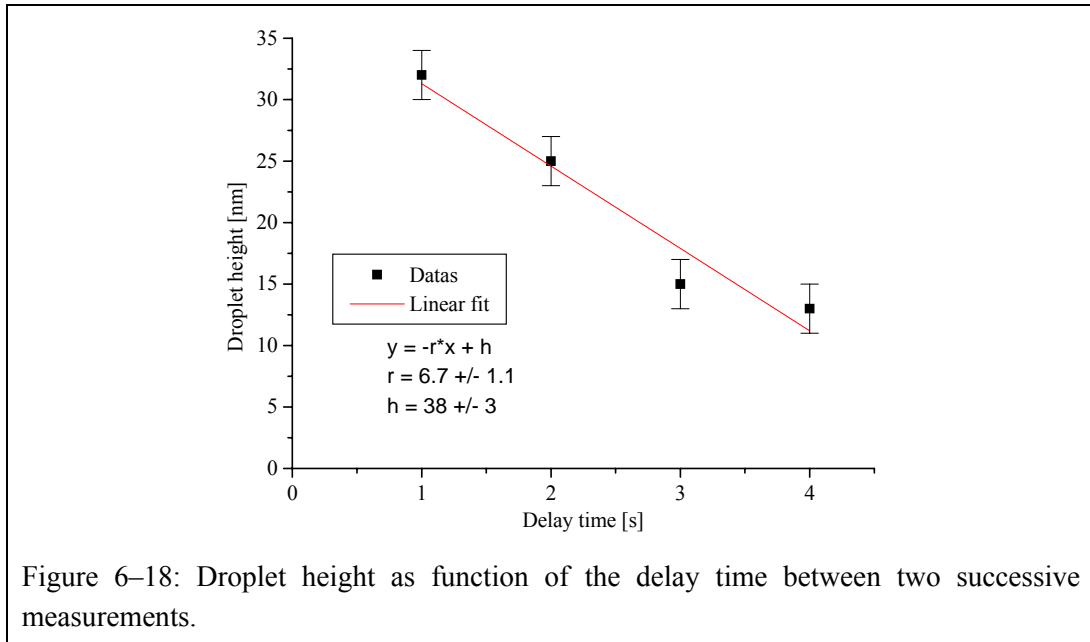
Droplet diameter $d [\mu\text{m}]$	Droplet height $h [\mu\text{m}]$	Droplet volume $V [\text{fl}]$	Evaporation time	
			$t_{evap,min} [\text{min}]$	$t_{evap,max} [\text{min}]$
20	1	160	13	37
5	0.3	3.0	3.8	11
1.5	0.15	0.13	1.9	5.5
0.5	0.07	0.007	0.9	2.5

Table 6–4: Calculated evaporation time for different droplet sizes ($r = 0.04 \text{ fl/min}/\mu\text{m}^2$).

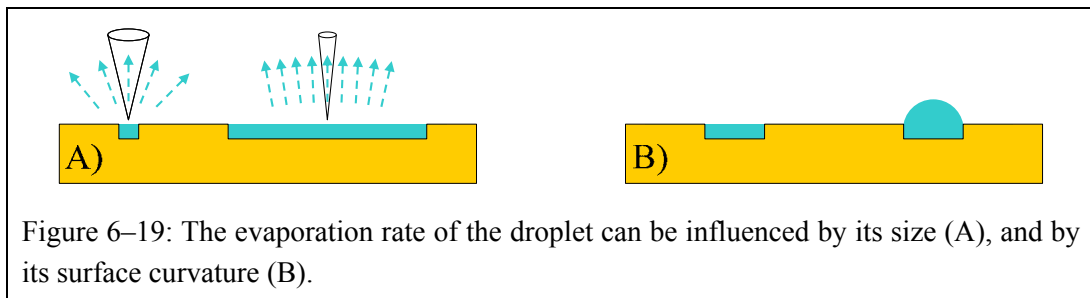
In Table 6–4 are given some calculated evaporation time for different droplet sizes. Similar values could be measured during the experiments. These values, from about one minute to a few tens of minutes, seem to be large, considering the small sizes of the droplets, but for the nanoscale dispensing method presented here, one has to intentionally chose to use liquids with extremely low evaporation rates.

These values can be compared with the evaporation of the droplets shown in Figure 6–17. The time needed to write one line of droplets was about 10 seconds. The droplet height was measured to be 130 nm, which corresponds approximately to an evaporation time of 130 seconds (for $dh/dt \approx 1 \text{ nm/s}$). In 130 seconds, about 13 lines of dots can be deposited. In Figure 6–17, about 7 lines are recognizable, twice less than expected. However, the next example will give a possible explanation.

In another experiment, droplet heights were measured using deflection-distance curves with different time delays between two successive ramps in z-direction. The time delays were applied as the z-scanner was retracted, to permit the droplet to evaporate. The curves were acquired after the leveling off of the droplet height (no change in the curve while continuously ramping the z-scanner). The sample surface was silicon dioxide cleaned with piranha, the liquid was anhydrous glycerol. Since the sample surface was highly hydrophilic, the droplet heights were small. After the experiment, no deposited droplet was optically observable. The results as well as the linear fit are shown in Figure 6–18.



The decrease in the droplet height was 6.7 nm/s, which is higher than the expected values from Table 6–3 (from 0.44 to 1.3 nm/s). This discrepancy can have two reasons. Firstly, the evaporation rate r was experimentally determined on the large drops loaded on the cantilever. Those drops have diameters of about 30 μm , which is much larger than the typical size of droplets deposited by a FIB-modified probe (about 1 μm). Furthermore, the solid angle per surface unit accessible for a molecule to evaporate is higher for a small droplet than for a large drop (see Figure 6–19 A), and an evaporated molecule can move easier from the liquid surface. Thus a lower relative vapor pressure will prevail over the smaller droplet, and the evaporation will be faster^{a)}. A small droplet will be subject to a higher evaporation rate than a large drop. An illustration of this phenomenon can be seen in Figure 6–17, where the droplets located at the periphery of the square-shaped array disappear faster than those in the center of the array.



Secondly, the smaller droplet has usually a higher mean surface curvature κ than the larger drop. From Kelvin’s equation (2-46) the ratio can be obtained of the relative vapor pressure P_{κ}^{rel} “felt” by a curved liquid surface to the usually defined relative vapor pressure P_0^{rel} (with respect to a flat liquid surface):

^{a)} The effective evaporation rate is given by the absolute evaporation rate minus the rate of adsorption. A change in relative vapor pressure will affect the adsorption rate, and thus the effective evaporation rate.

$$\frac{P_{\kappa}^{rel}}{P_0^{rel}} = \frac{P/P_{\kappa}^{sat}}{P/P_0^{sat}} = \frac{1}{\exp\left(\frac{V_m \cdot \gamma_L}{R \cdot T} \cdot \kappa\right)} \quad (6-1)$$

An increase in the mean curvature κ of the liquid surface will therefore induce a decrease of the relative vapor pressure P_{κ}^{rel} , as shown in Figure 6–20. And a lower relative vapor pressure induces a higher evaporation rate. A droplet with a higher surface curvature, which is usually the case for small droplets, will therefore evaporate faster.

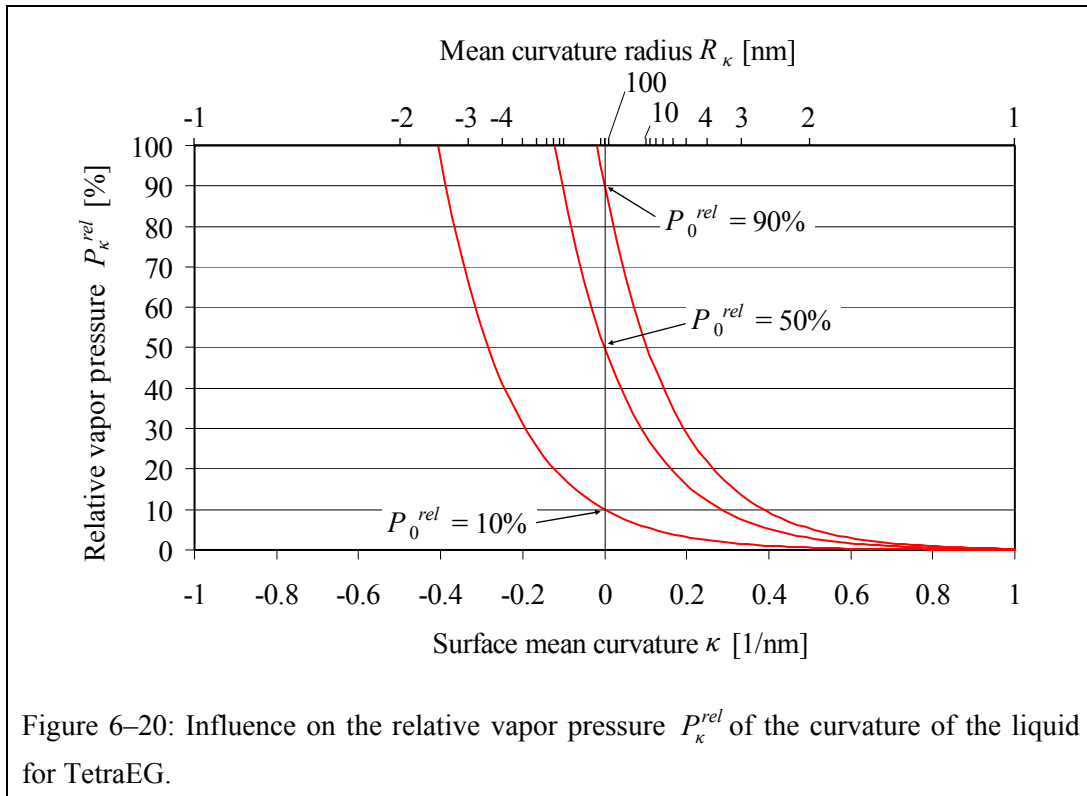


Figure 6–20: Influence on the relative vapor pressure P_{κ}^{rel} of the curvature of the liquid for TetraEG.

The height of droplets measured with deflection-distance curves will need a correction, in order to compensate the evaporation of the droplet during the two successive extending-retracting ramps of the z-scanner. Usually, the deflection-distance curves are acquired with a scan rate (in z-direction) of 1 Hz and without any other time delays. Thus, between the droplet deposition and the height measurement, there is a time delay of 1 second. The measured droplet height should therefore be corrected by an addition of ~ 7 nm.

In section 5.5.1.1 a method to estimate the droplet diameter was given. The method relies on the merging of the droplet into the meniscus when another deposition occurs at a distance smaller than the droplet diameter. A mandatory condition is that the deposited droplet does not evaporate before the next deposition occurs. It was shown that the decrease in height of a droplet was about 7 nm/s, because of evaporation. In the experiments presented here, the displacement time to move the tip from one spot to the next while creating an array is usually less than 1 second. The heights of deposited droplets were usually much larger than 10 nm. Thus, a merging of the droplets can occur, as expected.

6.4.2. Residual dots after the evaporation

The liquids used to be deposited were not 100% pure. There is usually some impurity in the liquid, even if the concentration of the contaminant is a fraction of a percent. E.g., for anhydrous glycerol, according to the provider, the purity is better than 99.5% and for TetraEG better than 99%. The impurities present in the liquid can for instance be non-volatile. Thus, after the evaporation of the liquid, such impurities would remain on the surface.

According to some common observations of the rings formed by dried coffee drops at the bottom of a cup, the perimeter of the stains look darker, indicating that the concentration of residue is higher at their border. This is because along a triple-phase contact line that is pinned^{a)} the evaporation is higher than for the rest of the drop. The reason is that at the contact line, the solid angle accessible for a molecule to evaporate is higher as over the drop. Thus, a net flow of liquid from the center of the drop towards its perimeter takes place, carrying the residues to the contact line where they get concentrated [88].

One could think that after the evaporation of the liquid deposited by the nanodispenser, similar rings although smaller should remain on the surface. However, the water of a coffee drop evaporates much faster as the liquids used with the nanodispenser. Thus, in a glycerol or TetraEG droplet, the flow toward the border is much weaker and the concentration at the perimeter should be less important.

Optically, the remaining impurities were not visible, even if the prior droplet was well recognizable. But topographic AFM micrographs revealed the remaining impurities. Some examples are given below.

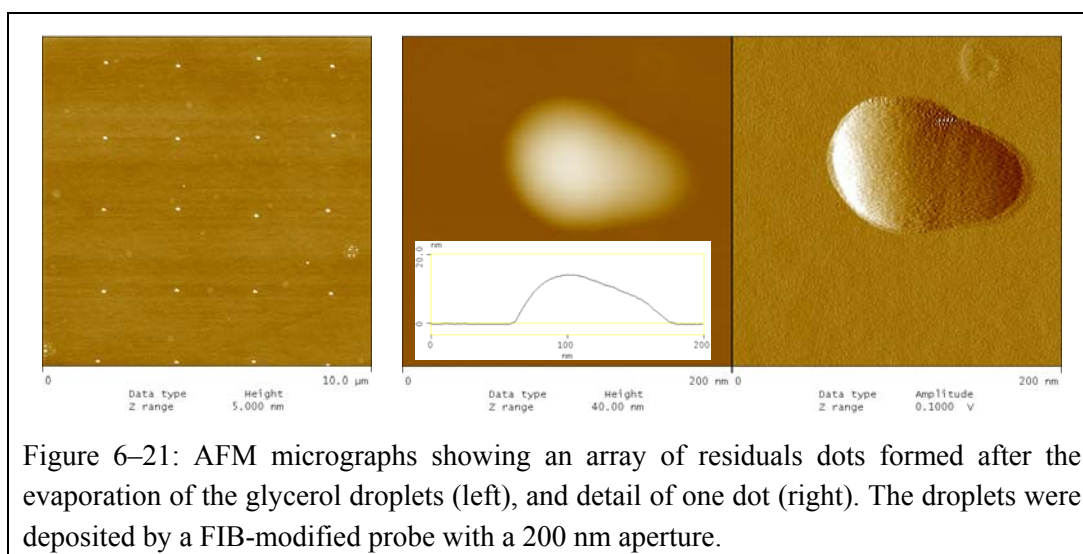


Figure 6–21: AFM micrographs showing an array of residuals dots formed after the evaporation of the glycerol droplets (left), and detail of one dot (right). The droplets were deposited by a FIB-modified probe with a 200 nm aperture.

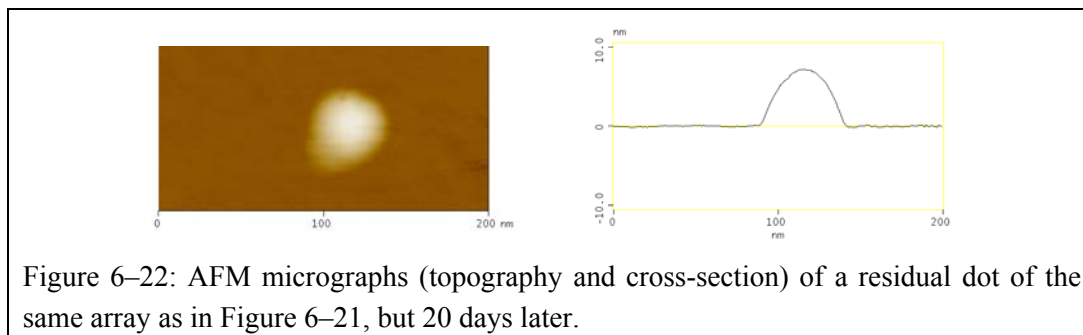
To form the residual dots^{b)} shown in Figure 6–21, glycerol droplets were deposited on a hydrophobic silicon dioxide surface (cleaned only with acetone, ethanol and Millipore water in ultrasonic bath) by a FIB-modified probe. The height of the initially deposited droplets was 80 ± 4 nm. During the deposition, the droplets could not be detected optically. If one assumes a contact angle of

^{a)} During the evaporation of a drop, the triple-phase contact line remains pinned until the receding contact angle is reached.

^{b)} To avoid any confusions, the term “droplet” will be exclusively used for the deposited liquid droplets, whereas the term “dot” will be used to describe the residual dot remaining on the substrate after the evaporation of a liquid droplet.

30°, a droplet volume of 10 μl (and a diameter of ~ 600 nm) could be estimated. The residual dots measure 85 nm in diameter and 14 nm in height, leading to a volume of about 0.04 μl , which is 250 times smaller than the volume of the liquid droplets.

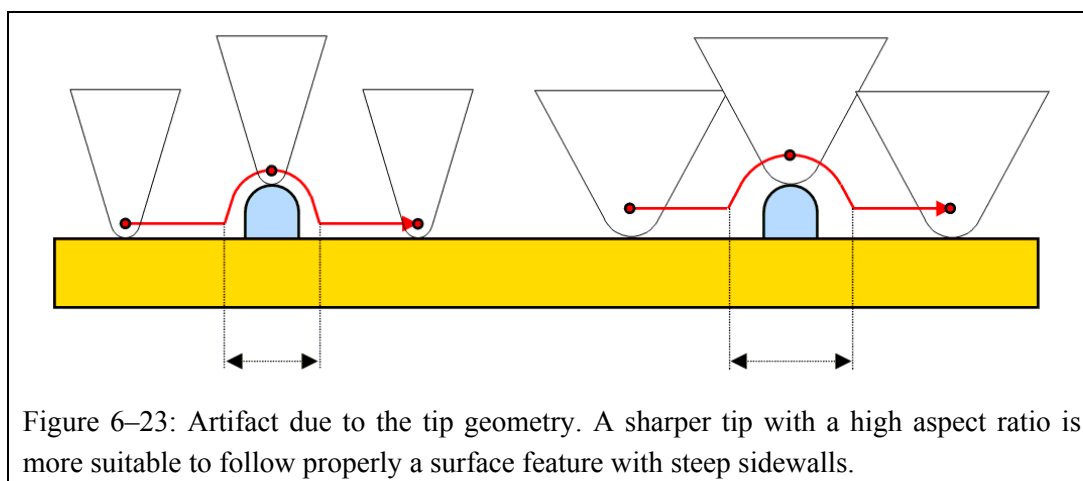
It should be noted that the array of residual dots shown in Figure 6–21 was acquired directly after the droplet dispensing (about 10 minutes later, the time needed to change the AFM tip). The same array of dots was again investigated 20 days later, after storage of the sample in ambient environment. The detail of one of those residual dots is shown in Figure 6–22.



The 20 days older dot has further decreased in size. The dimensions of the dot are 50 nm in diameter and 7 nm in height, which corresponds to a volume of 0.007 μl . This is about three orders of magnitude smaller than the initial liquid droplet volume. The volume decrease of the residual dots over the 20 days shows that even if most of the solvent evaporate within minutes, they are still some other elements inside the dots that continue to evaporate, but on a longer time scale. Even if the composition of the residual dots is unknown, they are probably made of molecules with different molecular weights, and the lighter ones can still evaporate.

Sometimes it could be observed when an array of dried droplets was imaged by AFM, that the dots were not stiff. In contact mode, they were smeared out, and in tapping mode, the tip got stuck.

The decrease in the drop diameter could also be explained by a tip artifact, since a sharper tip with a high aspect ratio will measure a smaller diameter (see Figure 6–23). However, both micrographs were acquired with a same kind of tapping tip. According to the provider, the nominal tip radius value of the used tapping tips was 10 nm, which is much smaller than observed dot diameter. But even if the decrease in diameter of the dots could be explained by such an artifact, it could not explain the measured decrease in height.



To be sure that the dots results really from the residue of the deposited liquid, a control experiment was performed. The FIB-modified probe was stored overnight in Millipore water to remove the exceeding glycerol from the tip, and the same lithographic program was run on the same sample, but with the probe unloaded. Then, the same surface area was investigated by a conventional tapping mode AFM tip, and no features were found on the surface. Thus, this confirms that the residual dots originate from the liquid droplets, and are not due to the contact of the tip alone.

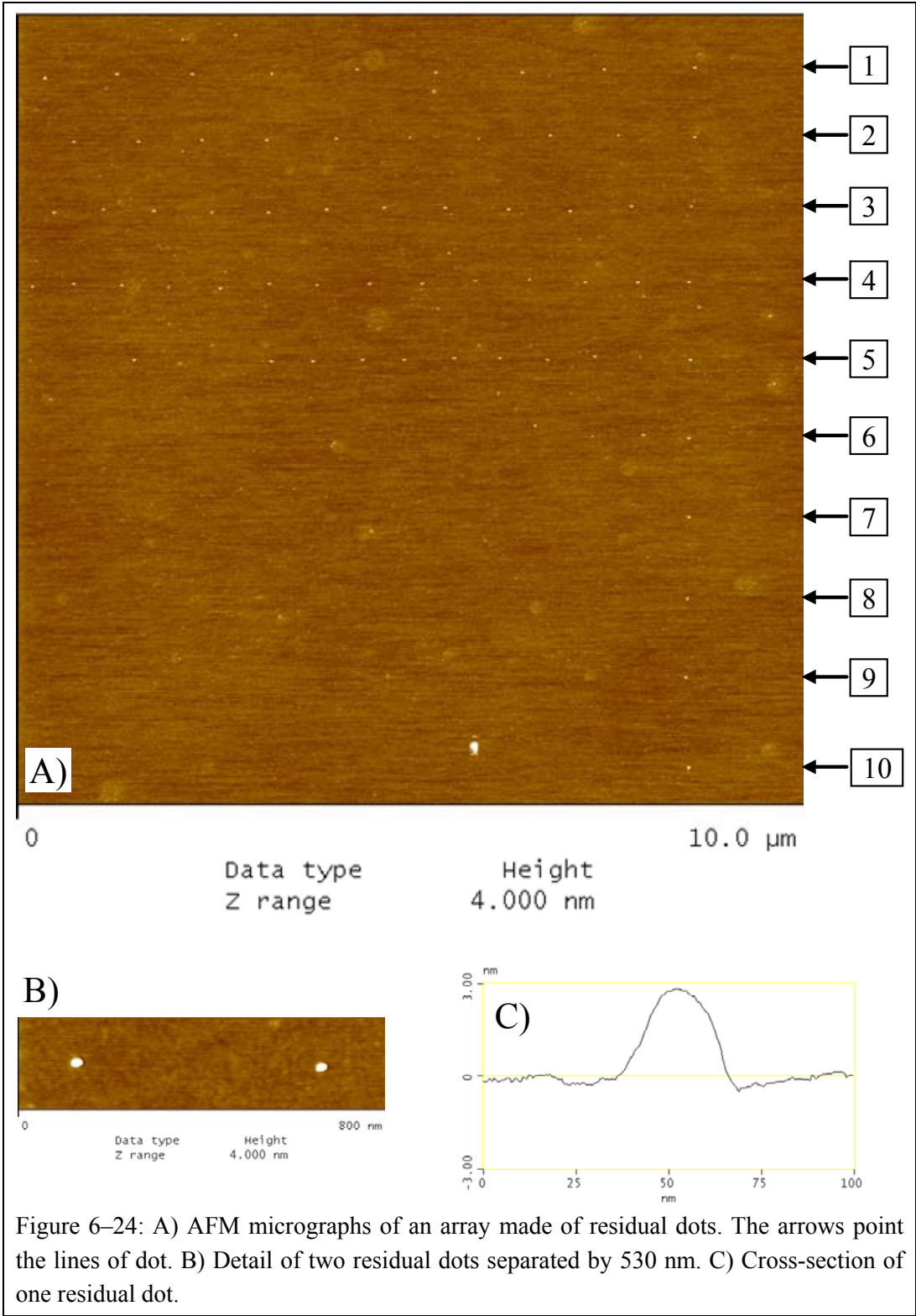


Figure 6–24: A) AFM micrographs of an array made of residual dots. The arrows point the lines of dot. B) Detail of two residual dots separated by 530 nm. C) Cross-section of one residual dot.

In another experiment, with the same FIB-modified probe and on the same sample surface, and also with glycerol, an array of droplets was dispensed, with a diminishing droplet spacing from line to line. The lithographic program drove the loaded probe in such a way to deposit 11 lines of droplets, with 11 droplets in the first line, 13 in the second line, 15 in the third and so forth, and with an identical total length for each line. The same area was then analyzed by tapping AFM the day after. The results are shown in Figure 6–24.

The residual dots are even smaller than in the prior examples. The residual dots have a diameter of about 30 nm and a height of 3 nm, corresponding to a volume of 0.001 al. In the micrograph (A), the arrows point to the first 10 lines of droplets deposited by the probe. In the first 5 lines, individual residual dots are visible. This means that in those lines, the deposited droplets were well separated. In the 6th line, only a few dots are visible, and from the line 7 and following lines, only one dot at the end of each line is visible. This indicates that during the deposition, the droplets have coalesced together, because the droplet diameter was smaller than the droplet spacing. In the 5th line (with 19 dots), the measured average dot spacing is 590 nm. Thus, in the 6th line (21 dots), the spacing should be about 530 nm ($590 \cdot 19 / 21$), and in the 7th line, 490 nm. Therefore, the liquid droplet diameter was between 490 and 590 nm. Prior to the deposition, the droplet height was measured to be 32 ± 5 nm (including the compensation due to evaporation during the measurement). The deposited amount of liquid was therefore less than 5 attoliters.

Specially the micrographs of Figure 6–24 point out the importance of a perfect flat and absolute clean sample surfaces. In a nanodispensing experiment that would be performed on a surface like that shown in Figure 5–3, the presence of the residual dots would be difficult to detect.

Note also that in the micrograph in the Figure 6–24 A, the scan size was 10 μm for an image resolution of 512 by 512 pixels (the maximum possible on those AFM's), which corresponds to a pixel size of 20 nm, about the size of one dot. Thus, increasing the scan size would result in a loss of recognizable dots. Therefore, it would be more difficult to find the location of the array on the substrate once the dispensing probe was changed for a tapping probe.

The shapes of the residual dots shown in the above micrographs are not the same as for the coffee rings in the cup, where the non-volatile residues are concentrated at the periphery of the dried drop. The explanation lies most probably in different evaporation rates. For droplets made of liquids with a low evaporation rates, the flow of the residues from the center to the border of the droplet is not strong enough to overcome the diffusion of the residues inside the droplet. Thus, the non-volatile elements remain dispersed in the liquid, get concentrated during the evaporation (and the decrease of the droplet diameter) and finally remain as a small dot on the substrate. However, the existence of dots with diameters smaller than the initial droplet diameters is only possible if the non-volatile residues do not adsorb onto the solid surface as soon the droplet is deposited, but remain in solution inside the liquid until the full evaporation of the solvent.

6.4.2.1. Position of the residual dot

By observing attentively the left micrograph in Figure 6–21, one notes that the dots are not perfectly aligned. Such misalignments cannot be explained by the hysteresis of the piezoelectric scanner. The probable reason is that during the drying of the droplet, the receding three-phase contact line can get pinned at some inhomogeneities present on the substrate. Thus, the final residual dot can be slightly off-center with respect to the initial position of the deposited droplet.

Another example is shown in Figure 6–25. On a silicon dioxide substrate, anhydrous glycerol droplets were deposited (probe with microfabricated aperture), and imaged by tapping mode AFM

after drying. Because the substrate was not perfectly clean, the areas that were wetted by the droplets are clearly visible, along with the residual dots.

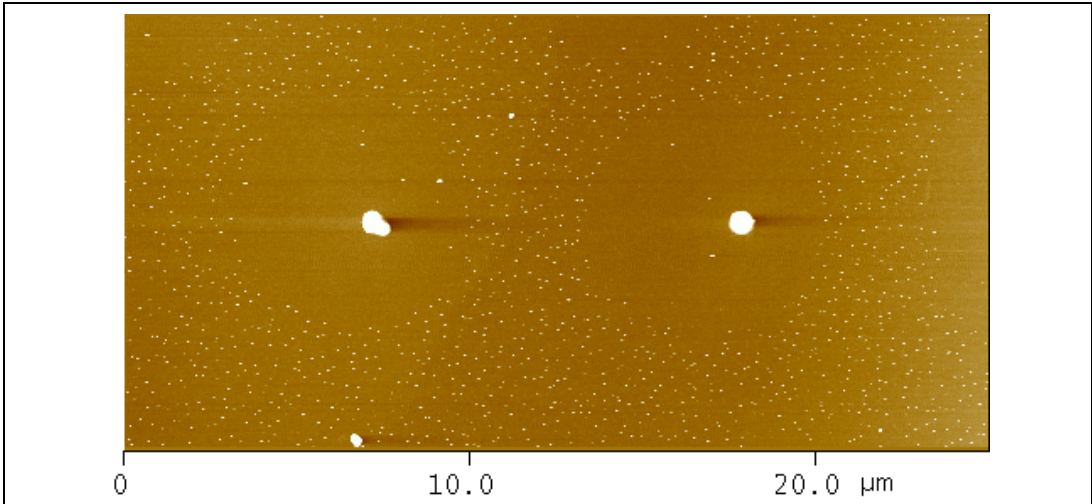


Figure 6–25: The position of the residual dot is not necessarily at the center of the droplet. (Topographic AFM micrograph, z-scale 10 nm)

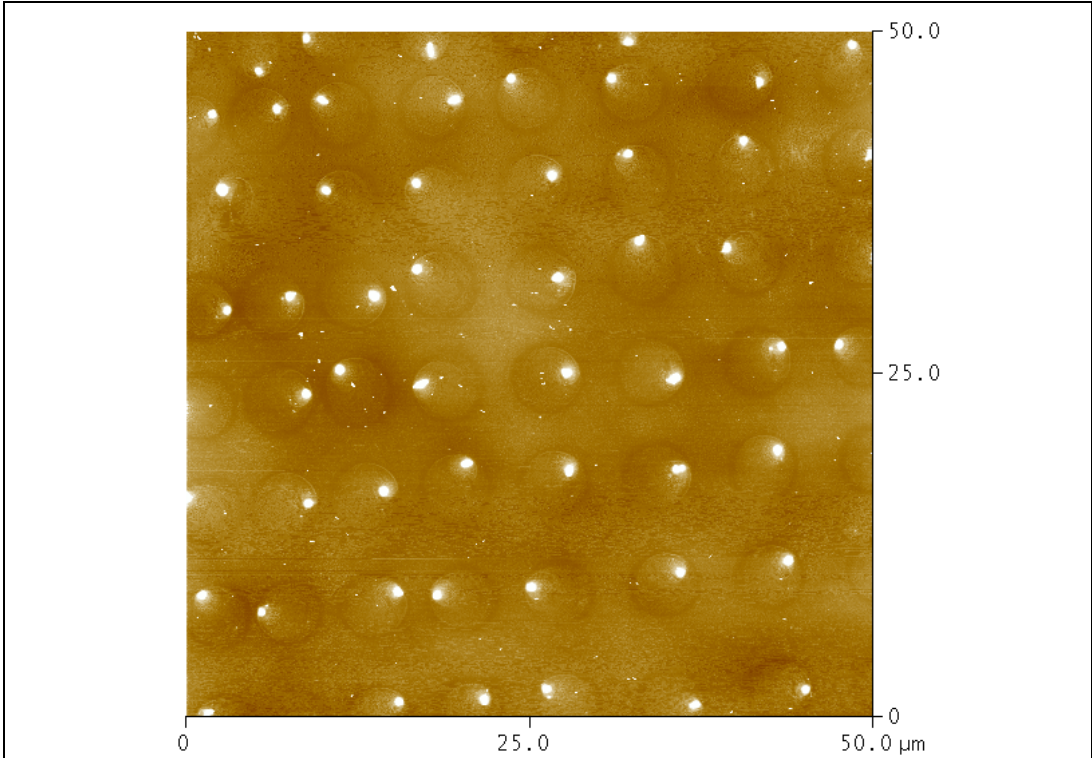


Figure 6–26: Residual dots on an unclean substrate (Topographic AFM micrograph, z-scale: 15 nm)

Figure 6–26 shows another example of residual dots which are not located in the middle of the deposited droplet (anhydrous glycerol on an unclean silicon dioxide substrate, deposited with a probe having a microfabricated aperture). The residual dots have a volume of about 6 pL, and the droplet volume was measured to be approximately 10 fL.

6.5. Deposition of molecules, and nanoparticles

The deposition of impure liquids by nanodispensing leads to residual dots after the evaporation of the droplets. In other words, the liquid has served as transport medium for the non-volatile elements present in the liquid. By voluntarily adding other specific element inside the liquid, the dispensing of the added species is possible. Fluorescent dye molecules and nanoparticles were used to demonstrate this technique.

6.5.1. Deposition of droplets with fluorescent molecules

In this first example, a 4 μM solution of Cy3 fluorescent dye (Amersham, [89]) in glycerol was dispensed on glass and led to the formation of an array of glycerol drops. The dispenser was a 2nd generation probe with microfabricated aperture. Prior to the droplet dispensing, the droplet height was measured to be about 450 nm.

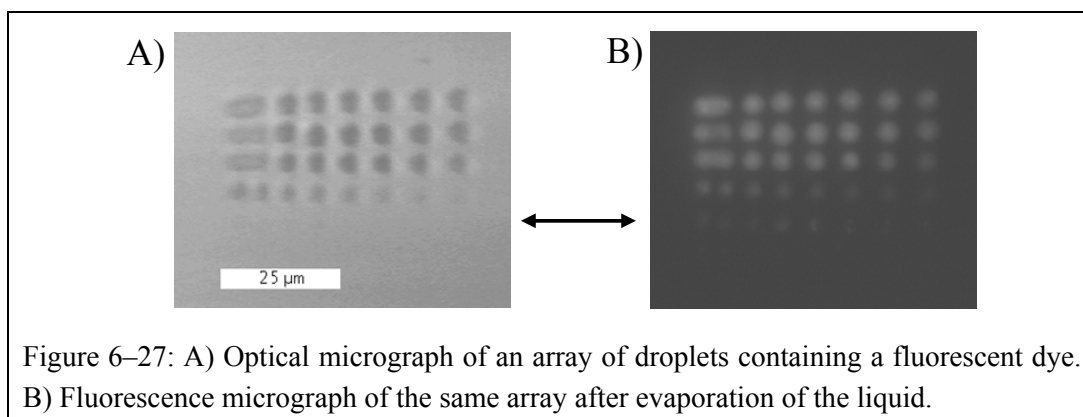


Figure 6–27: A) Optical micrograph of an array of droplets containing a fluorescent dye. B) Fluorescence micrograph of the same array after evaporation of the liquid.

The lithography program was used to dispense an 8 by 8 array of droplets. The optical micrograph in Figure 6–27 A shows the array of droplets after the deposition. Unfortunately, the probe got empty before the whole array was created. The array is distorted at its left edge due to hysteresis of the piezoelectric scanner. In Figure 6–27 B, the same array is shown after evaporation of the droplets, observed with a fluorescence microscope. Note that a 5th line is visible in the fluorescence image (pointed out by the arrow).

During this experiment, the evaporation of the droplets leads to fluorescence spots, with sizes that are almost identical to the size of the liquid droplet. This can be explained by two reasons. Firstly, the fluorescent molecules had adsorbed onto the substrate before the disappearance of the droplet by evaporation. Or secondly, the receding angle was zero, i.e. the diameter of the droplet did not decrease during the evaporation.

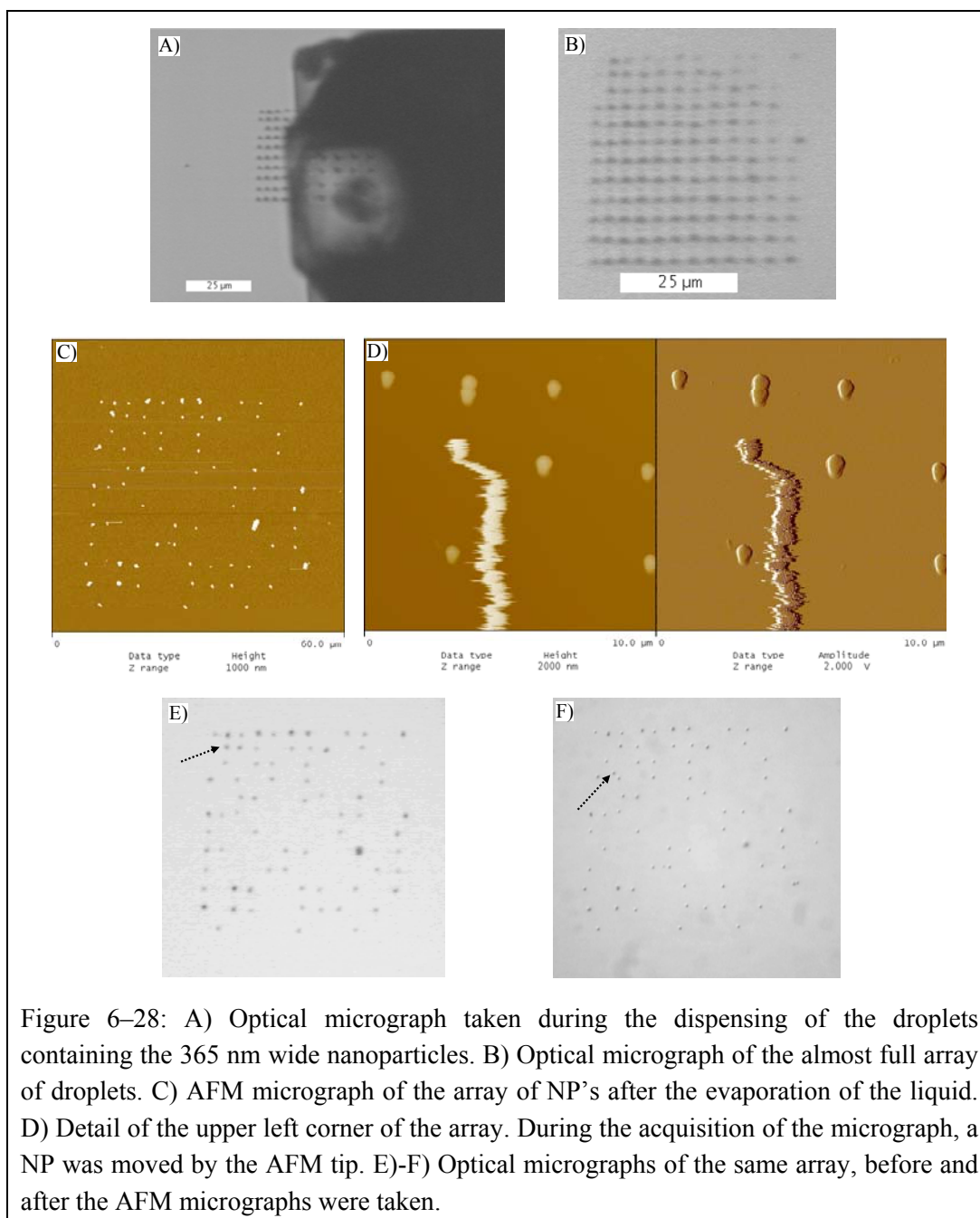
6.5.2. Deposition of droplets with nanoparticles

Similar to fluorescent molecules, nanoparticles could be suspended in the liquid and deposited on the substrate.

6.5.2.1. Deposition of droplets with 365 nm wide silicon dioxide particles

In this experiment, a probe with a microfabricated aperture was loaded with a solution of silicon dioxide nanoparticles (NP's) in glycerol at a concentration of ~ 1 NP/fl. The nanoparticles (Microparticles, Berlin, Germany [90]) had a diameter of 365 nm.

One should note that the concentration of NP's is not constant during the operation of the nanodispenser. Because of evaporation of the liquid, the concentration increases slowly but continuously. Nevertheless, the loss of liquid due to evaporation (about 60 pg/min) compared to the total amount of liquid (about 30 ng) should only weakly affect the concentration of NP's if the dispensing is done immediately after the loading of the probe.



The optical micrograph in the Figure 6–28 A shows the probe during dispensing of an array of 12 by 12 droplets on a silicon dioxide substrate treated with octadecylchlorosilane. Note that the liquid

inside the loading area acts as an optical lens. The optical micrograph B shows the full array of droplets. Some of the droplets are missing, mainly because of evaporation and also because not every contact of the tip on the substrate lead to a deposition. The tapping mode AFM micrograph C shows the array after the evaporation of the liquid. Not every spot is occupied by NP's, even if the liquid droplet was present. Some spots are occupied with more than one nanoparticle, as shown in the micrograph D. During the acquisition of the micrograph D (tapping mode), the AFM tip has involuntarily pushed one NP to the bottom border of the scan area. The displacement of the NP is also visible in the two last optical micrographs, where the first (E) was acquired before the AFM picture was taken, and the second (F) afterwards. The two arrows point out the respective positions of the NP.

The height of the droplets was measured with deflection-distance curves to be about 300 nm. The spacing of the droplets is about 4 μm , which determines the upper limit for the droplet diameter. Thus the upper limit for the deposited volume was about 2 fl. Compared with the concentration of NP's present in the liquid (~ 1 NP/fl), this corresponds approximately to maximum 2 nanoparticles per droplet, in accordance with the number of NP's per spot observed in the micrograph D).

It is worthwhile to compare the volume of one deposited droplet, i.e. about 1 fl, with the volume of one nanoparticle, which is about 25 al. Thus, the volume of one nanoparticle is much larger than the volume of the impurities inside one droplet (typically less than 1% of the liquid).

6.5.2.2. Deposition of droplets with 20 nm wide polystyrene nanoparticles

The nanoparticle discussed here are smaller than those of the previous section. The nanoparticles (Fluospheres F8787, Molecular Probes, Eugene, USA, [91]) are made of polystyrene and have a diameter of 20 nm.

6.5.2.2a. Dispensing with probes having a microfabricated aperture

A solution of 20 nm wide polystyrene nanoparticles was prepared at a concentration of about 20 NP/fl in glycerol.

In a first experiment, the solution of polystyrene NP's was loaded on a probe with microfabricated aperture, and an array of 5 by 5 droplets was deposited on a glass substrate. The deposited droplets, visible in the micrograph in Figure 6–29 A, had a diameter of about 7 μm . The amount of liquid per droplet was determined by the shift in the resonance frequency of the cantilever (the loss of liquid due to evaporation was taken into account). The droplet volume was determined to be about 13 fl. This volume together with the diameter of the droplet allowed the calculation of the contact angle of about 20°, which is a reasonable value for glycerol on glass.

After evaporation of the liquid, the array was imaged by AFM. The micrograph in Figure 6–29 B shows the array of dots, and the micrograph C the detail of one dot. The dots are less regularly aligned than the droplets, due to pinning effects of the three-phase contact line during drying. The pinning of the contact line was favored by the surface roughness and by the presence of surface defects or dust.

The dot in the micrograph C is about 190 nm in height, and has a volume of about 70 al, which corresponds to 0.5% of the initial droplet volume. The concentration of NP's present in the glycerol (~ 20 NP/fl) allows one to calculate the number of NP's and their total volume per droplet (one NP has a volume of 0.0042 al). There are about 260 NP's per droplet. These NP's have a total volume of 1.1 al, which is much smaller than the 70 al of the dot. Thus, it is probable that the dots are mainly made of the impurities of the glycerol, and that the nanoparticles are embedded in the dots.

This shows that the deposition of small nanoparticles which should not be embedded in a matrix made of the impurities of the liquid necessitates having either a liquid with a high purity or a liquid with a high concentration of NP's.

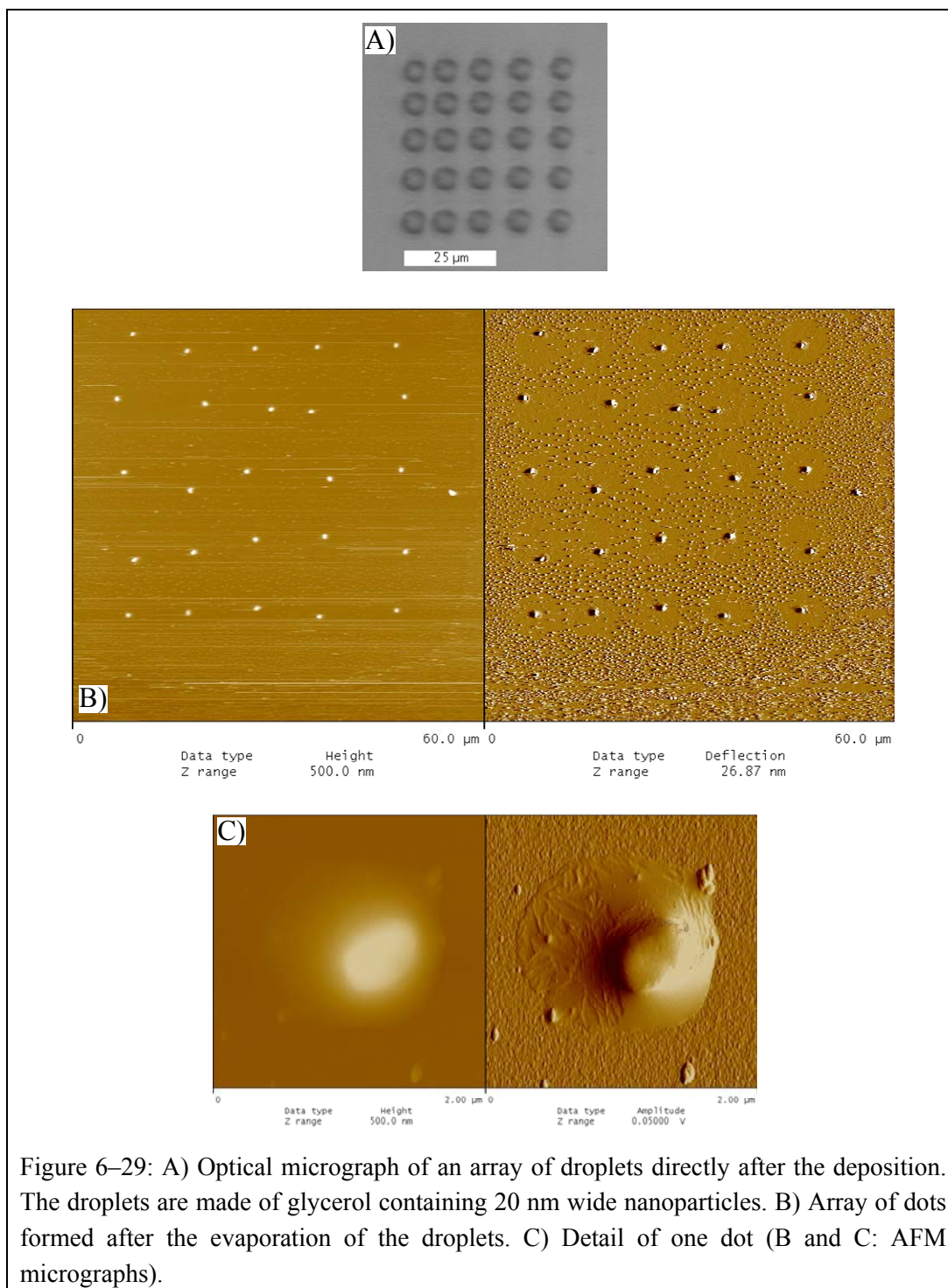
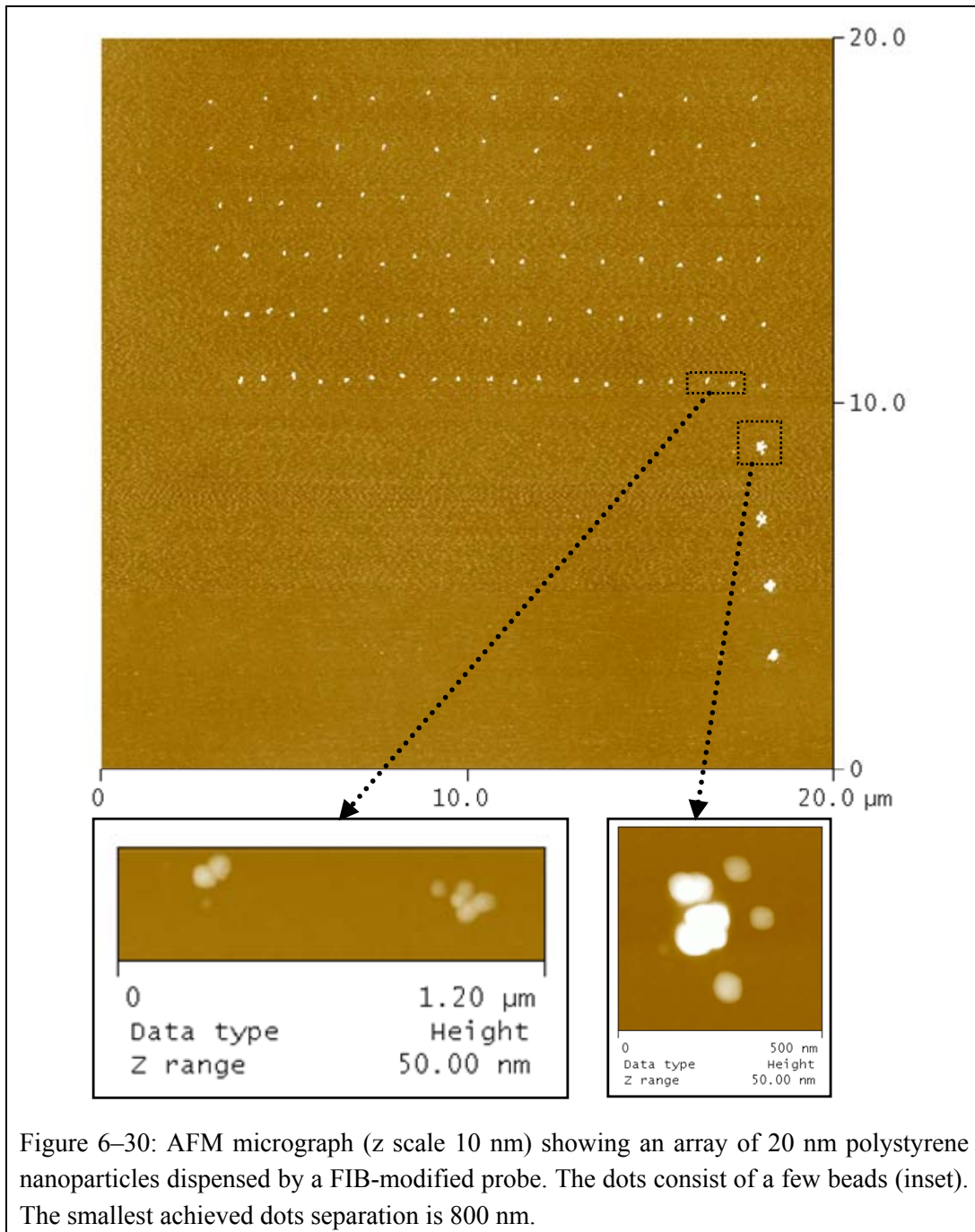


Figure 6–29: A) Optical micrograph of an array of droplets directly after the deposition. The droplets are made of glycerol containing 20 nm wide nanoparticles. B) Array of dots formed after the evaporation of the droplets. C) Detail of one dot (B and C: AFM micrographs).

6.5.2.2b. Dispensing with probe modified by FIB

In another experiment, the solution of polystyrene NP's in glycerol was loaded on a FIB modified probe (gold-coated on both sides, aperture ~200 nm). An array of 10 lines was deposited on a hydrophilic silicon dioxide surface (previously cleaned with piranha and SC-1, and stored in water). In the first line 10 droplets were deposited, 12 droplets in the 2nd line, 14 droplets in the 3rd, and so forth. The contact time for the deposition of each droplet was 0.5 second. Directly after the deposition of the array, the droplets were not recognizable by optical microscopy. The array was imaged by AFM in tapping mode. The result is show in Figure 6–30.

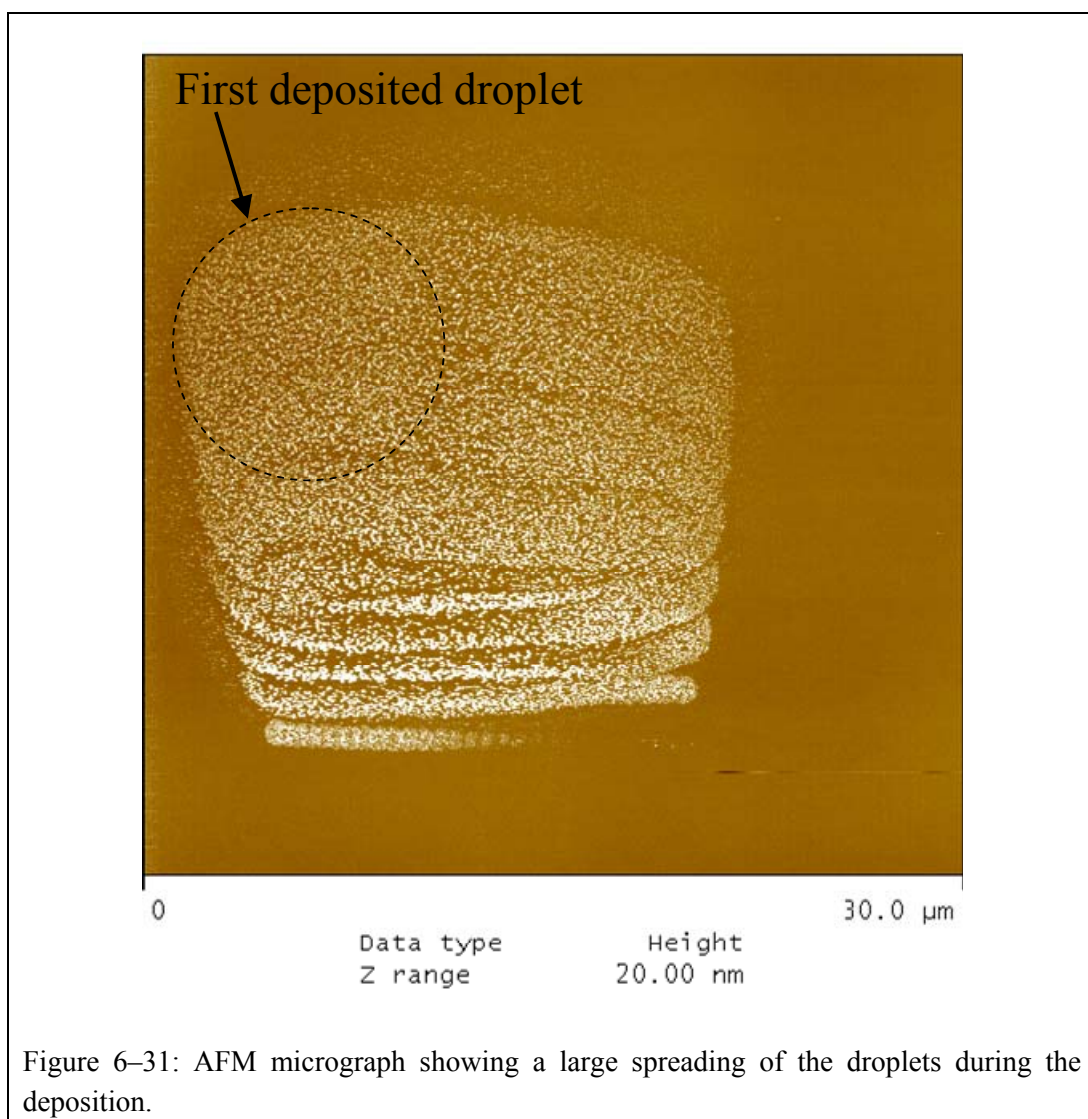


In the 6 first lines, individual dots are clearly visible. In the 4 last lines, only one larger dot is visible at the end of each line, because the merging of the droplets during the deposition process (see section 5.5.1.1). In the 6th line (20 spots), the average dot spacing is about 800 nm. The expected spacing in the 7th line (22 spots) is 730 nm. Thus the droplet diameter was between 730 and 800 nm. By assuming a contact angle smaller than 30° (because the surface is rather hydrophilic), a maximal volume of about 25 attoliters can be calculated.

If one assumes that the concentration remained identical (20 NP/fl), one droplet would have maximum 0.5 nanoparticles. However, the inset in Figure 6–30 shows that one dot is made of several particles. The particles are probably the nanoparticles, because the particles are distinct, which was not observed with dots made of impurities of the liquid. This would imply that the concentration of NP in the liquid was higher than initially, may be due to evaporation of the prepared solution.

It is interesting to notice that the residual dots located at the end of the 4 last deposited lines are much larger than the individual dots of the first lines. The reason is that during the writing of the last lines, each contact of the tip provoked, besides a coalescing of the droplet, also an increase in its volume. This is similar to the situation where a probe touches several times the same spot, and continuously increases the droplet volume until the equilibrium is reached (see section 6.2.3).

A similar deposition experiment was performed with a different contact time (3 seconds) compared to the previous experiment (0.5 seconds). The other parameters were identical: the same solution of NP's in glycerol, the same probe, one an identically prepared substrate, and same dispensing process to produce an identical array. After the dispensing, the area, imaged by AFM, shows a different structure. The result is seen in Figure 6–31. Individual dots are not anymore visible. Instead, one recognizes that a large spreading of the droplets occurred in the first lines. The spreading was less important in the last line, because the tip got empty during the deposition process.

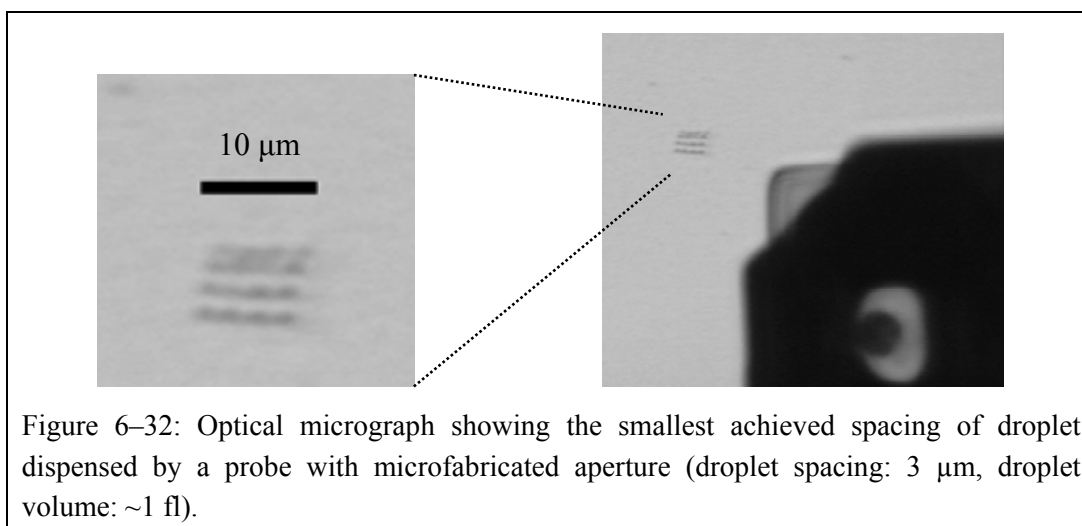


This example shows clearly that a slight change in one experimental parameter (contact time) can result in a huge difference in the deposition result. But other parameters that are only indirectly controllable, such as e.g. the Laplace pressure inside the liquid, could also have an influence on the deposition, and thus explain partially the observed difference.

6.6. Deposition on hydrophobic substrates for small droplet spacing

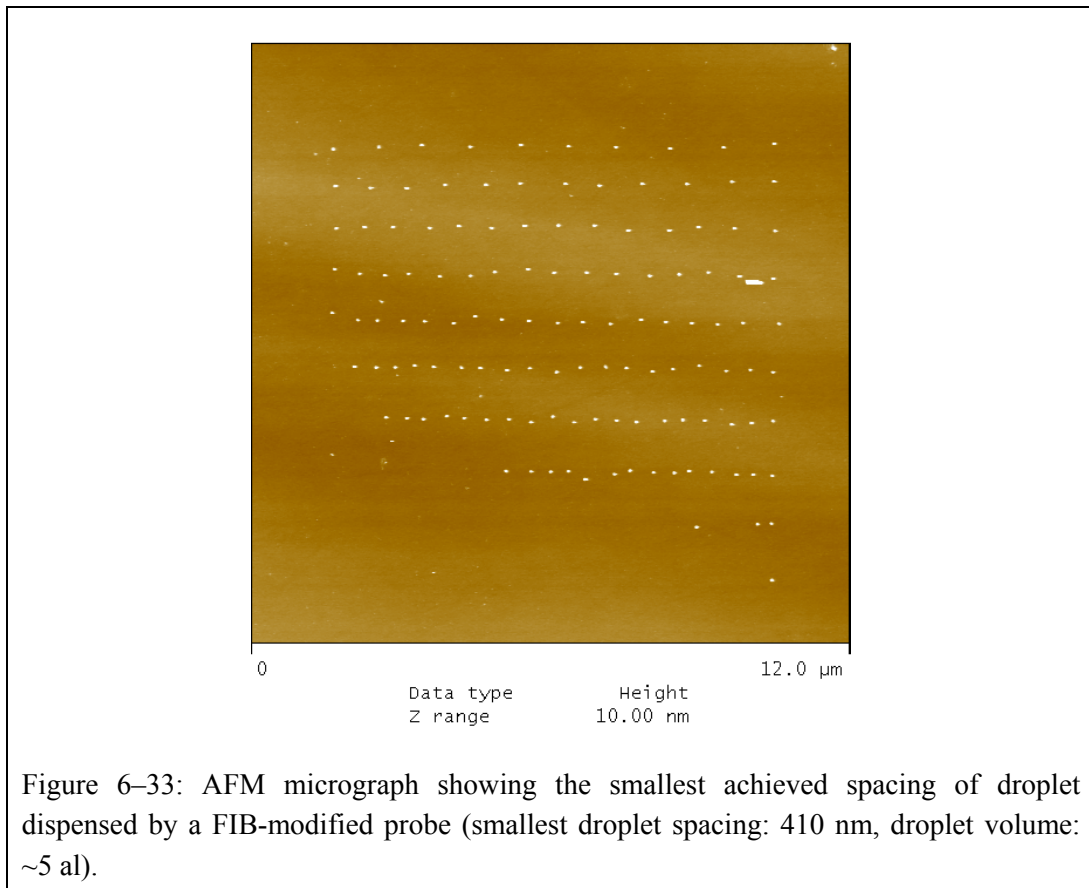
This section will present the smallest spacing that were achieved with both kinds of probes (microfabricated and FIB-milled apertures). A highly hydrophobic surface is more appropriated for the deposition of smaller droplets, for the reasons that were already pointed out in the section 6.2.2.

A 4 by 4 array of glycerol droplets was dispensed on a gold surface treated with hexadecanethiol, with a probe having a microfabricated aperture. The smallest droplet spacing achieved was about 3 μm , as shown in the optical micrograph in Figure 6–32. When a similar dispensing was performed, but with a smaller droplet spacing (2 μm), the droplets coalesced together. Thus the droplet diameter was between 2 and 3 μm . The droplet height, measured with deflection-distance curves, was 300 nm. This allows one to calculate a maximum value for the droplet volume of about 1 femtoliter, i.e. 1 μm^3 .



It is not surprising that it was not possible to achieve smaller droplet spacings with a probe having a microfabricated aperture, because the observed spacings (~ 3 μm) have already the typical size of the flat area surrounding the aperture (see Figure 6–3).

The smallest droplet achieved with the FIB-modified probes was on a hydrophobic silicon dioxide substrate. The dispensed liquid was glycerol containing polystyrene nanoparticles (20 nm wide). The droplet height was measured to be 70 nm. The array of dots with diminishing pitches from line to line is shown in Figure 6–33. The smallest spacing of residual dots is about 410 nm (8th line of the array), which corresponds to an upper limit for the droplet diameter. Thus, the estimated droplet volume was about 5 attoliters.



6.7. Modification of block-copolymer micelle layers

In this section an example of surface modification is given, which is different from the deposition of non-volatile material, molecules or nanoparticles.

The substrate is composed of a layer of polystyrene-*b*-poly(2-vinylpyridine) block-copolymer (PS-P2VP, 96500-*b*-10500 g/mol, Polymer Source, Montreal, Canada, [92]) micelles placed on silicon dioxide substrate. The micelles are formed by dissolving the polymer in toluene (0.5% w/w), which is a selective solvent for the polystyrene. The core of the micelle is composed of P2VP, and the corona of PS. The preparation of micelles is then spin-coated on the substrate previously treated with a piranha and SC-1 cleaning. Polystyrene is more hydrophobic, whereas poly(2-vinylpyridine) is hydrophilic.

The micelles lying on the substrate expose the hydrophobic polystyrene corona. In presence of a polar solvent such as glycerol, the micelles will change their shape in order to expose the hydrophilic part (the P2VP segments) against the polar liquid, since it is energetically more favorable. After the evaporation of the solvent the micelles remain in the transformed shape. This is sketched in Figure 6–34. The exact morphology of the transformed micelle layers is still under investigation.

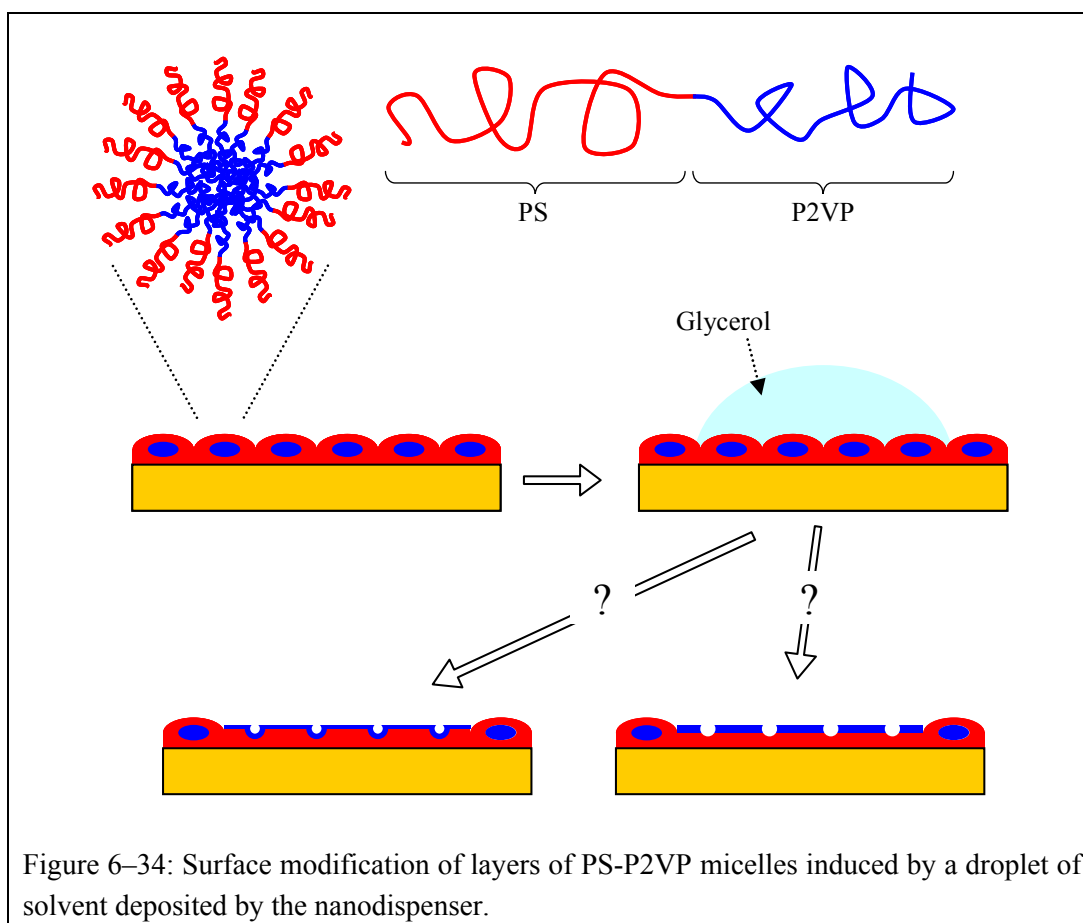


Figure 6–34: Surface modification of layers of PS-P2VP micelles induced by a droplet of solvent deposited by the nanodispenser.

The modification of the micelle layer occurs only due to the presence of the solvent on the surface. Thus, by depositing the solvent in a controlled way using the nanoscale dispensing, it was possible to induce the modification of the micelles only at local areas on the substrate.

In contrast to a glass or a silicon dioxide surface, a layer of micelles is much softer and could be easily damaged if large forces were applied by an AFM probe. Thus, only the FIB-modified probes, which had low spring constants, were used.

A first example is given in Figure 6–35, where anhydrous glycerol was loaded on a FIB-modified probe ($c \approx 0.2$ N/m, aperture ~ 200 nm).

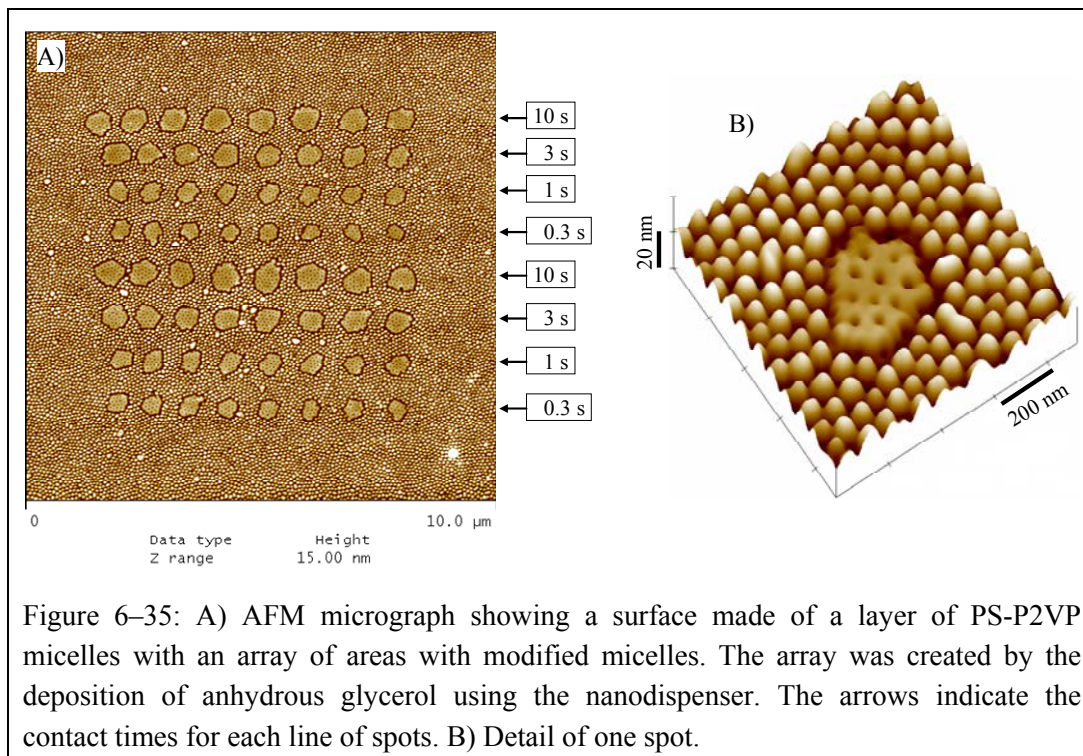


Figure 6–35: A) AFM micrograph showing a surface made of a layer of PS-P2VP micelles with an array of areas with modified micelles. The array was created by the deposition of anhydrous glycerol using the nanodispenser. The arrows indicate the contact times for each line of spots. B) Detail of one spot.

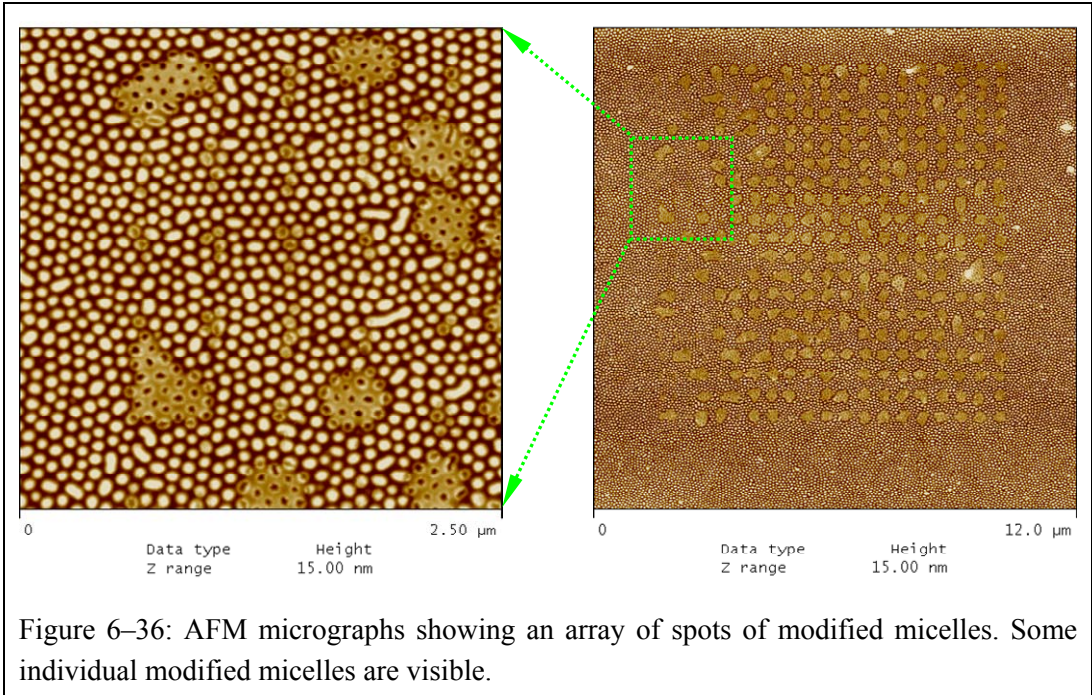
The deposition of the array of 8 by 8 droplets was done with different contact time per line. The time for each line is indicated at the right hand side of Figure 6–35 A. An influence of the contact time is clearly visible. The smaller spots, corresponding to the shorter contact time, have a diameter of about 400 nm. The micrograph Figure 6–35 B represents a detail of one spot. The modification of the micelles is clearly recognizable.

Figure 6–36 shows the micelle layer after the deposition of an array of 20 by 20 droplets (anhydrous glycerol) with the same probe. Not each tip contact has led to a liquid transfer and to a spot of modified micelles, in particular at the beginning of each line. The reason can be that during the displacement of the probe from the end of one line to the beginning of the next line, the liquid at the tip aperture had more time to reach an hydrostatic equilibrium, e.g. by being pulled back by capillarity. Despite the fact that larger spots of modified micelle are not always present where the tip touched the substrate, one can recognize in the left hand side AFM micrograph that some individual micelles were modified.

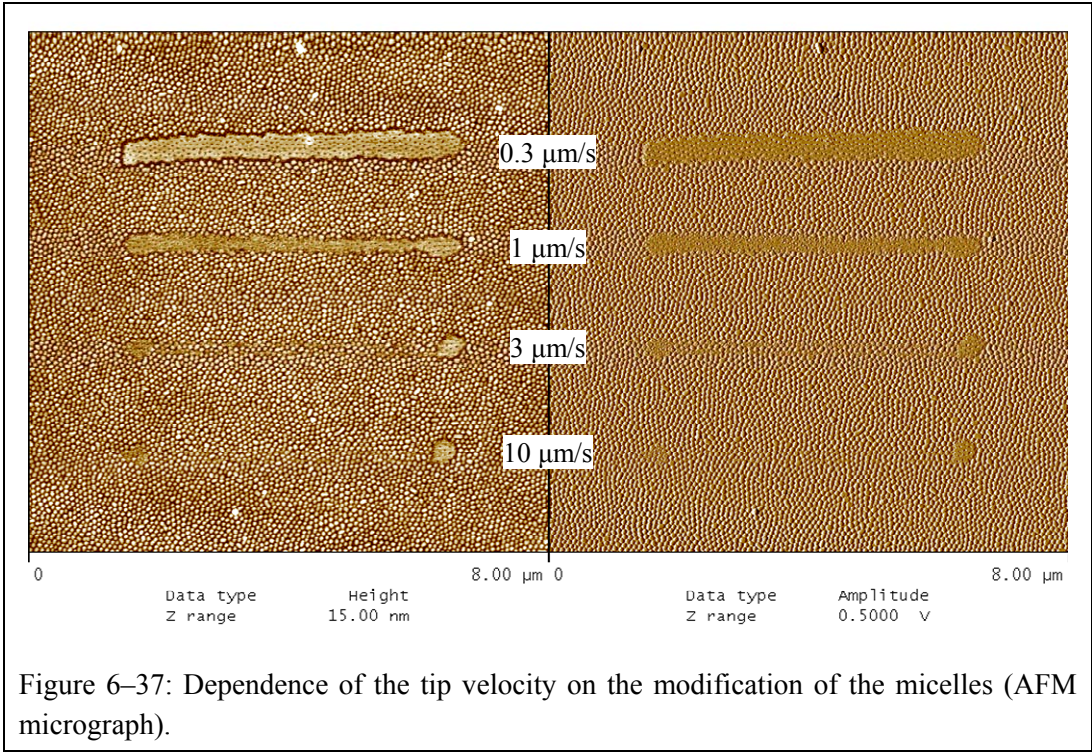
The creation of structures different from more or less circular spots induced by deposited droplets was also possible. To do that, the micelle modification was induced by the presence of the meniscus located between tip and surface. The probe was in contact with the micelle layer, and was moved in the xy-plane.

The first experiments showed that the displacement velocity plays an important role. Lower velocities led to broader lines, and when the tip velocity was too high, no modification of the micelles occurred. This was probably due to the liquid meniscus that kept stuck to the tip during its moving (no

deposition of a line of solvent), and the exposure time of the micelles to the liquid was not long enough to permit their opening.

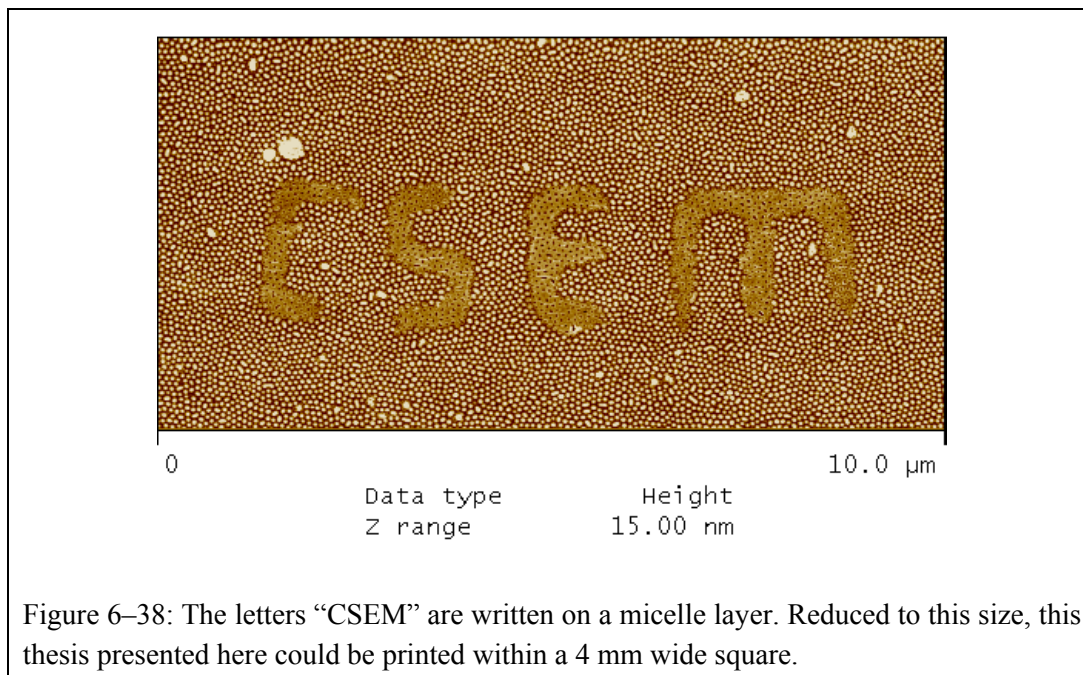


An example of tip-velocity dependence is shown in Figure 6–37. During this experiment, four lines were written by keeping the tip in contact with the sample, with four different tip velocities. At the slower velocity ($0.3 \mu\text{m/s}$), the line of modified micelles is well visible. With the faster tip velocity, only one spot at the end of the line is visible, because at the end of the line, the tip withdrawal left a droplet on the surface.



By assuming the meniscus around the tip to be circular with a diameter of 400 nm, a micelle located in the center of the path was exposed to the anhydrous glycerol during about 1.3 second in the first line, and 0.4 s, 0.13 s and 0.04s in the other lines respectively. Thus the time needed to induce a micelle modification seems to be around 0.1 s. But this is a rather rough approximation, since the exact shape of the meniscus during the tip displacement is not known.

The improving of this writing process to create more complicated figures than lines is in fact limited only by the imagination of the experimentalist.



7. Conclusion

Nanoscale dispensing (NADIS) has shown its ability to deposit single ultrasmall droplet in a controlled way, which permits the direct creation of droplet arrays with a high lateral accuracy. Arrays with droplet spacing down to 1 μm and droplet volumes down to some tens of attoliters were routinely created. Arrays of fluorescent molecules or nanoparticles were also created by NADIS.

At the beginning of this thesis there was only one idea: the dispensing of attoliter volumes of liquid with an AFM probe, similarly to a SNOM probe that contains an optical aperture. One obvious key point to achievedroplet dispensing was that the probe must have a real aperture to permit the transfer of liquid through the tip. The droplets were dispensed by contacting and withdrawing the tip on the substrate. No external pressure was applied to the liquid. The liquid transfer was driven only by capillarity and surface wettability.

Two approaches were investigated to fabricate the apertures. Firstly, the creation of the apertures was done during the probe microfabrication itself. Such apertures had a size of about 1-2 μm . Such apertures were located at the apex of the tip, because of the creation process itself. The possibility to create suitable probes for nanoscale dispensing of liquids at the wafer scale is of great interest, since such a kind of production has obvious advantages for an economical point of view. However, the precise control of the aperture size was rendered difficult by the numerous parameters that are involved in the microfabrication. Secondly, an aperture was milled by FIB into existing commercially available AFM probes. Those apertures had a size of about 200 nm, and could be milled at a freely chosen location. But only the probes with an aperture in the vicinity of the tip apex could lead to a liquid transfer. If the aperture is too far from the tip apex, the liquid did not reach the substrate and could not flow as the tip contacts the substrate.

A loading area was created on the cantilever, which allowed a better confinement of the liquid at the extremity of the cantilever. This permitted also to guarantee a liquid free area for the laser beam reflection.

All experiments were performed in ambient environment. Since the amounts of liquid loaded on the cantilevers were small, and because the loaded liquids were exposed to air, we concentrated on the use of liquids with low evaporation rates. Glycerol and tetraethylene glycol were the two main liquids employed in the experiments.

The droplet volumes were defined by several parameters. The most important were the aperture size, and the wettability character of the substrate. Both the smallest volume and the smallest droplet spacing were achieved on hydrophobic substrates with the smaller tip apertures.

The smallest droplet volume achieved with the probes having a microfabricated aperture was about 1 femtoliter, which corresponds to a cube with an edge length of 1 μm . The smallest achieved droplet spacing was 3 μm .

The smaller apertures of the FIB-modified probes allowed the deposition of smaller droplets. With those probes, the smallest droplet volume achieved was about 5 attoliters, which corresponds to a cube with an edge length of 170 nm. The smallest achieved droplet separation was measured to be 410 nm.

Nanoparticles as well as fluorescent molecules could also be deposited to create arrays. The nanoparticles were suspended in the liquid, which was used as transport medium.

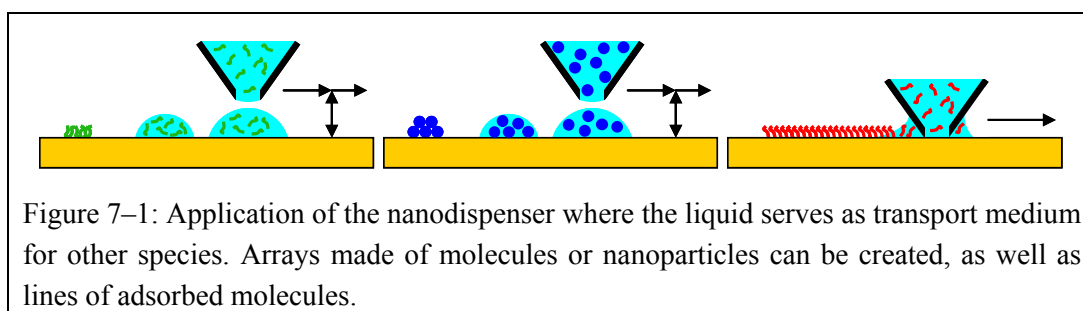
An example of local surface modification induced alone by the presence of the dispensed liquid was shown. By exposing to glycerol, micelles made of block-copolymer were modified. Both arrays and lines were created. The smallest width of the lines or circular areas with modified micelles was about 400 nm.

Some theoretical aspects describing the capillarity, more particularly the behavior of small volume of liquids such as sessile droplets or axisymmetric liquid menisci, were also discussed. It was shown that capillary forces have two components, one induced by the Laplace pressure that acts on the surface of the cross section of the liquid bridge, and another induced by the surface tension acting on the perimeter of the cross section of the liquid.

7.1. Application of nanodispensing

The dispensing of ultrasmall amount of liquid by NADIS has several advantages, such as the small size of the deposited droplets, the small droplet spacing, and the high accuracy in the lateral positioning of the droplets. NADIS thus permit the production of high-density arrays of droplets. Furthermore, the small size of the droplets allows an economical use of the liquid itself.

Two distinct domains of application can be envisaged with the nanodispenser. The first domain of application is to use the liquid as transport medium for molecules or nanoparticles (see Figure 7–1), and the second is to use the pure liquid as it is.



The most promising application of NADIS is in the creation of high density microarrays. Microarrays are widely used since the last decade in proteomics and genomics. Protein microarrays (such as antibody microarrays) and protein-detecting microarrays (arrays made of protein-binding agents such as antigens) are involved in disease diagnostics or immunoassays [93,94]. DNA microarrays or oligonucleotide microarrays are used in functional genomics for drugs development [95,96]. Some molecules used are difficult to synthesize or to extract. Thus, the possibility to create arrays with low molecule consumption is of interest. It is also an advantage to have microarrays with a high density of spots, and thus a smaller array size, because they permit a vast reduction in the amount of the analyzed solution. Furthermore, a high density of spots allows the creation of arrays with a higher number of different functionalities per unit surface. In addition, ultraminiaturized microarrays could also be integrated into microfluidic devices, and other lab-on-a-chip technologies.

Another application can also be the creation of nanoparticles arrays, which could be used as catalyst.

The second application of NADIS is to use the dispensed liquid directly, as shown with the micelle modification. A pattern of resist could thus be deposited on a substrate without any other step of common photolithography, and without any masks. This is particularly of interest in rapid prototyping.

In a more general case, nanodispensing can be used each time single ultrasmall droplets need to be deposited on a controlled way and with high lateral accuracy on a substrate.

7.2. Outlook

Further investigations will include the integration of microfluidics for supplying and controlling the liquid to the tip. Instead the open loading area, a closed volume for the liquid storage will prevent a premature liquid evaporation, thus making possible the use of water based liquids or other volatile solvents. The creation of a larger available volume for the liquid inside the probe chip will also be studied.

Another investigation direction will be the creation of a nanodispenser with several cantilevers in parallel, each tip being provided with a different liquid. This would circumvent the serial manner of writing with a single probe. Furthermore, an entire 2-dimensional array of dispenser can be imagined [97], which could, together with an appropriate microfluidic network to supply each tip, dispense a whole array at once with different functionalities at each spot.

8. Annexes

8.1. Annex 1

8.1.1. Young's equation

In this annex, the equation (2-24), leading to the Young's equation, will be derived.

The spherical cap is the region of a sphere that lies above (or below) a given plane. Let the sphere have radius R , the cap height h , and the base radius a .

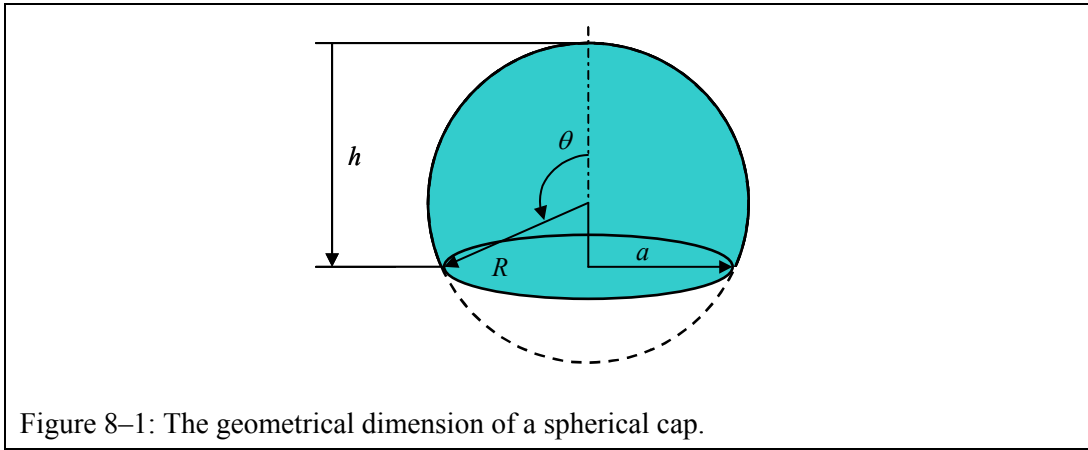


Figure 8-1: The geometrical dimension of a spherical cap.

The Pythagorean Theorem gives:

$$a^2 = R^2 - (h - R)^2 = 2Rh - h^2 \quad (8-1)$$

The contact angle θ is defined as the angle between a normal to the base and a normal to the sphere going through the base perimeter. The relation between R , h and θ is given by:

$$h = R \cdot (1 - \cos\theta) \quad (8-2)$$

The volume V of the cap can be calculated using the integral

$$V = \pi R^3 \int_0^\theta \sin^3(\theta') \cdot d\theta' = \frac{\pi R^3}{12} (8 - 9\cos(\theta) + \cos(3\theta)) \quad (8-3)$$

and can be further treated with basic trigonometry to

$$V = \frac{\pi R^3}{3} (2 - (2 + \sin^2(\theta)) \cdot \cos(\theta)) \quad (8-4)$$

$$V = \frac{\pi}{3} (2R^3 - (2R^2 + R^2 \sin^2(\theta)) \cdot R \cos(\theta)) = \frac{\pi}{3} (2R^3 - (2R^2 + a^2) \cdot R \cos(\theta)) \quad (8-5)$$

Using Equation (8-2),

$$V = \frac{\pi}{3} (2R^3 - (2R^2 + a^2) \cdot (R - h))$$

$$V = \frac{\pi}{3} (2R^2 h + a^2 (h - R)) \quad (8-6)$$

and Equation (8-1), one obtains:

$$V = \frac{\pi}{3} (2R^2 h + (2Rh - h^2) (h - R))$$

$$V = \frac{\pi h^2}{3} (3R - h) \quad \Leftrightarrow \quad R = \frac{V}{\pi h^2} + \frac{h}{3} \quad (8-7)$$

The lateral area A_{Lat} is

$$A_{Lat} = 2\pi R^2 \int_0^\theta \sin(\theta) \cdot d\theta = 2\pi R^2 (1 - \cos\theta) \quad (8-8)$$

Using equation (8-2) and equation (8-7), one obtains:

$$A_{Lat} = 2\pi R h = \frac{2V}{h} + \frac{2\pi h^2}{3} \quad (8-9)$$

The area of the base A_{Base} is:

$$A_{Base} = \pi a^2 = \pi (2Rh - h^2) = \pi \left(2h \left(\frac{V}{\pi h^2} + \frac{h}{3} \right) - h^2 \right) = \frac{2V}{h} - \frac{\pi h^2}{3} \quad (8-10)$$

In the next lines, the Equation (2-24) will be derived. The differential can be written as

$$\left. \frac{dA_{LG}}{dA_{SL}} \right|_{V=\text{const.}} = \frac{\left. \frac{dA_{Lat}}{dh} \right|_{V=\text{const.}}}{\left. \frac{dA_{Base}}{dh} \right|_{V=\text{const.}}} = \frac{\frac{d}{dh} \left(\frac{2V}{h} + \frac{2\pi h^2}{3} \right)}{\frac{d}{dh} \left(\frac{2V}{h} - \frac{\pi h^2}{3} \right)} = \frac{-\frac{2V}{h^2} + \frac{4\pi h}{3}}{-\frac{2V}{h^2} - \frac{2\pi h}{3}} \quad (8-11)$$

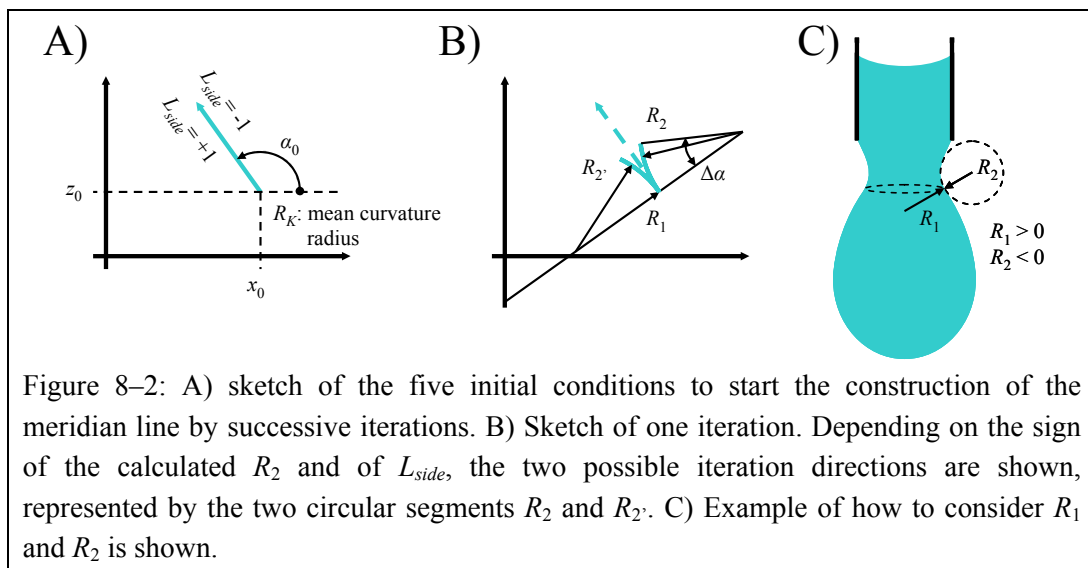
After reducing equation (8-11), replacing V by Equation (8-7), and using Equation (8-2), one obtains:

$$\left. \frac{dA_{LG}}{dA_{SL}} \right|_{V=\text{const.}} = \frac{-6V + 4\pi h^3}{-6V + 2\pi h^3} = \frac{R - h}{R} = \cos(\theta) \quad (8-12)$$

8.2. Annex 2

In this annex a short program will be described that constructs by iteration the meridian of an axisymmetric surface, based on the equations in section 2.3.4. The program is written in such a way that it can be used with the software "Scilab", a free scientific software package [98]. Let us first describe the start conditions and the iteration parameters.

- In the lines 11, 12, 13 the liquid-gas interfacial tension, the liquid density, and the strength of the gravitational field are given.
- In line 15 the start value of the x-coordinate (coordinate x_0 in Figure 8–2 A). The x-coordinate cannot be negative is given.
- The z-coordinate of the start point is given in line 18 (coordinate z_0 in Figure 8–2 A).
- The radius corresponding to the mean surface curvature at the z-coordinate of the start point is given in line 19.
- The slope of the meridian at the start point in line 20 (α_0 in Figure 8–2 A).
- To be able to distinguish between a sessile drop from a pendent drop, a parameter L_{side} is used, that describes on which side the liquid is, left ($L_{side} = +1$) or right ($L_{side} = -1$), with respect to the direction α_0 (line 23).
- The parameter in line 28 corresponds to the angular increment ($\Delta\alpha$ in Figure 8–2 B).
- The parameter in line 29 gives the maximum length for one iteration. For large value R_2 , the angular increment will be accordingly reduced.
- The number of iteration that will be performed is given in line 30.



The program calculates four different meridians. The first is the meridian resulting from the initial parameters. The second is the retrace curve of the previously calculated meridian. The retrace curve starts from the last calculated point in the previous meridian, in the opposite direction. A good superposition of both plotted curves indicates that the iteration parameters are well chosen. The third and fourth curves are identical to the first two, with the only difference that the effect of the gravitational field is not taken into consideration.

One iteration step is as follows:

- From the initial values $x(i)$, $z(i)$ and $\alpha(i)$, the length of the radius $R_1(i)$ is calculated. Normally, $R_1(i)$ is positive. But since it can happen that the calculated meniscus is self-crossing (for

nodoids), even if such a case has no physical meaning, one can still consider the curve as a mathematical solution. Knowing $R_K(1)$, $R_1(i)$ and $z(i)$, one can calculate the radius $R_2(i)$. (Line 53 to 70).

- A circular segment of angle $\Delta\alpha$ and radius $R_2(i)$ can be drawn, starting from the point $(x(i), z(i))$ and tangentially to the direction $\alpha(i)$. Two possibilities exist for such a segment as shown in Figure 2–18 B. The choice will depend on the sign of $R_2(i)$: if $R_2(i)$ is positive, the center of $R_2(i)$ has to be on the liquid side, whereas if $R_2(i)$ is negative, the center of $R_2(i)$ will be on the gaseous side. (Line 71). Where which phase is, is defined by the sign of L_{side} .
- The incremental angle $\Delta\alpha(i)$ can now be determined, while taking account on the maximum length for one iteration. (Line 72).
- The end-point $(x(i+1), z(i+1))$ of the circular segment along $R_2(i)$ can now be determined. (Lines 73 to 76). It will be the starting point of the next iteration.
- The slope at the new point will be $\alpha(i+1) = \alpha(i) + \Delta\alpha(i)$. (Line 77).

The last part of the program is related to displaying the curves on the screen.

8.2.1. Program

Line: Code:

```

1 // =====
2 // Calculation by iteration of the meridian
3 // of an axisymmetric liquid surfaces
4 // =====
5 //
6 //
7 // Datas for liquid,
8 // start conditions, and
9 // iteration parameters
10 // =====
11 gammaLV = 0.06; // [N/m] Surface tension of the liquid
12 rho = 1000; // [kg/m^3] Density of the liquid
13 g0 = 9.81; // [m/s^2] Strength of gravitational field
14 //
15 x0 = 6 /1e6; // [[mu]m]/1e6 = [m] Radius value of start point.
16 // for meniscus: x0 > 0
17 // for sessile or pendent drop: x0 = 0
18 y0 = 0 /1e6; // [[mu]m]/1e6 = [m] Height value of start point
19 Rk0 = -1 /1e6; // [[mu]m]/1e6 = [m] Mean surface curvature radius @ y0
20 alpha0 = 90 *%pi/180; // [deg]*PI/180 = [Rad] Angle value of start point. Only for meniscus required
21 // for meniscus: 0 <= alpha0 < 360 deg
22 // for sessile or pendent drop: alpha0 = 0
23 Lside0 = 1; //define on which side the liquid is, with respect to the incremental direction
24 // left: Lside0 = 1 (always for a pendent drop)
25 // right: Lside0 = -1 (always for a sessile drop)
26 // for a meniscus, if alpha0 not equal to 0 or 180 deg, Lside0 = sign(sin(alpha0))
27 //
28 da0 = .5 *%pi/180; // [deg]*PI/180 = [Rad] incremental angle for each iteration
29 ds0 = 0.009 /1e6; // [mu]m => [m] maximal incremental distance, reduces the incremental angle da if necessary
30 lengthV0 = 1000; // Number of points in one calculated curve
31 // lengthV => 2
32 //
33 //
```

```

34 // Calculation of the meniscus shape
35 // =====
36 grg0 = g0*rho/gammaLV; // [m^2]
37 R1=0; R2=0;
38 da=da0; ds=ds0; lengthV=lengthV0;
39 if abs(sin(alpha0))>1e-12 then
40     if Lside0 <> sign(sin(alpha0)) then "The value Lside seems to be wrong"
41     end
42 end
43 //
44 for i=1:4
45     select i
46     case 1 then x=x0; y=y0; alpha=alpha0; Lside=Lside0; g=g0; grg=grg0; //"1 trace, with g"
47     case 2 then x=x1($); y=y1($); alpha=alpha+%pi; Lside=-Lside0; //"2 retrace, with g"
48     case 3 then x=x0; y=y0; alpha=alpha0; Lside=Lside0; g=0; grg=0; //"1_ trace, without g"
49     case 4 then x=x1_($); y=y1_($); alpha=alpha+%pi; Lside=-Lside0; //"2_ retrace, without g"
50     end
51     for k=1:lengthV-1,
52         //
53         if x(k)==0 then // if x=0 then the 1st iteration of a sessile or pendent drop is to calculate
54             alpha = 0;
55             R1=2*Rk0;
56             R2=2*Rk0;
57         else // for all other iterations
58             if x(k)<=0 then // x should always be positive, at least in the 1st curve
59                 if i==1 then
60                     " !!! x value should remain positive !!!"
61                     " change initial iteration parameters "
62                 end
63             end
64             signR1 = sign(-cos(alpha+Lside*%pi/2));
65             if signR1==0 then signR1=1;
66             end
67             R1 = signR1*sqrt(x(k)^2+(x(k)*tan(alpha+%pi/2))^2);
68             R2 = 1/(1/Rk0-(y(k)-y0)*grg-1/R1);
69             end
70         //
71         dirR2 = sign(R2)*Lside;
72         daTemp = dirR2*min(da, abs(ds/R2));
73         dx = abs(R2) * (cos(alpha+dirR2*%pi/2)+cos(alpha-dirR2*%pi/2+daTemp));
74         dy = abs(R2) * (sin(alpha+dirR2*%pi/2)+sin(alpha-dirR2*%pi/2+daTemp));
75         x(k+1) = x(k)+dx;
76         y(k+1) = y(k)+dy;
77         alpha = alpha+daTemp;
78         if alpha >= 2*%pi then alpha = alpha - 2*%pi;
79         end
80         if alpha < 0 then alpha = alpha + 2*%pi;
81         end
82     end
83     select i
84     case 1 then x1 = x; y1 = y;
85     case 2 then x2 = x; y2 = y;
86     case 3 then x1_ = x; y1_ = y;
87     case 4 then x2_ = x; y2_ = y;
88     end
89 end

```

```

90 //
91 // set the length unit to [[mu]m]
92 x1=x1*1e6; x2=x2*1e6;
93 y1=y1*1e6; y2=y2*1e6;
94 x1_=x1_*1e6; x2_=x2_*1e6;
95 y1_=y1_*1e6; y2_=y2_*1e6;
96 //
97 //
98 // Ploting the results
99 // =====
100 // determine the scale sizes of the graphics
101 xmax=max([max(x1);max(x2);max(x1_);max(x2_);0]);
102 ymax=max([max(y1);max(y2);max(y1_);max(y2_);0]);
103 ymin=min([min(y1);min(y2);min(y1_);min(y2_);0]);
104 Hwin=max([xmax, ymax-ymin]);
105 rect=[-Hwin,ymin,Hwin,Hwin+ymin];
106 //
107 // plots the curves
108 xbaso();
109 //xset("default");
110 // upper plot, curve with gravity
111 subplot(2,1,1)
112 plot2d(0, 0, frameflag=5, rect=rect); // empty plot with axis
113 xset("pattern",32);
114 plot2d([ x1, x2],[y1,y2], style=[11,12],...
115 leg="Trace with gravity @Retrace with gravity", frameflag=0, axesflag=0);
116 plot2d([-x1,-x2],[y1,y2], style=[11,12], frameflag=0, axesflag=0);
117 xgrid(1);
118 // lower plot, curves without gravity
119 subplot(2,1,2)
120 plot2d(0, 0, frameflag=5, rect=rect); // empty plot with axis
121 xset("pattern",32);
122 plot2d([ x1_, x2_],[y1_,y2_], style=[11,12],...
123 leg="Trace without gravity @Retrace without gravity ", frameflag=0, axesflag=0);
124 plot2d([-x1_,-x2_],[y1_,y2_], style=[11,12], frameflag=0, axesflag=0);
125 xgrid(1);
126 //
127 // End of Program
128 // =====

```

8.3. Annex 3

This annex gives an example of the programs used to control the dispensing of droplet arrays using the MultiMode AFM, with the NanoScope IV controller. The actual version of the program given here dispenses an array with an increasing number of droplets from line to line.

The procedure to run such a program is as follows:

- Engage the probe with a zero scan-size in contact mode outside of the expected deposition area (using the xy-offset).
- Reduce the range of the z-piezoelectric element (Zlimit value in the DI software). This will prevent the scanner from damages when fully retracted.
- Put the deflection set-point to a lower value in order to get the scanner fully retracted in z-direction, correct the xy-offset values, and set the scan-size to a value that include all programmed probe movements. The probe will scan above the surface.
- Run the lithography program.
- At the end of the program, the probe will again scan above the surface.
- The probe can be withdrawn.

```
// === Start of program ===
// For Multimode AFM
//
// write an array of "n" * "n+dn" points in a square of side "size" [mu]m. centred on ("xc","yc")
// 1st line: n points
// 2nd line: n+dn points
// i-th ligne: n+(i-1)*dn points
//
//
// Debug window: press Ctr+Alt+d on Nanoscope Control screen,
// select Lithography, LogAllChecked and SayError in Filter tab.
//
#include <litho.h>
#include <gui.h>          // **** only for MultiMode ****
#include <sysdefs.h>     // **** only for MultiMode ****
//
//
//
// === subprogram ===
//
bool moveX (double x_final, double speed, double sens){
    //      [mu]m      [mu]m/s      [mu]m/V
    double x_initial, time;
    bool b;
    x_initial = LithoGet(lsX); // [V]
    x_final = x_final/sens; // [V]
    speed = speed/sens; // [V/s]
    time = (x_initial-x_final)/speed; // [s]
    if (time < 0) time = -time;
    b = LithoRamp (lsX, x_initial, x_final, time);
    return b;
}
//
```

```

bool moveY (double y_final, double speed, double sens){
    //      [mu]m      [mu]m/s      [mu]m/V
    double y_initial, time;
    bool b;
    y_initial = LithoGet(IsY); // [V]
    y_final = y_final/sens; // [V]
    speed = speed/sens; // [V/s]
    time = (y_initial-y_final)/speed; // [s]
    if (time < 0) time = -time;
    b = LithoRamp (IsY, y_initial, y_final, time);
    return b;
}
//
bool moveZ(double z_final, double speed, double sens){
    //      [mu]m      [mu]m/s      [mu]m/V
    double z_initial, time;
    bool b;
    z_initial = LithoGet(IsZ); // [V]
    z_final = z_final/sens; // [V]
    speed = speed/sens; // [V/s]
    time = (z_initial-z_final)/speed; // [s]
    if (time < 0) time = -time;
    b = LithoRamp (IsZ, z_initial, z_final, time);
    return b;
}
//
void initialize (double posX, double posY, double HalfSizeIni, double speed, double sens){ // to minimize hysteresis at
beginning
    //      [mu]m      [mu]m      [mu]m      [mu]m/s      [mu]m/V
    double sizeTemp;
    moveX (posX, speed, sens);
    moveY (posY, speed, sens);
    sizeTemp = posX + HalfSizeIni;
    moveX (sizeTemp, speed, sens);
    sizeTemp = posY + HalfSizeIni;
    moveY (sizeTemp, speed, sens);
    while (HalfSizeIni>1 || HalfSizeIni<-1) {
        HalfSizeIni = -HalfSizeIni/1.2;
        sizeTemp = posX + HalfSizeIni;
        moveX (sizeTemp, speed, sens);
        HalfSizeIni = HalfSizeIni/1.2;
        sizeTemp = posY + HalfSizeIni;
        moveY (sizeTemp, speed, sens);
    }
    moveX (posX, speed, sens);
    moveY (posY, speed, sens);
}
//
//
// === main program ===
//
extern "C" _declspec(dllexport) int macroMain()
{
    Debug("\n*** Start Lithography ***\n\n");
    //
    LITHO_BEGIN

```

```

//
int YesNo;
double posZ;
Debug("\n*** Position of Z piezo when retracted ***");
Debug("\n*** Should be: Z < 220V ***\n\n");
posZ = LithoGet(lsZ); // [V]
YesNo = AskYesNo(" *** Lithography *** ", "\n Run dots_n v07 ? \n\n Get Zscan < 220V ? \n");
if (YesNo==0) LithoAbort();
//
// Variables (unit for distance: [mu]m)
//
double size, xc, yc, sizeIni, sizeIniStart, time, speedXY;
double stepX, stepY, temp;
double delaypiezo, delayretract;
double setpointdown;
double setpointup, sensXY, sensZ;
int i, j, n, dn, nX;
//
size = 5; // full size of square in [mu]m
xc = 7.5; // position in [mu]m of the center of the square "size"
yc = 0; // position in [mu]m of the center of the square "size"
n = 5; // dimension of the n x n array
dn = 2;
sizeIni = 15; // full size of initialisation in [mu]m at (xc, yc)
sizeIniStart = 35.; // full size of initialisation in [mu]m at x=0 y=0
speedXY = 50; // fast speed of tip in [mu]m/s (when in z_move or retracted)
time = .1; // time in s for deposit the dots
setpointdown = .5; // deflection setpoint (force) in V witch them the dots are drawn
setpointup = LithoGet(lsSetpoint);
//
delaypiezo = .2; // delay time before engaging tip to stabilize piezo in x-y direction
delayretract = .2; // delay time between retracting tip and fast move
//
sensXY = .40; // [mu]m/V for xy-piezo
sensZ = 0.01295; // [mu]m/V for z piezo
//
// Calculated variables
//
stepY = size/(n-1); // step between two lines in [mu]m
size = size/2; // half length array size in [mu]m
sizeIni = sizeIni/2; // half length of sizeIni in [mu]m
sizeIniStart = sizeIniStart/2; // half length area of initialization in [mu]m
//
// Moving the tip
//
LithoDisplayStatusBox(); // display litho status box
LithoScan(FALSE); // turn off scanning
LithoCenterXY(); // move tip to center of field
//
initialize(0.0, 0.0, sizeIniStart, speedXY, sensXY);
initialize(xc, yc, sizeIni, speedXY, sensXY);
//
moveY(sizeIni+yc, speedXY, sensXY);
moveY(size+yc, speedXY, sensXY); // start first line
//
// deposition of the n x n dots

```



```

for (i=1; i<=n; i++){          // loop for the n lines
  moveX(-sizeIni+xc, speedXY, sensXY); // left
  moveX(-size+xc, speedXY, sensXY); // start first point
  LithoPause(2*delaypiezo);
  nX = n + (i-1)*dn; // #points in the i'th line
  stepX = 2*size/(nX-1); // step between two dots in [mu]m in i'th line
  for (j=1; j<=nX; j++){      // loop for the n dots per line
    temp = -size + (j-1)*stepX;
    moveX (temp+xc, speedXY, sensXY);
    LithoPause(delaypiezo); // Waiting-time to stabilize piezo
    LithoSet(IsSetpoint, setpointdown); // engage the tip on the surface
    LithoPause(time); // waiting-time deposition first dot of line 1
    LithoSet(IsSetpoint, setpointup); // retract the tip from the surface
    LithoPause(delayretract); // waiting-time before fast move
  }
  temp = size - i*stepY;
  moveY (temp+yc, speedXY, sensXY); //start (i+1)'th line
}
//
moveY (-sizeIniStart, speedXY, sensXY);
moveX (sizeIniStart, speedXY, sensXY);
//
LithoPause(3);
LithoPause(3);
LithoPause(3);
LithoPause(3);
//
LITHO_END
//
Debug("\n*** End Lithography ***\n\n"); // ***** only for MultiMode *****
return 0; // 0 makes macro unload // ***** only for MultiMode *****
}
// === End of program===

```

8.4. Annex 4

8.4.1. Evaporation of a sessile droplet

8.4.1.1. With a pinned three-phase contact line

In this approximation for the evaporation time of a droplet, one assumes that the three-phase contact line remains pinned during the evaporation, i.e. the variable a remains constant, and that the evaporation surface is A_{Lat} . For the variable noun definition, see Annex 1. Let r be the evaporation rate. The change in volume V per unit time is:

$$\frac{dV}{dt} = \frac{dV}{dh} \frac{dh}{dt} = -r \cdot A_{Lat} \quad (8-13)$$

Using equation (8-1), the equations (8-7) and (8-8) leads to:

$$V = \frac{\pi}{6} h(3a^2 + h^2) \quad (8-14)$$

$$A_{Lat} = \pi(a^2 + h^2) \quad (8-15)$$

Placing the equations (8-14) and (8-15) into the differential equation (8-13) leads to:

$$\frac{dh}{dt} = -2r \cdot \quad (8-16)$$

Thus, the time $t_{evap,min}$ needed to evaporate the droplet is:

$$t_{evap,min} = \frac{h}{2r} \quad (8-17)$$

8.4.1.2. With a constant contact angle

For this approximation, the contact angle is assumed to be constant during the evaporation. The loss of volume per unit time is given by

$$\frac{dV}{dt} = -r \cdot A_{Lat} = -2\pi r(1 - \cos\theta)R^2 \quad (8-18)$$

From equation (8-3) one knows

$$R = \left(\frac{V}{Const} \right)^{\frac{1}{3}} ; \quad Const = \frac{\pi}{12} (8 - 9\cos(\theta) + \cos(3\theta)) \quad (8-19)$$

By putting equation (8-19) into equation (8-18), one obtains the differential equation:

$$\frac{dV}{dt} = -2\pi r(1 - \cos\theta) \left(\frac{V}{Const} \right)^{\frac{2}{3}} \quad (8-20)$$

which can be solved by assuming the contact angle θ to remain constant

$$V(t) = \left(V_i^{1/3} - \frac{2\pi r(1 - \cos \theta)}{3Const^{2/3}} t \right)^3 \quad (8-21)$$

Here V_i is the initial volume of the droplet. The time $t_{evap,max}$ needed to a full evaporation is determined by setting $V(t) = 0$.

$$t_{evap,max} = V_i^{1/3} \frac{3Const^{2/3}}{2\pi r(1 - \cos \theta)} = \frac{3}{2\pi r(1 - \cos \theta)} \frac{V_i}{R_i^2} \quad (8-22)$$

which can be , using equations (8-2), (8-1) and (8-7) simplified to:

$$t_{evap,max} = \frac{1}{2} \frac{h}{r} \frac{3a^2 + h^2}{a^2 + h^2} \quad (8-23)$$

Two borderline cases can further be derived from equation (8-23). The first is when the droplet is a hemisphere ($\theta = 90^\circ$), i.e. $a = R = h$. Then:

$$t_{evap,max} \Big|_{a=R=h} = \frac{h}{r} \quad (8-24)$$

The second is when θ is infinitesimal small ($h \ll a$):

$$\lim_{\theta \rightarrow 0} t_{evap,max} = \frac{3}{2} \frac{h}{r} \quad (8-25)$$

9. References

- 1 <http://www.hamiltoncomp.com>
- 2 http://www.cybio-vpn.de/english/liquid_handling.html
- 3 <http://www.seyonic.com>
- 4 <http://www.affymetrix.com/technology/manufacturing/index.affx>
- 5 http://www.imtek.de/anwendungen/index_en.php
- 6 <http://www.arrayit.com/Products/Printing>
- 7 P. Belaubre, M. Guirardel, G. Garcia, J.B. Pourciel, V. Leberre, A. Dagkessamanskaia, E. Trévisiol, J.M. François, and C. Bergaud, "*Fabrication of biological microarrays using microcantilevers*", *Appl. Phys. Lett.* **82**, 3122 (2003). (DOI: 10.1063/1.1565685)
- 8 J. Xu, M. Lynch, J.L. Huff, C. Mosher, S. Vengasandra, G. Ding, and E. Henderson, "*Microfabricated Quill-Type Surface Patterning Tools for the Creation of Biological Micro/Nano Arrays*", *Biomed. Microdevices* **6**, 117 (2004). (DOI: 10.1023/B:BMMD.0000031748.13353.10)
- 9 M.-H. Hong, K.H. Kim, J. Bae, and W. Jhe, "*Scanning nanolithography using a material-filled nanopipette*", *Appl. Phys. Lett.* **77**, 2604 (1999). (DOI: 10.1063/1.1319181)
- 10 A. Lewis, Y. Kheifetz, E. Shambrodt, A. Radko, E. Khatchatryan, and C. Sukenik, "*Fountain pen nanochemistry: Atomic force control of chrome etching*", *Appl. Phys. Lett.* **75**, 2689 (1999). (DOI: 10.1063/1.125120)
- 11 A. Bruckbauer, L. Ying, A.M. Rothery, D. Zhou, A.I. Shevchuk, C. Abell, Y.E. Korchev, and D. Klenerman, "*Writing with DNA and Protein Using a Nanopipet for Controlled Delivery*", *J. Am. Chem. Soc.* **124**, 8810 (2002). (DOI: 10.1021/ja026816c)
- 12 A. Meister, S. Jeney, M. Liley, T. Akiyama, U. Staufer, N.F. de Rooij, and H. Heinzelmann, "*Nanoscale dispensing of liquids through cantilevered probes*", *Microelec. Eng.* **67–68**, 644 (2003). (DOI: 10.1016/S0167-9317(03)00126-6)
- 13 <http://www.visualgenomics.ca>
- 14 J. Israelachvili, "*Intermolecular and Surface Forces*", 2nd edition, Academic Press Limited, London (1992)
- 15 <http://www.nobel.se/physics/laureates/1910/index.html>
- 16 "*Handbook of Chemistry and Physics*", 79th edition, CRC Press LLC, Boca Raton (1998)
- 17 A.W. Adamson and A.P. Gast, "*Physical Chemistry of Surfaces*", 6th edition, Wiley-Interscience Publication, New-York (1997)

- 18 H. Ibach,
"The role of surface stress in reconstruction, epitaxial growth and stabilization of mesoscopic structures",
 Surf. Sci. Rep. **29**, 193 (1997). (DOI: 10.1016/S0167-5729(97)00010-1)
- 19 R. Berger, E. Delamarche, H. P. Lang, C. Gerber, J. K. Gimzewski, E. Meyer, H.-J. Güntherodt,
"Surface Stress in the Self-Assembly of Alkanethiols on Gold"
 Science **276**, 2021 (1997). (DOI: 10.1126/science.276.5321.2021)
- 20 D. J. Eaglesham, A. E. White, L. C. Feldman, N. Moriya, and D. C. Jacobson,
"Equilibrium shape of Si",
 Phys. Rev. Lett. **70**, 1643 (1993). (DOI: 10.1103/PhysRevLett.70.1643)
- 21 R. J. Good,
"Contact angle, wetting, and adhesion: a critical review",
 pp. 3-36 in *"Contact Angle, Wettability and Adhesion"*, Volume 1, VSP, Utrecht (1993).
- 22 Z. Łodziana, N.-Y. Topsøe, J. K. Nørskov,
"A negative surface energy for alumina",
 Nature Materials **3**, 289 (2004). (DOI: 10.1038/nmat1106)
- 23 B. Cappella and G. Dietler,
"Force-distance curves by atomic force microscopy",
 Surf. Sci. Rep. **34**, 1 (1999). (DOI: 10.1016/S0167-5729(99)00003-5)
- 24 P. S. Swain and R. Lipowsky,
"Contact Angles on Heterogeneous Surfaces: A New Look at Cassie's and Wenzel's Laws",
 Langmuir **14**, 6772 (1998). (DOI: 10.1021/la980602k)
- 25 L.-H. Lee,
"Roles of molecular interactions in adhesion, adsorption, contact angle and wettability",
 pp. 45-96 in *"Contact Angle, Wettability and Adhesion"*, Volume 1, VSP, Utrecht (1993).
- 26 G. J. Hirasaki,
"Structural interactions in the wetting and spreading of van der Waals fluids",
 pp. 183-220 in *"Contact Angle, Wettability and Adhesion"*, Volume 1, VSP, Utrecht (1993).
- 27 R. N. Wenzel,
"Resistance of Solid Surfaces to Wetting by Water",
 Ind. Eng. Chem. **28**, 988 (1936).
- 28 R. N. Wenzel,
"Surface Roughness and Contact Angle",
 J. Phys. Chem. **53**, 1466 (1949).
- 29 A. B. D. Cassie and S. Baxter,
"Wettability of porous surfaces",
 Trans. Faraday Soc. **40**, 546 (1944). (DOI: 10.1039/TF9444000546)
- 30 A. D. B. Cassie,
"Contact angles",
 Discuss. Faraday Soc. **3**, 11 (1948). (DOI: 10.1039/DF9480300011)
- 31 N. A. Patankar,
"On the Modeling of Hydrophobic Contact Angles on Rough Surfaces",
 Langmuir **19**, 1249 (2003). (DOI: 10.1021/la026612+)

- 32 J. Kim and C.-J. Kim,
"Nanostructured surfaces for dramatic reduction of flow resistance in droplet-based microfluidics",
 The Fifteenth IEEE International Conference on Micro Electro Mechanical Systems 2002, 479 (2002).
- 33 D. Öner and T. J. McCarthy,
"Ultrahydrophobic Surfaces. Effects of Topography Length Scales on Wettability",
 Langmuir **16**, 7777 (2000). (DOI: 10.1021/la000598o)
- 34 J. C. Love, B. D. Gates, D. B. Wolfe, K. E. Paul, and G. M. Whitesides,
"Fabrication and Wetting Properties of Metallic Half-Shells with Submicron Diameters",
 Nano Letters **2**, 891 (2002). (DOI: 10.1021/nl025633l)
- 35 S. Shibuichi, T. Onda, N. Satoh, and K. Tsujii,
"Super Water-Repellent Surfaces Resulting from Fractal Structure",
 J. Phys. Chem. **100**, 19512 (1996). (DOI: 10.1021/jp9616728)
- 36 J. Drelich,
"The significance and magnitude of the line tension in three-phase (solid-liquid-fluid) systems",
 Colloids Surf. A **116**, 43 (1996). (DOI: 10.1016/0927-7757(96)03651-5)
- 37 T. Pompe and S. Herminghaus,
"Three-Phase Contact Line Energetics from Nanoscale Liquid Surface Topographies",
 Phys. Rev. Lett. **85**, 1930 (2000). (DOI: 10.1103/PhysRevLett.85.1930)
- 38 A. Checco, P. Guenoun, and J. Daillant,
"Nonlinear Dependence of the Contact Angle of Nanodroplets on Contact Line Curvature",
 Phys. Rev. Lett. **91**, 186101 (2003). (DOI: 10.1103/PhysRevLett.91.186101)
- 39 J. Y. Wang, S. Betelu, and B. M. Law,
"Line tension approaching a first-order wetting transition: Experimental results from contact angle measurements",
 Phys. Rev. E **63**, 031601 (2001). (DOI: 10.1103/PhysRevE.63.031601)
- 40 F. M. Orr, L. E. Scriven and A. P. Rivas,
"Pendular rings between solids: meniscus properties and capillary force",
 J. Fluid Mech. **67**, 723 (1975).
- 41 E. A. Boucher,
"Capillary phenomena: Properties of systems with fluid/fluid interfaces",
 Rep. Prog. Phys. **43**, 497 (1980). (DOI: 10.1088/0034-4885/43/4/003)
- 42 L. D. Landau and E. M. Lifshitz,
"Fluid Mechanics", 2nd edition, Butterworth-Heinemann, Oxford (1987).
- 43 J. Plateau,
"Statique expérimentale et théorique des liquides soumis aux seules forces moléculaires",
 Gauthier-Villars, Paris (1873).
- 44 L. A. Slobozhanin, J. I. D. Alexander, and V. D. Patel,
"The stability margin for stable weightless liquid bridges",
 Phys. Fluids **14**, 209 (2002). (DOI 10.1063/1.1420736)
- 45 M. A. Erle, R. D. Gillette and D. C. Dyson,
"Stability of interfaces of revolution with constant surface tension—the case of the catenoid"
 Chem. Eng. J. **1**, 97 (1970). (DOI: 10.1016/0300-9467(70)85003-1)

- 46 D. H. Michael,
"Meniscus stability",
Ann. Rev. Fluid Mech. 13, 189 (1981). (DOI: 10.1146/annurev.fl.13.010181.001201)
- 47 G. A. Somorjai,
"Introduction to surface chemistry and catalysis", Wiley-Interscience Publication, New-York
(1994)
- 48 Y. Ando,
"The effect of relative humidity on friction and pull-off forces measured on submicron-size
asperity arrays",
Wear 238, 12 (2000). (DOI: 10.1016/S0043-1648(99)00334-8)
- 49 G. Binnig, H. Rohrer, Ch. Gerber, and E. Weibel,
"Tunneling through a controllable vacuum gap",
Appl. Phys. Lett. **40**, 178 (1982). (DOI: 10.1063/1.92999)
- 50 G. Binnig, H. Rohrer, Ch. Gerber, and E. Weibel,
"Surface Studies by Scanning Tunneling Microscopy",
Phys. Rev. Lett. **49**, 57 (1982). (DOI: 10.1103/PhysRevLett.49.57)
- 51 G. Binnig, C. F. Quate, and Ch. Gerber,
"Atomic Force Microscope",
Phys. Rev. Lett. **56**, 930 (1986). (DOI: 10.1103/PhysRevLett.56.930)
- 52 <http://www.veeco.com>
- 53 <http://www.kruss.de>
- 54 <http://www.kappa.de>
- 55 <http://www.oxford-instruments.com>
- 56 <http://www.bandelin.com>
- 57 <http://www.millipore.com>
- 58 <http://www.bocedwards.com>
- 59 <http://www.research-instruments.com>
- 60 M. J. Madou,
"Fundamentals of microfabrication", CRC Press LLC, Boca Raton (1997)
- 61 <http://www.uwgb.edu>
- 62 <http://www.ee.ucla.edu>
- 63 <http://www-imt.unine.ch>
- 64 <http://www.csem.ch>
- 65 <http://www.feicompany.com>
- 66 <http://www.empa.ch>
- 67 <http://www.veecoprobes.com>
- 68 <http://www.af-fe.de>
- 69 <http://www.merck.de>
- 70 <http://www.sigmaldrich.com>
- 71 <http://www.lancastersynthesis.com>

- 72 <http://www.abcr.de>
- 73 <http://www.rockemat.com>
- 74 <http://www.siltronic.com>
- 75 <http://www.2spi.com>
- 76 <http://www.menzel.de>
- 77 A. Ulman,
"An Introduction to Ultrathin Organic Films: From Langmuir-Blodgett to Self-Assembly",
 Academic Press Inc, San Diego (1991).
- 78 F.-J. Elmer and M. Dreier,
"Eigenfrequencies of a rectangular atomic force microscope cantilever in a medium",
 J. Appl. Phys. **81**, 7709 (1997). (DOI: 10.1063/1.365379)
- 79 J.E. Sader, I. Larson, P. Mulvaney, and L.R. White,
"Method for the calibration of atomic force microscope cantilevers",
 Rev. Sci. Instrum. **66**, 3789 (1995). (DOI: 10.1063/1.1145439)
- 80 J.J. Wortman and R. A. Evans,
"Young's Modulus, Shear Modulus, and Poisson's Ratio in Silicon and Germanium",
 J. Appl. Phys. **36**, 153 (1965).
- 81 C. Bourgeois, J. Hermann, N. Blanc, N.F. de Rooij, and F. Rudolf,
"Determination Of The Elastic Temperature Coefficients Of Monocrystalline Silicon"
 Proceeding of "The 8th International Conference on Solid-State Sensors and Actuators, 1995 and
 Eurosensors IX. Transducers '95", **2**, 92 (1995).
- $$E_{\langle 110 \rangle} = \frac{1}{\frac{s_{11}}{2} + \frac{s_{12}}{2} + \frac{s_{44}}{4}}$$
- 82 J.L. Hutter and J. Bechhoefer,
"Calibration of atomic-force microscope tips",
 Rev. Sci. Instrum. **64**, 1868 (1993). (DOI: 10.1063/1.1143970)
- 83 E.O. Brigham,
"The Fast Fourier Transform",
 Prentice-Hall Inc, Englewood Cliffs (1974).
- 84 R Lévy and M Maaloum,
*"Measuring the spring constant of atomic force microscope cantilevers: thermal fluctuations and
 other methods"*,
 Nanotechnology **13**, 33 (2002). (DOI: 10.1088/0957-4484/13/1/307)
- 85 <http://www.vwr.com>
- 86 J.P. Cleveland, S. Manne, D. Bocek, and P.K. Hansma,
*"A nondestructive method for determining the spring constant of cantilevers for scanning force
 microscopy"*,
 Rev. Sci. Instrum. **64**, 403 (1993). (DOI: 10.1063/1.1144209)
- 87 <http://www.ntmdt.ru>
- 88 R.D. Deegan, O. Bakajin, T.F. Dupont, G. Huber, S.R. Nagel, and T.A. Witten,
"Contact line deposits in an evaporating drop",
 Phys. Rev. E **62**, (2000). (DOI: 10.1103/PhysRevE.62.756)
- 89 <http://www4.amershambiosciences.com>

- 90 <http://www.microparticles.de>
- 91 <http://www.probes.com>
- 92 <http://www.polymersource.com>
- 93 T. Kodadek,
"Protein microarrays: prospects and problems",
Chem. Biol. **8**, 105 (2001). (DOI: 10.1016/S1074-5521(00)90067-X)
- 94 G. MacBeath,
"*Protein microarrays and proteomics*",
Nature Genetics **32** supplement, 526 (2002). (DOI: 10.1038/ng1037)
- 95 A. Butte,
"*The use and analysis of microarray data*",
Nature Reviews Drug Discovery **1**, 951 (2002). (DOI: 10.1038/nrd961)
- 96 D.L. Gerhold, R.V. Jensen, and S.R. Gullans,
"*Better therapeutics through microarrays*",
Nature Genetics **32** supplement, 547 (2002). (DOI: 10.1038/ng1042)
- 97 P. Vettiger, M. Despont, U. Drechsler, U. Dürig, W. Häberle, M.I. Lutwyche, H.E. Rothuizen, R. Stutz, R. Widmer, and G.K. Binnig,
"The 'Millipede' -- More than one thousand tips for future AFM data storage",
IBM J. Res. Dev. **44**, 323 (2000), (DOI: 10.1147/rd.443.0323)
- 98 <http://scilabsoft.inria.fr>

Curriculum Vitae

Vorname, Name: André Meister
Adresse: Rue Neuve 3, 2314 La Sagne
Geburtsdatum: 11 Februar 1963
Heimatort: Matzendorf (SO)
Nationalität: Schweiz

- 2001-2004 Promotionsstudium an der Universität Basel.
Arbeit an vorliegender Dissertation unter der Leitung von PD Dr. H. Heinzelmann
an der Universität Basel und am Centre Suisse d'Electronique et de
Microtechnique in Neuchâtel.
- 2001 **Diplom** in Experimental Physik.
- 1996-2001 Studium der Physik an der Universität Basel.
- 1990-1996 Angestellt bei Georges Ruedin S.A. in Bassecourt.
- 1986-1990 Temporär Angestellt bei Black & Decker S.A. in Delémont,
Temporär Angestellt bei Von Roll S.A. in Delémont
Kulturelle Reise nach Asien.
- 1986 **Diplom** als Ingenieur HTL.
- 1983-1986 Studium an der Abteilung Maschinentechnik, Höhere Technische Lehranstalt des
Staates Bern in Biel.
- 1983 **Fähigkeitszeugnis** als Maschinenzeichner.
- 1979-1983 Lehre als Maschinenzeichner bei Von Roll S.A. in Delémont.

Folgenden Dozentinnen und Dozenten der Universität Basel verdanke ich meine wissenschaftliche Ausbildung:

C. Bandle, G. Baur, B. Binggeli, C. Bruder, R. Buser, A. Bussmann-Holder, F.J. Elmer, J.
Jourdan, M. Hegner, H. Heinzelmann, H. Kraft, B. Krusche, D. Loss, D. Masser, E. Meyer, P.
Oelhafen, C. Schönenberger, I. Sick, G. Tammann, L. Tauscher, F.K. Thielemann, H. Thomas,
D. Trautmann, C. Trefzger, C. Ullrich, P. Zimak.